Stationaire, MR-compatibele hersen-SPECT-beeldvorming
met behulp van 'multi-pinhole'-collimatoren

Stationary, MR-Compatible Brain SPECT Imaging
Based on Multi-Pinhole Collimators

Karen Van Audenhaege

Promotoren: prof. dr. S. Vandenberghe, prof. dr. R. Van Holen
Proefschrift ingediend tot het behalen van de graad van
Doctor in de Ingenieurswetenschappen: Biomedische Ingenieurstechnieken

Vakgroep Elektronica en Informatiesystemen
Voorzitter: prof. dr. ir. R. Van de Walle
Faculteit Ingenieurswetenschappen en Architectuur
Academiejaar 2014 - 2015

UNIVERSITEIT
GENT

ISBN 978-90-8578-822-5
NUR 954
Wettelijk depot: D/2015/10.500/66

Department of Electronics and Information Systems
Faculty of Engineering and Architecture
Ghent University

MEDISIP
IBiTech - iMinds
Campus Heymans, Block B
De Pintelaan 185
9000 Ghent
Belgium

Promotors:
Prof. dr. Stefaan Vandenberghe
Prof. dr. Roel Van Holen

Board of examiners:
Prof. dr. ir. Hendrik Van Landeghem, Ghent University, chairman
Prof. dr. ir. Wout Joseph, Ghent University, secretary
Prof. dr. Christian Vanhove, Ghent University
Prof. dr. Marlies Goorden, Delft University of Technology
Prof. dr. Stephen C. Moore, Harvard Medical School
Prof. dr. Brian F. Hutton, University College London
Prof. dr. Jan Booij, University of Amsterdam
Prof. dr. Stefaan Vandenberghe, Ghent University
Prof. dr. Roel Van Holen, Ghent University

This work was funded by a PhD grant of the Institute for the Promotion of Innovation through Science and Technology in Flanders (IWT-Vlaanderen).

Table of Contents

List of Figures

List of Tables

List of acronyms

A

AC	Attenuation correction
APD	Avalenche photodiode

B

Bq	Becquerel
BOLD	Blood-oxygen-level dependent
BKE	Background-known-exactly
BKS	Background-known-statistically
BS	Body support

C

CAD	Computer-aided design
CFD	Convolution-based forced detection
CFOV	Central point of the field of view
CHO	Channelized Hotelling observers
CNR	Contrast-to-Noise Ration
conv	converging
CRB	Cramer-Rao lower bound
CRC	Contrast recovery coefficient
CROSEM	Count-regulated ordered subset maximum likelihood expectation maximization
CT	Computed Tomography

D

DM	De-multiplexed
dSiPM	Digital silicon photomultiplier
DTI	Diffusion tensor imaging
DWI	Diffusion weighted imaging

F

FAN	Fan-beam
FBP	Filtered back projection
FD	Forced detection
FFT	Fast Fourier transform
FID	Free induction decay
FIM	Fisher information matrix
fMRI	Functional magnetic resonance imaging
FOV	Field of view
FWHM	Full width at half maximum

G

GATE	GEANT application for tomographic emission
GEANT4	Geometry and tracking 4
GPU	Graphical processing unit

I

it	iteration

L

LEHR	Low energy high resolution
LOR	Line of response
LSI	local shift invariant
LSYO	Lutetium Yttrium Orthosilicate

M

M	Multiplexed
MRI	Magnetic resonance imaging
MLEM	Maximum likelihood expectation maximization
MoM	Method of moments
MPH	Multi-pinhole

N

NM	Non-multiplexed
NPW-SNR	Non-prewhitening signal-to-noise ratio

O

OSEM	Ordered subset expectation maximization

P

PAR	Parallel-hole
PDF	Probability density function
PEC	Perfect electric conductor
PET	Positron emission tomography
PiHo	Pinhole
PMMA	Polymethyl Methacrylate
PMT	Photomultiplier tube
PSF	Point spread function

R

rCBF	Regional cerebral blood flow
RF	Radio Frequency
ROC	receiver-operator characteristic
ROI	Region of interest
ROR	Radius of rotation
Rx	Receiver

S

SNR	Signal-to-noise ratio
SFIM	Sub-sampled Fisher information matrix
SiPM	Silicon photomultiplier
SKE	Signal-known-exactly
SPECT	Single photon computed tomography
SPH	Single pinhole
subs	OSEM subsets

T

Tx	Transmitter

U

UHR	Ultra high resolution

V

VEP	Volume equivalence principle

English summary

The aim of this dissertation is to increase the image quality of human brain SPECT (Single Photon Emission Computed Tomography) and make it MR-compatible (MR: Magnetic Resonance Imaging). Currently, brain SPECT imaging is mostly performed with clinical dual- or triple-head gamma cameras, which are bulky, non-stationary, non-adaptive, non-MR-compatible and which have a low sensitivity and a bad resolution. We want to overcome these limitations using innovative multi-pinhole collimator design.

Introduction

SPECT is a nuclear imaging technique. It visualizes biochemical and physiological functions and allows one to detect abnormalities long before any anatomical changes appear and is therefore an important tool for evaluating and managing patients. Nuclear imaging is based on a radioactive tracer that is administered to the patient and distributes in the patient's body by participating in a physiological process. Photons are emitted following radioactive decay and can be detected with a gamma camera, which consists of a collimator that restrict the direction of the incoming photons to a well-known angle, and a detector. In most clinical systems, the gamma camera rotates around the patient to acquire projection data at different angles. A reconstruction algorithm can then be used to reconstruct the three-dimensional (3D) distribution of the molecules.

Motivation for improving brain SPECT

SPECT is commonly used for the diagnosis of brain diseases. Clinical application are for example the diagnosis and follow-up of dementia, cerebrovascular disease, brain trauma, epilepsy and brain tumors. Dementia is a

broad category of brain diseases that affects more and more people (globally about 36 million people). There are several forms of dementia, including Alzheimer's disease, vascular dementia and dementia with Lewy Bodies and SPECT imaging can help to make a differential diagnosis which potentially can aid in patient management.

Current SPECT systems have a limited spatial resolution (8-10 mm) and sensitivity (about $4x10^{-4}$ cps/Bq). This is quite low in comparison with Position Emission Tomography (PET) where a spatial resolution of about 5 mm can be achieved with a sensitivity on the order of 10^{-2} cps/Bq. Therefore, many researchers believed for a long time that PET would rapidly replace SPECT. However, market research has shown that an increased number of PET sales did not result in a decreased number of SPECT sales. An important reason for this is the high pricing and practical issues associated with PET systems and tracers. PET tracers have a shorter half-life than SPECT tracers and require expensive cyclotron infrastructure and specialists within the hospital. There are also applications where the SPECT tracer has a higher specificity and sensitivity, which results in a better clinical diagnosis with SPECT than with PET, for example for differentiating dementia with Lewy Bodies from Alzheimer's disease [118]. SPECT is also particularly suited for studying focal epilepsy because the tracer can be administered during the ictal phase (during the seizure), after which it gets trapped in the brain so that we can wait until the seizure stopped to perform the SPECT scan. This cannot be done with any of the currently available PET tracers.

In conclusion, it is important to keep investing in improving SPECT systems. A better resolution and/or sensitivity would result in a better diagnosis and thus in an earlier and better treatment of the patient. This is not only a social advantage but it also results in cost reductions for hospitals and health insurances. In addition, improving SPECT imaging will also allow smaller hospitals to have access to molecular brain imaging.

Motivation for making SPECT MR-compatible

Nowadays, most commercial SPECT systems are combined with X-ray Computed tomography (CT) in so-called SPECT/CT systems to obtain an anatomical background for the functional information. However, while CT images have a high spatial resolution, they have a low soft-tissue contrast, which is an important disadvantage for brain imaging. MRI on the other hand, has a very high soft-tissue contrast and allows one to further adapt

the contrast to the needs of a specific application by using different sequences. In addition, MRI does not come with extra ionizing radiation dose for the patient (unlike CT), which is particularly important in pediatric cases or for sensitive organs like the brain. Truly integrated SPECT/MRI will enhance patient comfort, result in higher throughput, allow accurate motion correction and guarantee a perfect coregistration of both images.

Until now, research on SPECT/MRI has been mostly focussing on preclinical systems (for imaging small animals) but it could also be interesting for clinical applications. In this dissertation, we want to design a brain SPECT insert that can be integrated in a clinical MRI system. Research centers and large hospitals that have such an MRI, can then use it for simultaneous SPECT/MR imaging so that both personnel and patients can save time.

Challenges

In this dissertation, we decided to focus on innovative multi-pinhole collimator design. This was inspired by the great progress that has been made in preclinical SPECT systems. While clinical SPECT systems are usually based on parallel-hole or fan-beam collimators, preclinical SPECT systems are typically equipped with multi-pinhole collimators. They use pinhole magnification to obtain sub-millimeter resolution in combination with a high sensitivity. A multi-pinhole collimator also allows the system to be stationary so that we can avoid calibration challenges that typically occur when a heavy collimator and/or detector needs to be rotated and so that it can be more easily integrated with an MRI (rotation would perturb the homogeneity of the magnetic field).

Unfortunately, these preclinical systems can not simply be rescaled to the size of a human brain and several challenges remain. Firstly, there is the challenge of obtaining sufficient angular sampling without rotating the system. The more pinholes, the better the angular sampling, but if we use magnification, we will need a very large detector to prevent the pinholes projections from overlapping. Secondly, there is the challenge of maintaining sufficient sensitivity because pinhole sensitivity is inversely quadratic with its distance to the source (which is bigger in a human brain than in a mouse) and because sensitivity typically decreases when resolution improves (this is called the sensivity-resolution trade-off). Finally, as we aim at making brain SPECT imaging MR-compatible, there is the challenge of using only MR-compatible materials, keeping eddy currents in the collimator minimal and making the system sufficiently compact such that it fits in the bore of

a clinical MR.

Solutions

As a solution to overcome these challenges and improve brain SPECT imaging, we proposed two different approaches. In the first approach, we used a very large detector ring based on current low resolution detector technology (intrinsic resolution of 4 mm) in combination with an innovative stationary multi-pinhole collimator equipped with a shutter mechanism. In the second approach we used new high-resolution detector technology (with an intrinsic resolution of 0.5 mm) in combination with minifying pinholes, which allows the system to be compact. We will now describe these two approaches in more detail and we will explain how we applied them in our research.

In **chapter 4** we focussed on improving brain SPECT imaging based on the first approach. We designed a stationary full-ring multi-lofthole collimator for brain SPECT imaging based on a large whole-body detector ring (the LaPET) with 4 mm intrinsic spatial resolution and we introduced the concept of a shutter mechanism (allowing to open/close loftholes) to ensure sufficient angular sampling without rotating the system. We used loftholes because they more efficiently use the available detector area. They have a rectangular exit window and were developed in our research group. In order to optimize the different system parameters, we developed a method that maximizes sensitivity given a target resolution, based on analytical simulations. We aimed at a system resolution of 6 mm and used the method to derive the optimal diameter of the collimator ring, the optimal lofthole aperture and the maximum number of loftholes that can be opened simultaneously without having the projections overlap with each other. However, despite the large detector ring and the multi-lofthole design, we obtained a sensitivity that was 2.5 times lower than the sensitivity of a dual-head system with LEHR (Low energy high resolution) parallel-hole collimators. This was the price paid for higher resolution (6 mm versus 9.8 mm). The multi-lofthole system was then compared with such a clinical dual-head system based on simulations and using contrast-to-noise ratio and NPW-SNR (non-prewhitening matched filter signal-to-noise ratio), which is a measure for lesion detectability. We found that the multi-lofthole system performs best for detecting hot lesions but shows a lower contrast-to-noise ratio in cold lesions. The main reason for that is insufficient sensitivity.

In **chapter 5** we therefore investigated the possibility of further increasing sensitivity by opening more loftholes simultaneously, even though this

causes the projections to overlap on the detector (also called multiplexing). Simulations showed that multiplexing can cause distortions in the reconstructed images but that these can be resolved by combining multiplexed with non-multiplexed projection data, which can be done by opening more or fewer loftholes with the shutter mechanism. Later in chapter 5, we investigated the conditions needed to obtain artifact-free images with overlapping projections. We showed that incomplete sampling is the cause of artifacts in multiplexing multi-pinhole systems and developed a method to evaluate the sampling completeness of a system, to predict whether the images could show artifacts or not. We also simulated images for different multiplexing multi-pinhole systems and compared them with a system with non-overlapping pinhole projections. The results showed that although multiplexing allows us to increase sensitivity dramatically, the improvement in contrast-to-noise ratio is not that obvious. The reconstruction of the images from the multiplexing setups appeared to converge slower. This counteracts the increased sensitivity and as a result we found only small differences in contrast-to-noise ratio, of the same order of magnitude as the standard deviation of the results. We also investigated NPW-SNR and for this task, we did find an improvement. We also found that multiplexing can improve angular sampling and concluded that multiplexing can be a good choice for practical reasons (when shielding is difficult) and that no artifacts are to be expected as long as sampling sufficiency is obtained.

In **chapter 6** we focussed on making brain SPECT MR-compatible using the second approach. We used high-resolution detector technology (with an intrinsic resolution of 0.5 mm) in combination with minifying pinholes to make a stationary and compact system. We used the optimization method that was developed in chapter 4 and optimized the different system parameters to maximize sensitivity for a system resolution of 7.2 mm. The MR-compability of the collimator was also investigated and the system performance was compared with a rotating triple-head fan-beam system, based on simulations. The image quality appeared to be similar, with the big difference that the triple-head system is not MR-compatible, while the multi-pinhole SPECT system is.

Conclusion

This dissertation resulted in a new alternative design for brain SPECT imaging, based on a shutters that ensure sufficient angular sampling without rotating the system.

We also developed an optimization method that maximizes sensitivity of a full-ring multi-pinhole collimator, given a target resolution.

Additionally, we gained fundamentally new insights on multiplexing artifacts: we showed that they are caused by incomplete sampling and we developed a method to evaluate sampling completeness in multiplexing pinhole designs.

Finally, we demonstrated the feasibility of designing a compact multi-pinhole brain SPECT system that fits inside a clinical MRI, is MR-compatible and that has a similar image quality as current clinical SPECT systems. A simultaneous SPECT/MRI has the potential to fundamentally change brain imaging in the future.

This research was performed at the research group MEDISIP (MEDical Image and Signal Processing) in the ELIS department of the faculty of engineering. The work presented here resulted in 1 patent, 4 A1 journal papers as a first author (of which one is still under review), 2 A1 journal publications as a co-author and 12 contributions at international conferences. The references to these publications are given in the next chapter.

Nederlandstalige samenvatting

Dit onderzoek situeert zich binnen het onderzoeksveld van SPECT (Eng.: Single Photon Emission Computed Tomography) en de combinatie van SPECT met MRI (Eng: Magnetic Resonance Imaging). Het hoofddoel van dit proefschrift is om humane hersen-SPECT-beeldvorming te verbeteren en MR-compatibel te maken. De huidige systemen die voor hersen-SPECT-beeldvorming gebruikt worden, zijn meestal twee- of driekoppige gammacamera's die niet stationair, niet adaptief en niet MR-compatibel zijn en een beperkte resolutie en sensitiviteit hebben. Wij willen deze beperkingen oplossen met behulp van innovatieve 'multi-pinhole'-collimatoren.

Inleiding

SPECT (Eng.: Single Photon Emission Computed Tomography) is een nucleaire beeldvormingstechniek die biochemische en fysiologische processen in beeld brengt. Het laat toe om vroegtijdig problemen op te sporen, nog voordat er anatomische veranderingen zichtbaar zijn en speelt daarom ook een belangrijke rol in de moderne geneeskunde. Nucleaire beeldvorming is gebaseerd op een radioactieve speurstof die in de bloedbaan wordt geïnjecteerd, vervolgens deelneemt aan een bepaald fysiologisch proces en zich daardoor verspreidt in het lichaam van de patiënt. De bij het radioactief verval vrijgekomen fotonen worden gedetecteerd met een gammacamera, bestaande uit een collimator, die enkel de fotonen uit een bepaalde, gekende invalshoek doorlaat, en een detector. Door projecties onder verschillende hoeken op te meten, kan de verdeling van de moleculen in het lichaam dan als 3D-beeld gereconstrueerd worden.

Motivatie voor de verbetering van hersen-SPECT

SPECT is een veelgebruikte modaliteit voor het stellen van diagnoses bij hersen-aandoeningen. Klinische toepassingen zijn bijvoorbeeld de diagnose en opvolging van dementie, cerebrovasculaire aandoeningen, hersentrauma, epilepsie en hersentumoren. Dementie is een veelvoorkomende hersenaandoening die door de vergrijzing van onze samenleving steeds meer mensen treft. Momenteel zijn er wereldwijd meer dan 36 miljoen dementiepatiënten. De meest voorkomende oorzaak van dementie is Alzheimer, maar dementie kan ook andere oorzaken hebben zoals vasculaire dementie of dementie met Lewy Bodies. Het is belangrijk om zo vroeg mogelijk een differentiële diagnose te stellen zodat de juiste behandeling kan geselecteerd worden en daarvoor is een goede beeldkwaliteit belangrijk.

De huidige klinische SPECT-systemen hebben echter een beperkte spatiale resolutie (8-10 mm) en sensitiviteit (in de orde van 10^{-4} cps/Bq), wat laag is in vergelijking met PET (Eng: Positron Emission Tomography) waar een spatiale resolutie van ongeveer 5 mm kan bekomen worden bij een sensitiviteit in de orde van 10^{-2} cps/Bq. Om die reden geloofden onderzoekers en artsen lange tijd dat SPECT snel vervangen zou worden door PET. Toch heeft marktonderzoek dit niet bevestigd en is er aangetoond dat een stijging in de verkoopcijfers van PET niet tot een daling leidde in de verkoopcijfers van SPECT. Een belangrijke reden hiervoor is de hoge kostprijs en de praktische problemen van PET systemen en speurstoffen. PET speurstoffen hebben een korter halfleven dan SPECT speurstoffen, waardoor het noodzakelijk is om naast het ziekenhuis een dure cyclotron te installeren en de daarbijbehorende specialisten in dienst te nemen. Verder zijn er ook toepassingen waarbij de SPECT speurstof een hogere specificiteit en sensitiviteit heeft waardoor de klinische diagnose met SPECT beter is dan met PET, bijvoorbeeld voor de differentiële diagnose tussen dementie met Lewy Bodies en Alzheimer [118]. SPECT is ook bijzonder geschikt voor studies in focale epilepsie omdat de speurstof tijdens de ictale fase (tijdens de aanval) kan ingespoten worden, waarna die vastgehouden wordt in de hersenen zodat we kunnen wachten tot de aanval voorbij is om de SPECT-scan uit te voeren. PET speurstoffen zijn hiervoor veel minder geschikt.

Tot slot is het belangrijk om te blijven investeren in de verbetering van SPECT-systemen. Een betere resolutie en/of sensitiviteit zou tot betere diagnoses leiden en dus ook tot een snellere en betere behandeling van de patiënt. Dit is niet alleen een maatschappelijk voordeel, maar leidt ook tot kostenbesparingen voor ziekenhuizen en ziektefondsen. Door SPECT-beeldvorming te verbeteren kunnen ook financieel minder sterke instanties

toegang krijgen tot een accurate beeldvorming van de hersenen.

Motivatie om SPECT MR-compatibel te maken

In de huidige systemen wordt SPECT meestal gecombineerd met X-stralen computertomografie (CT), waarbij aan de ene kant van de patiënt een X-stralen bron geplaatst wordt en aan de andere kant een detector, wat anatomische beelden oplevert. Door SPECT en CT te combineren kunnen functionele en anatomische beelden eenvoudig over elkaar geplaatst worden, wat tot een betere diagnose leidt. Een belangrijk nadeel van CT voor hersenbeeldvorming is zijn laag zachtweefselcontrast. MRI, daarentegen, heeft wel een hoog zachtweefselcontrast, is ook een anatomische modaliteit en laat ook toe om verschillende sequenties te gebruiken om het contrast verder aan te passen aan de noden van de specifieke toepassing. Bij MRI wordt de patiënt ook niet blootgesteld aan extra ioniserende straling (zoals X-rays bij CT), wat vooral belangrijk is in de pediatrie of voor erg gevoelige organen, zoals de hersenen. Met simultane SPECT/MRI zal het comfort van de patiënt verbeteren, het aantal scans per dag verhogen, kunnen de beelden gecorrigeerd worden voor beweging en kan een perfecte coregistratie van beide beelden gegarandeerd worden.

SPECT/MRI is tot nu toe vooral onderzocht geweest in de context van preklinische systemen (voor de beeldvorming van kleine proefdieren). In dit proefschrift willen we een hersen-SPECT systeem ontwikkelen dat kan ingebracht worden in een klinische MRI zodat onderzoekscentra en grotere ziekenhuizen die over een dergelijk systeem beschikken hun MRI kunnen gebruiken als een SPECT/MRI-systeem en op die manier tijd besparen voor zowel het personeel als de patiënten.

Probleemstelling

In dit proefschrift werd beslist om te focussen op het ontwerp van innovatieve 'multi-pinhole'-collimatoren, geïnspireerd op de grote vooruitgang die daarmee gemaakt werd in preklinische SPECT-systemen, waar pinholes gebruikt worden om het object te vergroten en zo sub-millimeter-resoluties behaald worden in combinatie met een hoge sensitiviteit. Verder maken 'multi-pinhole'-collimatoren het ook mogelijk om stationaire systemen te bouwen, zodat we calibratie-artefacten kunnen vermijden die typisch optreden wanneer een zware collimator en/of detector geroteerd moet worden

en zodat het systeem ook makkelijk kan geïntegreerd worden in een MRI (rotatie zou de homogeniteit van het magnetisch veld verstoren).

Helaas kunnen de bestaande preklinische systemen niet eenvoudig herschaald worden naar de afmetingen van de humane hersenen. De voornaamste reden hiervoor is dat de sensitiviteit van een pinhole omgekeerd evenredig is met de afstand tot de bron (welke groter is bij de hersenen dan bij bv. een muis), waardoor het moeilijk is om voldoende sensitiviteit te bekomen. Verder is het ook een uitdaging om voldoende hoekbemonstering te bekomen zonder het systeem te roteren. Hoe meer pinholes, hoe beter de hoekbemonstering, maar aangezien de projecties vergrotingen zijn van de hersenen, hebben we een zeer groot detectoroppervlakte nodig om te voorkomen dat de pinholeprojecties overlappen. Tot slot, aangezien het ons doel is om hersen-SPECT-beeldvorming MR-compatibel te maken, is het belangrijk om enkel MR-compatibele materialen te gebruiken, eddy currents zoveel mogelijk te beperken en het systeem voldoende compact te maken zodat het in een klinisch MR-systeem past.

Oplossingen

Als oplossing voor deze problemen en met het doel om hersen-SPECT-beeldvorming te verbeteren, hebben we twee verschillende benaderingen voorgesteld. In de eerste benadering vertrekken we van een zeer grote detector ring met een intrinsieke resolutie vergelijkbaar met wat momenteel in de klinische praktijk gebruikt wordt (4 mm) in combinatie met een innovatieve, stationaire 'multi-pinhole'-collimator uitgerust met een shuttermechanisme. In de tweede benadering vertrekken we van nieuwe, hoge-resolutie-detectoren (met een intrinsieke resolutie van 0.5 mm) in combinatie met verkleinende pinholes, wat toelaat om een compact systeem te ontwerpen. In de volgende paragrafen beschrijven we deze benaderingen in meer detail en leggen we uit hoe we ze toegepast hebben in dit proefschrift.

In **hoofdstuk 4** lag de focus vooral op het verbeteren van hersen-SPECT-beeldvorming op basis van de eerste benadering en ontwierpen we een stationaire, ringvormige 'multi-lofthole'-collimator voor hersen-SPECT-beeldvorming vertrekkende van een grote humane detector ring (de LaPET) met een intrinsieke resolutie van 4 mm. Als oplossing om rotatie te vermijden, stelden we het concept van een shuttermechanisme voor. Hiermee kunnen loftholes geopend/afgesloten worden en door beurtelings verschillende loftholes te openen, kan uiteindelijk voldoende bemonstering bekomen worden zonder dat het systeem moet geroteerd worden. Verder gebruikten

we loftholes (welke in onze onderzoeksgroep ontwikkeld werden) in plaats van pinholes omdat aangetoond is dat deze tot een beter gebruik van de detector oppervlakte leidt (omdat de projecties vierkant zijn en niet rond).

Vervolgens optimaliseerden we de collimator. Hiervoor ontwikkelden we een methode die de sensitiviteit maximaliseert op basis van analytische berekeningen, gegeven een beoogde spatiale resolutie. We gebruikten deze methode om de optimale diameter van de collimator ring, de optimale lofthole opening en het maximaal aantal loftholes te berekenen dat gelijktijdig geopend kan zijn zonder dat de projecties met elkaar overlappen. Ondanks de grote detector ring en het 'multi-lofthole'-ontwerp, was de sensitiviteit van het systeem 2.5 keer lager dan dat van een tweekopssysteem met LEHR PAR (Eng: Low energy high resolution parallel-hole) collimatoren. Dit was de prijs die betaald werd voor een hogere resolutie (6 mm versus 9.8 mm).

Tot slot vergeleken we het 'multi-lofthole'-systeem met het tweekopssysteem op basis van contrast-ruis-verhouding en NPW-SNR (Eng: non-prewhitening matched filter signal-to-noise ratio), wat een maat is voor lesiedetecteerbaarheid. Simulaties toonden aan dat het 'multi-lofthole'-systeem betere resultaten opleverde in warme lesies, maar slechtere in koude lesies. De belangrijkste reden hiervoor is de beperkte sensitiviteit.

In **hoofdstuk 5** onderzochten we daarom de mogelijkheid om de sensitiviteit verder te verhogen door meer loftholes gelijktijdig te openen, ook al betekent dit dat de projecties onderling overlappen. Met simulaties toonden we aan dat overlap ervoor kan zorgen dat er artefacten ontstaan in het gereconstrueerde beeld, maar dat deze ook kunnen opgelost worden door overlappende en niet-overlappende projectie data te combineren, wat mogelijk is door meer of minder loftholes te openen, gebruik makende van het shutter mechanisme.

Verder onderzochten we in hoofdstuk 5 ook de voorwaarden die nodig zijn om artefact-vrije beelden te bekomen met overlappende projecties. We toonden aan dat onvolledige bemonstering de oorzaak is van artefacten in overlappende systemen en we ontwikkelden een methode om de bemonstering van een systeem te evalueren om zo te kunnen voorspellen of de beelden artefacten kunnen vertonen of niet.

We simuleerden ook beelden voor verschillende overlappende systemen en vergeleken deze met een niet-overlappend systeem. De resultaten toonden aan dat hoewel overlap kan zorgen voor een drastische verhoging in sensitiviteit, de verbetering in contrast-ruis-verhouding minder voor de hand liggend is. De reconstructie van de beelden van de overlappende setups bleken trager te convergeren. Dit doet de verhoogde sensitiviteit teniet en

als gevolg vonden we slechts kleine verschillen in contrast-ruis-verhouding, in de grootteorde van de standaarddeviatie. We onderzochten ook NPW-SNR en voor deze taak vonden we wel een verbetering met de overlappende systemen. We toonden ook aan dat overlap kan zorgen voor een betere hoekbemonstering en concludeerden dat overlap een goede optie is wanneer het om praktische redenen moeilijk blijkt om de overlap te verwijderen en dat geen artefacten hoeven verwacht worden zolang de voorwaarden voor voldoende bemonstering voldaan zijn.

In **hoofdstuk 6** lag de focus vooral op het MR-compatibel maken van hersen-SPECT-beeldvorming op basis van de tweede benadering. We gebruikten hoge-resolutie-detectoren (met een intrinsieke resolutie van 0.5 mm) in combinatie met verkleinende pinholes om een stationair en compact systeem te maken. We gebruikten de optimalisatiemethode uit hoofdstuk 4 om de verschillende systeemparameters te bepalen en zo de sensitiviteit te maximaliseren voor een systeemresolutie van 7.2 mm. Verder werd ook de MR-compatibiliteit van de collimator onderzocht en vergeleken we de performantie van het systeem met een driekopsfanbeamsysteem op basis van simulaties. De beeldkwaliteit bleek daarbij vergelijkbaar, met als grote verschil dat het driekopssysteem niet MR-compatibel is, terwijl het pinholesysteem dat wel is.

Samenvatting

Dit proefschrift leidde tot een nieuw alternatief ontwerp voor hersen-SPECT-beeldvorming, gebaseerd op shutters die voor voldoende hoekbemonstering zorgen zonder dat het systeem moet geroteerd worden.

Verder ontwikkelden we ook een optimalisatiemethode dat de sensitiviteit van een ringvormig 'multi-pinhole'-systeem optimaliseert, gegeven een gewenste resolutie.

Daarenboven hebben we ook fundamenteel nieuwe inzichten verworven met betrekking tot artefacten door overlap: we toonden aan dat deze veroorzaakt worden door onvolledige bemonstering en ontwikkelden een methode om de bemonstering te evalueren.

Tot slot toonden we ook aan dat het mogelijk is om een compact hersen-SPECT-systeem te ontwerpen dat voldoende klein is om in een klinisch MR-systeem te passen, dat MR-compatibel is en dat een beeldkwaliteit heeft die vergelijkbaar is met huidige klinische SPECT-systemen. Simultane SPECT/MRI heeft het potentieel om hersen-SPECT-beeldvorming in de

toekomst fundamenteel te veranderen.

Dit onderzoek werd uitgevoerd in de onderzoeksgroep MEDISIP (MEDical Image and Signal Processing) in de vakgroep ELIS van de faculteit ingenieurswetenschappen. Het voorgestelde werk resulteerde in 1 patent, 4 A1-tijdschriftpublicaties als eerste auteur (waarvan er 1 momenteel nog onder review is), 2 A1-tijdschriftpublicaties als co-auteur en 12 bijdrages op internationale conferenties. De referenties van deze publicaties zijn in het volgende hoofdstuk opgesomd.

List of Publications

List of Publications

[1] Van Audenhaege K, Vandenberghe S, Deprez K, Vandeghinste B, Van Holen R. Design and simulation of a full-ring multi-lofthole collimator for brain SPECT *Phys. Med. Biol.* 2013; 58(18): p.6317-6336.

[2] Van Audenhaege K, Vanhove C, Vandenberghe S, Van Holen R. The evaluation of data completeness and image quality in multiplexing multi-pinhole SPECT *IEEE Trans. Med. Imag.* 2014; 34(2): p.474 - 486.

[3] Van Audenhaege K, Vandenberghe S, Vanhove C, Van Holen R. Collimator design for a multi-pinhole brain SPECT insert for MRI *Med. Phys.* 2015; Under review.

[4] Van Audenhaege K, Vanhove C, Vandenberghe S, Van Holen R. Review of SPECT collimator selection, optimization, and fabrication for clinical and preclinical imaging *Med. Phys.* 2015; 42(8): p.4796-4813.

[5] Deprez K, Vandenberghe S, Van Audenhaege K, Van Vaerenbergh J, Van Holen R. Rapid additive manufacturing of MR compatible multipinhole collimators with selective laser melting of tungsten powder *Med. Phys.* 2013; 40(1): p.1-11.

[6] Samoudi A M, Van Audenhaege K, Vermeeren G, Poole M, Tanghe E, Martens L, Van Holen R, Joseph W. Analysis of eddy currents induced by transverse and longitudinal gradient coils in different tungsten collimators geometries for SPECT/MRI integration *Magn. Res. Med.* 2014; published online.

Patent applications

[1] Van Audenhaege K, Deprez K, Vandenberghe S, Van Holen R. Methods and systems for collimating, filing date May 9th 2012, App. nr. PCT/EP2012/058589

Conference proceedings

[1] Van Audenhaege K, Vanhove C, Vandenberghe S, Van Holen R. Data completeness in multiplexing multi-pinhole SPECT *2013 IEEE Nuclear Science Symposium and Medical Imaging Conference Record* 2013; published online.

[2] Van Audenhaege K, Vandeghinste B, Vandenberghe S, Van Holen R. Time-multiplexing using a static full-ring multi-pinhole collimator for brain SPECT *2012 IEEE Nuclear Science Symposium and Medical Imaging Conference Record* 2012; p.3097-3100.

[3] Van Audenhaege K, Van Holen R, Deprez K, Karp JS, Metzler S, Vandenberghe S. Design of a static full-ring multi-pinhole collimator for brain SPECT *2011 IEEE Nuclear Science Symposium and Medical Imaging Conference Record* 2011; p.4393-4397.

[4] Pato L, Vandenberghe S, Van Audenhaege K, Van Holen R. Design and simulation of a stationary SPECT imaging system based on axially varying tilted parallel-hole collimation *2014 IEEE Nuclear Science Symposium and Medical Imaging Conference Record* 2014; published online.

Conference abstracts

[1] Van Audenhaege K, Vandenberghe S, Vanhove C, Van Holen R. Collimator design for a multi-pinhole brain SPECT insert for MRI *2014 IEEE Nuclear Science Symposium and Medical Imaging Conference Record* 2014; published online.

[2] Van Audenhaege K, Van Holen R, Vandenberghe, S. Analysis of the trade-off between sensitivity and resolution of a pinhole collimator for SPECT *Journal of Nuclear Medicine* 2012; 53(suppl.1): p.2410-2410.

[3] Deprez K, Van Holen R, Van Audenhaege K, Vandenberghe, S. Additive manufacturing of high density tungsten collimators *Journal of Nuclear Medicine* 2012; 53(suppl.1): p.2394-2394.

[4] Van Holen R, Van Audenhaege K, Deprez K, Vandenberghe S. Development of a compact MicroSPECT system for sequential SPECT-MRI *PET/MR and SPECT/MR: New Paradigms for Combined Modalities in Molecular Imaging Conference* 2012; p.18.

[5] Van Audenhaege K, Bovijn D, Van Holen R, Deprez K, Vandenberghe S. An MR-compatible shutter mechanism for stationary multi-pinhole SPECT of large objects *PET/MR and SPECT/MR: New Paradigms for Combined Modalities in Molecular Imaging Conference* 2012; p.65.

[6] Van Audenhaege K, Vandenberghe, S. Optimization of collimator combinations for brain SPECT *11e UGent-FirW Doctoraatssymposium* 2010; p.66.

[7] Samoudi AM, Van Audenhaege K, Vermeeren G, Poole M, Martens L, Van Holen R, Joseph W. Temporal Analysis of Z-Gradient Coil Eddy Current in Tungsten Collimator with different resistivities for SPECT/MRI *EJNMMI Physics* 2014; 1(Suppl.1) A22.

[8] Samoudi AM, Van Audenhaege K, Vermeeren G, Poole M, Van Holen R, Martens L, Joseph W. Influence of Collimator Insertion on Eddy Currents for different Resistivities of Tungsten *ISMRM* 2014; p.2545

Chapter 1

Introduction

The work presented in this dissertation is situated in the field of nuclear medicine, more specifically in Single Photon Emission Computed Tomography (SPECT) and the combination of SPECT with Magnetic Resonance Imaging (MRI). Firstly, we will give a general overview of medical imaging modalities and more specifically those that can be found in the radiology department and in nuclear medicine. Secondly, we will discuss the motivation and major challenges in improving brain SPECT and making it MR-compatible, followed by a description of our objectives. Finally, we will give an outline of this dissertation.

1.1 Medical imaging

Medical imaging makes it possible to obtain information about a patient's anatomy or physiological functions. It is part of every-day clinical practice, where it is used for diagnosis, staging, treatment planning and follow-up. Medical imaging is also used for research purposes, for example, to investigate the functioning of the brain or to evaluate new treatments.

Several different medical imaging modalities exist and they all have their specific applications. X-ray Radiography (RX) and Computed Tomography (CT) (Fig. 1.1e) provide 2D and 3D anatomical images respectively, and can be found in the radiology department. Other radiological modalities include Ultrasound (US) and Magnetic Resonance Imaging (MRI) (Fig. 1.1d). They are based on ultra sound waves and radio frequency (RF) fields respectively, and are therefore less invasive than RX and CT, which are based on an external X-ray source. All these radiological modalities mainly visualize

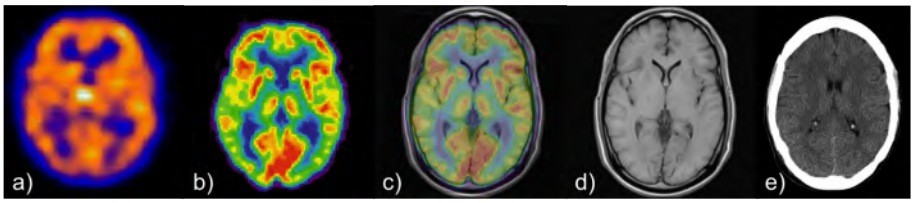

Figure 1.1: Brain imaging (a) ^{99m}Tc-HMPAO SPECT (b) ^{18}F-FDG PET (c) combined PET/MRI (d) MRI (e) CT

anatomical information.

However, in many diseases, functional changes appear long before any anatomical modifications can be detected. In these cases, molecular imaging modalities like Single Photon Emission Computed Tomography (SPECT) (Fig. 1.1a) and Positron Emission Tomography (PET) (Fig. 1.1b), can be used.They are based on an injection of a radio-active tracer and can be found in the nuclear medicine department.

Every modality has its advantages and disadvantages. Therefore, patients are often scanned using different modalities, especially when diagnosis is difficult. Lately, there is also a trend towards multimodality imaging, which we will discuss in section 2.3.

1.1.1 Radiology

1.1.1.1 X-ray radiography and computed tomography

X-ray radiography (RX) and computed tomography (CT) are based on the same principle, except that RX is planar (2D) while CT provides 3D information. An external X-ray tube is placed at one side of the patient and emits X-rays that are detected on the other side of the patient, with an X-ray detector. Part of the X-ray beams are attenuated in the patient's body (mainly due to photoelectric absorption) so that only a certain fraction reaches the detector. The probability for an X-ray to be attenuated depends on the attenuation coefficient of the different tissues that the X-ray crosses. By comparing the number of emitted X-rays with the number of detected X-rays, we obtain a planar attenuation map of the patient (an RX). In order to reconstruct a 3-dimensional (3D) attenuation map, different projection angles need to be acquired by rotating the source-detector pair. The patient's tissue density can then be calculated using tomographic

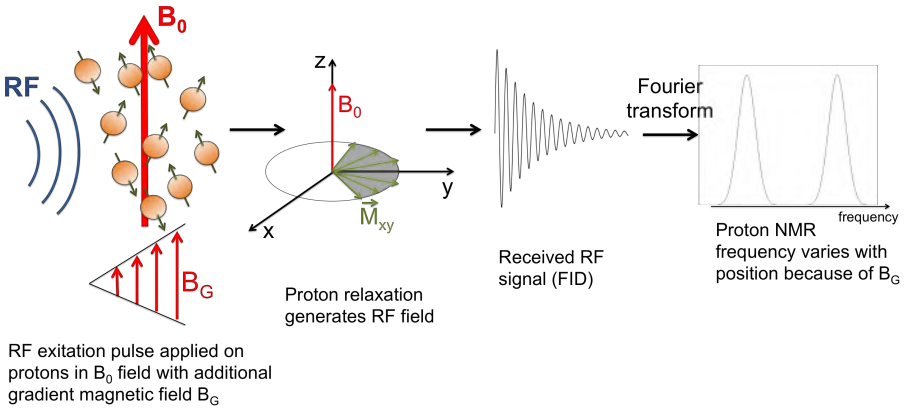

Figure 1.2: Basic principles of MRI: An RF pulse excites protons that are subjected to a static magnetic field B_0, together with a gradient magnetic field B_G, which is position dependent. After turning off the RF pulse, the protons relax back to their polarized state and while doing so, they emit an RF signal (FID). After Fourier transforming the FID, every frequency corresponds to a different location in the patient (due to B_G) .

reconstruction. Typical applications for RX are images of the skeleton (to support or exclude a bone fracture), the teeth (for caries), the lungs (for tumors) and the arteries. The most common CT applications are for staging oncological patients and in the brain for internal bleeding, infarctions and trauma to the skull. An example of a CT of the brain is shown in Fig. 1.1e.

1.1.1.2 Magnetic resonance imaging

Magnetic resonance imaging (MRI) is based on the principle of proton nuclear magnetic resonance (NMR). An MRI system consists of 4 main components: a strong magnet (on the order of 0.2-14.1 Tesla), gradient coils and two radio frequency (RF) coils (a transmit (Tx), and a receiver coil (Rx)) (Fig. 2.12). We will now explain the function of these components in more detail. The magnet is used to generate a static magnetic field (the B_0 field), which partially aligns the magnetic moments of protons in the patient's body to a polarized state. This magnetization alignment is then briefly excited (depolarized) using a properly tuned RF pulse sent by the Tx coil. After excitation, when the RF pulse is turned off, the protons relax back to their polarized state. This relaxation process results in a changing magnetic flux density and the protons will re-emit RF radiation. This RF

signal is measured by the Rx coil and gives information about the proton density. As proton density is different for each type of body tissue, this gives information about the different tissues present. Without a gradient coil, however, the signals from different locations in the body cannot be separated. To solve this, spatial encoding is obtained by applying 3 different well-calibrated magnetic field gradients across the patient (in X-, Y- and Z-direction) so that a certain value of magnetic field can be associated with a given location in the tissue. More details about MR imaging are given in section 2.2. Typical applications of MRI are in the field of neuroimaging, where it is often preferred over CT (Fig. 1.1e) due to its high contrast between grey and white matter (Fig. 1.1d). For example, MRI is the imaging modality of choice for neurooncology. It is used for follow-up (e.g. after radiotherapy) but also for the diagnosis, as MRI is very sensitive for the detection of small tumors. Contrast-enhanced MRI is able to detect very small intracranial metastases with a higher sensitivity than any other imaging modality. Interestingly, MRI can also be used for functional imaging. One example is functional MRI (fMRI), which is a functional neuroimaging procedure based on the blood-oxygen-level dependent (BOLD) contrast. Oxygen-poor and oxygen-rich blood have a different magnetic susceptibility, which induces small magnetic field distortions and reflects in the decay process of the protons in these areas.

1.1.2 Nuclear medicine

Single photon emission computed tomography (SPECT) (Fig. 1.4a) and positron emission tomography (PET) (Fig. 1.4b) are both nuclear imaging modalities. They rely on a tracer that is administered to the patient and that participates in the body's metabolism and distributes accordingly. The tracer principle was first described by George Charles de Hevesy in 1911 and first used in animals in 1924. A molecule can be turned into a radioactive tracer by attaching a radionuclide to it, or by replacing one or more atoms in that molecule by a radionuclide. It will then participate in the physiological processes of an organism in a manner indistinguishable from the same nonradioactive nuclide. Following radioactive decay, photons will be emitted in all directions and exit the body to be detected by a gamma camera. The detected information can then be used to reconstruct and visualize physiological functions in the body. The main difference between PET and SPECT is the type of radionuclide used and the way they decay. As the name explains, SPECT is based on single photon emission, while PET relies on positron emitters.

Figure 1.3: Clinical PET system.

1.1.2.1 Positron emission tomography

Firstly, we describe the principle of PET. When a positron is emitted inside the patient's body, it travels a small path (the positron range is typically 1-2 mm in water) and then annihilates with an electron to form two back-to-back gamma-rays with an energy of 511 keV (Fig. 1.4b). These gamma-rays can then be detected using a PET system (Fig. 1.3), which mainly consists of a full ring of detectors and read-out electronics. When two photon detections fall within a short time frame, we assume that they came from the same annihilation and we call this a coincidence. By connecting the two places of incidence, we can determine the line of response (LOR) on which the annihilation took place. Finally, after registering many of these LORs, the original activity distribution can be calculated using a reconstruction algorithm. Different reconstruction algorithms are discussed in section 2.1.4.

1.1.2.2 Single photon emission computed tomography

SPECT radionuclides, on the other hand, are single photon emitters and therefore, we cannot use coincidences to determine the LOR. For this reason SPECT cameras do not only have a detector, but also a collimator which limits the incoming photons to only those traveling in a certain direction. The collimator can be described as a solid plate made of a dense material with one or multiple holes. Only a fraction of all photons pass through the

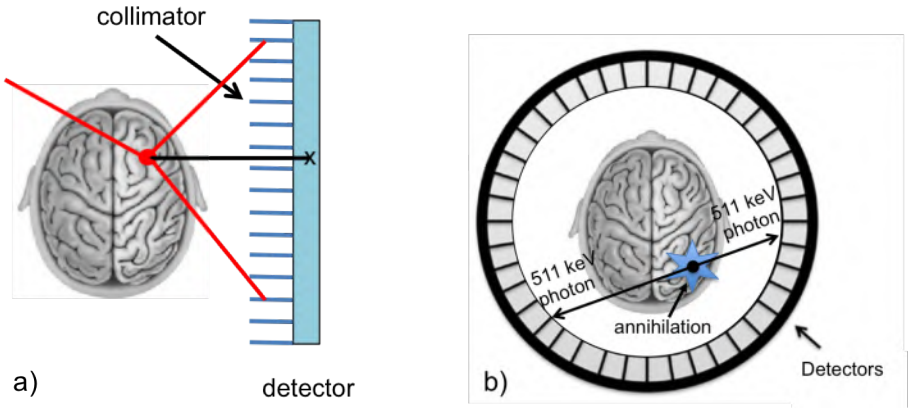

Figure 1.4: (a) The basic principle of SPECT: a detector and a collimator that limits the incoming photons to only those traveling in a certain direction. (b) The basic principle of PET: positron annihilation forming two back-to-back gamma-rays with an energy of 511 keV.

hole(s) and reach the detector. This allows us to determine the direction of incidence of the photon but it also reduces the sensitivity of the system. Different types of collimators are described in chapter 3. A typical clinical SPECT scanner consists of 1 or more (maximally 3) detectors heads with a parallel-hole or fan-beam collimator, rotating around the patient (Fig. 1.5a). Other systems, for example preclinical systems, are stationary and have a full-ring multi-pinhole geometry (Fig. 1.5b). Lately, very compact preclinical systems, that fit on a bench top, have also become available (Fig. 1.6). The most popular applications for SPECT are bone imaging and myocardial imaging but SPECT is also very interesting for preclinical applications (imaging small animals like rats and mice) and is commonly used in the field of neurology and psychiatry, which is the focus of this dissertation. For these different applications, various tracers exist, based on different radionuclides, like ^{99m}Tc, which is the most commonly used radionuclide in SPECT. ^{99m}Tc has interesting properties, like a long half-life (6.01 h) and a clear photo peak at 140 keV. Other SPECT radionuclides like ^{123}I, ^{131}I and ^{111}In have a higher energy which will more likely penetrate the collimator.

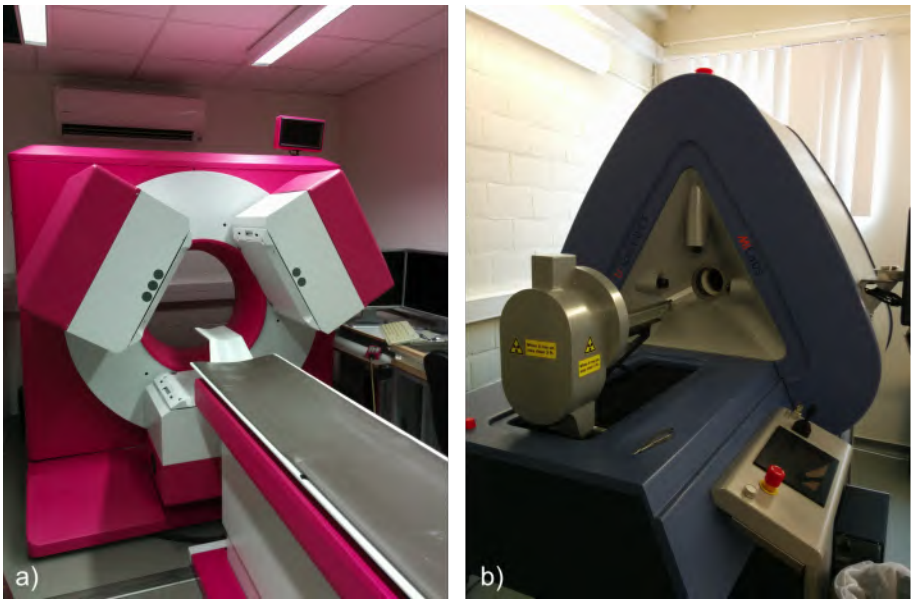

Figure 1.5: (a) The Prism 3000XP from Picker (Philips): a clinical triple-head SPECT system (b) The U-SPECT II from MILabs: a preclinical multi-pinhole SPECT system.

1.2 Motivation and challenges

In this section we will motivate why we focus on improving SPECT for brain imaging and why we aim at making SPECT MR-compatible. Firstly, we will discuss applications of SPECT in neurology. Secondly, we will show that SPECT is still relevant and that we do not expect it to be completely replaced by PET. And thirdly, we will explain why SPECT/MRI is more interesting than SPECT/CT, which is the current standard.

SPECT has many interesting applications in neurology, like for example the diagnosis and follow-up of dementia, cerebrovascular disease, epilepsy, brain trauma and brain tumors [30]. Dementia is a broad category of brain diseases that affects more and more people (globally about 36 million people). There are several forms of dementia, including Alzheimer's disease, vascular dementia and dementia with Lewy Bodies and SPECT imaging can help to make a differential diagnosis which potentially can aid in patient management. SPECT is also the preferred modality for ictal imaging in focal epilepsy. This is due to the fact that the tracers ^{99m}Tc-HMPAO and ^{99m}Tc-ECD are trapped in the tissue compartment after passing the

Figure 1.6: Benchtop SPECT system.

blood brain-barrier, which allows us to inject the tracer during the ictal phase (during the seizure) and wait until the seizure has stopped to perform the SPECT scan. Another unique application of SPECT is dual-tracer imaging (imaging two different tracers at the same time), which has applications in Parkinson and Alzheimer's diseases [191]. Finally, in section 2.1.1.3 we discuss some applications where the specificity of the tracer is the key strength, like in the differential diagnosis between dementia with Lewy Bodies and Alzheimer's disease [118], where the SPECT tracer shows a higher specificity than its PET alternative, despite the fact that SPECT suffers from low sensitivity and bad spatial resolution.

Most clinical SPECT systems have a spatial resolution in the range of 8-10 mm and a sensitivity on the order of 10^{-4} cps/Bq. This is quite low in comparison with PET, where a spatial resolution of about 5 mm can be achieved with a sensitivity on the order of 10^{-2} cps/Bq. A better resolution and/or sensitivity would result in a better diagnosis and thus in an earlier and better treatment of the patient. This is not only an advantage for

society as a whole but it also results in cost reductions for hospitals and health insurance providers. In addition, improving SPECT imaging will also allow smaller or more remote hospitals to have access to molecular brain imaging because the key competitive advantages of SPECT over PET lie in the lower cost price of the system and the availability of longer half-life radionuclides.

At this moment, SPECT has a much larger installed base and has in the US yearly 14.5 million patients compared to 1.6 million scans with PET. This is partially because of historical reasons (PET was introduced more recently) but also because of clinical and economical reasons. Because, despite the growth of PET examinations in recent years, the number of SPECT procedures has remained stable or even increased, e.g., in Europe, between 2005 and 2008, the number of SPECT procedures increased by 2% for brain and myocardial perfusion, by 17.4% for infection/inflammation imaging, by 17.5% for sentinel node scintigraphy and by 42.1% for brain receptor imaging [133]. Data from a 2012 report on Europe's nuclear medicine market from Medical Options in London showed that the total number of SPECT procedures increased by 1% a year in Europe between 2007 and 2011. In the US, showed an average decline of 2.5% per year between 2008 and 2013 (data from the 2013 nuclear medicine market summary report from IMV, a recognized leader in market research for the medical imaging market), but regardless of what many authors suggest, this is not due to an increase of PET examinations because data from the 2014 PET market summary report from IMV shows that the number of PET procedures in the US also declined (yearly 4% between 2011 and 2014). This recent decline is most probably due to the economical crisis. So, the debate on SPECT versus PET imaging is far from being concluded [133, 72, 191, 131]. Therefore, it is important to keep innovating SPECT.

The true competition might not be between SPECT and PET but instead, between nuclear imaging and MRI, which can not only be used for anatomical, but also for perfusion and molecular imaging. However, brain perfusion using fMRI is based on the indirect and semi-quantitative relation between the BOLD signal and the underlying physiology. fMRI images are also quite noisy and statistical procedures need to be used to extract the underlying signal. In addition, molecular imaging with MRI is based on spectroscopy (where sensitivity is limited by the concentration of the molecules) or relies on a contrast agent but the sensitivity of MRI for existing molecular probes is relatively poor. Based on these two arguments, we can state that at this moment many SPECT studies cannot be replaced by MRI studies yet and it is not clear whether this will be possible in the future.

Even more interesting would be a fully MR-compatible SPECT system for simultaneous SPECT/MRI brain imaging. At this moment, SPECT is often combined with CT to obtain an anatomical background for the functional information. However, the use of CT in brain imaging is limited, due to its low soft-tissue contrast (Fig. 1.1e). CT also comes with extra radiation dose which is particularly a problem in sensitive organs, like the brain. Therefore, we suggest to improve brain SPECT by combining it with MRI (Fig. 1.1d). Clinical PET/MRI systems are currently already available and an example of a brain PET/MRI is shown in Fig. 1.1c. Research on SPECT/MR, on the other hand, is still mainly focussing on preclinical systems.

1.3 Ojectives

This dissertation aims at improving the image quality of human brain SPECT and making it MR-compatible. For this, we focus on innovative and stationary, compact systems based on innovative multi-pinhole collimator design.

For improving SPECT image quality, we focus on increasing the resolution and sensitivity of the system and making it stationary so that it does not suffer from the calibration issues that typically occur when a heavy collimator and/or detector needs to be rotated. Inspired by collimator design in preclinical systems, where sub-millimeter resolutions can be obtained with high sensitivity, we propose to use full-ring multi-pinhole collimators for brain SPECT. Multi-pinhole collimators have the potential to overcome the sensitivity-resolution trade-off of traditional clinical SPECT systems and a full-ring design allows the system to be stationary. We also want to investigate the potential of multiplexing pinholes (i.e. two or more pinhole projections overlap on the detector). Multiplexing yields increased count sensitivity, since more pinholes can be placed on the collimator for the same detector size, but it is unclear whether this also results in improved image quality.

For making SPECT MR-compatible, we focus on designing a compact stationary system so that it is small enough to fit inside a clinical MRI system and so that no rotation is needed, as this would perturb the homogeneity of the magnetic field. We propose to use high-resolution MR-compatible detectors in combination with minifying pinholes, i.e. pinholes that generate a minified projection of the object of interest on the detector, to achieve that goal.

The premise in this work is that innovative multi-pinhole collimator design

will lead to better spatial resolution, higher sensitivity and MR-compatibility of brain SPECT systems.

1.4 Outline

In **chapter 2** we explain SPECT and MRI in more detail. Firstly, we explain the complete chain of a SPECT image acquisition. This includes injecting the tracer (we will discuss the different tracers and their applications), acquiring projection data using either a SPECT system or simulations (we will discuss the different components of a SPECT system and different types of simulations) and reconstructing the data (we will discuss different iterative reconstruction techniques). Secondly, we explain the basic principles of proton nuclear magnetic resonance and of magnetic resonance imaging, followed by an explanation of the different components in an MRI system. Finally, we will discuss the challenges and latest developments in hybrid SPECT/MRI.

Chapter 3 is completely dedicated to the principles behind SPECT collimator design, which is the focus of this dissertation. We explain the different types of collimators, their geometrical properties, and concepts like sampling completeness, multiplexing and septal penetration. We also give an update of new production techniques and explain their specific advantages. In addition, we give guidelines for selecting the best collimator and optimizing a SPECT system for a specific task.

In **chapter 4** we design a stationary full-ring collimator for brain SPECT imaging based on an existing whole-body detector ring with limited intrinsic resolution (4 mm). Firstly, we introduce the concept of a shutter mechanism to ensure sufficient angular sampling without rotating the system. Secondly, we develop an optimization method to maximize the system sensitivity given a target resolution of 6 mm and use it to derive the optimal system parameters. Finally, we compare the image quality of our brain SPECT system with a clinical SPECT system, based on both noiseless and Monte-Carlo simulations.

In **chapter 5** we use the shutter mechanism to control the amount of overlap of the different pinhole projections (also called multiplexing). We investigate whether we can increase image quality by acquiring both multiplexed and non-multiplexed data in the same measurement (time-multiplexing) and we develop a method to evaluate data completeness in multiplexing multi-pinhole SPECT systems. Finally, we compare image quality in multiplexed and non-multiplexed systems using simulated data.

In **chapter 6** we use high-resolution detectors (0.5 mm) to design a compact and stationary MR-compatible SPECT system that can be used as an insert in clinical MR-systems with a bore of 70 cm. We perform Monte-Carlo simulations of both the multi-pinhole SPECT insert and a clinical triple-head fan-beam system and compare image quality in a contrast phantom. We also evaluated the MR-compatibility of tungsten sample material produced with additive manufacturing and investigated eddy currents due to the MR gradients.

Finally, in **chapter 7**, general conclusions are made and possible future research is discussed. We end this dissertation with a final conclusion.

Chapter 2

Background

In chapter 1 we gave a general overview of imaging modalities used in radiology and nuclear medicine. We also motivated why we aim at improving brain SPECT and make it MR-compatible. In order to fully understand why designing an MR-compatible brain SPECT system is a challenging task, we will now discuss SPECT and MRI in more detail.

Firstly, in section 2.1 we explain the clinical applications and the general principles behind SPECT imaging, including the principles of detection and collimation. We also discuss methods for SPECT simulations and image reconstruction, which will be extensively used in the simulation studies of chapter 4, 5 and 6.

Secondly, in section 2.2 we explain the general principles behind MRI and discuss the different components of an MRI system (the magnet, the gradients and the RF coils).

Finally, in section 2.3 we give a general overview of multimodality imaging, followed by a detailed explanation of the challenges and latest developments in SPECT/MRI.

2.1 Single photon emission computed tomography

Fig. 2.1 illustrates the different steps needed for obtaining a SPECT image. Firstly, the tracer needs to be prepared. This happens at the radiopharmacy, where a radionuclide is bound to a tracer molecule. Once the radiopharmaceutical is ready, the syringes are prepared and the patient is injected (or sometimes, the tracer is administered in the form of a capsule). Once the tracer distribution in the patient has stabilized, the SPECT scanning

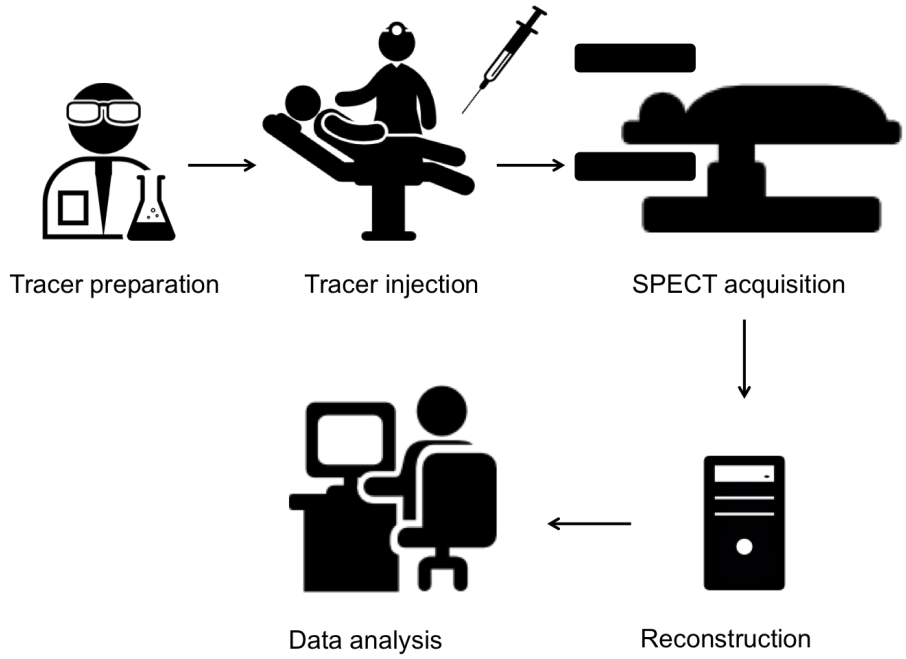

Figure 2.1: The different steps of a SPECT study: the tracer preparation, the tracer injection, the actual acquisition, the image reconstruction and the analysis by the physicist.

protocol can be run, which usually takes 20-30 minutes. After the scan, the images are reconstructed, examined and reported by a nuclear medical physicist so that the medical doctor can then make a diagnosis. So, in order to obtain a SPECT image, we need 4 elements: the tracer, the system, the acquisition and the reconstruction. These 4 elements will be covered one-by-one in the following sections.

2.1.1 SPECT tracers and applications

The first element needed for obtaining a SPECT image, is the tracer. There exist many different SPECT tracers but they are all based on the tracer principle as explained in section 1.1.2. SPECT tracers directly emit photons (and not positrons that result in pairs of annihilation photons like in PET). In this section, we will discuss the most common SPECT tracers and their applications.

The most commonly used radionuclide for SPECT is 99m-technetium

(^{99m}Tc), which has a main photo peak at 140.5 keV and a half-life of 6.01 h. ^{99m}Tc-HMPAO (e.g. [36]) and ^{99m}Tc-ECD (e.g. [103]) are two examples of SPECT tracers that are widely used in clinical practice for inflammation, for cerebral perfusion imaging, including ictal SPECT (for studying epilepsy). The latter two applications are further discussed in section 2.1.1.2, which is dedicated to applications in neurology.

Other ^{99m}Tc-based tracers are ^{99m}Tc-sestamibi, with applications in cardiac imaging [186] and oncology, ^{99m}Tc-methylene diphosphonate (MDP) for bone scintigraphy [87], ^{99m}Tc-microaggregated albulin (MAA) for lung perfusion and ^{99m}Tc-labeled colloids for sentinel lymph node visualization.

Other radionuclides include, for example, ^{111}In and ^{123}I with ^{111}In-pentetreotide being used in octreotide scans for diagnosing carcinoid tumors [132] and paragangliomas [110] and with ^{123}I being most commonly used in Na^{123}I for the evaluation of thyroid disease [276].

The amount of administered radioactivity depends on the tracer and the application and is expressed in becquerel (Bq) or in Curie (Ci). The becquerel is the SI-unit. 1 Bq corresponds to 1 nucleus decay per second and 1 mCi corresponds to 37 MBq. Administered doses are typical in the range of 5-30 mCi. For example, the recommended dosage of ^{111}In-pentetreotide is 6 mCi in adults, while the typical dosage for bone scintigraphy is 20-30 mCi.

2.1.1.1 Preclinical applications

The same radiotracers are also used in small animals (mostly mice and rats) for preclinical and translational studies [140]. For the development of new tracers and new therapies (for e.g. treatment of neurodegenerative diseases or cancer therapy), (small) animal studies are performed using representative animal models. These small animal studies are usually performed on dedicated preclinical cameras that provide high resolution images (up to 0.35 mm) such that similar relative detail can be visualized, compared to human images. For more information about preclinical SPECT imaging, the interested reader is referred to [140].

2.1.1.2 Applications in neurology

An ideal tracer for brain imaging should fulfil the following criteria:

- Simple synthesis procedure for reliable production and low radiation burden for personnel

- High specific activity so that binding of the tracers is minimally affected by non-radioactive counterparts
- Good binding between the tracer and the target of interest
- Metabolic stability
- Low affinity for P-glycoprotein as this could transport the tracer out of the brain
- Half-life should be low enough to be in agreement with the rate of the physiological process of interest
- Easily penetrate the lipophilic blood-brain barrier

The blood-brain barrier is a barrier that prevents materials from the blood from entering the brain to maintain a constant environment and is semi-permeable, i.e. it is highly selective. This is an effective protection against for example bacterial infections. Molecules that do pass are small and are highly lipid soluble, such as glucose.

Most neurological tracers are used for imaging cerebral perfusion, the dopaminergic system or brain tumors. We will now explain these applications in more detail.

2.1.1.2.1 Cerebral perfusion imaging Cerebral perfusion imaging provides a map of the regional cerebral blood flow (rCBF). The most common tracers for cerebral perfusion are ^{99m}Tc-HMPAO or ^{99m}Tc-ECD [132]. Fig. 2.2a shows an example of a perfusion study acquired using ^{99m}Tc-HMPAO. Typical administered doses for brain perfusion imaging are 20 mCi for HMPAO or 30 mCi for ECD. However, only 5% of that activity reaches the brain [135]. We will now discuss the most important clinical applications of cerebral perfusion imaging, which are dementia, cerebrovascular diseases, trauma, tumors and epilepsy.

The first application is **dementia**, which is a generic term used for a broad category of neurological diseases that affect the cognitive abilities. There are several forms of dementia, including Alzheimer's disease, vascular dementia and dementia with Lewy Bodies and SPECT imaging can help to make a differential diagnosis which potentially can aid in patient management. This differential diagnosis can be done with cerebral perfusion imaging, which typically shows low posterior cingulate and bilateral temporal-parietal hypoperfusion in the rCBF when the patient has Alzheimer's disease [9].

The second application is **cerebrovascular disease**, which is a condition that affects the circulation of the blood to the brain causing a decrease in blood flow to the affected areas in the brain. The most common forms of cerebrovascular disease are cerebral thrombosis (40% of cases) and cerebral embolism (30%), followed by cerebral hemorrhage (20%). In all types of cerebrovascular disease, significant changes in brain perfusion occur and this can be imaged with perfusion SPECT. Although CT and MRI can also be used, SPECT has shown to be superior in demonstrating decreased blood flow in the early hours of stroke onset. Additionally, rCBF studies are useful for therapy monitoring in the case of thrombosis [232].

The third application is **traumatic brain injury**, for example after a car or sports accident. While the initial evaluation is typically performed with MRI or CT, SPECT has been introduced as a method to provide information about secondary pathophysiological processes.

The last application that we discuss here is **focal epilepsy**, where cerebral perfusion imaging is used to compare the rCBF during a seizure (ictal SPECT) with a baseline rCBF (interictal SPECT). ^{99m}Tc-HMPAO and ^{99m}Tc-ECD are particularly suited for studying epilepsy because after passing the blood brain-barrier, they are trapped in the tissue compartment. This allows one to inject the tracer during the ictal phase and wait until the seizure stopped to perform the SPECT scan and thus avoid any movement distortions.

2.1.1.2.2 Dopaminergic system imaging (^{123}I-N-ω-fluoropropyl)-2β-carbomethoxy-3β-(4-iodophenyl)nortropan (FP-CIT; marketed as DaTSCAN) [118] or ^{123}I-iodobenzamide (IBZM) [90] can be used to measure the amount of dopamine neurons and dopamine $D_{2/3}$ receptors, respectively, in a person's brain. FP-CIT can be used to support or exclude the diagnosis of Parkinson's disease, while IBZM can be used in the differential diagnosis of parkinsonism. In patients suffering from Parkinson's disease, dopaminergic neurons that project to the striatum degenerate. The motor symptoms typically start at one side of the body. On an FP-CIT-SPECT scan (see Fig. 2.2b), the uptake in the striatum is typically asymmetric, and the degeneration starts at the posterior part of the striatum. However, losing dopaminergic neurons is also part of normal ageing and it takes an expert to evaluate the data.

2.1.1.2.3 Neurooncology While the detection of brain tumors is often performed with MRI or CT, SPECT provides information about its metabolic

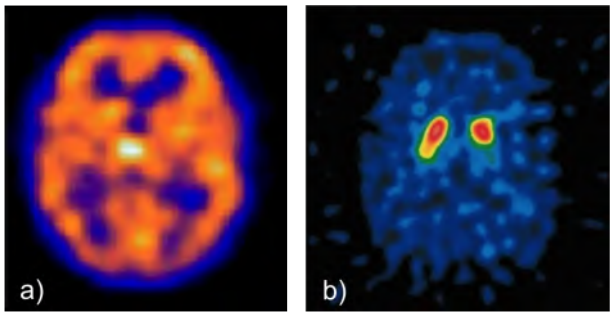

Figure 2.2: (a) Cerebral perfusion using ^{99m}Tc-HMPAO (b) DaTscan of a patient with Parkinson disease, showing asymmetric defects at the level of the striatum [189].

status which can be used to evaluate the tumor aggressiveness or to differentiate residual tumor infiltration versus surrounding oedema or to differentiate recurrent tumor tissue versus radiation necrosis following treatment [207].

2.1.1.3 SPECT versus PET tracers

The key competitive advantages of SPECT over PET lie in the lower cost price of the system and the availability of longer half-life radionuclides. SPECT radionuclides have an intermediate half-life – typically ranging from a few hours to a few days – and are therefore easy to handle. They can be produced in large quantities and distributed by pharmaceutical companies. PET tracers, on the other hand, have a half-life ranging from a few minutes to a few hours so that more remote hospitals need to have their own cyclotron infrastructure, which drastically increases the operational costs. Also, PET has some fundamental limitations on the resolution due to the positron physics, namely the positron range (typically 1-2 mm in water), and a slight non-colinearity (about 0.25°) of the two 511 keV photons, which causes significant deviations in clinical systems. The positron range is currently an important limitation for preclinical studies, where SPECT systems typically achieve sub-millimeter resolutions. It might not seem so important for clinical systems but this could change if detectors continue to improve.

Another advantage of SPECT over PET is the possibility to do dual-tracer imaging, enabling specific targeting abilities. The dual-tracer approach is

difficult to implement in PET as all radiotracers have the same energy (511 keV), while in SPECT two tracers with different energies can be used simultaneously and separated in the image. An example for dual-tracer brain imaging is the simultaneous use of a ^{99m}Tc-based tracer and a ^{123}I neurotransmitter agent, which has applications in neurodegenerative diseases, like Parkinson and Alzheimer's diseases [191].

Another important aspect of the discussion is clinical superiority of the tracer, i.e. improved specificity and/or sensitivity of the diagnosis. Spatial resolution and sensitivity are important, but the specificity of the tracer is also important. In some applications, the PET alternative has shown to be superior (e.g. ^{11}C-MET PET is superior to ^{201}Tl SPECT for the differentiation of tumor recurrence from radiation necrosis [219]), but in many other applications, the superiority of the PET tracer was not clinically proven yet [131]. There are also examples where the SPECT tracer was shown to be superior for clinical diagnosis. For example, a recent study demonstrated superior diagnostic accuracy for differentiating dementia with Lewy Bodies from Alzheimer's disease using a DaTscan compared to PET [118]. Another example is for imaging intracranial lesions, where SPECT imaging with radiolabeled amino acids proved to be superior to ^{18}F-FDG for detecting the tumors and delineating them. This is because the accumulation of ^{18}F-FDG in normal gray matter and many malignant tumors is difficult to differentiate [266]. Finally, our last example is focal epilepsy, which we explained in the previous section. One of the limitations of PET for the evaluation of epilepsy during the ictal phase is its low temporal resolution. PET tracers have a significantly longer tracer uptake period than SPECT tracers, which leads to a mixture of interictal-, ictal-, and postictal-phase images. The trapping of PET tracers is also shorter lasting, making SPECT the preferred modality for ictal imaging.

2.1.2 Conventional gamma cameras

Once the tracer has been administered and the activity distribution has stabilized, the patient is inserted in the SPECT system and photons emitted following radioactive decay can be detected with a gamma camera. Conventional gamma cameras mainly consist of a detector and a collimator. Both are equally important for good image quality and will be discussed in this section. The collimator part in this section is only a brief introduction to chapter 3, which is entirely dedicated to collimator design in order to give the reader an in-depth understanding of the principles that are used in the rest of this dissertation.

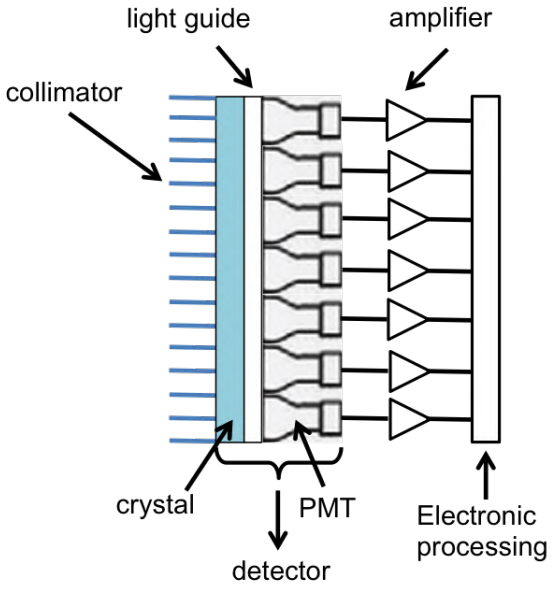

Figure 2.3: A traditional clinical SPECT detector based on a scintillator (crystal) and photomultiplier tubes

2.1.2.1 The detector

A detector detects gamma-rays (photons) and determines the energy of photons and their location of incidence. Its system characteristics are typically described by 3 important parameters: intrinsic spatial resolution, intrinsic energy resolution and efficiency (the fraction of incident photons that is effectively detected).

2.1.2.1.1 Scintillation detectors Traditional clinical SPECT detectors consist of a scintillator (also called crystal), coupled to a light guide and an array of photomultiplier tubes (PMTs) (Fig. 2.3). The scintillator converts gamma photons to visible light, with an intensity proportional to the photon energy. Next, the light guide distributes the light among neighboring PMTs, which converts the visible light to an electrical signal. Different positioning algorithms exist to accurately determine the location of incidence, with the Anger-logic being the most common one [10]. Clinical gamma cameras are traditionally based on scintillator crystals of sodium iodine doped with thallium (NaI(Tl)) and have an intrinsic spatial resolution of 3-4 mm.

More recently, alternatives have been developed for the PMT, e.g. the avalanche photodiode (APD) and the silicon photomultiplier tube (SiPM). In 2009, Philips introduced the first digital SiPM (dSiPM) which has a fully digital readout (while the PMT, APD and SiPM readout is analog) and is therefore very compact. SiPMs and dSiPMs have also been used for the development of novel high-resolution detector technologies, like in [206], where a SiPM was coupled to a 10 mm thick monolithic LYSO:Ce^{3+} crystal or like in [69], where a dSiPM was coupled to an array of 3 mm thick CsI(Tl) crystals , resulting in an intrinsic spatial resolution of 1.6 mm and 2 mm, respectively. In our research group, we developed a dSiPM coupled to a 2 mm thick LYSO crystal, resulting in an intrinsic resolution of 0.5 mm [23].

2.1.2.1.2 Direct conversion detectors Direct conversion detectors, based on semiconductors are also becoming more common. They do not have a scintillator crystal nor a light guide but convert gamma photons directly to electrical signals. Direct conversion detectors have superior energy resolution and improved photon statistics compared to traditional detectors because they do not rely on any intermediate visible-light pulse generation. Cadmium telluride (CdTe) and cadmium zinc telluride (CZT) are the most frequently used semiconductor detectors for SPECT because they can operate at room temperature and have a high efficiency. CZT detectors also have a high intrinsic resolution. The D-SPECT [58] for example, is a commercial system for cardiac imaging based on CZT detectors with a pixel pitch of 2.46 mm. Another commercial system based on CZT detectors is the Discovery NM530c [60], which is also dedicated to cardiac imaging.

For a more extensive overview of SPECT detectors, we would like to refer the interested reader to the review paper of Peterson and Furenlid [188].

2.1.2.2 The collimator

The detector can determine the position, but not the angle of incidence of the incoming photon. So, with only a detector, it is impossible to determine where the photon originated from. Therefore we use a collimator, which can be described as a solid plate made of a dense material with holes that allow only those photons traveling along desired paths to pass through. Only a small fraction (typically $\sim 10^{-4}$ to 10^{-2}) of emitted photons pass through the holes and are detected, which seriously limits sensitivity. Making the holes larger increases the sensitivity but degrades the resolution; this effect is often called the resolution-sensitivity trade-off and is illustrated in Fig. 2.5. In Fig. 2.4 we show two types of collimators: (a) a parallel-hole collimator,

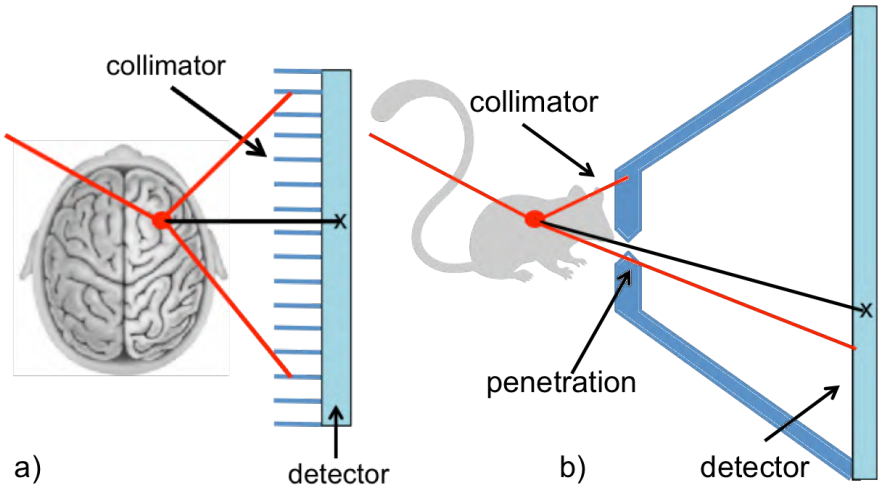

Figure 2.4: (a) A parallel-hole collimator (b) A single pinhole collimator with one ray penetrating the pinhole knife-edge.

which is typically used in clinical settings and (b) a pinhole collimator, which is more commonly used in preclinical settings. The best collimator materials have a high density and a high atomic number, such as lead, tungsten, gold, and platinum. The higher the density and atomic number, the higher

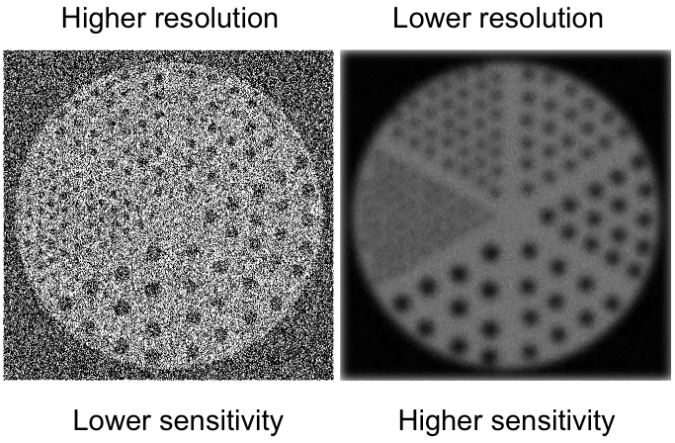

Figure 2.5: An illustration of the resolution-sensitivity trade-off. Higher sensitivity comes at the cost of lower resolution.

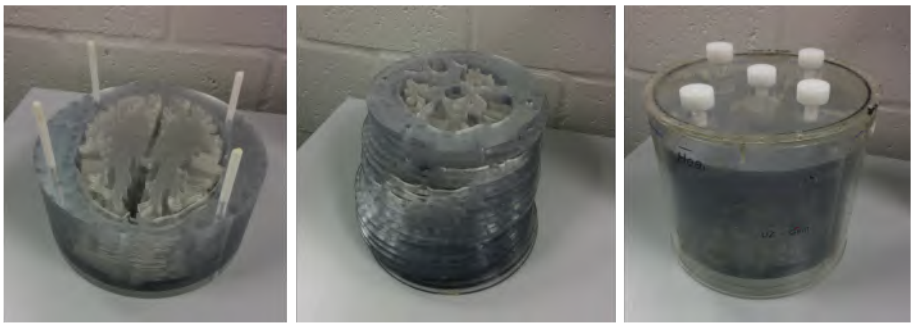

Figure 2.6: A physical Hoffman phantom.

the stopping power, which is important in order to prevent photons from penetrating the collimator. An overview of other types of collimators and more information about collimator selection, optimization, and fabrication for human and small animal imaging is given in chapter 3.

2.1.3 SPECT simulations

The aim of this dissertation is to improve brain imaging using innovative collimator design. However, instead of building different prototype SPECT systems (which would have been very costly), we used simulation tools that have been developed to accurately model the physics of a full SPECT system and that allow us to generate simulated projection data based on phantoms. A phantom can be a physical object, specially designed to substitute human scans or to evaluate imaging performance. An example is the Hoffman phantom, which mimics the activity distribution of a brain perfusion study (Fig. 2.6). A phantom can also be a digital representation of an activity distribution and be used for simulating projection data that can then be reconstructed and compared with the phantom data. Knowing the ground truth is another advantage of simulations, as well as having complete freedom for testing different parameter settings. With simulations, it is also easy and less time-consuming to repeat a certain study multiple times to have better statistics for comparing image quality between two different systems.

In this section we present the two different types of simulations that were used in this dissertation: analytical and Monte Carlo-based simulations.

2.1.3.1 Analytical simulations

Analytical simulations are deterministic. They typically start from a voxelized phantom and then model the camera geometry, the point spread function (PSF) and the sensitivity to generate projection data. For a realistic simulation, it is important to choose the voxel size small enough to approximate a continuous activity distribution. Analytical simulations are intrinsically noiseless, but noisy data can be generated by a Poisson random number generator using the forward-projected data as mean values. We will now discuss the two different types of analytical simulations: based on ray-tracing or matrix operations.

2.1.3.1.1 Ray-tracing Of all ray-tracing methods, Joseph's method [98] is the most commonly used nowadays. It is pixel-driven, meaning that the rays starts from the detector pixels and are traced through the collimator aperture towards the image space as shown in Fig. 2.8a, in contrast with a voxel-driven ray-tracer where the rays would start from the image voxels. In a pixel-driven ray-tracer, the value ending up in the detector pixel is a weighted sum of the voxels that it passes. We will now describe how to incorporate different physical effects in a ray-tracing simulator.

Firstly, we need to model **point sensitivity**, i.e. the probability that a photon from a certain voxel would actually travel through the collimator aperture. This is implemented as a weighting factor with the weight being calculated analytically according to the appropriate sensitivity formula. An overview of these formulae for different types of collimators is given in chapter 3.

Secondly, **attenuation** needs to be modeled. This is also implemented as a weighting factor, i.e. the probability that a photon from a certain voxel would actually exit the phantom and not be attenuated inside the phantom.Therefore, we need a map of the attenuation coefficients of the phantom materials and calculate the cross section for each material in the phantom. The probability of a photon escaping without interaction from a material with attenuation value μ, is given by $P = \exp(-\mu L)$, with L the length of the cross section.

Thirdly, the **geometrical resolution** of the collimator is typically modeled using a multi-ray approach [254], i.e. not one but multiple rays (sometimes hundreds) are traced from each pixel through the collimator apertures, subsampling the aperture and thus modeling the geometrical resolution of the collimator (Fig. 2.7a).

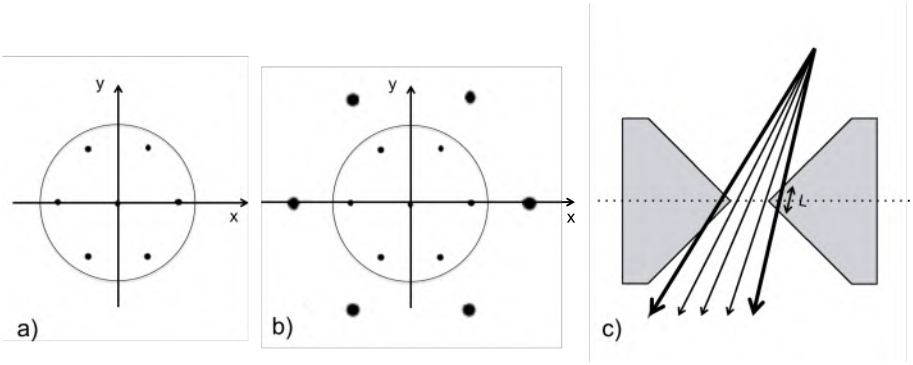

Figure 2.7: (a) Top view of a pinhole showing pinhole subsampling with 7 rays (b) Top view of a pinhole showing extra rays used for modeling pinhole penetration (c) Side view of a pinhole showing extra rays used for modeling pinhole penetration, based on the cross section of the ray with the collimator (e.g. L).

Fourthly, two different strategies exist for modeling **aperture penetration**. The first one is to use an effective pinhole diameter (e.g. Eq. 5.12 and Eq. 4.15 for pinhole penetration) instead of the physical pinhole diameter for the aperture subsampling. The second strategy has only been used in pinholes and uses an extended pinhole aperture and more rays for subsampling in order to include rays that might penetrate the pinhole edge [73] (Fig. 2.7b,c).

Finally, **detector resolution** is typically modeled by applying a Gaussian blurring operation with the intrinsic detector resolution as full-width-at-half-maximum (FWHM).

2.1.3.1.2 Matrix operations When the collimator has many apertures (e.g. in case of a parallel-hole collimator) the multi-ray approach is too compute-intensive and simulations are typically based on matrix operations. For the example of the parallel-hole collimator, the forward projection is simply a weighted sum of voxel rows with the weights being determined by a pre-calculated attenuation map. The geometrical resolution of the collimator is modeled using a filter. For each voxel, the expected spatial resolution is calculated using the analytical formulae given in section 3.1.1 and before the forward projection, a Gaussian blurring operation is applied with this spatial resolution as FWHM. Matrix operations are not so compute-intensive as ray-tracer simulations but they are also less accurate.

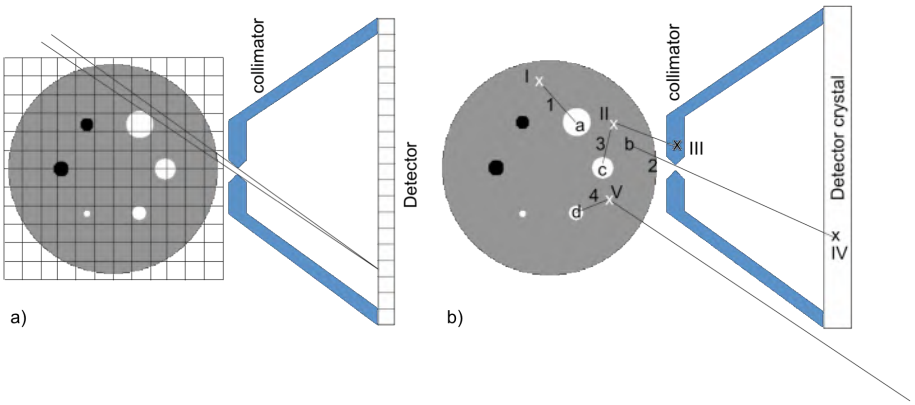

Figure 2.8: (a) Analytical simulation with 2 rays based on a pixel-driven forward projector (b)Monte Carlo simulation for 4 photon tracks with their track IDs (1,2,3,4), their physical interactions (I,II,III,IV,V) and the generated photon locations (a,b,c,d).

2.1.3.2 Monte Carlo simulations

In the previous section, we discussed analytical simulations, which are deterministic and intrinsically noiseless. Monte Carlo simulations, on the other hand are intrinsically noisy, as they model a complex statistical system by performing many random experiments such that the mean value of the experimental outcome is the quantity of interest. They use pseudo-random number generators to model physical interactions with a certain probability and have been applied in many research fields, like e.g. the study of materials [64], earthquakes [5] or DNA sequence evolution [192].

For imaging systems, the essence of a Monte Carlo simulator is to randomly generate millions of photons that are tracked from their emission until they are either absorbed or leave the system. The simulator typically allows the user to configure the imaging system's geometry and a source distribution which results in a number of particles that will be simulated over time. Every particle is transported one step at a time from interaction point to interaction point, taking into account all photon-electron interactions in the phantom, in the collimator and in the detector. Photon transport and interaction mechanisms are based on three processes: the photoelectric effect, Compton scatter, and to a lesser extent, Rayleigh scatter. The initial photon directions and the location and outcome of all interactions are assigned by pseudo-random number generators, mimicking the actual physical

processes. This is illustrated in Fig. 2.8b and can be summarized in 5 steps:

1. The first step is to choose the emission point of the photon. This should be according to the activity distribution defined by the user and assuming that the activity is the mean of a Poisson random process. In the example, the pseudo-random number generator chose 4 emission points (a,b,c and d) but in a realistic Monte-Carlo simulation, there are typically millions of them.

2. The second step is to launch a photon from the emission point in a random direction according to a uniform distribution.

3. The next step is to decide w.b.her the photon interacts with the phantom before escaping it. Therefore, it is necessary to know the attenuation map of the phantom and to calculate the cross section for each material in the phantom. In the example, the photon with track ID 2 escapes without interaction.

4. If the photon does not escape, the next step is to decide where it interacts and whether it is attenuated or scattered and in which direction. In the example, the photon with track ID 1 attenuates in the phantom (interaction I), while the photon with track ID 3 scatters (interaction II) and then travels in the direction of the collimator. The location of interaction, the kind of interaction and the scatter direction are all decisions made by drawing random numbers according to a suitable probability density function (PDF).

5. If the photon eventually escapes the phantom, it can interact with the collimator (e.g. the photon with track ID 3 is attenuated in the collimator, interaction III), it can escape the system (e.g. the photon with track ID 4) or it can interact with the detector (e.g. the photon with track ID 2 is attenuated in the detector crystal and detected, interaction IV). Again, these decisions are made by the pseudo-random number generator.

To conclude, Monte Carlo simulations are very accurate, but they are also very compute-intensive. Because of the random nature, each experiment will be different, unless the seed of the pseudo-random number generator is re-used.

2.1.4 SPECT Image Reconstruction

In the previous sections we described the different components of the SPECT system and how to obtain planar projection data by either measurements or simulations. In order to derive a 3D image of the activity distribution, we need to acquire projection data at different angles and reconstruct it. There are two classes of image reconstruction: analytical reconstruction algorithms that are based on the mathematical inverse of the imaging process (e.g. Filtered Back Projection) and iterative reconstruction algorithms, that are based on a forward and back projection and also incorporate the noise model (e.g. maximum likelihood expectation maximization).

The Filtered Back Projection (FBP) algorithm is based on the work of Johann Radon [190] who showed that an activity distribution can be reconstructed by back projecting a filtered version of the projection data, on the condition that projections were acquired at a large number of different angles over 360°, with a sufficiently fine and regular sampling. A back projection distributes the activity in every pixel over the incident ray in the image space and is a blurred version of the actual distribution. In order to remove this blurring step, we apply a filter prior to back projecting which is the inverse of the blurring operation. The algorithm is very fast but assumes exact (and noiseless) projection data.

The Maximum Likelihood Expectation Maximization (MLEM) algorithm on the other hand, incorporates the SPECT noise model (which is Poisson) and maximizes the log-likelihood of the activity distribution, given the measured projection data. The algorithm is based on an iterative process where each iteration consist of a forward projection, a back projection and a correction step. In SPECT, MLEM is preferred over FBP because it incorporates the Poisson nature of the measured data, because it allows an accurate modeling of the physics and collimator geometry and because it does not require such a large number of angles in the dataset. Nowadays, almost all SPECT systems use iterative reconstruction, with MLEM (and related, OSEM) being the most common ones.

2.1.4.1 Maximum Likelihood Expectation Maximization

2.1.4.1.1 Forward model The process of emission tomography can be described as:

$$p_i = \iiint_{FOV} f(x,y,z)h_i(x,y,z)dxdydz, \tag{2.1}$$

where f is the activity distribution, p_i is the value of detector pixel/angle i and h_i(x,y,z) is the probability that a photon emitted at position (x,y,z) is detected at pixel/angle i. The projection data p is discretized due to the subdivision of the detector in N pixels and due to the finite number of projection angles A. p is a $1XL$ matrix with $L = N.A$. The activity distribution f, on the other hand, is intrinsically continuous but for the reconstruction, we usually approximate the activity distribution using voxels as basis functions. The forward projection step then becomes:

$$p_i = \sum_{k=1}^{K} f_k h_{ik}, \tag{2.2}$$

where f_k is the activity in voxel k, K is the total number of voxels in the image space and h_{ik} is the probability that a photon emitted in voxel k is detected by detector pixel/angle i. The matrix **H** with elements h_{ik} is referred to as the system matrix.

2.1.4.1.2 The algorithm For the reconstruction algorithm we aim at reconstructing a voxelized representation of the activity distribution f, based on the measured projection data p. Each iteration consists of 4 steps (Fig. 2.9):

1. Forward project an initial estimate of the activity distribution
2. Compare the estimated projection data with the measured data
3. Back project the error
4. Correct the initial estimate of the activity distribution based on the back projected correction term (after normalization).

We repeat these 4 steps until convergence or a certain noise level is reached. Noise increases at every iteration and therefore, the images are often filtered before being presented to the physician.

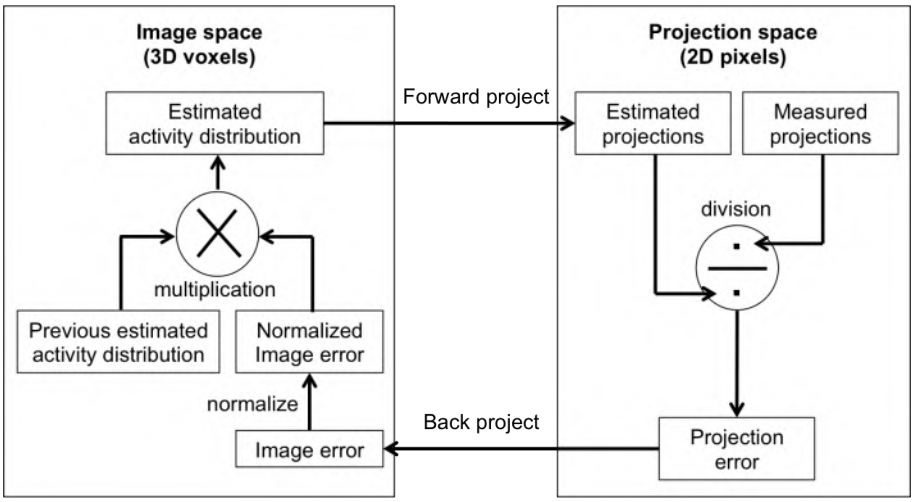

Figure 2.9: MLEM (Iterative reconstruction algorithm).

A formal expression of the update step is given by:

$$f_k^{t+1} = \frac{f_k^t}{\sum_{i=1}^{I} h_{ik}} \sum_{i=1}^{L} h_{ik} \frac{p_i}{\overline{p_i}^t}, \tag{2.3}$$

where t is the iteration number, f_k^t is the estimated activity in voxel k at iteration t and $\overline{p_i}^t$ is the forward projection of the estimated data at iteration t:

$$\overline{p_i}^t = \sum_{k=1}^{K} h_{ik} f_k, \tag{2.4}$$

The back projection step that is referred to in Fig. 2.9 is described by:

$$b_k^t = \sum_{i=1}^{L} h_{ik} \frac{p_i}{\overline{p_i}^t} \tag{2.5}$$

A useful property of MLEM is its guaranteed convergence.

2.1.4.2 Ordered Subset Maximum Likelihood Expectation Maximization

One of the downsides of MLEM is that it is computationally intensive and converges slowly. To speed up reconstructions, Ordered Subset Maximum Likelihood Expectation Maximization (OSEM) is used. OSEM is similar to MLEM, except that each update step is based on only a subset of the projection data. The update step of OSEM is given by:

$$f_k^{t+1} = \frac{f_k^t}{\sum_{i \in S} h_{ik}} \sum_{i \in S} h_{ik} \frac{p_i}{\overline{p_i}^t}, \tag{2.6}$$

where $i \in S$ indicates the detector pixels/angles of subset S. One global iteration of OSEM is defined as a single pass through all subsets.

However, OSEM can diverge when the subsets are not carefully chosen, for example when insufficient counts are available in a subset, causing false zeros which cannot be resolved in later iterations. Therefore modified OSEM algorithms were proposed, like for example Count-Regulated OSEM (CROSEM) [230] or rescaled block-iterative (RBI) algorithms [28].

2.1.4.3 System matrix

In the previous section we described two iterative image reconstruction algorithms (MLEM and OSEM). Both algorithms are based on a forward and back projection and are described by Eq. 2.4 and Eq. 2.5, respectively. Both equations require a model of the system matrix **H** and for the best reconstruction result it is important to model the system matrix as accurately as possible. It should at least include the geometrical model of the collimator, but it can also model more complex physical interactions that we want to correct for. For example, in SPECT, attenuation is an unwanted effect that we need to correct for. For example, photons originating from the centre of the brain need to cross more tissue and have more chance to be attenuated (by photoelectric absorption or by compton scattering) than photons originating from the edge of the brain (in Fig. 2.10a). If we do not model attenuation during the reconstruction, we get an underestimation of the activity at the centre of the FOV 2.10b). This is only one example that shows how important it is to use an accurate system matrix.

We will now explain how to obtain that system matrix. The system matrix can be measured or calculated in advance and be stored in computer memory. However, this requires a large amount of memory space and therefore,

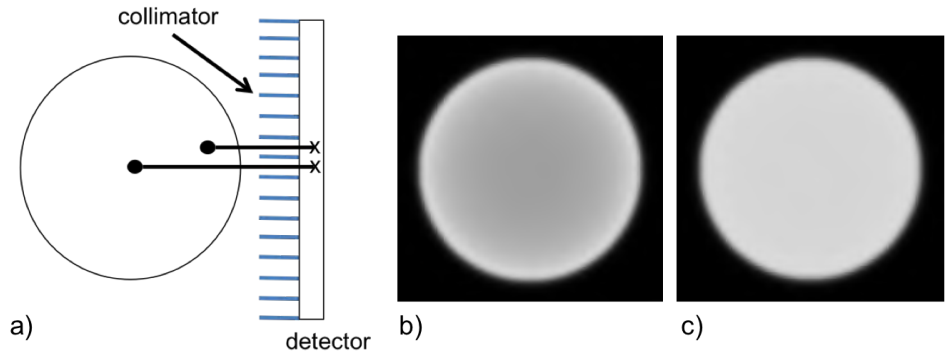

Figure 2.10: Attenuation correction (a) Photons originating from the center of the FOV need to cross more tissue and have a higher chance to be attenuated than photons originating from the edge of the FOV. (b) A SPECT image of a uniform distribution, without attenuation correction. (c) A SPECT image of a uniform distribution, with attenuation correction.

it is more common to calculate the system matrix on the the fly, using for example a ray-tracer. Ray-tracing was explained in section 2.1.3.1 in the context of analytical simulation models but can as well be used for the forward and back projector of the reconstruction algorithm. A good projector models the system matrix as accurately as a simulator would. However, in practice, the projectors are often simplified in order to reduce computation time. It has also been shown that unmatched projector/back projector pairs can be used to further speed up the reconstructions [277] and therefore, it is also common to model attenuation, sensitivity and resolution only in the forward projector.

2.2 Magnetic Resonance Imaging basics

While the first part of this dissertation mainly focusses on improving brain SPECT in itself, the second part concentrates more on combined SPECT/MRI. To understand the challenges related to SPECT/MRI, we will now give more information about proton nuclear magnetic resonance, which is the physical principle behind magnetic resonance imaging.

2.2.1 Nuclear Magnetic Resonance

Atomic nuclei are composed of protons and neutrons. Both protons and neutrons have a spin, i.e. they rotate about their own axis. In some nuclei the spins of protons and neutrons add to zero. In others, they add to a number other than zero, which results in a net spin. The spinning motion of these nuclei creates a tiny magnetic field, which is called the magnetic moment. The most important example of a nucleus with net spin is the hydrogen nucleus. Luckily our body is composed of about 65% water and thus contains many hydrogen nuclei. The more water, the better. MRI is thus particularly suited for soft tissue structures, like the brain.

In the presence of an external magnetic field B_0, the magnetic moment of the nuclei lines up with the magnetic field. This will cause a macroscopic magnetization M_0 whose strength depends on the spin density and the magnetic field strength. Next to this magnetization, nuclei will tend to precess in phase around the magnetic field (Fig. 2.11a) with a frequency determined by the Larmor frequency $\omega_0 = \gamma B_0$, where $\gamma = 2\pi 42.57$ MHz/Tesla is the gyro-magnetic ratio of a proton. However, energy loss due to interactions with the surroundings causes this precession to decrease and the nuclei reach a stable state in which they are aligned along the B_0 field. This process is called spin-lattice relaxation (T_1).

Generating an MR-signal requires two steps: a transmit and receive phase. Firstly, during the transmit phase, a radiofrequency (RF) pulse at the Larmor frequency is applied to induce a spin flip, i.e. the nuclei start precessing in a wider arc (Fig. 2.11b). This results in a rotating magnetization in the plane perpendicular to the B_0 magnetic field and a residual longitudinal magnetization in the direction parallel to the B_0-field (unless the flip angle is exactly 90°). Secondly, after the RF pulse has been switched off, the receive phase starts, during which the nucleus spins dephase (called T_2 relaxation) (Fig. 2.11c) and realign with B_0 because of spin-lattice relaxation. This causes a changing magnetic flux density and the protons will re-emit RF radiation at their Larmor frequency which is picked up to generate the MR signal, also called the Free Induction Decay (FID) signal. The FID is thus dominated by two effects: T_1 and T_2 relaxation. T_1 relaxation typically has a longer time constant (832 ms for white matter and 1331 ms for gray matter in a 3T magnetic field). T_2 relaxation typically has a shorter time constant (79.6 ms for white matter and 110 ms for gray matter in a 3T magnetic field) and is also referred to as spin-spin relaxation [264].

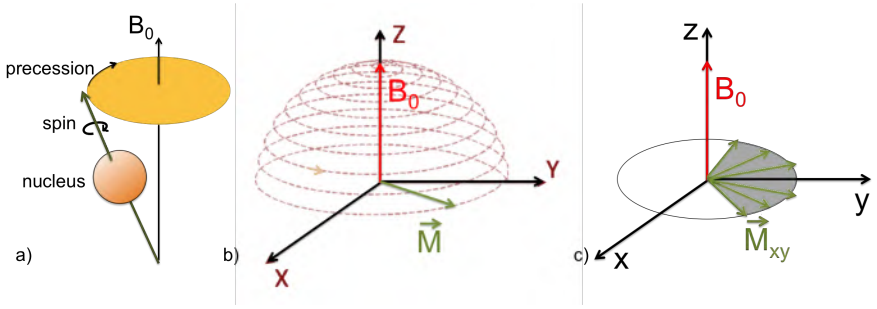

Figure 2.11: (a) The precession of a spin around an external magnetic field B_0 at Larmor frequency (b) Spiral motion of the magnetization $\vec{M}$ under the influence of an external magnetic field B_0 and a 90° RF pulse at Larmor frequency (c) Dephasing: after switching off the RF pulse, local variations in Larmor frequency cause the dipoles to dephase which results in a loss of transverse magnetization.

2.2.2 Imaging principles

In order to construct an anatomical image of the different tissue types, we need localization. This can be obtained by applying a well-calibrated set of magnetic field gradients so that there is a slightly different magnetic field at every position. Remember that the frequency of precession depends on the size of the magnetic field, which is now different for every position in the patient.

In the longitudinal direction, a slice selection is performed by applying a z-gradient. This way, the RF excitation fulfils the resonance conditions only in a specific slice such that the spin flip is only applied for these nuclei and the signal is only coming from that slice. Then, a gradient is applied in the y-direction (one of the transverse directions) for a brief time just before applying the RF signal. Due to the brief additional magnetic field in that direction, the spins are dephased and the signal is phase-encoded. Finally, a gradient is applied in the x-direction (the other transverse direction) during readout. This way, the signal is frequency-encoded.

2.2.3 MRI System

Fig. 2.12 shows the main parts of an MR system. Firstly, there is the magnet, which generates the static magnetic field B_0. Secondly, there is the gradient coil, which is actually composed of an X-, Y- and Z- gradient coil. And finally there is the RF coil. Most commercial systems come with a

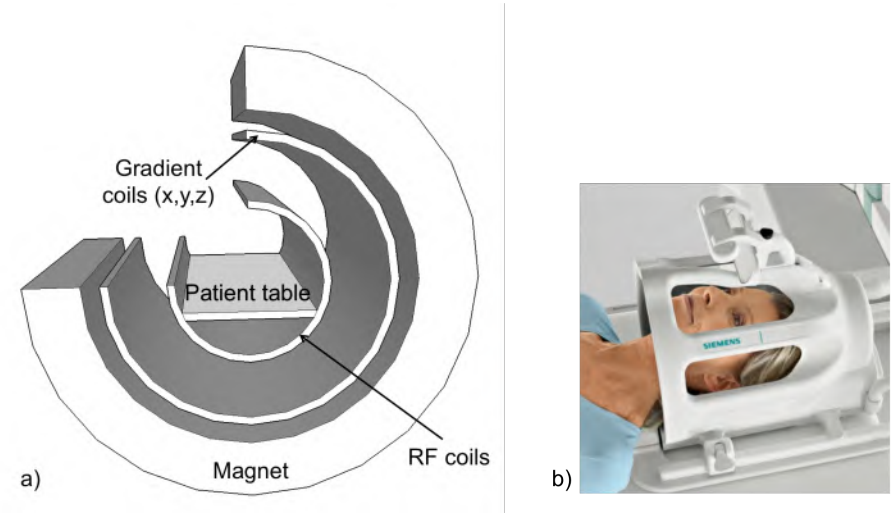

Figure 2.12: (a) An MR system with the magnet, the gradient coils and the RF coil (b) An 8-channel RF coil for clinical brain imaging

whole set of RF coils, for different applications (brain imaging, whole body, wrist, etc). Some RF coils are both transmitter (Tx) and receiver (Rx) coils, while others have only an Rx or Tx function. The closer the Rx coil can be brought to the object of interest, the better the signal sensitivity.

2.3 Hybrid SPECT/MRI

In the previous two sections, we explained SPECT and MRI in more detail. Both modalities are interesting for imaging the brain and it would be even more interesting if we can combine them in one hybrid SPECT/MRI system. In this section, we will therefore explain the principles of multimodality imaging and describe the specific challenges in hybrid SPECT/MRI brain imaging.

2.3.1 Principles of multimodality imaging

Multimodality imaging is the combination of different imaging modalities to obtain more information in a single scan and increase the specificity and sensitivity of diagnostic findings.

Most commercial SPECT and PET systems are combined with CT

(SPECT/CT and PET/CT) to obtain an anatomical background for the functional information. In addition, the CT images also provide the necessary information for attenuation correction during SPECT reconstruction, as explained in section 2.1.4.3.

More recently, there is increased interest for combined SPECT/MRI and PET/MRI, dual-modality techniques that have many advantages, certainly for neurological applications. Firstly, MRI has a higher soft-tissue contrast, which is important in brain imaging as the brain consists mainly of cerebrospinal fluid and white and gray matter. Secondly, MRI does not involve any radiation dose like CT. Moreover, if both modalities could be fully integrated, it would improve patients' comfort, avoid coregistration errors, allow to correct for motion artifacts, increase patient throughput and reduce total patient examination time. In addition, SPECT/MRI is also interesting for certain specific clinical applications. In acute brain infarction, for example, the combination of HMPAO-SPECT and dynamic susceptibility contrast MRI has shown to be more interesting than each modality separately [83] because SPECT (CBF) is better at predicting the evolution of the infarction while the bolus passage (MRI) is better at detecting brain regions that can potentially be rescued in the penumbra with decreased blood flow. There has also been some effort put into the development of dual-modality SPECT/MRI bioprobes, e.g., Gadolinium - ^{99m}Tc which permits the detection of small tumors in large tissue volumes using SPECT and simultaneously high-resolution MR characterization of tumor neovasculature [117]. Another clinical application of brain SPECT/MRI is the simultaneous assessment of brain function with fMRI (BOLD) and the localization of an epileptic focus or brain tumor with SPECT. This can be used for surgical planning but is even more interesting for intraoperative assessment because the information provided by preoperative fMRI is hampered by the brain deformation that is secondary to surgical procedures [125].

Finally, SPECT/MRI will also be highly valuable for more fundamental biomedical research and allow correlation of different radionuclides with more functional MR measurements [40].

2.3.2 Challenges in brain SPECT/MRI

Integrating SPECT with MRI is challenging for a number of reasons:

1. The collimator should not contain any ferro-magnetic materials in order not to disturb the B_0-field of the MRI. It should ideally be made of a material with a magnetic susceptibility close to human

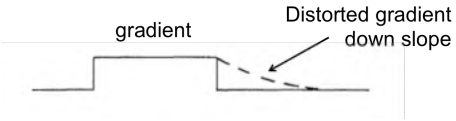

Figure 2.13: Distortion of gradient field due to Eddy currents

tissue. However, the most commonly used collimator materials are lead and tungsten-alloys that contain ferro-magnetic materials.

2. The detectors need to be able to operate in the strong magnetic field. Currently, most clinical SPECT detectors are based on photomultiplier tubes (PMTs), that cannot operate in a magnetic field and give rise to B_0 magnetic field distortions.

3. The SPECT system should be stationary in order not perturb the magnetic field. A stationary system does not require any translational or rotational steps and is therefore not only more stable, it also makes it possible to perform dynamic studies. However, most current SPECT systems rely on rotation to acquire images at different projection angles and it is challenging to obtain sufficient angular sampling with a stationary system.

4. The MR gradients cause eddy currents in the collimator material which can perturb the MR gradient field and should be minimized for successfully integrating SPECT and MRI [223].

5. The SPECT system should fit within the bore of a clinical MRI scanner with a diameter of 70 cm. However, current clinical systems are bulky dual- or triple-head gamma cameras equipped with fan-beam or parallel beam collimators.

6. The attenuation maps that are used during SPECT reconstruction and that are normally derived from CT, cannot directly be obtained from the MRI and an intermediate step is needed to obtain the attenuation map [104]. Techniques to derive the attenuation map from MRI are based on segmentation and atlas registration, which has some drawbacks related to inter-patient variability.

Some of the above challenges have already been addressed during the development of MR-compatible PET systems. For example, the MRI-compatibility of different gamma shielding materials has been investigated

for PET, but the results can also be used for SPECT [222]. Also useful are the MRI-compatibility tests of different PET detectors. The first MR-compatible PET systems were based on avalanche photodiodes (APDs) [193]. More recently, most MR-compatible PET designs are based on Silicon Photomultiplier (SiPM) detectors [26, 198] or digital Silicon Photomultiplier (dSiPM) detectors [267]. We refer the interested reader to [252] for an extensive review of PET/MRI.

Additional challenges of SPECT/MRI (compared to PET/MRI) are the space required for the collimator and incompatibility of the collimator, which might cause distortions in the MR image. These two issues are the subject of chapter 6. Incompatibility of the collimator can be due to two reasons: due to a disturbance of the B_0 field or due to eddy currents. The first issue can (to a certain extend) be resolved using shimming, which is discussed in section 2.3.2.1 and the second issue is explained in more detail in section 2.3.2.2.

2.3.2.1 Adjusting the magnetic field homogeneity with shimming

Shimming is the fine adjustment of the magnetic field homogeneity via field gradients produced by shim coils. Shimming is the solution of the linear equation:

$$B_0^* = B_0(x, y, z) + \sum S_i(x, y, z) \tag{2.7}$$

with B_0^* the desired homogeneous magnetic field, $B_0(x, y, z)$ the measured field distribution within an object, $S_i(x, y, z)$ the field distribution caused by the shim coil i (in case of active shimming) or by an extra metal piece i (in case of passive shimming). Depending on the system, first, second or even third order shimming can be performed. First order shimming means that $S_i(x, y, z)$ is a linear function of x,y and z. Different shimming strategies exist, e.g manual/automated, local/global, active/passive shimming strategies. For a full description of shimming strategies, we refer to [137].

2.3.2.2 Eddy currents

In MRI, localization is based on gradient fields that are rapidly switching on and off. One of the major problems of the switching gradient coils is

that, due to Faraday's law of induction, a changing magnetic field induces circular electric currents (called eddy currents) within conducting structures. These eddy currents flow in closed loops within any conductor, including in the gradient coils themselves, but also in the SPECT collimator. The magnetic field produced by these eddy currents opposes and distorts the linear gradient fields (Fig. 2.13) in the region of interest, which results in image artifacts [164]. Although many approaches have been proposed to minimize the generation of eddy currents (active and passive shielding coils, current pulse pre-emphasis, less conductive magnet bore materials and alternative cryostat configurations), significant distortions will often remain. This is particularly the case in the presence of highly conductive objects where eddy currents are characterized by long time constants [96]. For the development of an MR-compatible collimator it is thus important to use materials with a conductivity that is as low as possible.

2.3.3 Latest developments in SPECT/MRI

While the developments in PET/MRI resulted in both clinical [109, 256, 77, 48] and pre-clinical systems [37, 99, 209, 269, 267], research on SPECT/MRI is still mainly focussed on small-animal systems. The earliest SPECT/MRI systems were based on cadmium-zinc-telluride (CZT) detectors. For example, the MRSPECT was developed in 2010 as a proof of concept and is based on a parallel hole collimator and a whole body 4T MRI system and requires a rotation of the object [82]. A fully stationary system was also developed using CZT detectors, for a 12-cm bore preclinical MRI system [13, 138, 139]. Similarly, Meng et al. developed a SPECT insert for a 22-cm bore 4.7T MRI [144, 225]. More recently, the MRC-SPECT [29] has been built. This ultrahigh resolution system is based on cadmium-telluride (CdTe) detectors and multi-pinhole collimators. It is also stationary and fits within a preclinical MRI system. Another small-animal system is still under development for the INSERT project [27]. It is designed to fit within a preclinical 7T or 9.4T MRI system with a 20 cm bore diameter and is based on Silicon PhotoMultipliers (SiPMs) and multi-pinhole collimators and is stationary. A human brain SPECT/MRI is also planned within the same project [27]. It is designed to fit within a 59-cm clinical 3T MRI system and is also stationary and based on SiPMs, with the collimator being based on slit-slats. This paper demonstrates the feasibility of designing a compact brain SPECT system that would fit in the MRI bore. However, it does not include a description of the collimator optimization or MRI compatibility, which is something that we do investigate in chapter

6. The INSERT project is still ongoing and in the meantime, subsequent reports and presentations also addressed these aspects [59, 57].

All these systems are still in research phase and no truly integrated SPECT/MRI systems are yet commercially available. At this moment, Mediso Medical Imaging Systems [2] is the only company offering a preclinical 1T sequential SPECT/MRI system (nanoScan SPECT/MRI).

2.4 Summary

In this introductory chapter, we gave a detailed description of SPECT and MRI.

Firstly, we discussed applications of SPECT in neurology and made the comparison with PET. Key advantages of SPECT over PET are related to cost and tracer half-life. We discussed a few clinical examples where SPECT outperforms PET even though clinical PET systems have a higher resolution and sensitivity than SPECT. We also described the two main components of a conventional gamma camera: the detector and the collimator, with the collimator section being an introduction to chapter 3, which is entirely dedicated to collimator design. Collimator design, in combination with SPECT reconstruction and simulation techniques (which we also discusses in this chapter), form the basis for our simulation studies of chapter 4, 5 and 6.

Secondly, we explained the basics of proton nuclear magnetic resonance, which is the physical principle behind magnetic resonance imaging and we described the different components of an MR system.

Finally, we discussed the major challenges of hybrid SPECT/MR imaging, which are (i) the need for a stationary and compact system (ii) MR-compatibility of the collimator (iii) MR-compatibility of the detector. In chapter 6 we will show how innovative collimator design can help to overcome the first two issues.

Chapter 3

SPECT collimator selection, optimization, and fabrication for clinical and preclinical imaging

3.1 Introduction

Single Photon Emission Computed Tomography (SPECT) is a nuclear imaging technique used to visualize functional information with radioactive tracers. A detailed description of SPECT was already given in section 2.1, where we first discussed the different applications of SPECT imaging, followed by an explanation of the gamma camera and a presentation of different types of simulation techniques, to conclude with an overview of different reconstruction algorithms. In section 2.1.2.2 we introduced the SPECT collimator, i.e. the part of the gamma camera that is responsible for limiting the incoming photons to only those traveling in a certain direction. The collimator design has an important impact on the final system performance, which is often expressed in terms of resolution and sensitivity.

Sensitivity is the ratio of emitted versus detected photons and spatial resolution is the full-width-at-half-maximum (FWHM) of the point spread function, which is determined by the detector intrinsic resolution and the geometrical resolution of the collimator. Both sensitivity and resolution can have different values across the field of view (FOV) but most manufacturers only mention one value. When comparing different systems it is therefore

important to understand what the values means. Sensitivity can be, e.g., a peak value, the value at the center of the FOV or an average over the complete FOV (volume sensitivity). It can be calculated theoretical or measured experimentally (in which case it might include attenuation in the phantom). Spatial resolution is often calculated in the center of the FOV or measured by evaluating the smallest rods that can be distinguished in a cold/hot rod phantom.

We aim at improving sensitivity and resolution for brain SPECT imaging through innovative collimator design. However, designing a new collimator is not straight-forward and the optimal design depends in a complicated manner on many parameters, such as the size of the region of interest (ROI) or organ(s) being imaged, the energy of the photon(s) to be detected, the detector's intrinsic spatial resolution, the size of the detector, the radius of rotation (ROR) and the requirements of the application. For example, in small animals, resolution is generally more important than in most human whole-body clinical applications. In gated cardiac imaging, on the other hand, sensitivity is generally considered to be more important than resolution. Furthermore, imaging of higher energy radionuclides presents additional challenges for reducing collimator penetration and scatter without seriously compromising either resolution or sensitivity. So, before we can actually start designing a dedicated brain SPECT collimator, we need to understand all these different effects.

The principles of collimator design were extensively described in a review article in 1992 [162] and in several textbook chapters; e.g. see [80] and [142] for clinical and preclinical collimators respectively. However, in the meantime, there have been a few important new developments. Firstly, new collimator production techniques have been introduced, which make the fabrication of more complex collimator designs possible. And secondly, new detector technologies, providing better intrinsic spatial resolution, have become available (section 2.1.2.1). This has influenced the optimal collimator requirements as high-resolution detector technologies also call for collimators with higher geometrical spatial resolution [196, 75, 250].

In this chapter, we want to provide some insights and useful guidelines for choosing, optimizing, and producing SPECT collimators with the latest developments in mind. In this introduction we first give an overview of the different collimator types with their characteristics (sensitivity and resolution). We then discuss some key concepts like septal penetration, high-energy applications, sampling completeness and multiplexing. We also discuss different manufacturing techniques and their respective advantages

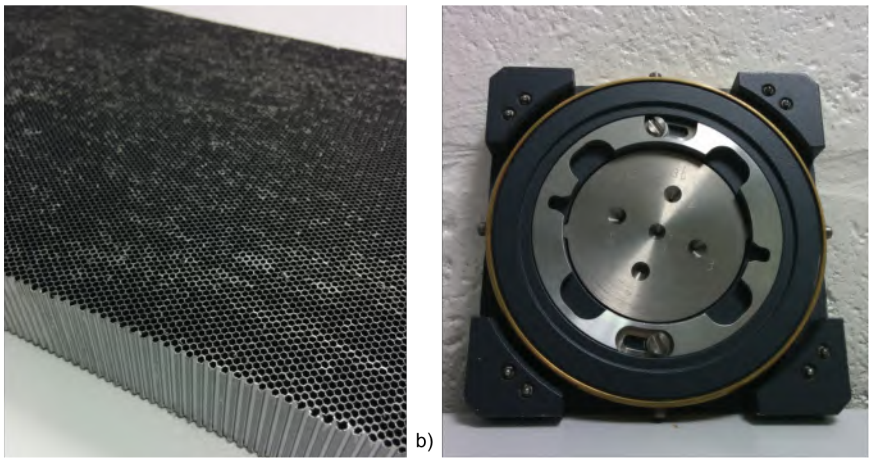

Figure 3.1: (a) A parallel-hole collimator (b) A multi-pinhole collimator.

and disadvantages. In the second part of this chapter (section 3.3) we give some general guidelines for selecting the best collimator type for different applications and target resolutions and in the last part (section 3.4) we introduce methods for sensitivity maximization and task-based collimator optimization. Finally, to conclude, we also give some examples and use the optimization methods to compare a parallel-hole, fan-beam, cone-beam and multi-pinhole collimator for different applications.

3.1.1 Collimator types

The decision about which type of collimator to use for a given imaging application depends most importantly on the ratio between the size of the field-of-view (FOV) and the size of the imaging detector, but also on the required spatial resolution and/or sensitivity. Therefore, we will first review several different types of collimation with their specific sensitivity and resolution properties. For simplicity, the collimator resolution formulae shown in this section do not include the mean interaction depth in the detector, which is generally much smaller than the distance from the source to the collimator and the collimator thickness.

3.1.1.1 Parallel-hole collimators

The parallel-hole collimator was first presented by Anger in 1964 [11] and is still used as the standard collimator in clinical practice. The collimator consists of a plate of dense material (most commonly an alloy of lead and a few percent antimony) containing a honeycomb structure of closely packed, parallel, hexagonal-shaped holes separated by lead septa (Fig. 3.1a). Other hole shapes (e.g., square, circular, or triangular) also exist, but are less common. Fig. 3.2a shows a cross section. Only photons traveling within a tight cone-shaped region in a direction perpendicular to the entrance surface of the collimator have a chance of fully traversing a collimator hole. Only those photons that are not absorbed by the collimator material can reach the detector. A parallel-hole collimator with hexagonal holes and a perfectly absorbing detector has a point-source sensitivity of [11, 79, 270]

$$Sens_{PAR} = \frac{\sqrt{3}}{8\pi}\frac{d^2}{a_{eff}^2}\frac{d^2}{(d+t)^2} \tag{3.1}$$

and a resolution of [11, 134, 70]

$$R_{PAR}(h) = d\frac{a+h}{a_{eff}}, \tag{3.2}$$

respectively, where d is the hole diameter (flat-to-flat distance), t is the septal thickness and h is the perpendicular distance from the point source to the collimator. $a_{eff} = a - 2/\mu$ is the physical hole length a (collimator thickness) approximately adjusted for penetration effects [134]. μ is the attenuation coefficient ($1/\mu = 0.37$ mm for ^{99m}Tc and lead). The system resolution is:

$$R_{sys}(h) = \sqrt{R_i^2 + [R_{PAR}(h)]^2}, \tag{3.3}$$

where R_i is the intrinsic spatial resolution of the detector. Both sensitivity and resolution formulae are given for a point source at a certain location in image space. For a parallel-hole system, the point source sensitivity is equal everywhere in the FOV, while resolution depends on the distance h. For the analytical derivation of the formulae and for other hole shapes, the reader is referred to the work of [270].

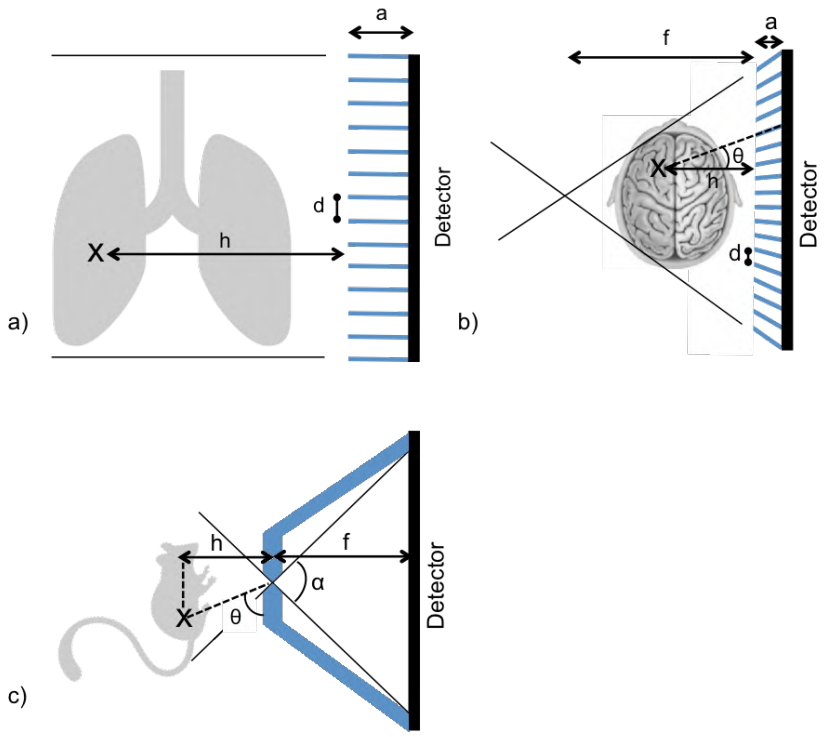

Figure 3.2: Transverse cut through a (a) parallel-hole collimator (b) fan-beam collimator (c) pinhole collimator. In these figures, *d* is the hole diameter, *h* is the perpendicular distance from the point source to the collimator, *a* is the collimator thickness, *f* is the focal length, θ is the angle of incidence and α is the pinhole opening angle.

3.1.1.2 Converging and diverging hole collimators

When the object of interest is smaller than the available detector area, an important performance gain may result from using converging collimators; this is because, for a small object, a parallel-hole collimator would leave most of the detector unused. For this reason, clinical brain SPECT imaging is often performed using fan-beam and not parallel-hole collimators. In a fan-beam collimator, the holes converge towards a focal line parallel to the axis of rotation (Fig. 3.2b). The holes are tilted in the transverse plane and parallel in the axial direction. In a cone-beam collimator, the holes are tilted both in the transverse plane and in the axial direction, and converge towards a focal point. Converging collimators magnify the ROI on the detector and,

therefore, the effect of the intrinsic resolution of the detector, R_i, on the total resolution is reduced to R_i/m:

$$R_{sys}(h,\theta) = \sqrt{(\frac{R_i}{m_{conv}(h)})^2 + [R_{conv}(h,\theta)]^2}, \tag{3.4}$$

where m_{conv}(h) is the collimator magnification, defined as:

$$m_{conv}(h) = \frac{f+a}{f-h} \tag{3.5}$$

and f is the focal length and $R_{conv}(h,\theta)$ is the geometric resolution of the collimator:

$$R_{conv}(h,\theta) = d\frac{a+h}{a_{eff}}\frac{1}{\cos\theta}\frac{f+a/2}{f+a} \tag{3.6}$$

where θ is the angle between the detected gamma ray and the perpendicular to the detector (θ=0 for perpendicular incidence). This resolution formula is based on the derivation given by Moyer [167] and the letter from Gerber [70] addressing the effect of collimator penetration.

The sensitivity of the converging hole collimator is:

$$Sens_{conv}(h,\theta) = \frac{\sqrt{3}}{8\pi}\frac{d^2}{a_{eff}^2}\frac{d^2}{(d+t)^2}(\frac{f}{f-h})^n\cos^2\theta, \tag{3.7}$$

where n=1 for fan-beam collimators and n=2 for cone-beam collimators.

The above resolution and sensitivity formulae are for a point source at a certain position in image space (where the position is determined by distance h and angle θ) and assume that the hole size is constant over the full length of the hole, and that it is identical for all holes [167, 162]. Different formulae apply to different hole shapes [63, 270], and it has also been shown that hole tapering provides improved sensitivity at equal resolution [180, 35].

When the object of interest is relatively large, it may be appropriate to use diverging collimators [168], e.g., for kinetic modelling in mice, it is important to see the organ of interest and the heart within a single bed position in order to obtain an arterial input curve [154]. Although diverging collimators have not been very common in the past, with the arrival of new

high-resolution detector technologies, it becomes possible to enlarge the FOV and still obtain a sufficiently high resolution [175].

3.1.1.3 Single and multi-pinhole collimators

A pinhole collimator consists of one or multiple small pinhole aperture(s) in a plate of lead, tungsten or any other dense material (Fig. 3.2c and Fig. 3.1b). The object of interest is projected through the aperture onto the detector. Pinhole collimators are very different from parallel-hole and converging beam collimators in the sense that every pinhole generates a full projection, while in the other collimators, only 1 projection is generated for the ensemble of holes. Pinhole collimators are also placed further away from the detector, while parallel-hole, fan- and cone-beam collimators are placed just in front of the detector.

The most common pinhole has a knife-edge profile (Fig. 3.2c) but other shapes, e.g., channeled (keel-edge) pinholes, have also been used [217]. Keel-edge pinholes are particularly interesting for high-energy radionuclides and pinholes with large acceptance angles, as they reduce penetration. Other solutions to reduce penetration include the use of truncated pinholes [120] or clustered pinholes [74].

The resolution and point-source sensitivity of a knife-edge pinhole collimator for a point source, are [179]:

$$Sens_{piho}(h,\theta) = \frac{d_{Seff}^2 \sin^3\theta}{16h^2}, \tag{3.8}$$

where θ and h determine the location of the point source in image space, with θ the angle of incidence measured from the plane of the pinhole aperture (θ=$\pi/2$ for perpendicular incidence) and h the perpendicular distance from the point in the FOV to the plane defined by the pinhole aperture. d_{Seff} is the sensitivity-effective pinhole diameter, which is the physical pinhole diameter, d, corrected for penetration at the edges of the aperture at normal incidence [179, 148]:

$$d_{Seff} = \sqrt{d(d + \frac{2}{\mu}\tan\frac{\alpha}{2}) + \frac{2}{\mu^2}\tan^2\frac{\alpha}{2}}, \tag{3.9}$$

where α is the opening angle of the pinhole and the attenuation coefficient μ for tungsten at 140.5 keV is 3.6 mm^{-1}.

$$R_{piho}(h,\theta) = \sqrt{\frac{R_i^2}{[m_{piho}(h)]^2} + (d_{Reff}(h,\theta)(1+\frac{1}{m_{piho}(h)}))^2}, \qquad (3.10)$$

where $d_{Reff}(h,\theta)$ is the resolution-effective pinhole diameter (corrected for penetration) and m_{piho} is the pinhole magnification:

$$m_{piho}(h) = \frac{f}{h} \qquad (3.11)$$

and f is the focal length (the pinhole-to-detector distance).

When $\theta \neq \pi/2$, the resolution-effective diameter $d_{Reff}(h,\theta)$ is broken into a parallel and perpendicular component, which are described by two equations [7]:

$$d_{re//}(h,\theta) = d + \frac{\ln 2}{\mu}(\tan^2\frac{\alpha}{2} - \cot^2\theta)\cot\frac{\alpha}{2}\sin\theta \qquad (3.12)$$

and

$$d_{re\perp}(h,\theta) = \sqrt{(d + \frac{\ln 2}{\mu}\tan\frac{\alpha}{2}\sin\theta)^2 - (\frac{\ln 2}{\mu})^2\cos^2\theta}, \qquad (3.13)$$

where $d_{re//}(h,\theta)$ and $d_{re\perp}(h,\theta)$ are the resolution-effective aperture sizes, respectively, in the parallel and perpendicular directions. The parallel direction is the perpendicular projection of the vector from the center of the pinhole aperture to the point source, on the plane of the pinhole. The perpendicular direction is perpendicular to the parallel direction in the detector plane. One can thus choose to calculate pinhole resolution (Eq. 5.10) in the two directions, or to pick the worst/best case at each position or to assume normal incidence, which results in an effective pinhole diameter d_{Reff} of:

$$d_{Reff} = d + \frac{\ln 2}{\mu}(\tan\frac{\alpha}{2}) \qquad (3.14)$$

Pinhole collimators are often used in small-animal imaging because they allow for high magnification so that sub-millimeter resolution can be achieved. The sensitivity of a single pinhole collimator is rather low, but if

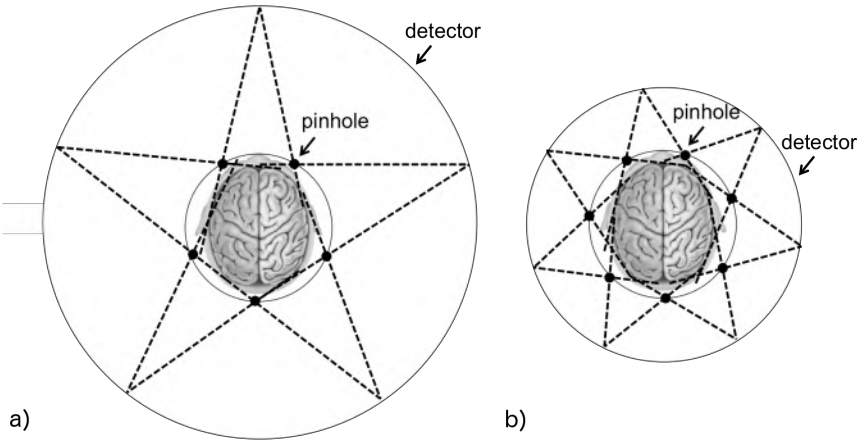

Figure 3.3: (a) Magnifying multi-pinhole system (b) Minifying multi-pinhole system

the detector is large enough, it can be improved by combining multiple pinholes into a multi-pinhole collimator. Examples of commercial small-animal multi-pinhole SPECT systems are the U-SPECT [246], the NanoSPECT [121] and the X-SPECT [208]. Multi-pinhole collimators have also been used for other applications, like cardiac [39, 53, 67] and brain SPECT imaging [75].

With the arrival of high-resolution detector technologies, different studies have also shown the potential of combining multi-pinhole collimators and object-minifying pinhole-detector geometries [250, 173, 75, 153, 196]. Minifying multi-pinhole collimators allow more projections on the detector (Fig. 3.3), which is beneficial for stationary SPECT systems. These offer potential advantages for dynamic scanning, for improved system stability and patient comfort, and for compatibility with MRI, enabling the development of truly simultaneous SPECT/MR for both preclinical and clinical use [138, 82, 29, 27].

Another possibility for obtaining more projections on the detector, is to allow overlap between the projections of multiple pinholes (Fig. 3.6), which is also referred to as multiplexing. On the other hand, multiplexed projection data contains less information (because it is impossible to determine the pinhole through which a photon traveled before it was detected) and this can result in artifacts in the reconstructed image. This will be discussed in more detail in section 3.1.5.

3.1.1.4 Other types of collimation

3.1.1.4.1 Coded apertures A coded-aperture mask is a specific arrangement of many pinholes (often >100) that has been applied in astronomy, but also in medical imaging (Fig. 3.4a). A coded aperture collimator can be regarded as a highly multiplexed pinhole collimator, and it allows substantially improved system sensitivity while maintaining very good spatial resolution. However, it has been shown that the increased sensitivity of coded apertures only provides an equivalent increase in image signal-to-noise ratio (SNR) for point sources or sparse distributions of point sources [68]. Coded apertures are, in a sense, just extremely multiplexed multi-pinhole collimators and, as a result, they suffer from a similar trade-off between sensitivity and data ambiguity (section 3.1.5). Coded apertures are most interesting for sparse activity distributions, and less so for non-sparse objects [6, 68]. Nevertheless, they have been successfully applied to high-resolution small animal imaging in some applications. [141, 143, 8].

3.1.1.4.2 Slit-slat and multi-slit slit-slat collimators A slit-slat collimator can be regarded as a mixture of a pinhole and a parallel-hole collimator (Fig. 3.4b). Most commonly, the slits are oriented parallel to the axis of rotation. They form long knife-edges so that the collimator has the properties of a pinhole collimator in the transverse plane [8]. Between the knife-edges and the detector, parallel slats collimate the radiation in the axial direction. Slit-slat collimators combine the advantages of both the pinhole and the parallel-hole collimator: the pinholes magnify the ROI so that a high spatial resolution can be achieved (in the transverse plane). They are well suited for fully stationary systems as multiple slits can be combined in a ring around the FOV (multi-slit slit-slat) providing sufficient angular sampling, while the parallel slats provide sufficient axial sampling. They are well-suited for medium-size objects with a long axial field of view, e.g., the human brain [145].

3.1.1.4.3 Rotating slat collimators Rotating slat collimators are made of parallel slats, and thus collimate in only one direction. They measure plane integrals instead of line integrals. Therefore, the projection data contains less information (is more ambiguous) and SPECT data acquisition with slat collimators requires two motions: one rotation around the axial direction (similar to all other collimators) and one rotation around its own central axis [275]. Its system characteristics have been described in [253]. Because the collimation is in only one direction, the sensitivity is much

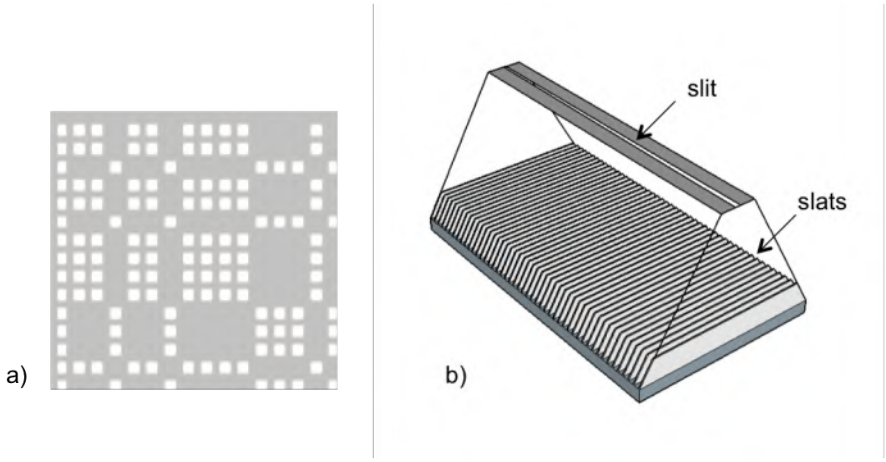

Figure 3.4: (a) Coded aperture collimator (b) Slit-slat collimator.

higher than that of a parallel-hole collimator. However, due to the large ambiguity, this increase in sensitivity does not necessarily result in better image quality (similar as in highly multiplexed multi-pinhole systems). In planar scans with clinical phantoms, a rotating slat collimator performed better than a parallel-hole collimator [251], but these results were not confirmed in the clinical setting of 3D-reconstructed heart-defect imaging [247]. Rotating slat collimators are well suited for 'hot-spot' imaging (sparse objects), but are outperformed by parallel-hole collimators for imaging 'cold' regions within a large background region (non-sparse objects) [282].

3.1.1.4.4 Hybrid collimators Hybrid collimators combine different types of collimation. Examples are multisegment slant-hole [42, 123, 15], variable angle slant-hole [158, 122], multifocal cone-beam [34], and cardiofocal collimators [85] as well as a hybrid ultra-short-cone-beam/slant-hole collimator [181, 160, 183]. They will not be further discussed here.

3.1.2 Septal penetration

Gamma rays that penetrate the collimator material can result in image degradation and this effect needs to be limited. In parallel-hole, fan-beam and cone-beam collimators, penetration typically occurs when gamma rays cross from one collimator hole to the next. With thicker septa, there is less penetration; however, more of the detector area is obstructed, which

degrades sensitivity. A proper trade-off is thus needed. A method for calculating the septal thickness, given a single-septal penetration of, e.g., 5% (which may be considered acceptable for some tasks), was described in [41, 105]. An even better solution is to include septal penetration in the optimization of the collimator [161]. For pinhole collimation, penetration typically occurs at the knife-edge of the pinholes, where the collimator material is thin. The degree of penetration is often very high but can be compensated during the reconstruction process by modeling the penetration during the ray-tracing process [73], by using a mathematical description of the penetrative point-spread function [216], or by using an effective pinhole aperture (eq. 5.15, 5.12, 4.15). The degree of penetration is mainly influenced by the opening angle of the pinhole and the collimator material. Solutions for limiting septal penetration include the use of asymmetric pinholes [120], pinholes with channels [217, 245], loftholes [50] (see also section 4.2.2), clustered pinholes [74] and very high-density materials, such as gold or iridium. However, these are mostly needed to obtain very high resolution (sub-millimeter) with higher energy radionuclides, such as ^{18}F or ^{131}I, when the desired system resolution cannot be achieved anymore because of the high degree of penetration [21].

3.1.3 High-energy applications

High-energy applications include imaging to follow patient response to therapy or to determine doses for radionuclide therapy, real-time proton beam range verification and high-resolution tomography of positron emitters. These applications call for adapted collimator design because of the higher energy photons (above 300 keV up to MeV range) penetrating the collimator.

^{131}I is a beta-emitter and is frequently used for radionuclide therapy in lymphoma. Interestingly, it also emits gamma rays (mainly at 284, 364, 637 and 723 keV), which makes it possible to monitor the delivered dose. Van Holen et al. [249] showed improved quantification using a rotating slat collimator for ^{131}I compared to a parallel-hole collimator, due to a relative lower number of photons that penetrated the collimator.

Yttrium-90 is another radionuclide used frequently for cancer therapy by beta-emission (2.28 MeV). No gamma rays are emitted by this radionuclide; however the betas also generate secondary bremsstrahlung X-rays in the patient body that form a continuous spectrum extending up to the maximum electron energy. Walrand et al. [263] showed improved quantification using a camera with 30-mm thick BGO crystal and a high-energy pinhole colli-

mator compared to a conventional NaI camera equipped with a high-energy parallel-hole collimator.

Hadron (proton and heavy ion) beam therapy is a radiotherapy treatment that is gaining importance, mainly because the hadron beams deliver their maximum energy within a defined range and heavy ions have a higher biological efficiency. Uncertainties in the determination of this range can be reduced using in vivo range verification. Therefore, Perali et al. [187] designed a tungsten slit collimator and used it to acquire prompt gamma rays in the 3-6 MeV energy range. Proton range verification is performed at projection level and is therefore not tomographic but nevertheless, we included it in this overview as an interesting high-energy application for slit collimators.

Finally, Goorden et al. [74] introduced the concept of clustered pinholes for the application of high-resolution tomography of ^{18}F, a positron emitter (511 keV). To deal with collimator edge penetration, every pinhole is replaced by a cluster of pinholes and every pinhole in a cluster has a narrow opening angle, which reduces photon penetration.

3.1.4 Sampling completeness

One of the major concerns when designing a collimator is the sampling completeness of the system. In the end, the purpose is to recover the 3D activity distribution from the projection data and this can only be successful if the acquired data contain sufficient information. We distinguish three types of sampling criteria: angular sampling, axial sampling and the number of angular views.

3.1.4.1 Angular sampling

Conditions for angular sampling completeness in a parallel-hole system were first described by Orlov [177] and are, therefore, also called the Orlov conditions. Orlov showed that a single-head parallel-hole system needs to be continuously rotated over at least 180° to provide sufficient angular sampling (assuming no truncation of the FOV). Later, the sampling conditions were also evaluated for fan- and cone-beam collimators [229, 215], which need to be rotated over 180° plus the fan angle for sampling completeness, or over 360° in the case of a half-cone beam [115]. Pinholes and slits (at least those that see the complete transverse FOV) have a sampling profile similar to that of cone-beam collimators and require the same rotation. As an alternative, multiple pinholes or multiple slits can also be combined in

a ring [239, 27, 246] or sphere [199, 75] so that the system can be used without rotation.

3.1.4.2 Axial sampling

Tuy showed that cone-beam and pinhole systems only achieve data completeness in the plane described by the rotating focal point (mostly the central slice) [229]. To obtain sufficient axial sampling in a longer object, they can be combined with a parallel-hole [221, 94] or a fan-beam collimator [274, 78, 182] using a dual-head system. Alternatively, axial sampling sufficiency can also be obtained by scanning along a helical path [93, 226]. However, one must be careful to use a sufficiently small helical pitch [273]. This helical movement can either be continuous or stepped, while acquiring data at each stop position of the camera, i.e., "step-and-shoot" mode. While helical orbits can also be used for pinhole collimators [149, 231], it is more common to use a multi-pinhole collimator with pinholes focusing at different axial planes to improve sampling [156, 255], or to translate a cylindrical system with one or more ring(s) of pinholes [246, 112]. One can even make a complete stationary system using multiple rings of pinholes focusing at different slices in the FOV (as in our design described in the next chapter) or in a hemispherical configuration [199, 75].

In more complicated collimators (e.g., when the pinholes are tilted or truncated [120]) one can use a numerical algorithm to assess sampling completeness [147]. It is also common to evaluate axial sampling completeness using a reconstructed Defrise phantom [95], a cylindrical phantom with a set of discs filled with activity (Fig. 3.5a). It is advisable to use a phantom of the same size as the required FOV and to choose a disc thickness in the same range as the target resolution of the system.

3.1.4.3 Angular views

The minimal number of angular views needed to reconstruct an object depends on the size of the object and the target resolution. In clinical whole-body and brain imaging, most systems rotate with a step size of 2-6 °. A stationary multi-pinhole system for brain imaging would thus require 60-180 pinholes per axial slice. However, depending on the FOV and the magnification, the use of such a large number of pinholes might result in overlapping projections, which is usually undesired. To provide sufficient angular views in a non-rotating system is therefore very challenging. As an alternative to rotation, some multi-pinhole systems include an axial/transverse translation

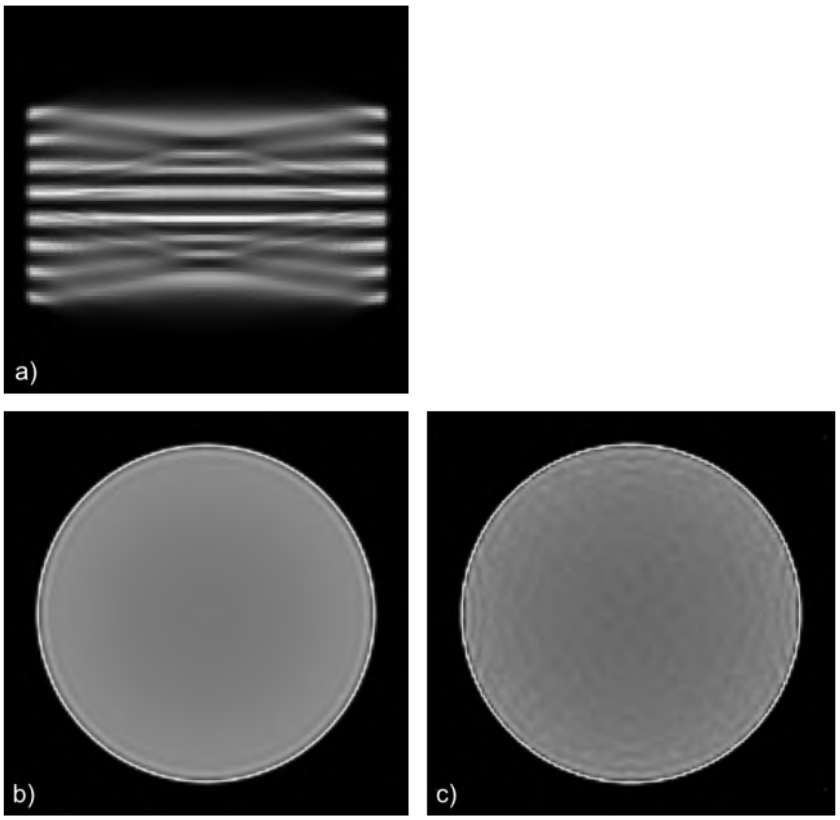

Figure 3.5: (a) Insufficient axial sampling in a Defrise phantom (coronal view) (b) Sufficient angular sampling in a uniform phantom (transverse view) (c) Artifacts due to insufficient angular sampling in a uniform phantom (transverse view).

to achieve sufficient sampling (e.g., the U-SPECT [246]). In the next chapter (4) we will also present a novel solution for multi-pinhole collimators, based on shutters, i.e. small blocks of tungsten connected to actuators that can be used to open/close pinholes. A sequence of shutter movements can then be used to obtain an acquisition that is equivalent to a rotational movement. According to the Nyquist-Shannon sampling theorem [211], the sampling period needs to be at least two times smaller than the target spatial resolution. Therefore, we need a minimal number of projection angles per voxel of [89]:

$$N_{min} = \frac{\pi D}{R_t/2} \tag{3.15}$$

over a rotation angle of 360 °, where D is the diameter of the FOV. For parallel-hole collimators, this also corresponds to the minimal number of rotation angles needed, while for pinholes, fan- and cone-beam collimators, a rebinning step is needed. However, other researchers have shown that the sampling requirement may be relaxed, at least for some types of projection geometries [20, 33]. The optimal number of angular views also depends on the activity distribution [116], the task and the availability of prior information. A practical way to check the sampling period is to simulate or acquire a scan of a uniform phantom. Poor sampling will manifest itself through the presence of non-uniformity artifacts in the reconstructed image.

3.1.4.4 Sampling uniformity

We have now discussed axial and angular sampling sufficiency, but another important aspect of collimator design is sampling uniformity. When certain voxels in the FOV are sampled more often (and thus with a much higher sensitivity than others), this will result in different noise characteristics that will be visible when reconstructing a uniform phantom. This is often the case when using truncating pinholes. Another issue with truncating pinholes is that the peripheral regions of the pinhole's response are difficult to model. This results in streak artifacts and is particularly disturbing when this peripheral region is back-projected somewhere in the center of the FOV, as is the case with truncating pinholes. However, little is known about this phenomenon and its underlying causes. Moore et al. [163] is one of the only ones publishing about this effect showing that it can be largely removed using rolled-off projection masks.

3.1.5 Multiplexing

Fig. 3.6 shows a multi-pinhole system with overlapping pinholes. Most multi-pinhole or multi-slit slit-slat collimators are designed to allow no overlap between the different projections because the ambiguity introduced by multiplexing pinholes can result in artifacts. Some use baffles [259] or extra shielding [246] to remove overlap. Yet, there are examples of multi-pinhole collimators that allow multiplexing and do not show any artifacts (e.g.,

[208],[184]) or only in certain phantoms [46]. Multiplexing also yields increased count sensitivity, since more pinholes can be placed on the collimator for the same detector size.

Over the last 10 years, many interesting studies have provided useful insights into how to obtain artifact-free images with multiplexing systems, and whether or not the increased sensitivity also results in better image quality. For example, in at least three different systems, it has been observed that irregular pinhole patterns are less likely to produce multiplexing artifacts [54, 32, 258]. This indicates that sampling is important, which is confirmed by a study on angular sampling [14] and by another about inconsistent projection data due to truncation [106]. To solve the sampling problem, different groups have successfully combined multiplexed and non-multiplexed projections. Vunckx et al. combined a multiplexing multi-pinhole collimator with a single pinhole collimator on a dual head camera [258] and Mahmood et al. designed a multi-slit slit-slat collimator with mixed multiplexed and non-multiplexed projections [129, 127]. Another solution to obtain sufficient data, is to obtain a number of projections at different pinhole-detector distances. This approach is known as "synthetic collimation" and was first proposed by Wilson et al. [271] and later also applied in the SiliSPECT system [213, 214] with two detectors for one collimator, resulting in a non-multiplexed low-resolution projection and a multiplexed high-resolution projection.

If sufficient data cannot be obtained, it also helps to reduce the solution space by using a body contour to provide prior information during the reconstruction[258]. Sparse activity distributions are also easier to reconstruct from multiplexed data than uniform activity distributions. Multiplexing can also be seen as a form of compressed sensing, a sampling technique based on the principle that a sparse image or signal can be recovered from far fewer samples than suggested from the Shannon-Niquist theorem [31, 55].

While multiplexing provides an increase in sensitivity, a corresponding increase in contrast-to-noise ratio does not necessarily follow in all cases. Reconstructions of multiplexed projection data generally converge more slowly than those of non-multiplexed data, in which case the sensitivity advantage from multiplexing could be essentially irrelevant [155] (see also section 5.2.7). In this context, the increased sensitivity from multiplexing may only compensate for increased ambiguity [259]. Some groups on the other hand, have observed a large increase in the contrast-to-noise ratio when comparing multiplexed with non-multiplexed setups [127, 119]. At first sight, these results seem to contradict the results from [155, 259] and section 5.2.7, but

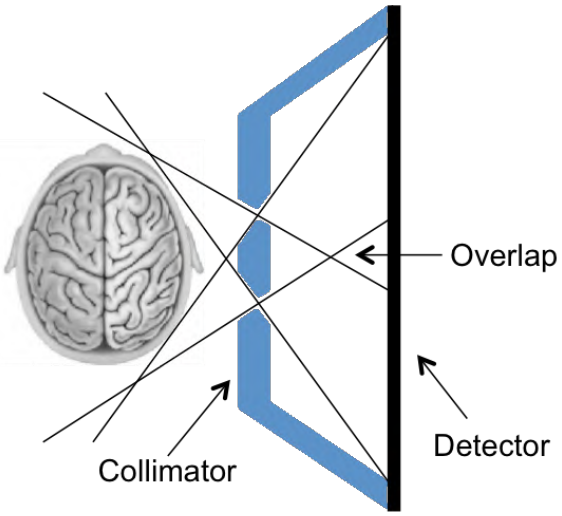

Figure 3.6: Overlapping projections in a multiplexing multi-pinhole system.

interestingly, there is an important difference between these studies, which is related to detector usage. In [155, 259] and section 5.2.7, all multiplexed and non-multiplexed setups use 100% of the detector, while in [127, 119], the degree of detector coverage varies between the multiplexed and non-multiplexed setups (although an approximate correction factor was used in [127]). This might explain the different findings and is supported by Vunckx et al. [259], who stated that once the detector area is entirely used, the contrast-to-noise ratio does not improve with increased multiplexing. This also explains why reconstructions of sparse activity distributions benefit more from multiplexing than do those of uniform distributions [155].

In the light of these diverging results, we conclude that more research is needed. To fully understand the advantages and disadvantages of multiplexing, we dedicated an important part of this dissertation to multiplexing (see chapter 5).

3.2 Production techniques

Collimator design also involves the practical issues related to manufacturing. Different production methods exist and they all have their specific advantages and disadvantages. Materials that are typically used include lead (Pb), tungsten (W), gold (Au), iridium (Ir) and platinum (Pt). Because of their

cost, Pb and W are by far the most commonly used.

This is important because it reduces penetration at the knife-edge, although it was shown that pinhole penetration can largely be compensated for by modeling it in the iterative reconstruction process, unless high-energy radionuclides and very large acceptance angles are used [21].

Parallel-, fan-, cone- and diverging-beam collimators are traditionally fabricated by stamping and stacking lead foils (Fig. 3.1), or by casting molten lead (Fig. 3.7a). These are relatively easy and cheap techniques, but they have their limitations. As a rule of thumb, the minimum hole diameter is 1.2 mm and the minimum septal thickness is 0.15 mm. These specifications are sufficient for traditional clinical collimators but to build very high-resolution collimators, smaller bores and septa are needed. As an alternative solution, X-ray lithography and metal electroforming allow very high-accuracy collimators to be produced (1μm) with a variety of metals (e.g., Cu, Ni, Pb, Ag and Au) (Fig. 3.7b). It has been demonstrated that 0.025 mm thick gold septa are feasible with this technique [130]. Another technique is based on photochemically etched tungsten foils that were stacked to form the collimator pattern [174] (Fig. 3.8a). However, the foils need very precise alignment and the manufacturing precision is limited by the foil thickness. Kastis et al. used this technique with 75 μm tungsten foil to produce a 7 mm-thick high-resolution parallel-hole collimator with 260 μm holes and 120 μm septal thickness [102]

Pinhole collimators are mostly made from tungsten, which has a higher density than lead (19.3 g/cm^3 versus 11.3 g/cm^3). However, tungsten has a high melting point and cannot be cast like lead. It is also very brittle and difficult to machine. Therefore, one often uses alloys (with nickel, iron and/or copper) which can then be milled or drilled with a diamond drill, or machined using electric discharge machining (EDM) (Fig. 3.8b). These techniques are very expensive, and complex shapes like strongly tilted pinholes, loftholes [50] or pinholes with small opening angles cannot be easily produced.

Cold casting is a novel technique based on tungsten powder mixed with epoxy resin. The density of the tungsten composite material is 9 g/cm^3 [151], which is much lower than the density of pure tungsten. Therefore, the technique is mostly used for the collimator body, in combination with pinhole inserts made from more dense materials such as tungsten, gold, platinum, iridium or titanium. In [151] the pinhole inserts were produced by lost-wax casting a platinum-iridium alloy which results in a density that is even higher than that of gold.

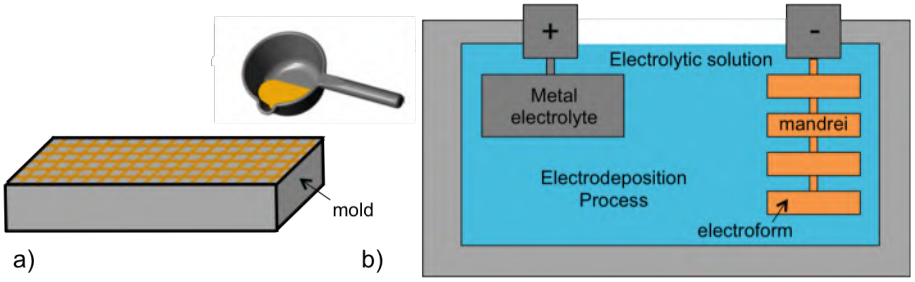

Figure 3.7: (a) Lead casting a parallel-hole collimator in a mold (b) metal electroforming.

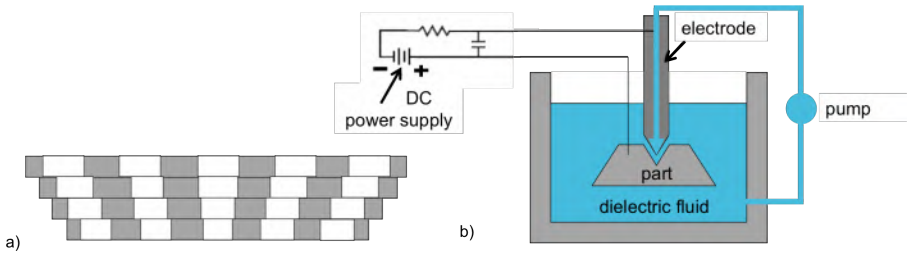

Figure 3.8: (a) Stacking tungsten foils to produce a cone-beam collimator (b) Electric discharge machining.

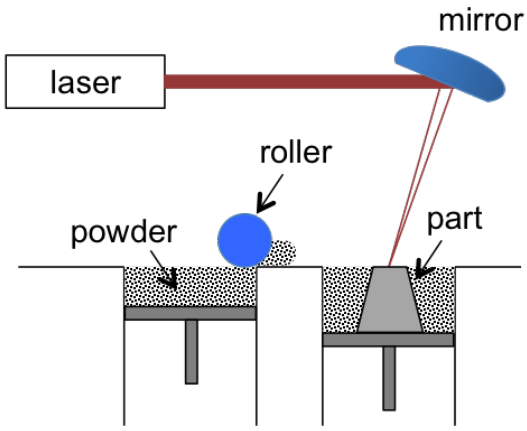

Figure 3.9: Additive manufacturing. Powder particles are distributed over the part by the roller. The laser selectively melts certain regions of the powder layer.

Another recent development includes metal additive manufacturing, which can be used to produce complex parts from a 3D computer-aided design (CAD) file [52]. It is based on selective laser melting of tungsten powder that is added in thin layers to build up the desired part (Fig. 3.9). A density of 18.56 g/cm^3 was recently reported [49] and a production accuracy of 35μm is now possible. A tungsten parallel-hole collimator was built using additive manufacturing with a hole size of 525 μm, a septal thickness of 150 μm and a hole length of 25 mm [49]. This technique seems also interesting for building MR-compatible SPECT systems because it is based on pure tungsten powder and does not contain any magnetic materials, in contrast to the tungsten alloys that are used in other production techniques. We will further evaluate the MR-compatibility of printed tungsten in chapter 6.

3.3 Collimator selection

When designing a new system, one of the most important decisions is which collimator to use. Unfortunately, there is no straightforward answer to this question. It depends on the size of the FOV, the intrinsic resolution of the detector, the size of the detector, the target resolution, the energy of the radionuclide being used, the space constraints, and whether the system should be stationary or not.

Pinholes are generally most interesting for imaging small animals because they allow for high magnification so that sub-millimeter resolutions can be achieved (even with low-resolution detectors). The sensitivity of a single-pinhole collimator is rather low but if the detector is large enough, this can be improved by combining multiple pinholes into a multi-pinhole collimator. Because the sensitivity decreases quadratically with the distance to the apertures, pinhole collimation was traditionally only interesting for imaging small objects; however, with the emergence of new high-resolution detector technologies, the possibility of using many minifying pinholes allows an increase in sensitivity so that multi-pinhole imaging also becomes beneficial for medium sized organ imaging (e.g., cerebral and cardiac imaging). Pinholes are also interesting for stationary systems although multi-slit slit-slat or coded-aperture collimators can also be used for that purpose.

Parallel-hole, fan-beam and cone-beam collimators have traditionally been the main choice in clinical settings. Parallel-hole collimators have a large FOV and their sensitivity does not decrease with distance, making them very suitable for whole body scanning. Brain SPECT imaging is still most

often performed with fan-beam collimation, but cone-beam and slit-slat collimators are also well-suited for medium-size organ or animal imaging [146]. With the emergence of high-resolution detector technologies, we also see new applications, e.g., the use of a fan-beam collimator for small-animal imaging [202].

If the size and the intrinsic spatial resolution of the detector are known, then we can make an initial selection according to the following algorithm:

1. If the size of the FOV is approximately the same size as that of the detector, then use a parallel-hole, a (multi-)pinhole or a (multi-slit) slit-slat collimator. The intrinsic resolution of the detector should be better than the desired system (or 'target') resolution.

2. If the FOV is larger than the detector, then use a diverging-hole collimator or minifying (multi-)pinhole or (multi-slit) slit-slat collimator. The intrinsic resolution of the detector should still be better than the target resolution.

3. If the FOV is smaller than the detector, then use a converging beam collimator or magnifying (multi-)pinhole or (multi-slit) slit-slat geometry. The intrinsic resolution of the detector needs to be better than the target resolution multiplied by the magnification factor.

The existing literature can also be of great help when selecting a collimator. For example, Goorden et al. [75] compared different multi-pinhole systems with both a clinical parallel-hole and fan-beam system. The results are interesting because they show what can be achieved with high-resolution detector technologies compared to clinical parallel-hole and fan-beam system. For example, it was shown that with a detector resolution of 0.05 mm and a multi-pinhole collimator, we could achieve a sensitivity that is 14.5 times larger than the sensitivity of a parallel-hole system and still keep the same system resolution.

Another interesting comparison was performed for (multi-slit) slit-slat and parallel-hole collimators [145] for a target resolution of 4, 5 and 10 mm, an intrinsic detector resolution of 3.5 mm and different FOVs (1-20 cm). It was shown that slit-slat collimators are likely a better choice than parallel-hole for small- to medium-sized objects with a long axial field of view.

In section 3.4.1.1 we also perform a comparison between a cylindrical multi-pinhole system and a parallel-hole, fan- and cone-beam system for the same detector surface area, intrinsic resolution, FOV and target resolution. We did this for a 30 mm FOV (representative for small animal applications)

and a 220 mm FOV (representative for brain or cardiac appliactions) and for an intrinsic detector resolution of 3.5 mm and 0.5 mm. In all cases, the detector was chosen to be larger than the object. Our results show that the cone-beam collimator outperforms the parallel-, fan-beam and multi-pinhole collimators in mostly all cases, except for the small FOV case with the high intrinsic detector resolution, where the multi-pinhole collimator showed to benefit more from the high-resolution detector.

Collimator selection is easiest if one can assume that the target resolution is known, and then simply maximize the sensitivity. However, the optimal resolution is also task-dependent. For example, it is clear that for small animal imaging, one needs a better resolution than for brain imaging. But how good should the resolution actually be and how much sensitivity can we give up for a better resolution? In 1985, Muehllehner showed with a simulation study that contrast-to-noise ratio increases with resolution, despite the loss in sensitivity. A resolution improvement of 2 mm compensated for a loss in sensitivity by a factor four [169]. Similar results (with a factor of 3) were later found in a measurement study [61]. These studies suggest that, at least for conventional parallel collimation, it may often be advantageous to aim for a high target resolution. On the other hand, there is little doubt that some minimum number of counts is also desirable [126]. Moreover, both of these earlier studies [169, 61] were performed using filtered back projection (FBP) as a reconstruction algorithm. Other studies have suggested a different outcome for the case of iterative reconstruction techniques utilizing resolution recovery, which is mostly used nowadays, and have indicated that it can certainly be useful to re-evaluate the theory. For example, Lau et al. [113] showed that when resolution recovery is included, a general-purpose (GP) collimator results in lower noise than a high-resolution (HR) collimator for cardiac SPECT, independent of the contrast achieved. Similar results were obtained by Kamphuis et al. [101], who showed that a better contrast-to-noise ratio could be achieved for 2-cm cold lesions in a uniform background when using a GP collimator, rather than a medium- or high- or ultra-high-resolution collimator. Likewise, McQuaid et al. [136], showed that better quantification of 16-mm hot lesions distributed throughout a human torso sized digital phantom could be obtained by using a GP collimator than a HR collimator. Interestingly, Zhou et al. found similar results for lesion detectability in an ideal observer study on sinogram data [280].

3.4 Collimator optimization

Collimator optimization should ideally be fully task-dependent, i.e., we wish to compute a metric that describes the task performance for a range of possible values of collimator resolution and septal penetration fractions and then search for where this metric achieves its maximum value. Examples of task metrics that are typically considered are signal-to-noise ratio, uncertainty in the reconstruction, or lesion detectability. We seek to determine the collimator resolution and septal penetration that maximize the given task-based figure-of-merit. But for each possible combination of collimator resolution and septal penetration, we also need to determine an appropriate set of collimator geometric parameters (hole size, hole length, and septal thickness) that will produce the desired resolution and penetration values. The obvious choice is simply to maximize the geometric sensitivity of the collimator. These three constraints then allow one to determine unambiguously the geometric parameters of each collimator for which we need to compute the task performance. Maximizing sensitivity for a certain resolution simply allows one to choose the appropriate set of collimator parameters to accomplish one step of a full task-dependent optimization.

3.4.1 Sensitivity maximization for a given target resolution

Once the target resolution is fixed, we need to choose an appropriate set of geometric parameters that will produce the desired resolution[1] and then maximize the sensitivity of the collimator. This problem can be solved analytically for parallel-hole, fan- and cone-beam collimators but becomes more complicated for multi-pinhole collimators because of the many degrees of freedom (pinhole aperture, opening angle, number of pinholes, focal length and radius of rotation). Nevertheless, most optimization methods are ultimately based on the same general procedures:

1. First, decrease the number of degrees of freedom by fixing some design parameters (optional)

2. Secondly, define subsets of parameters that result in the given target

[1]Most optimization papers use the resolution in the center of the FOV, although an average or sensitivity-weighted average resolution has also been used. Furthermore, for this discussion, we have implicitly included effects of collimator penetration within the definition of 'target resolution'; however, we recognize that a more general approach can treat resolution and penetration as two different variables that can both affect task performance (e.g., Moore et al. [161]).

resolution[1] (analytically, if possible, and numerically, otherwise)

3. Finally, determine which of these subsets provide the highest sensitivity[2]. This is the optimal design.

In 1999, Gunter et al. [79] described the optimal design of a parallel-hole collimator based on a fixed target resolution and the "University of Chicago Penetration Criterion" [80]. Later, Smith et al. [218] proposed a slightly different method based on a self-chosen maximum allowable septal-penetration factor and including the finite detector resolution and resolution degradation due to septal penetration.

Gunter et al. [79] extended his theory for non-parallel hole collimators (e.g., fan- and cone-beam) by assuming that, locally, these collimator geometries look like parallel-hole designs. This results in fan- and cone-beam collimators that become thinner near the edges. Another approach that results in more conventional fan- and cone-beam collimator designs is presented in [35]. This is based on the same principle of local optimization but it assumes that the optimal collimator thickness and hole diameter are constant and equal to their values near the center of the collimator and that the focal point lies as close as possible behind the object, given the constraint that the FOV must contain the whole body/organ. The optimization was first applied to continuous detectors and then extended to pixelated detectors, with an extra constraint to match the pixels with the collimator holes to improve detector utilization. This was inspired by two earlier optimization studies on matched parallel-hole collimators for scintimammography [268, 195].

As mentioned above, multi-pinhole collimators are typically more difficult to optimize because of the many degrees of freedom. In most studies, all pinholes are assumed to have the same aperture and focal length but they still need to be positioned (on a ring, a sphere, a flat plate, a helix, ...) and oriented (e.g., all pointing orthogonally toward the central axis of the system, or focused on the CFOV). To limit the degrees of freedom, most researchers make a few assumptions about the geometry before starting the optimization. For example, Nillius et al. [173], Goorden et al. [75] and Rentmeester et al. [194] assume a spherical detector and collimator with all pinholes focusing on the CFOV without truncation. Both Nillius et al. [173]

[2]Many papers use the point sensitivity in the center of the FOV. However, this might not be the best choice for, e.g., multi-pinhole collimators where not all pinholes see the complete FOV. In that case, the volume sensitivity, defined as the average point sensitivity for all points in the FOV, is a better choice.

Table 3.1: Detectors used for the optimization example

diameter of the FOV	parallel-hole, fan- and cone-beam	multi-pinhole
30 mm	3 flat detectors of 7.5x7.5 cm^2	cylindrical detector with active area of 56.25 cm^2
220 mm	3 flat detectors of 40x40 cm^2	cylindrical detector with active area of 1600 cm^2

and Goorden et al. [75] found that the number of pinholes increases faster than the sensitivity decreases due to a larger collimator radius and therefore the optimal system is infinitely large. However, we usually can achieve a sensitivity that is around 95% of the upper bound with a realistic setup. Goorden also showed that this conclusion is only valid for low resolution detectors and that for higher resolution detectors, the system's optimal collimator radius is smaller [75]. Van Holen modified this approach to a cylindrical instead of a spherical geometry [250] and determined the optimal collimator and detector ring radii given the constraint that the detector ring consists of a single ring of predefined flat detectors. Additionally, Van Holen maximized the volume sensitivity, instead of the point sensitivity in the center of the FOV, which is an approach that we also used in this dissertation (e.g., section 4.3.1).

A similar technique was used to optimize a multi-slit slit-slat collimator for brain imaging [128], based on point source sensitivity in the center of the FOV.

Finally, it is important to note that high resolution and high sensitivity are no guarantee for a good image quality. Other important elements that influence image quality include axial sampling sufficiency, angular sampling, penetration, edge effects and scatter, especially for higher energy radionuclides [220].

3.4.1.1 Optimizing resolution-sensitivity trade-off

As an application of the previous section, we include a comparison between (multiple-) pinhole, parallel-hole, fan- and cone-beam collimators for two different detector resolutions (0.5 mm and 3.5 mm), and two different spherical FOVs with a diameter of 30 mm (for small animal applications) and 220 mm (for brain, cardiac or other organ-specific applications), respectively.

We optimized each collimator by maximizing the volume sensitivity for

different target resolutions R_t, given the intrinsic detector resolution, the FOV, the detector size (Table 3.1) and the degree of penetration. Volume sensitivity is defined as the average point sensitivity for all points in the FOV and target resolutions R_t is defined as the system resolution at the center of the object being imaged. The calculations of the optimal values of volume sensitivity were all based on analytical formulae described in literature:

1. The parallel-hole optimization was performed based on Eq. (11) from [218], using 5% septal penetration.

2. The fan- and cone-beam optimization was based on [35], also for 5% septal penetration and for a continuous detector but with an adapted formula for calculating the focal length, which is more exact:

$$f = \frac{z_0}{cos(\pi - atan(\frac{G/2}{z_0+L_0}) - acos(\frac{z_0}{\sqrt{(G/2)^2+(z_0+L_0)^2}}))} + z_0, \quad (3.16)$$

   with G the detector length, z_0 the point source distance and L_0 the collimator height, as in the reference paper [35]. So, we looped over different values of L_0, calculated f according to Eq. (3.16), calculated the hole sizes needed to obtain the target resolution using equations (2), (3) and (5) from [35], calculated the volume sensitivity using equations (1), (4), (6) and (7) from [35] and compared them to find the maximum volume sensitivity.

3. For the multiple-pinhole collimator optimization, we assumed a cylindrical collimator geometry with pinholes arranged along concentrical rings. All pinholes had the same aperture, no axial tilt and viewed the complete transverse FOV without multiplexing. We optimized the collimator radius c and the detector radius D while keeping the total detector surface area constant and equal to that of the triple head system used for parallel-hole, fan- and cone-beam, by adapting the detector length. This optimization method will later be explained in more detail (see section 6.3.3).

Fig. 3.10a and Fig. 3.10b show sensitivity vs. target resolution for a FOV of 220 mm, which corresponds to the size of e.g., the human brain. The figures show that the cone-beam collimator achieves the highest sensitivity, which is consistent with Park et al. [182]. We also observe that the cone-beam collimator can achieve the highest target resolution (3 mm for R_i=3.5 mm and 0.5 mm for R_i=0.5 mm) and that the parallel-hole, fan- and cone-beam systems do not benefit as much from the high-resolution detector

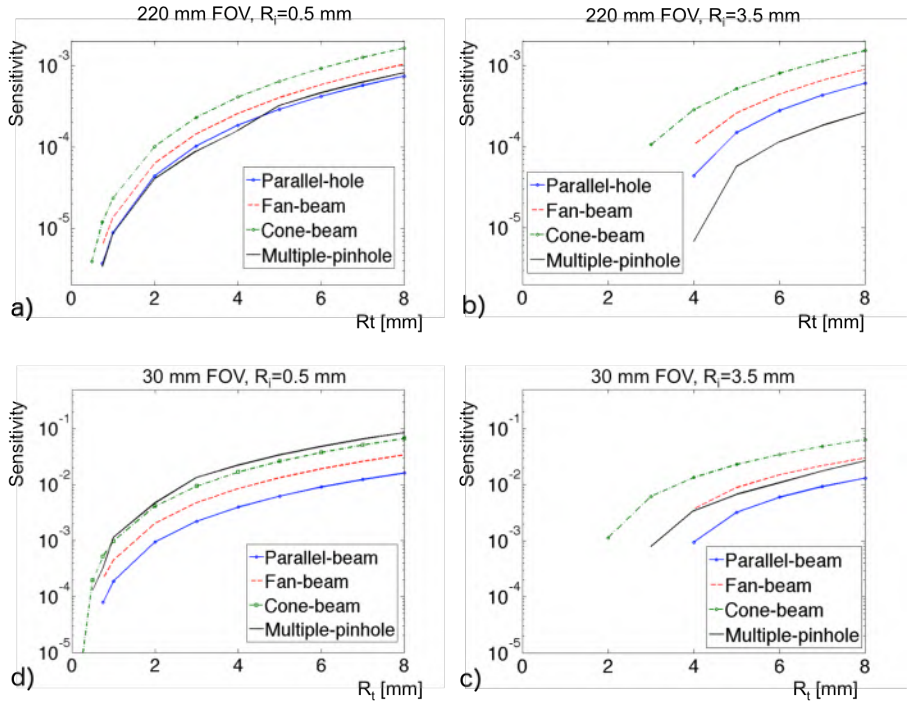

Figure 3.10: Sensitivity vs. target resolution for (a) a FOV of 220 mm with an intrinsic detector resolution of 0.5 mm (b) a FOV of 220 mm with an intrinsic detector resolution of 3.5 mm (c) a FOV of 30 mm with an intrinsic detector resolution of 0.5 mm (d) a FOV of 30 mm with an intrinsic detector resolution of 3.5 mm

technologies. The multi-pinhole system, on the other hand, can minify its projections, allowing a higher number of pinholes and thus a higher sensitivity, as shown by Rogulski et al. [196].

It is important to note that each graph in Fig. 3.10 compares different collimators for a certain detector resolution while keeping the detector surface area constant so the conclusion might be different for larger or smaller detectors.

This is also the case for Fig. 3.10c and Fig. 3.10d which show sensitivity vs. target resolution for a FOV of 30 mm, which corresponds to the size of e.g., a rat brain. Again, we observe that the multi-pinhole collimator benefits most from the high-resolution detector. For R_i=0.5 mm, the multi-pinhole collimator can achieve the highest sensitivity, except when targeting sub-millimeter resolutions, where it is outperformed by the cone-beam colli-

mator. For the low-resolution detector, the cone-beam is the best choice for all target resolutions. This finding might seem to be at odds with the many commercial small-animal systems, which are all pinhole-based, e.g., the U-SPECT II [246]. However, these systems utilize large clinical triple-head detectors, which need to be placed at a larger distance and for such a setup it is not possible to achieve sub-millimeter resolution with parallel-hole, fan- or cone-beam collimators. Moreover, most preclinical multi-pinhole systems aim to be stationary, which can also not be achieved with parallel-hole, fan- or cone-beam collimators.

3.4.2 Task-dependent optimization

Ultimately, the goal is to obtain the best possible task performance, regardless of the sensitivity or the resolution of the system. The imaging tasks most relevant to clinical and preclinical SPECT can be broadly classified into two types: (i) lesion-detection tasks and (ii) parameter-estimation tasks. Within each of these categories, there are several different sub-categories – for example, detection of lesions in known or unknown locations, or embedded within different types of noisy, structured backgrounds, or estimation of lesion activity concentration, lesion size, and/or local background activity concentration.

While lesion-detection or discrimination perceptual experiments can be performed for collimator optimization – using either receiver-operator characteristic (ROC), or localization ROC, or alternative forced-choice methodologies [228, 227] – such studies can be very time-consuming, especially when images from many different collimator-design conditions must be read by multiple observers to determine which design provides the best human-perceptual performance in the diagnostic task being evaluated. For this reason, considerable effort has gone into developing numerical observers of various types.

In 1985, Wagner and Brown reviewed the performance of ideal observers, which attempt to use all of the available image information to calculate a "physical" signal-to-noise ratio (SNR) for any hypothesized lesion [262]. Most observer models compute a decision variable for each of many noisy images; the value of this decision variable is closely related to the likelihood that a lesion is present within a given noisy image. The distribution of decision-variable values when a lesion is known to be present or known to be absent can, in turn, be used to compute a signal-to-noise ratio (SNR) for detection (or detection and localization, or some other relevant diagnostic task). Therefore, it is possible to optimize collimation by maximizing the

relevant task SNR, computed using such an ideal observer.

However, the ideal observer operates on the projection data and sets the upper bar for classification performance which may be useful for providing a standard against which the performance of other observers may be compared, but in clinical practice, most tasks are performed using reconstructed images. Therefore, other numerical observers have been developed that operate on the reconstructed images.

Observers that have been used for lesion detection include the non-prewhitening observer [261, 212, 178] and the Hotelling-trace and channelized Hotelling observers (CHO), which have also been shown to correlate well with human observer performance under a variety of different experimental conditions. For example, Fiete et al. [62] showed a good correlation between the Hotelling-trace and the human observer for detecting liver tumors, which was later adjusted by Barrett et al. [18] who showed that this is only true if the postdetection filtering has a low-pass character and who shows that the channelized hotelling observer matches better with the human observer. Rolland and Barrett [197], Eckstein et al. [56], Abbey and Barrett [3] and Abbey and Barrett [4] respectively investigated the effect of a non-uniform background, JPEG image compression, linear iterative reconstruction and noise regularization on different observer models.

For useful reviews of various numerical observers used for assessment of image quality, the reader is referred to Barrett et al. [18], Sharp et al. [212], and Barrett and Myers [17].

Metrics related to performance in quantitative parameter estimation from images have also been used for collimator optimization. Moore et al. [161] evaluated the performance of different medium-energy collimator designs for ^{67}Ga activity estimation by computing a SNR based on the Cramer-Rao lower bound (CRB) on the variance with which tumor activity concentration could be estimated when simultaneously estimating the local background activity concentration. They also showed in this work that the collimator resolution and septal penetration fraction that proved optimal for the activity-estimation task were also close to those that were optimal for lesion detection using the channelized Hotelling observer.

Image reconstruction, itself, can also be considered to be an estimation task, in which the goal is to estimate simultaneously all voxel values in the image. Therefore, we can also use the CRB to determine the uncertainty in voxel values to optimize SPECT imaging systems [66]. The calculation of this CRB requires the inversion of the Fisher information matrix, which is challenging, certainly for large image volumes and approximations need to be

used. The local shift invariant (LSI) approximation is most commonly used but Fuin et al. [66] showed that the conditions for the LSI approximation are easily broken and described an alternative using a sub-sampled Fisher information matrix (SFIM). The interested reader is referred to [185], where an overview of different approximation methods and guidelines for a careful choice are given.

Most conventional collimator design studies have optimized the collimation based on the projection data. However, in clinical practice, most imaging tasks are performed using reconstructed images and it has recently been shown [281, 136] that joint optimization of collimation and SPECT reconstruction parameters yields improved performance compared to independent sequential optimization of collimation and reconstruction. In both lesion-detection tasks [281] and activity-estimation tasks [136], the jointly optimized system resolution full-width-at-half-maximum (FWHM) was somewhat larger than the average lesion size, consistent with earlier findings of Zeng and Gullberg [278] and the resolution was further improved by modeling the collimator and detector response function (see section 2.1.4.3) within the iterative reconstruction algorithm. Other examples of reconstruction parameters that can be optimized include a noise regularization term that controls the noise-resolution tradeoff in the reconstructed image or a priori source information.

The distinction between sequential and joint optimization of apertures and reconstruction parameters is not such an important issue for preclinical imaging with multiple pinhole apertures because such systems are almost never used for planar imaging. Because reconstructed image volumes are always produced, this means that preclinical detection and estimation tasks required by physicians and scientists are generally performed on reconstructed images.

Meng and Clinthorne [111] utilized a modified uniform CRB calculation for optimizing multi-pinhole collimation. In 2005, Cao et al. [32] then used simulated data for optimizing the number of pinholes to use on a single rotating gamma camera for mouse brain imaging. These authors simulated different numbers of pinholes projecting onto a gamma camera (40cm x 40cm), and multiplexing was allowed. Using a variety of qualitative and quantitative metrics, e.g., the accuracy and precision of the striatum-to-cerebral background ratio, they determined, for this particular camera and scan geometry, that 9 pinholes provided optimal performance. Vunckx et al. [260] described an interesting approach, also based on the Fisher information matrix, for optimization of single and multiple pinhole collimators

for small-animal SPECT; this method required maximizing a contrast-to-noise ratio computed from the linearized local impulse response and its covariance. Finally, Lee et al. [114] numerically optimized a multi-pinhole collimator for mouse cardiac imaging. These authors considered different numbers of pinholes and different degrees of multiplexed data, for a relatively low-magnification geometry, and they used the CHO to estimate the area under the ROC curve for signal-known-exactly (SKE) / background-known-statistically (BKS) detection of myocardial defects. For a small camera (49mm x 49mm) these authors determined that the optimal number of pinholes was 4, with the camera rotated by 22.5 degrees about the center of the camera. The optimal magnification factor was 1.52, with 20% multiplexing.

3.4.3 Adaptive SPECT

In the previous sections, we have shown that the optimal collimator depends on the detector properties and the size of the FOV [156] but also on the detection task [43], the activity distribution [116] and the target resolution. These parameters can greatly vary between different patients and scans and therefore adaptive SPECT systems have been proposed. These systems make it possible, for example, to acquire an initial scout image and then focus on suspicious regions to improve performance [16]. This was first tested with a prototype single pinhole system with an adaptable object-to-pinhole distance, pinhole-to-detector distance and pinhole aperture sizes[65]. Later, the same group developed an adaptive multi-pinhole system for small animal imaging [248, 38] with three regions (low, medium and high magnification) and adaptable pinhole apertures. The same principle has also been applied to the multi-slit slit-slat collimator of the C-SPECT cardiac platform using interchangeable slits [200]. The location and size of the heart is first estimated during a scout scan to increase the image quality of the actual image acquisition. Another interesting application is described by Li et al. [116] and Fuin et al. [66] who used adaptive angular sampling, i.e. they optimized the time spent at each angle depending on the activity distribution.

3.5 Concluding discussion

In this chapter, we gave an overview of recent advances in collimator technology, both for human and small-animal molecular imaging systems. New production techniques have become available (e.g., direct 3-D printing of

metals and 'cold casting' of tungsten-composite materials) opening up new possibilities for fabrication of complex new collimator designs that would be impossible or extremely expensive to construct by more conventional means. Many new detectors have also become available with greatly improved intrinsic spatial resolution; these call for the use of diverging and minifying collimators and change the requirements for optimal collimation.

We also provided guidelines for optimizing a SPECT collimator for a specific imaging task and discussed the necessary sampling conditions needed for reconstructing data from stationary systems. These guidelines will form the basis for the rest of this dissertation and more specifically for optimizing the collimators of two different brain SPECT systems, described in chapter 4 and 6.

3.6 Original contributions

The work presented in this chapter resulted in a review paper that was recently accepted for the peer-reviewed A1 journal *Medical Physics* [244].

Chapter 4

Design and simulation of a full-ring multi-lofthole collimator for brain SPECT

In the previous chapter we explained the challenges of collimator design. We showed how difficult it is to improve resolution without reducing sensitivity and FOV and gave the reader some guidelines for designing dedicated systems in order to overcome the resolution-sensitivity trade-off.

In this chapter, we apply these guidelines to design a stationary brain SPECT system. We investigate whether we can overcome the resolution-sensitivity trade-off by using a much larger detector than those commonly used in clinical SPECT systems. More specifically, we use the LaPET detector ring [45], which has an intrinsic resolution of 4 mm (comparable to a clinical SPECT system) and is one of the largest cylindrical detector rings that has been built. We design a full-ring multi-lofthole collimator for this detector ring. The collimator is equipped with a shutter mechanism to open/close loftholes, which allows one to obtain sufficient angular sampling without rotating the system and to control the degree of multiplexing.

In this chapter, we focus purely on optimizing the collimator without any multiplexing and developed an optimization method to maximize sensitivity for a target resolution of 6 mm, given the fixed diameter of the cylindrical detector ring. In the next chapter we will then investigate whether we can further improve the system by allowing different degrees of multiplexing. The target resolution of 6 mm was determined based on a prior study investigating the trade-off between sensitivity and resolution [236].

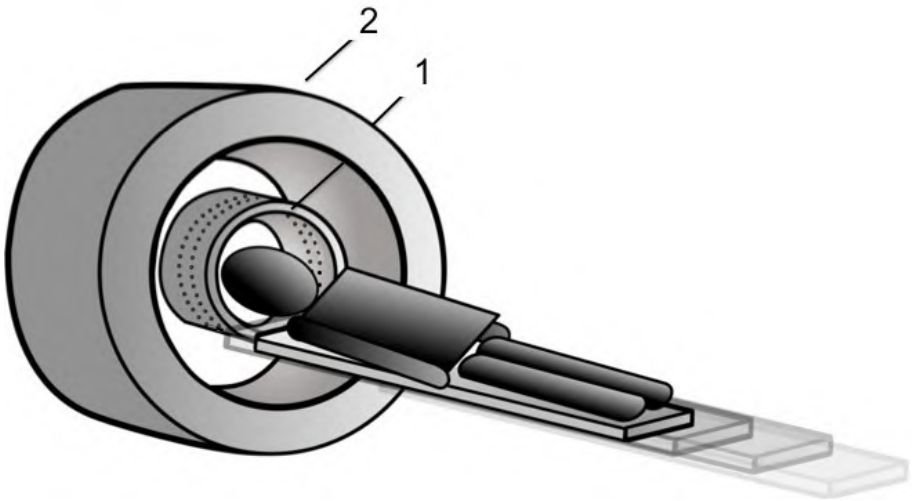

Figure 4.1: Multi-pinhole brain SPECT collimator (1) for the LaPET system (2), a full-ring of gamma detector modules.

4.1 Introduction

Currently, clinical brain SPECT is mostly performed using rotating dual-head gamma cameras equipped with low-energy-high-resolution parallel-beam collimators (LEHR PAR). Despite their low sensitivity (0.022 %) and poor spatial resolution (8-10 mm), these systems were shown to be clinically useful in a wide range of neurological diseases like dementia, cerebrovascular diseases and epilepsy [9]. However, a better sensitivity or resolution could result in better diagnosis and more effective treatment.

To improve sensitivity or resolution in brain SPECT imaging, dedicated collimators and systems have been simulated and developed in the past [81, 86, 97, 128, 283]. Cone-beam collimators are a good choice because of their high sensitivity [93, 100, 115, 182, 221, 226], while multi-pinhole collimators are the best choice for high-resolution systems [75, 108, 196, 199]. Due to the magnification effect, pinholes can overcome the poor intrinsic resolution of the standard SPECT detectors that are used today (3-4 mm). Pinholes also have better penetration characteristics which makes them more suited for radionuclides with higher energy photopeaks (e.g. ^{111}In).

Our goal is to build a brain SPECT system with a target spatial resolution of 6 mm. Therefore, we design and simulate a stationary multi-lofthole

collimator insert for the LaPET, an existing Positron Emission Tomography (PET) detector ring made of 24 $LaBr_3$ (5% Ce) detectors (Fig. 4.1) [45]. Loftholes are similar to pinholes but with better penetration and penumbra characteristics [50] (Fig. 4.2). We choose to develop a stationary system because it is typically more robust and experiences less calibration issues. A stationary collimator insert is also easier to integrate with MRI for simultaneous SPECT-MRI. This could be interesting for longitudinal or interictal studies and could be another step towards improved brain imaging.

Firstly, we will describe the detector and the general design of the collimator. Secondly, we will describe the optimization process used to maximize the system performance. Finally, we will reconstruct simulated phantom data to assess sampling completeness, reconstructed spatial resolution and image quality. We will also compare the system performance to a clinical dual-head SPECT camera equipped with LEHR PAR collimators.

4.2 The system

4.2.1 Detector

The collimator is optimized for the LaPET detector ring [45]. This is a PET detector ring made of 24 $LaBr_3$ (5% Ce) detectors of 27 by 60 pixels, each 4 mm x 4 mm x 30 mm large. The crystal pitch is 4.3 mm. The radius of the detector ring is 466.65 mm and its axial field-of-view (FOV) is 258 mm.

$LaBr_3$ (5% Ce) detectors have a very good energy resolution (6% at 140 keV) and a high density (5.3 g/cm^3) [165] and as the LaPET system has the possibility to read out singles, the detector assembly can be used as a SPECT system.

4.2.2 Collimator

The collimator consists of a tungsten ring with loftholes (Fig. 4.3(a)), a shutter mechanism (section 4.2.4) and lead shielding to remove background radiation. Loftholes have a circular aperture (similar to pinholes) and a rectangular exit window that results in a rectangular projection on the detector for optimal detector coverage (Fig. 4.2). Loftholes also have better penetration and penumbra characteristics than pinholes [50].

The loftholes are equally distributed along two axially spaced rings (Fig. 4.3) and they are truncated to limit knife-edge penetration, similar to the truncated pinholes in [120]. The loftholes in the first ring sample one half

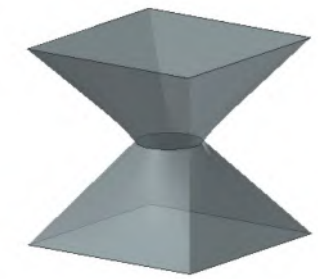

Figure 4.2: Lofthole with a circular aperture that gradually turns into a rectangular exit window

of the transverse FOV (Fig. 4.3(a)) and the loftholes in the second ring sample the other half of the transverse FOV (Fig. 4.3(c)). They all project on the complete axial length of the detector (Fig. 4.3(b)(d)) and as a consequence, loftholes of the first ring should not be opened simultaneously with loftholes of the second ring (unless overlap is desired).

4.2.3 Collimator parameterization

The collimator can be described by a number of parameters (Fig. 4.3(a)(c)): the collimator thickness t, the radius of the collimator ring c, the number of loftholes and finally the position, opening angle α, aperture diameter d, tilt in the axial plane γ and tilt in the transverse plane β. To simplify the collimator design, all the loftholes have the same aperture diameter, opening angle and tilt. The loftholes of the first and second ring have an axial offset (A_o) of respectively 12 mm and -12 mm and they are axially tilted towards the center of the detector. The two rings of loftholes are thus separated by 24 mm, which is enough to guarantee the manufacturability and mechanical strength of the collimator. The collimator thickness is 5 mm.

4.2.4 Shutter mechanism

In a stationary multi-lofthole collimator, the number of loftholes must be large enough to assure sufficient angular sampling (see section 3.1.4.1). Depending on the collimator radius, however, this will result in overlapping projections, which causes artifacts in the reconstructed image. To control

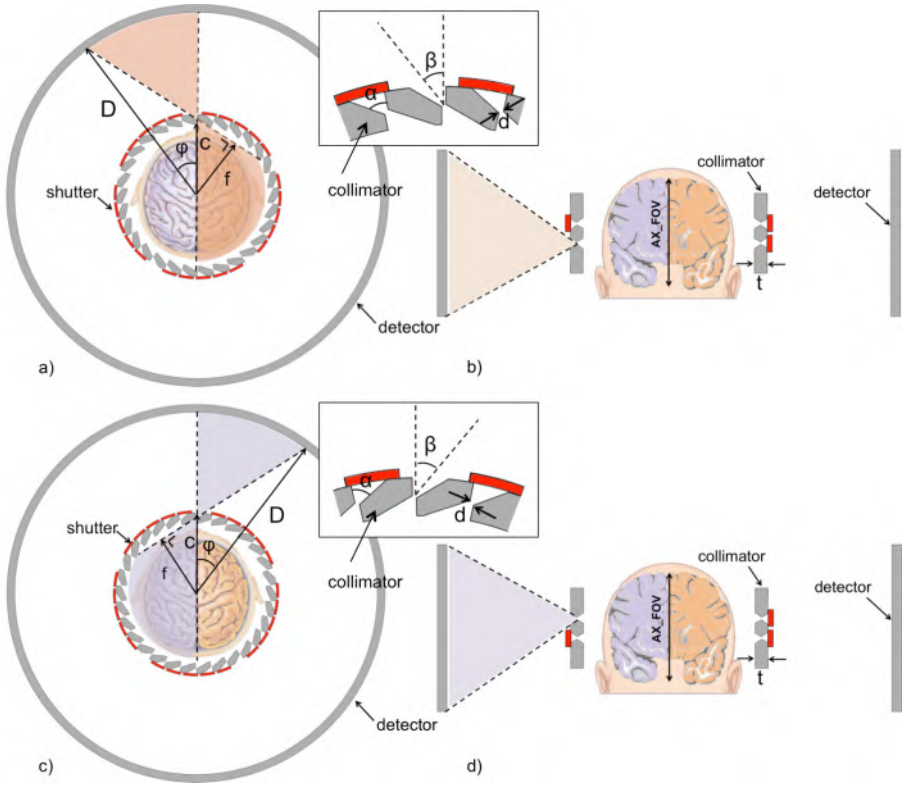

Figure 4.3: (a) Transverse cut through the first ring of loftholes with a close-up of the collimator. (b) Axial cut showing the two rows of loftholes on the collimator ring corresponding with the previous transverse view. Loftholes from the first ring are never opened at the same time as the loftholes from the second ring. (c) Transverse cut through the second ring of loftholes with a close-up of the collimator. (d) Axial cut showing the two rows of loftholes on the collimator ring corresponding with the previous transverse view. D is the detector radius, c is the radius of the collimator ring, f is the radius of the FOV, ϕ is the angular span of one lofthole's projection, α is the opening angle of the loftholes, d is the aperture of the loftholes and β is the transverse tilt. t is the collimator thickness.

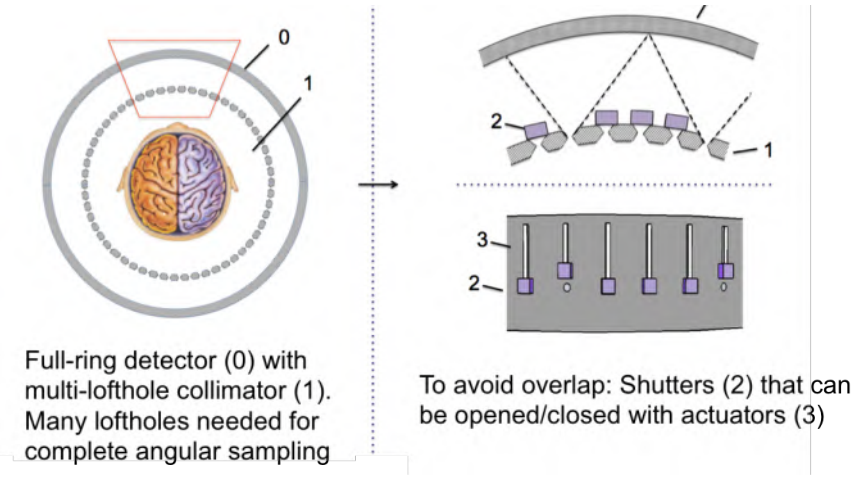

Figure 4.4: The shutter mechanism implemented with actuators.

the amount of overlap, the collimator is equipped with a shutter mechanism that blocks radiation from certain loftholes. In this way, a limited amount of loftholes can be selected to obtain a first set of projections. After a certain acquisition time, these loftholes are closed and the neighboring loftholes are opened. This process can be repeated multiple times. A sequence of shutter movements is thus performed to obtain an acquisition setup that is equivalent to a rotational movement.

For the practical implementation, we investigated different options (Fig. 4.5) and compared them based on cost and flexibility [25]. The first option (Fig. 4.5a) is a shutter mechanism where every lofthole has a separate shutter block (small tungsten block) attached to an actuator so that it can be shifted in front of a lofthole to block its radiation. This solution offers a high degree of flexibility as every actuator can be controlled individually. It is also the most expensive solution, as it requires a controller with 128 channels and 128 actuators that are fast, sufficiently small to fit next to each other and sufficiently strong to move the tungsten block. Such a system would easily cost $12,000. The second option (Fig. 4.5b) is based on a tungsten ring with different rows, where every row has a number of holes, corresponding to the loftholes that need to be opened. The shutter ring slides over the collimator ring and by translating it, it opens/closes loftholes following a sequence similar to a rotational movement. This solution offers less flexibility (as it does not allow us to adapt the number of loftholes that is opened simultaneously) but it is more cost-effective. It does not require

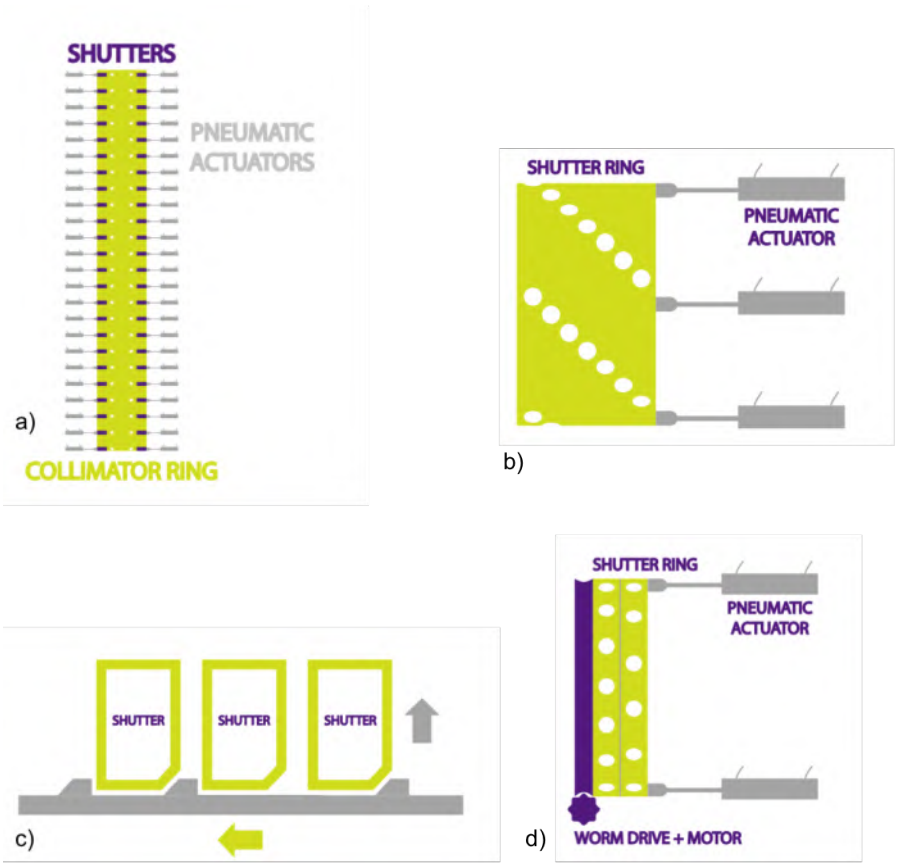

Figure 4.5: The shutter mechanism implemented with (a) actuators, (b) a translating ring (c) a take-along ring (d) a translating ring with worm drive [25].

any rotation and a system with such a shutter mechanism is expected to be more easy to calibrate than a rotating system. The third option (Fig. 4.5c) is based on a Nylon 'take-along' ring with a tungsten shutter block per lofthole. By rotating the Nylon ring, it takes along the shutter blocks and pushes them forward. To push the shutter blocks back, we can use a second take-along ring at the opposite side, but this is difficult to implement if the collimator has multiple rows of loftholes which are close to each other (as in the case of our design). Finally, the last option (Fig. 4.5d) is based on both translation and rotation of a set of tungsten rings with holes. An actuator is used to select the ring with the right number of holes (which corresponds to the number of loftholes that is simultaneously opened) and a

worm drive is used to rotate the shutter ring. This gives sufficient flexibility, and it is expected to give less calibration issues that a traditional rotation, because the shutter ring is only used for opening/closing loftholes and not for positioning the loftholes. It is also expected to be less expensive than the first option.

4.2.5 Acquisition setup

The following protocol is then used for the acquisition: First, a limited set of loftholes is opened to obtain a non-overlapping set of projections. After a certain acquisition time, these loftholes are closed and another set of non-overlapping loftholes is opened. This process can be repeated multiple times until all loftholes have been opened at least once, which allows us to acquire sufficient angular sampling without any overlap. This sequence of shutter movements is then repeated for the second ring of loftholes. For axial sampling completeness, 16 bed positions are used (with a step size of 8 mm).

4.3 Collimator optimization

4.3.1 Analytical model

To determine the optimal collimator radius, we will use an analytical optimization procedure that maximizes the volume sensitivity given a target spatial resolution of 6 mm in the center of the field-of-view (R_{CFOV}=6 mm). The complete FOV is assumed to be a cylinder with a diameter of 220 mm and an axial length of 124 mm which is representative for an adult human brain [75]. The volume sensitivity is the ratio between the number of detected counts and the total number of emitted photons during the complete acquisition. It is the mean sensitivity in the brain, averaged over all bed positions. We define the volume sensitivity at one bed position as follows:

$$g_i = \frac{N_p}{JL} \sum_{l=1}^{L} \sum_{j=1}^{J} g_{i,j,l} \tag{4.1}$$

with $g_{i,j,l}$ the point sensitivity at voxel j for lofthole l and at bed position i, with J the number of voxels in the cylinder representing the FOV, with L

the total number of loftholes and with N_p the number of loftholes that can be opened simultaneously.

The final volume sensitivity g is an average over 16 bed positions:

$$g = \frac{1}{16}\sum_{i=1}^{16} g_i \tag{4.2}$$

To limit simulation time, a few approximations are made:

- The sensitivity and resolution of the loftholes are approximated using the formulae for pinhole sensitivity [179] and resolution [12].
- The axial tilt γ of the loftholes is ignored (it is maximally 3.7°, which is small enough to have little influence on the optimal collimator radius).
- The detector is approximated as a perfect ring, while in reality it is composed of 24 flat detectors.
- Each lofthole samples exactly one half of the complete transverse FOV, while in reality they will have to sample somewhat more to avoid truncation artifacts.

The point sensitivity $g_{i,j}$ is described by the following equations [179]:

$$g_{i,j} = \frac{d_{Seff}^2 \sin^3\theta}{16b^2} \tag{4.3}$$

$$d_{Seff} = \sqrt{d(d + \frac{2}{\mu}tan\frac{\alpha}{2}) + \frac{2}{\mu^2}tan^2\frac{\alpha}{2}} \tag{4.4}$$

with θ the angle of incidence measured from the plane of the pinhole aperture, α the opening angle of the pinhole, b the perpendicular distance from the point in the FOV to the plane defined by the pinhole aperture and d_{Seff} the physical diameter d corrected for penetration at the edges of the aperture. The attenuation coefficient μ for tungsten at 140.5 keV is 3.3976 mm^{-1}.

The volume sensitivity thus depends on a number of parameters. We will show that given a fixed spatial resolution R_{CFOV}, all these parameters can be expressed as a function of the collimator radius c. By plotting the

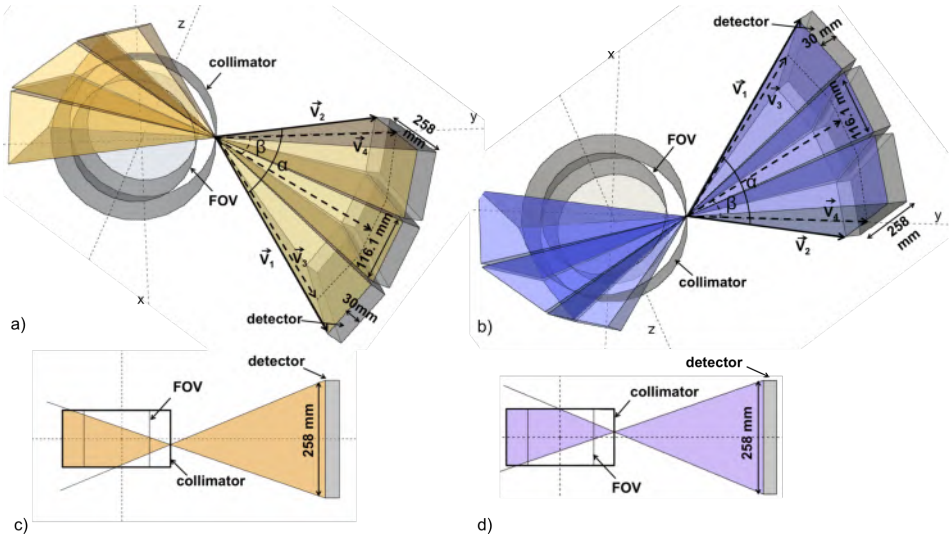

Figure 4.6: (a) Part of the FOV sampled by the first lofthole of the first ring. (b) Part of the FOV sampled by the first lofthole of the second ring. The gaps are due to the gaps between the flat detectors in the ring configuration. The opening angle α of the loftholes is a solid angle defined by $\vec{v_1}$ and $\vec{v_2}$. The tilt β in the transverse plane is defined by $\vec{v_3}$ and $\vec{v_4}$. (c) Axial view of the first lofthole of the first ring. (d) Axial view of the first lofthole of the second ring.

volume sensitivity as a function of the collimator radius, the maximum can be found.

Firstly, we derive the maximum number of loftholes that can be opened simultaneously without causing overlap on the detector. The larger the collimator radius c, the smaller the projections and the larger the number of loftholes that can be opened simultaneously:

$$N_p = \frac{2\pi}{\phi} = \frac{2\pi}{\cos^{-1}(\frac{f}{D}) - \cos^{-1}(\frac{f}{c})} \tag{4.5}$$

with ϕ the angular span of one lofthole's projection, f the radius of the FOV (120 mm) and D the detector radius (466.65 mm) (Fig. 4.3). N_p can thus be expressed as a function of c.

Secondly, we describe the opening angle α of the lofthole and its tilt β in the transverse plane (Fig. 4.6). The opening angle of the lofthole is the angle between two opposite vectors from the center of the pinhole aperture

to the detector corners:

$$\alpha = \cos^{-1}\left(\frac{\vec{v_1} \cdot \vec{v_2}}{||\vec{v_1}||.||\vec{v_2}||}\right) \tag{4.6}$$

$$\vec{v_1} = \left(D\sin\phi, D\cos\phi - c, \frac{H}{2} - A_o\right) \tag{4.7}$$

$$\vec{v_2} = \left(0, D - c, -\frac{H}{2} + A_o\right) \tag{4.8}$$

with H the axial length of the detector (258 mm) and A_o the axial offset of the lofthole (12 mm or -12 mm). The tilt of the lofthole is zero in the axial direction and in the transverse direction it is β:

$$\beta = \frac{1}{2}\cos^{-1}\left(\frac{\vec{v_3} \cdot \vec{v_4}}{||\vec{v_3}||.||\vec{v_4}||}\right) \tag{4.9}$$

$$\vec{v_3} = \left(D\sin\phi, D\cos\phi - c, 0\right) \tag{4.10}$$

$$\vec{v_4} = \left(0, D - c, 0\right) \tag{4.11}$$

Now that we have described the opening angle and the tilt as a function of c, the perpendicular distance b and the incidence angle θ can be calculated for each point in the FOV.

Next, we will show that the pinhole diameter d can be expressed as a function of c given a fixed target resolution in the CFOV R_{CFOV} [12]:

$$R_{CFOV} = \sqrt{\frac{R_i^2}{m^2} + \left(d_{Reff}\left(1 + \frac{1}{m}\right)\right)^2} \tag{4.12}$$

R_i is the intrinsic resolution of the detector, which is assumed to be 4 mm (the physical pixel size), d_{Reff} is the resolution effective diameter (corrected for penetration), R_{CFOV} is the target resolution (6 mm) and m is the magnification of the system and is described by:

$$m = \frac{D - c}{c} \tag{4.13}$$

The resolution effective diameter d_{Reff} is described by two equations [7]:

$$d_{re//} = d + \frac{ln2}{\mu}(tan^2\frac{\alpha}{2} - cot^2\theta)cot\frac{\alpha}{2}sin\theta \tag{4.14}$$

$$d_{re\perp} = \sqrt{(d + \frac{ln2}{\mu}tan\frac{\alpha}{2}sin\theta)^2 - (\frac{ln2}{\mu})^2cos^2\theta} \tag{4.15}$$

$d_{re//}$ and $d_{re\perp}$ are the resolution effective aperture in the parallel and the perpendicular direction. The parallel direction is the intersection between the detector plane and the plane defined by the normal to the detector plane and the vector from the center of the aperture to the CFOV. The perpendicular direction is perpendicular to the parallel direction in the detector plane. For the setup we consider, the resolution in the perpendicular direction is always worse than in the parallel direction. Therefore, we will use the resolution in the perpendicular direction (the worst-case scenario). Also, in the center of the FOV, the incidence angle θ is equal to the lofthole tilt ($\theta = \beta$). Equation (5.10), (5.11) and (4.15) are then combined and rearranged to explicitly show d:

$$d = \sqrt{\frac{(D-c)^2.R_{CFOV}^2 - c^2R_i^2}{D^2} + (\frac{ln2}{\mu})^2cos^2\beta} - \frac{ln2}{\mu}tan\frac{\alpha}{2}sin\beta \tag{4.16}$$

In the previous equations, we have shown that all the parameters of the volume sensitivity (eq. 7.2) can be expressed as a function of the collimator radius. We can now plot the volume sensitivity as a function of c. The result of the optimization process is discussed in the next section.

4.3.2 Optimization result

Fig. 4.7 shows the result of the optimization process: the volume sensitivity is plotted as a function of the collimator radius. The maximum volume sensitivity is achieved for a collimator radius of 138.7 mm. At this distance, the

pinhole diameter needed to achieve the target resolution of 6 mm is 3.98 mm, the opening angle of the pinholes is 71.06 °, the tilt in the transverse plane is 29.95 ° and the maximum number of pinholes that can be opened simultaneously without causing overlap is 8. The volume sensitivity with these collimator parameters is $1.60\text{x}10^{-4}$ cps/Bq. This configuration appears to be the optimal combination of sensitivity per pinhole and number of pinholes that can be opened simultaneously. A smaller collimator radius results in a higher sensitivity per pinhole, but a lower number of pinholes that can be opened simultaneously (due to a higher magnification and thus larger projections).

4.3.3 Final simulated system

The final collimator design differs slightly from the one obtained from the optimization process. First, the apertures are loftholes instead of pinholes. Second, the loftholes all have a small axial tilt (they are directed towards the centre of the detector). Finally, the collimator needed to be adapted to sample slightly more than exactly one half of the complete transverse FOV in order to have some margin and avoid truncation in case of manufacturing errors. Therefore, the radius was slightly increased to 145 mm. 8 loftholes

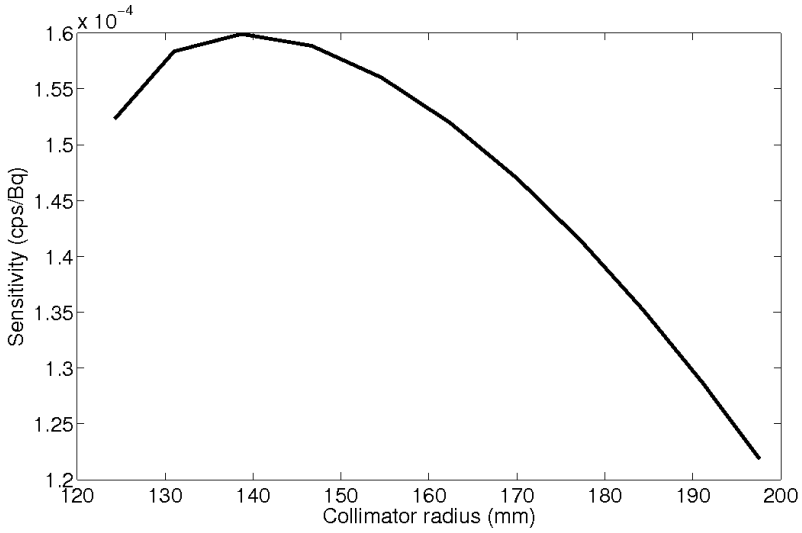

Figure 4.7: Volume sensitivity as a function of the collimator radius

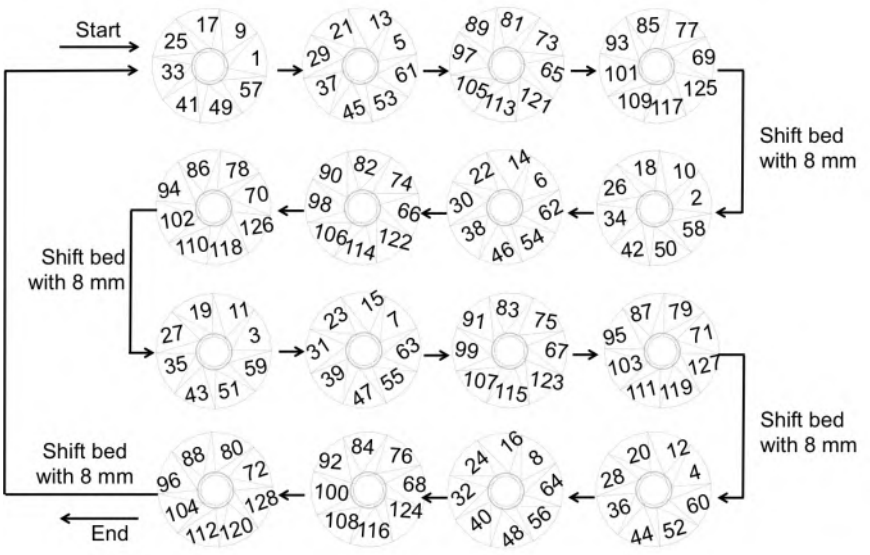

Figure 4.8: Final acquisition protocol. The numbers represent the loftholes that are opened. At each bed position, 4 different setups are acquired. In each setup 8 loftholes are opened simultaneously.

can then be opened simultaneously. All loftholes have the same opening angle (72.6 °) and aperture (4.0 mm). The collimator has a total of 128 loftholes (64 in each axial ring). The loftholes in the first and second ring have an axial offset of respectively 12 mm and -12 mm, a tilt of 1.6 ° and $-1.6\,^\circ$ in the axial plane and a tilt of $26.1\,^\circ + \tau$ and $-26.1\,^\circ + \tau$ in the transverse plane, with τ the angle at which the lofthole is positioned on the ring.

The part of the FOV sampled by one lofthole is shown in Fig. 4.6. The gaps are due to the gaps between the flat detectors in the ring configuration.

The calculated spatial resolution at the center of the FOV is 6 mm and the volume sensitivity of this system is $1.55\text{x}10^{-4}$ cps/Bq.

4.3.4 Final acquisition protocol

We will now describe the final acquisition protocol used to simulate the phantom data (Fig. 4.8). The collimator has a total of 128 loftholes. The loftholes in the first and second ring are numbered 1-64 and 65-128

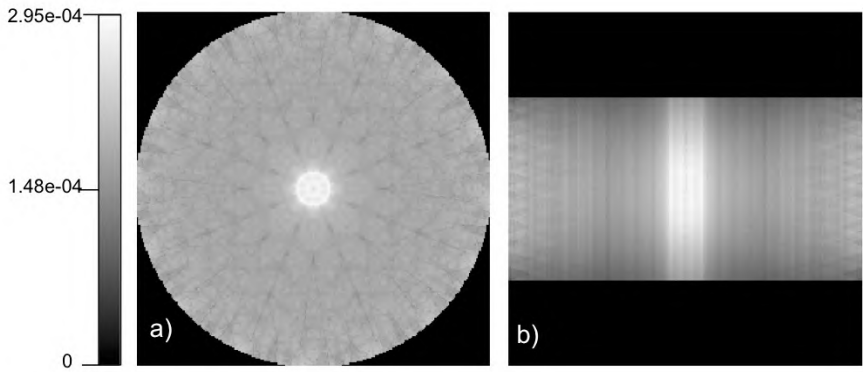

Figure 4.9: Sensitivity map (a) central transverse slice (b) central axial slice

respectively. Loftholes 1, 2 , 3, ... are positioned at respectively 0°, 5.625°, 11.25°, 16.875°, ... on the collimator.

For axial sampling completeness, 16 bed positions are used (with a step size of 8 mm). The protocol starts with the bed positioned at -64 mm. Secondly, loftholes 1, 9, 17, 25, 33, 41, 49 and 57 are opened simultaneously during 28.125 seconds (Fig. 4.8). Thirdly, those loftholes are closed and loftholes 5, 13, 21, 29, 37, 45, 53 and 61 are opened during 28.125 seconds. After 4 of those setups, the bed is axially shifted with 8 mm. At the second bed position 4 other sets of loftholes are opened sequentially and the bed is shifted again. The protocol ends when 16 bed positions are acquired.

The sensitivity map for this acquisition protocol is shown in Fig. 4.9. The sensitivity map is quite uniform except for an inner ring which is due to the fact that each lofthole samples slightly more than half the transverse FOV. The central region is sampled twice as much as the other regions of the FOV.

4.4 Phantom studies

Using the results from section 4.3.2 we finalized the collimator design. We then used this design to simulate and reconstruct phantom data to assess sampling completeness and image quality. The acquisition protocol that was simulated is described in 4.3.4

4.4.1 Data generation

For the multi-lofthole system, data were simulated using a GPU-based pixel-driven forward projector [98]. The basics of ray-tracing were explained in section 2.1.3.1.1. In this study, we use a multi-ray approach (pinhole subsampling with 456 weighted rays [254]) in combination with an effective pinhole diameter (Eq. 4.15) to model resolution and pinhole penetration. Sensitivity was modeled analytically, using equation (7.2). Attenuation in the object space was also modeled analytically. We used an attenuation coefficient of 0.015 mm^{-1} for both PMMA (non-active regions) and water (active regions) at 140.5 keV. The outer dimensions of all phantoms are equal: a cylinder with a diameter of 220 mm and a length of 124 mm. Phantoms were represented using a grid with 240x240x240 voxels of 1x1x1 mm^3 and the detector pixel size was 2.15x2.15 mm^2. A Gaussian blurring operation was applied on the projection data (FWHM=4 mm) to model the intrinsic resolution of the detector (R_i=4 mm). Poisson noise was added to the projection data.

Projection data were also simulated for a dual-head SPECT system with LEHR PAR collimators (hole size of 1.40 mm, hole length of 27.0 mm and radius of rotation of 145 mm) and a detector with an intrinsic resolution of 4 mm. This system has a calculated system resolution of 9.8 mm and sensitivity of 3.875x10−4 cps/Bq. Projection data were simulated using a cubic spline rotator [201] and a pixel-driven forward projection. Sensitivity and attenuation were modeled analytically and resolution was modeled using a blurring operation in image space with a distance dependent FWHM. The detector-heads were rotated over 120 angles, equally distributed over 360°.

4.4.2 Image reconstruction

Ordered subset expectation maximization (OSEM) [88] (see section 2.1.4.2) was used to reconstruct all data and all images were reconstructed to 128x128x128 voxels with a voxel size of 1.875x1.875x1.875 mm^3. To further speed up the reconstructions, we used unmatched projector/back projector pairs [277] and only modeled attenuation, sensitivity and resolution in the forward projector.

For the multi-lofthole system, OSEM was implemented using a pixel-driven forward projector with 7 rays and a voxel-driven back projector with one ray.

For the LEHR PAR system, the OSEM implementation was based on a cubic spline rotator [201], a pixel-driven forward projector and a voxel-driven

back projector. Resolution was modeled using a blurring operation in image space with a distance dependent FWHM.

4.4.3 Phantoms

4.4.3.1 Uniform phantom

A noiseless uniform phantom (a cylinder with a radius of 110 mm and an axial length of 120 mm) was simulated and reconstructed and visually inspected on the presence of artifacts.

4.4.3.2 Defrise phantom

A noiseless Defrise phantom (a cylinder with a radius of 110 mm, an axial length of 128 mm and discs of 8 mm thickness and spacing) was used to assess the axial sampling of the multi-lofthole system.

4.4.3.3 Hot-rod phantom

To compare the reconstructed spatial resolution of the multi-lofthole system and a standard dual-head SPECT system with LEHR PAR collimators, we simulated and reconstructed a noiseless hot-rod phantom: a cylinder with a radius of 110 mm, an axial length of 128 mm and hot rods with a diameter ranging from 4 mm to 10 mm. The distance between the center of two neighboring rods is twice their diameter.

4.4.3.4 Hoffman phantom

A Hoffman phantom was simulated at a realistic noise level for both the multi-lofthole system and a standard dual-head SPECT system with LEHR PAR collimators. We assumed 4.34M counts for the multi-lofthole system and 8.82M counts for the parallel-hole system. This corresponds to the number of counts that would be detected when the phantom would be uniformly filled with 1 mCi of Tc-99m and scanned during 30 minutes (a clinically realistic situation), taking both the system's sensitivity and the phantom's attenuation into account. The phantom has one hot lesion of 6 mm (Fig. 4.15(a)) with an uptake ratio of 2:1 and one cold lesion of 8 mm with zero uptake (Fig. 4.15(e)). The uptake ratio between grey and white matter in the phantom is 5:1 to simulate the 5:1 ratio in the physical phantom [107].

4.4.3.5 Lesion detectability phantom

Lesion detectability was assessed for both the multi-lofthole system and a standard dual-head SPECT system with LEHR PAR collimators at a realistic noise level (respectively 4.34M and 8.82M counts) using two phantoms (Fig. 4.10): the first phantom has 10 mm hot lesions with an uptake ratio of 7:1 (Fig. 4.10(a),(b)) and the second phantom has 16 mm cold lesions (Fig. 4.10(c),(d)). Both phantoms are cylinders with a radius of 110 mm and an axial length of 128 mm. The lesions are positioned along two rings with a radius of respectively 40 mm and 80 mm. These two rings are repeated at 3 different axial positions and we simulated 3 noise realizations of both phantoms, resulting in 207 cold and 207 hot lesion realizations. For each noise realization we also simulated a uniform phantom (signal absent class).

To evaluate and compare the lesion detectability quantitatively, we calculated the non-prewhitening matched filter signal-to-noise ratio (NPW-SNR) of the lesions. The NPW-SNR is a linear observer valid for a signal-known exactly and background-known exactly task (SKE/BKE) that has been shown to agree well with human observer performance [171][172]. The observer response λ_i is defined for both the signal present ($i = 1$) and signal absent ($i = 0$) class:

$$\lambda_i = T/N \sum_{j \in ROI} f_{ij} \tag{4.17}$$

with f_{ij} voxel j in the reconstructed image f_i, N the number of voxels in the ROI and T the true difference between the lesion and background activity concentration.

NPW-SNR is then defined as:

$$\text{NPW-SNR} = \frac{\overline{\lambda_1} - \overline{\lambda_0}}{\sqrt{\frac{1}{2}(\sigma_1^2 + \sigma_0^2)}} \tag{4.18}$$

with $\overline{\lambda_i}$ the observer response averaged over all lesions and all realizations. σ_i is the standard deviation of the observer response.

We first calculated the NPW-SNR for the lesions in the inner and outer rings separately and then for all lesions together.

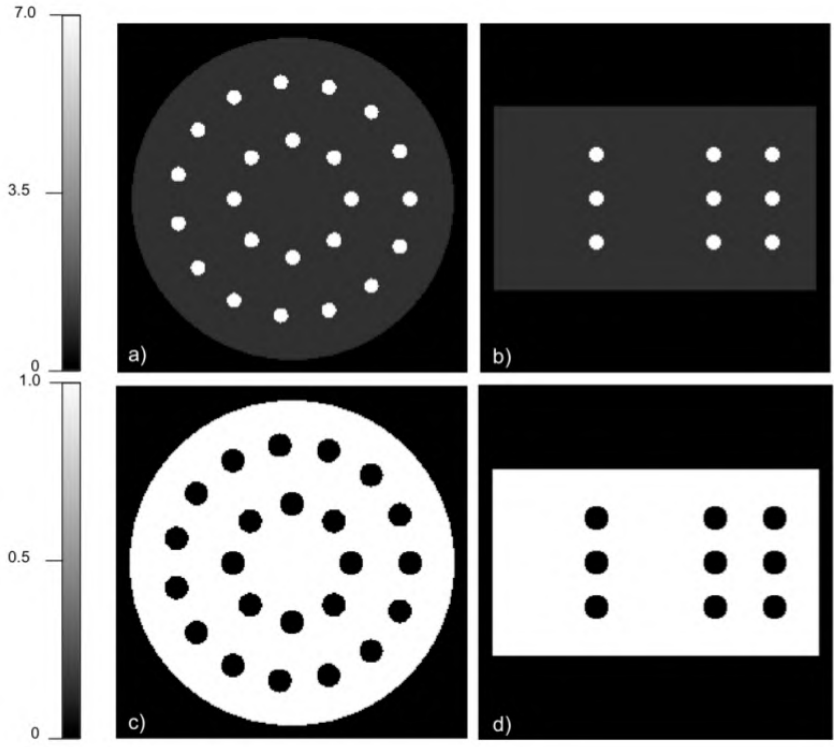

Figure 4.10: Two lesion detectability phantoms (a) Transverse slice with hot lesions of 10 mm diameter (b) Axial slice with hot lesions of 10 mm diameter (c) Transverse slice with cold lesions of 16 mm diameter (d) Axial slice with cold lesions of 16 mm diameter

4.4.3.6 Contrast phantom

Finally, we evaluated contrast-to-noise in a contrast phantom (Fig. 4.11) at low noise (respectively 43.4M and 88.2M counts). The contrast phantom is a cylinder with a radius of 110 mm and an axial length of 128 mm. It has 4 hot lesions with a diameter of 6, 8, 10 and 12 mm (uptake ratio of 7:1) and two cold lesions with zero uptake and a diameter of 14 and 16 mm (Fig. 4.11(a)). All lesions are positioned along a ring with a radius of 54.5 mm. 18 noise realizations showed to be sufficient for the results to stabilize.

The contrast recovery coefficient (CRC) is defined as follows:

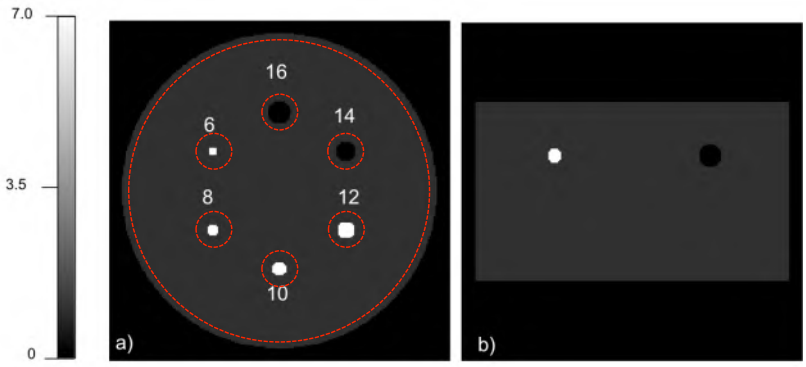

Figure 4.11: Contrast phantom (a) Transverse slice with hot and cold lesions of different sizes All hot lesions have an uptake ratio of 7:1 (b) Axial view - The red dotted lines indicate the background region (where the COV was determined).

$$\text{CRC} = (\frac{\mu_l - \mu_b}{\mu_b})/(C-1) \times 100\% \tag{4.19}$$

with μ_l is the mean lesion count, μ_b the mean background count and C the true lesion-background ratio.

The CRC values are plotted against the coefficient of variation (COV):

$$COV = \frac{1}{N_n} \sum_{j=1}^{N_n} \frac{\sigma_{b,j}}{\mu_{b,j}} \times 100\% \tag{4.20}$$

with $\sigma_{b,j}$ the pixel-to-pixel percent standard deviation (%SD) in the background region of the j^{th} noise realization.

We used the contrast-noise curves to quantify the image quality in the contrast phantom. The contrast values were evaluated by placing spherical ROIs over each lesion and an annular ROI on the hot background.

4.4.4 Simulation results

4.4.4.0.1 Uniform and Defrise phantom Fig. 4.12 (a), (b) and Fig. 4.13 (a), (b) respectively show simulated images of the uniform and the

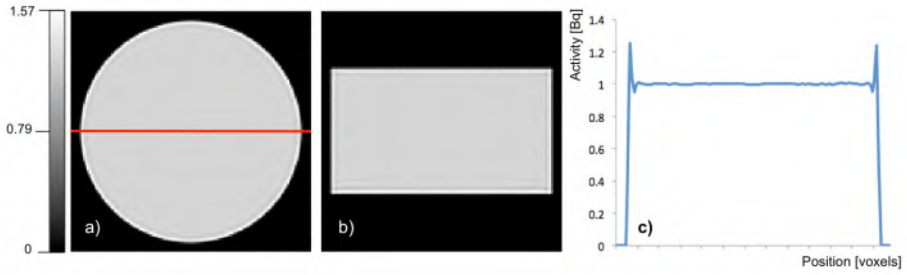

Figure 4.12: Uniform phantom (a) Transverse view (b) Axial view (c) Line profile

Defrise phantom after 100 iterations (4 subsets). The images are noiseless. Line profiles are drawn in the central transverse slice of the uniform phantom (Fig. 4.12 (c)) and in the axial direction of the Defrise phantom (Fig. 4.13 (c)). The absence of artifacts demonstrates transverse and axial sampling completeness.

4.4.4.0.2 Hot-rod phantom Fig. 4.14 shows simulated noiseless images of the hot-rod phantom at convergence for both the multi-lofthole system and the LEHR PAR system. The iteration number at which convergence occurs, is determined based on the contrast-to-noise curves of the contrast study (respectively 100 and 300 iterations (4 subsets) for the multi-lofthole and the LEHR PAR system). We say that the contrast-recovery-coefficient has convergenced when the difference between two successive iterations is smaller than 0.1 %. With the multi-lofthole system, the 4 mm rods can still be distinguished. The smallest rods that can be seen with the LEHR PAR system are 5 mm in diameter. This improved resolution was expected since

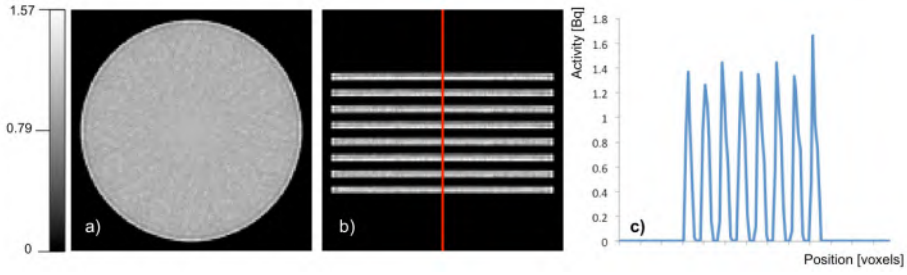

Figure 4.13: Defrise phantom (a) Transverse view (b) Axial view (c) Line profile

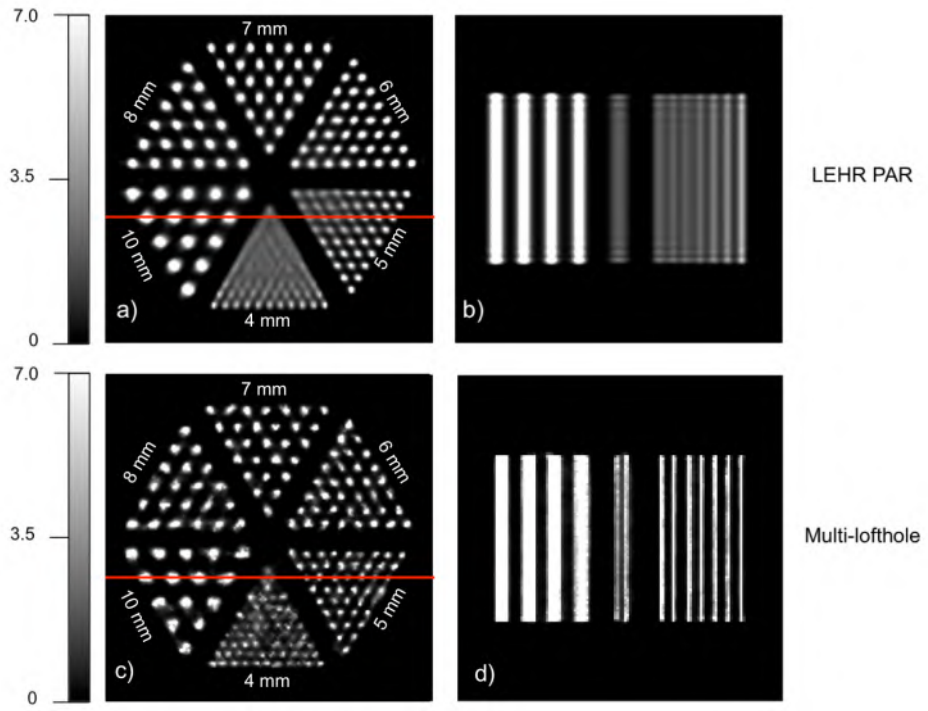

Figure 4.14: Hot-rod phantom (a) Transverse view of the hot rods with LEHR PAR (300 iterations, 4 subsets) (b) Axial view of the hot rods with LEHR PAR (c) Transverse view of the hot rods with the multi-lofthole system (100 iterations, 4 subsets) (d) Axial view of the hot rods with the multi-lofthole system

the multi-lofthole system was designed to have a better spatial resolution.

4.4.4.0.3 Hoffman phantom Fig. 4.15 shows simulated images of the Hoffman phantom for both the LEHR PAR system and the multi-lofthole system, at equal noise (16.3%) after post-smoothing. We calculated the coefficient of variation in uniform parts of the phantom (the thalamus and the cerebellum) and used a Gaussian filter with a FWHM of 7.5 mm and a kernel size of 25 voxels. The images show no artifacts but in none of the images the lesions are clearly visible. With the parallel-hole system, a small increase can be seen in the line profile, close to where the hot lesion is located, but it is not very convincing.

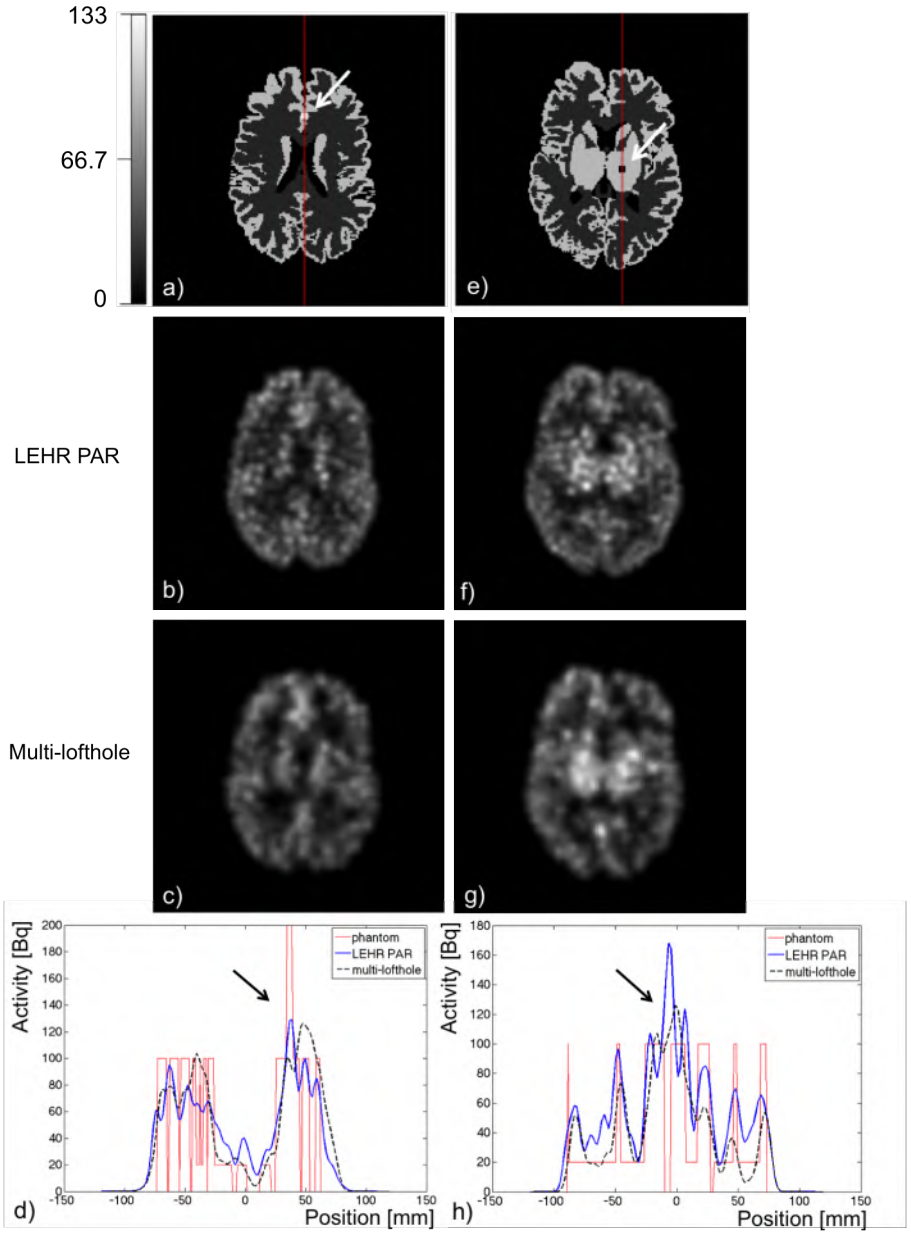

Figure 4.15: Hoffman phantom (a) Transverse slice with a hot lesion of 6 mm (b) LEHR PAR image of slice with hot lesion (300 iterations, 4 subsets) (c) multi-lofhole image of slice with hot lesion (33 iterations, 4 subsets) (d) line profile of hot lesion for LEHR PAR (solid line) and multi-lofthole (dashed line) (e) Transverse slice with a cold lesion of 6 mm (f) LEHR PAR image of slice with cold lesion (300 iterations, 4 subsets) (g) multi-lofhole image of slice with cold lesion (33 iterations, 4 subsets) (h) line profile of cold lesion for LEHR PAR (solid line) and multi-lofthole (dashed line)

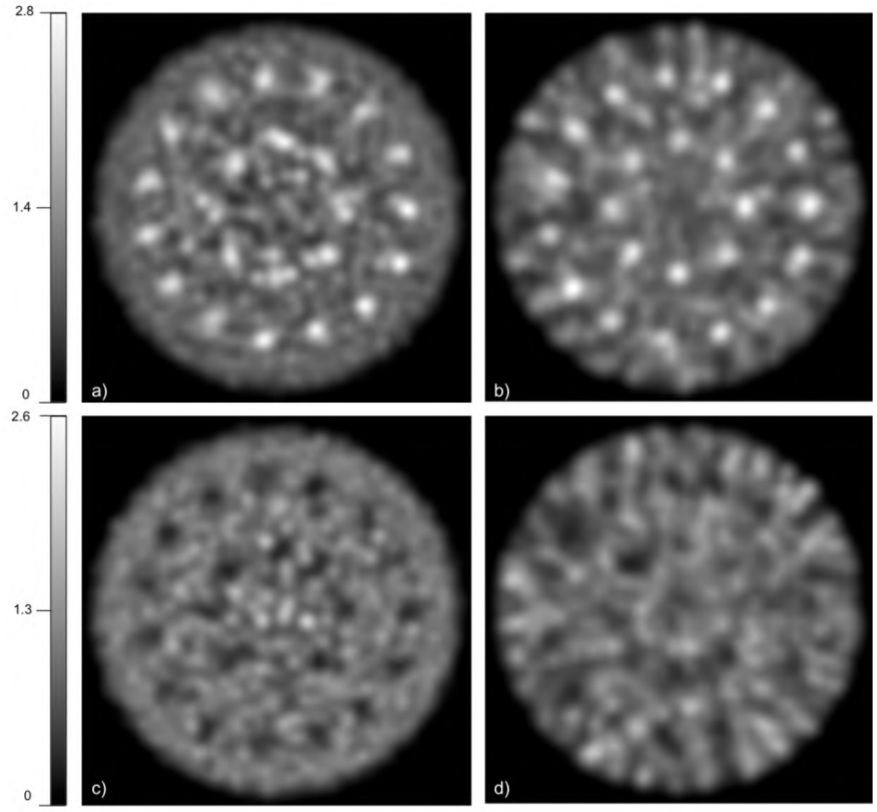

Figure 4.16: Lesion detectability phantom (a) LEHR PAR image with hot lesions (296 iterations, 4 subsets) (b) multi-lofthole image with hot lesions (31 iterations, 4 subsets) (c) LEHR PAR image with cold lesions (296 iterations, 4 subsets) (d) multi-lofthole image with cold lesions (32 iterations, 4 subsets)

4.4.4.0.4 Lesion detectability phantom We determined the NPW-SNR on the lesion detectability phantoms at convergence (Table 4.1). The multi-lofthole system shows better detectability for the inner ring of lesions and the LEHR PAR system for the outer ring. In average (when both inner and outer lesions are considered), the multi-lofthole system performs slightly better for the hot lesions and slightly worse for the cold lesions. No post-smoothing was applied to calculate the NPW-SNR. Fig. 4.16 shows the reconstructed phantoms at equal noise after post-smoothing (21.2% for the hot lesion phantom and 20.4% for the cold lesion phantom). A Gaussian filter with a FWHM of 9.375 mm and a kernel size of 25 voxels was used.

	LEHR PAR	multi-lofthole
hot lesions - inner ring	2.5	3.7
hot lesions - outer ring	4.0	3.7
hot lesions - all	3.5	3.7
cold lesions - inner ring	1.8	2.2
cold lesions - outer ring	3.2	1.7
cold lesions - all	2.7	1.9

Table 4.1: NPW-SNR at convergence

4.4.4.0.5 Contrast phantom Finally, we reconstructed the contrast phantom and plotted the contrast-to-noise curves of the lesions at different iteration numbers for both the multi-lofthole and the parallel-hole collimator (Fig. 4.18). Fig. 4.17 shows two images at equal noise after post-smoothing (16.2%). A Gaussian filter with a FWHM of 7.5 mm and a kernel size of 25 voxels was applied. We simulated multiple realizations and defined the mean CRC and error bars based on these different realizations (plus and minus the standard error). 18 realizations showed to be sufficient for the error bars to stabilize. No post-smoothing was applied to calculate the CRC. The contrast-to-noise curves show that the multi-lofthole collimator performs better on the hot lesions and worse on the cold lesions.

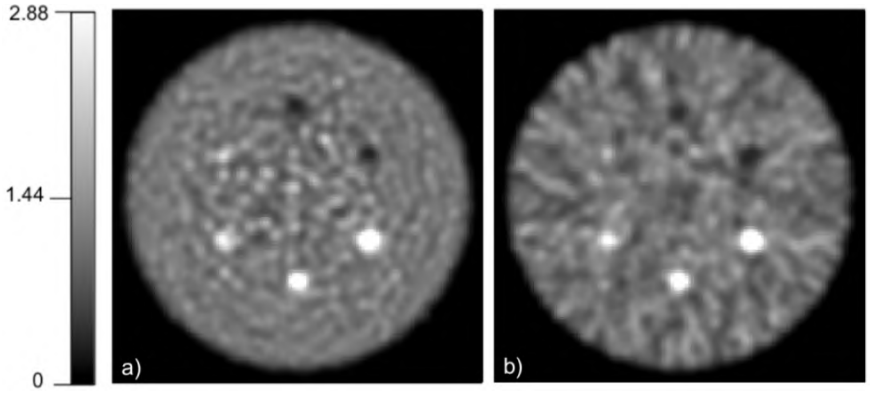

Figure 4.17: Contrast phantom (a) LEHR PAR image (170 iterations, 4 subsets) (b) multi-lofthole image (96 iterations, 4 subsets)

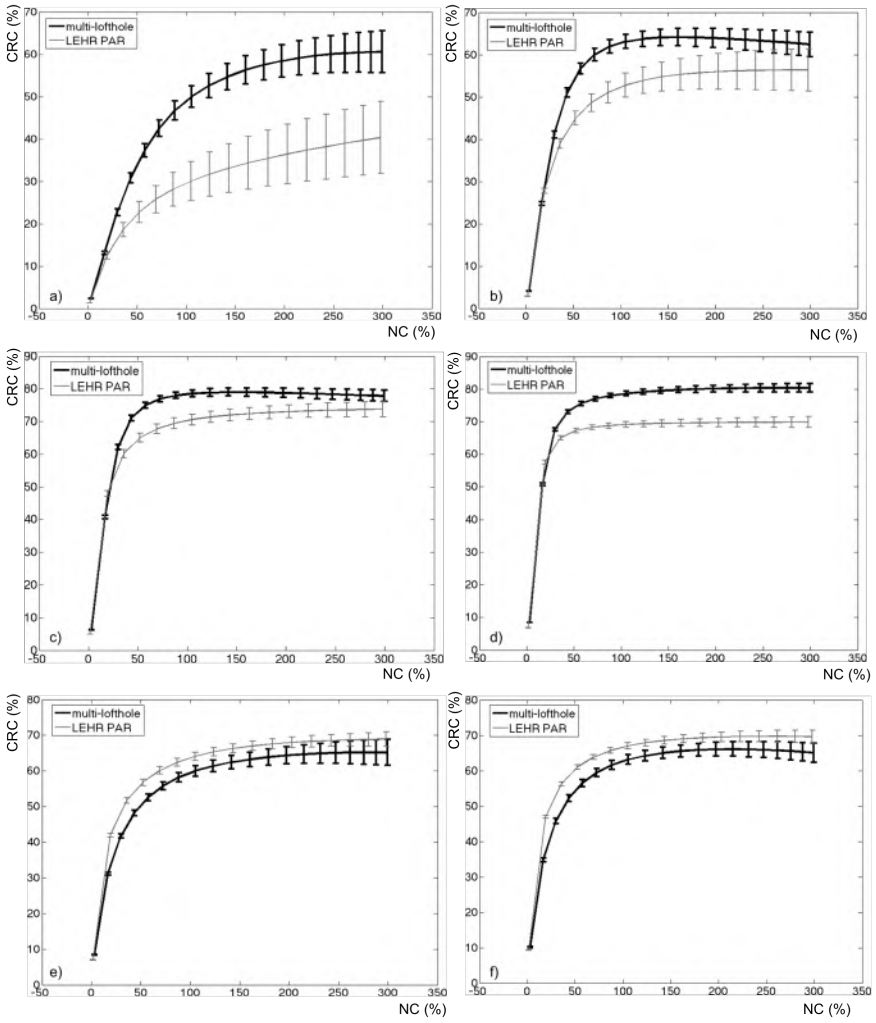

Figure 4.18: Contrast-to-noise plots with error bars (plus and minus the standard error) for both the multi-lofthole (black) and the parallel-hole collimator (grey): (a) 6 mm hot lesion (b) 8 mm hot lesion (c) 10 mm hot lesion (d) 12 mm hot lesion (e) 14 mm cold lesion (f) 16 mm cold lesion

4.5 Discussion

The volume sensitivity of the final multi-lofthole system design is 1.55x10^{-4} cps/Bq which is approximately 2.5 times lower than the sensitivity of a dual-head system with LEHR PAR collimators (3.79x10^{-4} cps/Bq). The theoretical spatial resolution at the CFOV, on the other hand is better (6.3 mm with the multi-lofthole collimator compared to 9.8 mm with LEHR PAR collimators). This improvement in spatial resolution can also be seen in the simulated image of the hot-rod phantom. According to Muehllehner [170], when the spatial resolution is improved by 2 mm, for example, then the count rates can be reduced by a factor of approximately four to achieve the same quality image in the same time period. Our lesion detectability and contrast study, however, do not confirm this statement. We believe that the difference in reconstruction algorithms explains these seemingly contradictory results. Muehllehner used filtered backprojection to reconstruct the projection data while we used OSEM with resolution recovery. It was already shown in the past that resolution recovery improves the trade-off between spatial resolution and noise (e.g. [254]). This also explains why in the hot-rod phantom, the difference in reconstructed spatial resolution is not as big as expected.

From the lesion detectability study it follows that the multi-lofthole system has an advantage over the LEHR PAR system for the inner ring of lesions but not for the outer ring. This is presumably caused by the small distortions that are seen with the multi-lofthole system. At the edge of the phantom, the image quality is degraded (Fig 4.16). However, when the same image is simulated without noise, these artifacts disappear. This indicates that the artifacts are caused by noise patterns, which is confirmed by the sensitivity map (Fig 4.9), which shows similar patterns. The multi-lofthole system has a higher sensitivity in certain areas of the FOV than in others and this causes inhomogeneity of the noise structure. This is not the case in the LEHR PAR system, which has a homogeneous sensitivity map. This difference also explains why the noise of the LEHR PAR images seems less correlated. On average (when both inner and outer lesions are considered), the multi-lofthole system performs slightly better for the hot lesions and slightly worse for the cold lesions. It is typical for systems with a lower sensitivity to perform worse on cold lesions.

From the contrast study we can conclude that the improvement in resolution gives a higher contrast for the small hot lesions but not for the larger cold lesions. Certainly in combination with resolution recovery, the improvement in spatial resolution of the multi-lofthole system is not giving

much advantage for the larger lesions. Also, cold lesions are typically more sensitive to noise. The lower sensitivity of the multi-lofthole system is thus an important drawback.

For completeness, we also included a Hoffman phantom simulated with a clinically realistic dose and scan time. Despite a spatial resolution of 6 mm, the multi-lofthole system does not succeed in visualizing the small lesions. This demonstrates again that sensitivity is too low to benefit from the good spatial resolution. An axially longer detector in combination with more loftholes (arranged in additional rings) would be a solution for this problem. We could also increase the lofthole apertures to increase sensitivity but this comes at the cost of resolution of course. For example, for a target resolution of 9.8 mm in the CFOV (which is the same as the LEHR PAR spatial resolution), we could obtain a volume sensitivity of $4.38\text{x}10^{-4}$ cps/Bq, which is 13% higher than the sensitivity of the LEHR PAR system.

The main advantage of our multi-lofthole collimator insert is its flexibility. The shutter mechanism allows one to adapt the degree of multiplexing to the object imaged or even change it during the acquisition. Multiplexing increases the sensitivity but the overlapping projections introduce ambiguities that can lead to artifacts. These ambiguities can be resolved by combining projection data with different degrees of multiplexing. This principle has been successfully applied in synthetic collimation systems [271][214][84] and other SPECT systems [258][129][127]. In the next chapter (Chapter 5) we will investigate the potential of the shutter mechanism to combine projection data with different degrees of multiplexing and increase the sensitivity.

The shutter mechanism does not only give flexibility, it also eliminates the need for rotating parts. This will improve the robustness of the SPECT system by itself and facilitate the integration with MRI. Ultimately, the stationary collimator could be inserted in an existing PET-MRI system and allow integrated SPECT-MRI brain imaging. Currently, there exist two commercially available clinical PET-MRI systems: the Siemens Biograph mMR [47] and the Philips Ingenuity TF [272]. The Philips Ingenuity TF PET-MRI is a hybrid imaging system with Philips time-of-flight GEMINI TF PET and Achieva 3T X-series MRI system and a turnable table in between. As the GEMINI TF PET has a similar geometry as the LaPET detector ring, our collimator insert could also be used in the Philips PET-MRI and turn it into a SPECT-MRI system.

4.6 Conclusion

We used the guidelines of chapter 3 to design a stationary brain SPECT insert for an existing PET ring (the LaPET [45]). The insert is a full-ring multi-lofthole collimator equipped with a shutter mechanism that ensures sufficient angular sampling without rotating the system. We developed an optimization method based on analytical simulations that maximizes the volume sensitivity of a full-ring multi-pinhole system given a specific target resolution in the center of the FOV and a fixed diameter for the detector ring. However, despite the large detector ring and the multi-lofthole design, we obtained a sensitivity of $1.55\text{x}10^{-4}$ cps/Bq, which is 2.5 times lower than the sensitivity of a dual-head system with low energy high resolution parallel-hole (LEHR PAR) collimators. This is the cost paid for improving the spatial resolution (6 mm with the LaPET insert versus 9.8 mm with the LEHR PAR system).

Simulations of a noiseless hot-rod phantom show that the spatial resolution has indeed improved: we successfully reconstructed 4 mm hot rods with the multi-lofthole system. This also resulted in improved CNR, as shown in noisy simulations of a contrast phantom, but only for the hot lesions. The CNR in the cold lesions decreased. Similar results are obtained in the lesion detectability study, where we see an overall increase in NPW-SNR for the phantom with the hot lesions and an overall decrease for the phantom with the cold lesions. Cold lesions typically suffer more from decreased sensitivity.

In the next chapter we will therefore investigate the potential of the shutter mechanism to combine projection data with different degrees of multiplexing and thus increase sensitivity.

4.7 Original contributions

The work presented in this chapter resulted in a patent application [234], an international conference proceeding [235], a national conference contribution [238], an international conference contribution [233] and a publication in the peer-reviewed A1 journal *Physics in medicine and biology* [239]. The practical implementation of the shutter mechanism was mostly done by Dries Bovijn during his master's thesis [25].

Chapter 5

Multiplexing multi-pinhole SPECT

In the previous chapter, we focused on increasing the system spatial resolution from 8-10 mm (typical values in clinical systems) to 6 mm. However, we found that even with a very large cylindrical detector, sensitivity is low, i.e. the mean sensitivity over the complete FOV is $1.5\text{x}10^{-4}$ cps/Bq, which is 2.5 times lower than a clinical dual-head SPECT system with low energy high resolution parallel-hole (LEHR PAR) collimators.

In this chapter, we therefore investigate the possibility of further increasing sensitivity by opening more loftholes simultaneously, even though this causes the projections to overlap on the detector (also called multiplexing). The shutter mechanism presented in the previous chapter (Fig 5.1) allows us to easily control the degree of multiplexing by opening more or less pinholes simultaneously. We can even change the amount of multiplexing during the acquisition and for example first acquire projection data with multiplexing and then use the remaining time to acquire projection data without multiplexing. This process is called time multiplexing and is investigated in the first part of this chapter (section 5.1).

The second part of this chapter (section 5.2) aims at a more fundamental understanding of multiplexing. We gave an overview of the existing literature on multiplexing in section 3.1.5 and from this, we know that multiplexing can cause artifacts in the reconstructed image due to the increased ambiguity of the projection data [260]. Yet, there are examples of multi-pinhole collimators that allow multiplexing and do not show any artifacts (e.g. [208][184]) or only in certain phantoms [46]. In section 5.2 we search for a deeper understanding of these observation. We develop a method

to predict whether a certain multiplexing design will result in artifacts or not and finally, we also investigate whether the increased sensitivity from multiplexing results in improved image quality.

5.1 Time multiplexing

5.1.1 Introduction

Time multiplexing is the process of acquiring both multiplexed and non-multiplexed projection data at different time intervals during the same acquisition and was first investigated by Mahmood et al. [129] who showed that the combination of multiplexed and non-multiplexed data can result in artifact-free images and improved image quality in slit-slat collimators. The idea of mixing multiplexed and non-multiplexed data was previously also applied by Vunckx et al. [258] who used two detector heads, one with a multiplexing collimator and one with a single pinhole collimator.

In this section we follow the first approach and investigate the potential of time-multiplexing for increasing the sensitivity and the image quality of our previously developed stationary full-ring multi-lofthole brain SPECT system (Chapter 4). We simulate and reconstruct a uniform phantom and a Hoffman phantom to assess the presence of artifacts and a contrast phantom to quantify the potential improvement in image quality. We compare different acquisition setups: without multiplexing, with only multiplexing and with time-multiplexing.

5.1.2 Simulations

5.1.2.1 Data generation

Projection data were simulated with the same GPU-based ray-tracer as described in the previous chapter, in section 4.4.1 but we briefly recapitulate the method here. The ray-tracer is a pixel-driven forward projector and uses a multi-ray approach to model resolution (pinhole subsampling with 456 weighted rays [254]). Pinhole penetration was modeled using an effective pinhole diameter [7]. We also modeled sensitivity and attenuation in the phantom. We simulated different phantoms which were represented using a grid with 240x240x240 voxels of 1x1x1 mm^3. The detector pixel size was 4.3x4.3 mm^2 and Poisson noise was added to the projection data.

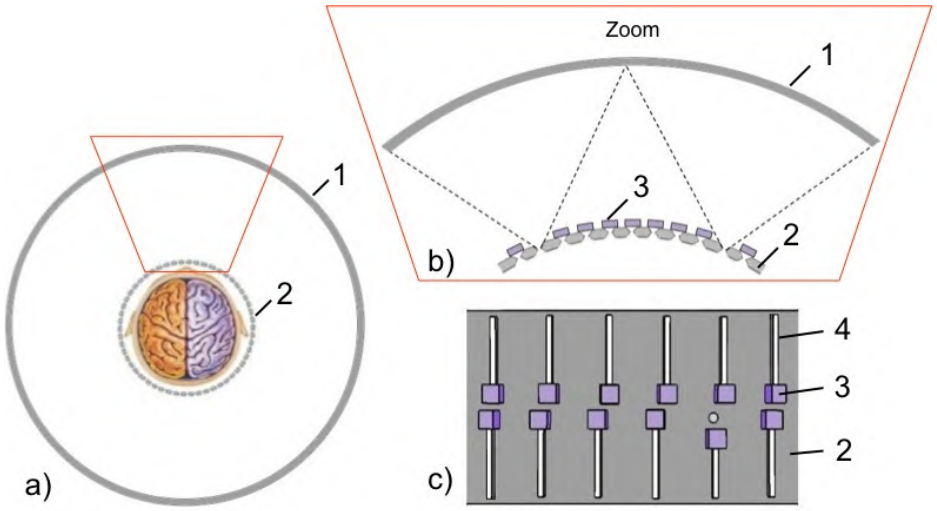

Figure 5.1: (a) A transverse view of the full system with (1) the detector ring and (2) the collimator ring (b) A zoom of the shutter mechanism in the transverse direction (c) A part of the collimator ring (top view) with (3) the shutters (4) and the pneumatic actuators

5.1.2.2 Acquisition setups

We simulated different setups (Table 5.1) and describe them using β, which is the relative scan-time used to acquire non-multiplexed data. The total scan time was 30 minutes for all the setups. In the first setup, 8 loftholes were opened simultaneously (Fig. 5.2(a)). The first setup includes no multiplexing (β=1). In the second setup, 16 loftholes were opened simultaneously (Fig. 5.2(b)). The second setup includes only multiplexed projections (β=0). In the third setup, we simulated an acquisition in which non-multiplexed data of the complete FOV were acquired during the first 6 minutes of the scan and multiplexed data were acquired during the remaining 24 minutes (β=0.2). This setup was chosen as it gave promising results after a pilot study with different values for β (0.8, 0.5 and 0.2). To generate the data, we simply weighted the projection data of the first (β=1) and second setup (β=0) before adding noise. When reconstructed separately, the acquisitions of the first setup would result in a noisy non-multiplexed image and the acquisitions of the second setup would result in a less noisy multiplexed image, possibly with artifacts. However, the acquisitions were not reconstructed separately but combined as explained in paragraph 5.1.3.1.

	8 loftholes	16 loftholes
no multiplexing	30'	-
only multiplexing	-	30'
time-multiplexing	6'	24'

Table 5.1: Acquisition setups

In order to decrease computation time, we simulated only 1 bed position and reduced the axial length of the phantoms to 30 mm.

5.1.3 Reconstruction

5.1.3.1 OSEM

The image formation process in a SPECT system is generally expressed as: $\mathbf{p} = \mathbf{Af}$ with $\mathbf{p}$ the projection data, $\mathbf{A}$ the system matrix and $\mathbf{f}$ the object that is being imaged. Similarly, we can express the image formation process of a multiplexing system as: $\mathbf{p'} = \mathbf{Bf}$ with $\mathbf{p'}$ the multiplexed projection data and $\mathbf{B}$ the system matrix of the multiplexed system. The time-multiplexed image formation process is a combination of both and can be be described as:

$$\mathbf{P} = \mathbf{Hf} \text{ with } \mathbf{P} = \begin{bmatrix} \mathbf{p} \\ \mathbf{p'} \end{bmatrix} \text{ and } \mathbf{H} = (\beta \begin{bmatrix} \mathbf{A} \\ \mathbf{0} \end{bmatrix} + (1-\beta) \begin{bmatrix} \mathbf{0} \\ \mathbf{B} \end{bmatrix}) \tag{5.1}$$

with β the relative scan-time used to acquire non-multiplexed data.

To solve the reconstruction problem, we used OSEM (which was explained in section 2.1.4.2) with system matrix $\mathbf{H}$ and the measured projection data $\mathbf{P}$ which is a combination of both the multiplexed and non-multiplexed data. The OSEM algorithm was implemented using a GPU-based ray-tracer which consists of a pixel-driven forward projector and a voxel-driven back projector. We used attenuation correction and modeled sensitivity and pinhole penetration in the forward projector. No scatter correction was used as scatter was not modeled in the simulator either. Resolution recovery was based on a multi-ray approach using 7 weighted rays [254]. All images were reconstructed to 120x120x120 voxels with 2x2x2 mm^3 voxel size.

5.1.3.2 OSEM+BS

Vunckx et al. [258] have shown that multiplexing artifacts can be reduced using a body support (BS), i.e. an image that is zero outside and non-zero inside the contours of the object. The body support is used as the starting image of the reconstruction algorithm and it reduces the solution space, which leads to better convergence. To define the body support, a quick reconstruction (only 2 iterations with 8 subsets) was performed using only the non-multiplexed data. The body support was defined using an empirically defined threshold on the resulting image and the reconstruction was then restarted using all the data (both multiplexed and non-multiplexed) and with the body support as starting image. In practice MRI or CT data could also deliver the body support information.

5.1.4 Phantoms

Uniform phantom

We simulated a uniform phantom as an extreme embodiment of a non-sparse object, in low noise circumstances to assess the presence of artifacts. The uniform phantom was cylindrical with a radius of 110 mm. We simulated projection data without multiplexing (β=1), with only multiplexing (β=0) and with time-multiplexing (β=0.2). These data sets were reconstructed using OSEM without body support. We also reconstructed the time-multiplexing data set with body support (β=0.2+BS). The reconstructed images were then compared at equal iteration number (first at 10 iterations, using 8 subsets and then also at 50 iterations, using 8 subsets). We assumed 30 million counts for the non-multiplexed projection data and thus 60 million counts for the multiplexed and 54 million counts for the time-multiplexed projection data.

Hoffman phantom

We also simulated a Hoffman brain phantom (Fig. 5.4(a)) with an uptake ratio of 5:1 between grey and white matter and reconstructed both non-multiplexed (β=1+BS) and time-multiplexed (β=0.2+BS) projection data sets. We simulated at two different noise levels: (i) in low noise circumstances (30 million counts in the non-multiplexed data set and thus 54 million counts in the time-multiplexed data set) to assess the presence of artifacts and (ii) at a realistic noise level (4.34M counts in the non-multiplexed

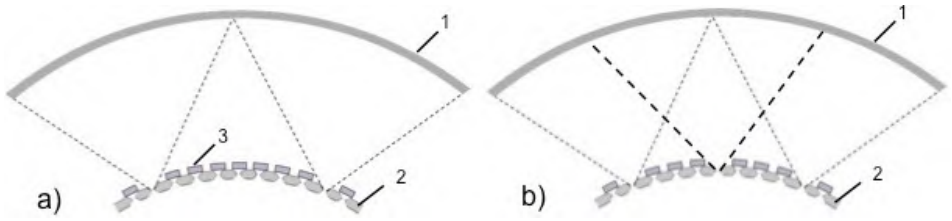

Figure 5.2: (a) no multiplexing, 8 loftholes are opened simultaneously (b) only multiplexing, 16 loftholes are opened simultaneously

data set and thus 7.81M counts in the time-multiplexed data set), similar to the simulation in chapter 4. We used a body support for all reconstructions and visually compared the reconstructed images at equal noise level, based on the coefficient of variation (COV), which was calculated in uniform parts of the phantom (the thalamus and the cerebellum). For the realistic noise simulation, we modified the phantom to include two lesions: one hot lesion of 6 mm (Fig. 5.5(a)) with an uptake ratio of 2:1 and one cold lesion of 8 mm with zero uptake (Fig. 5.5(e)).

Contrast phantom

We simulated a contrast phantom (Fig. 5.6(a)) in high noise circumstances to evaluate whether the increase in sensitivity due to multiplexing results in increased image quality. The contrast phantom had a radius of 90 mm and 5 hot sources with a diameter of 8 mm and an uptake ratio of 7:1. We simulated non-multiplexed (β=1+BS) and time-multiplexed (β=0.2+BS) projection data and reconstructed both data sets using a body support. We assumed 3 million counts in the non-multiplexed projection data and thus 5.4 million counts in the time-multiplexed projection data. After reconstruction, image quality was assessed using contrast-to-noise plots. The images were visually compared at equal noise level (COV=58%).

5.1.5 Contrast-to-noise plots

The contrast recovery coefficient of each hot sphere is defined as follows:

$$CRC = \frac{\frac{\mu_l - \mu_b}{\mu_b}}{C - 1} \times 100\% \tag{5.2}$$

with μ_l the mean activity in the hot sphere and μ_b the mean activity in the background, C the true sphere-background ratio (7 in this case). The CRC is then averaged over all hot spheres.

We measured the CRC value at each image reconstruction iteration and plotted it against the coefficient of variation (COV):

$$COV = \frac{\sigma_b}{\mu_b} \times 100\% \tag{5.3}$$

with $\sigma_{b,j}$ the pixel-to-pixel percent standard deviation (%SD) in the background region.

5.1.6 Results

Uniform phantom

The reconstructed images of the uniform phantom are compared at equal iteration number: first at 10 iterations using 8 subsets (Fig. 5.3(a),(b),(c),(d)) and then also at 50 iterations using 8 subsets (Fig. 5.3(e),(f),(g),(h)). All images were post-filtered with a Gaussian filter with a 4 mm FWHM and a kernel size of 25 voxels. Compared to the reconstruction of the non-multiplexed data (Fig. 5.3(a)), the reconstructed image with only multiplexed data shows severe artifacts (Fig. 5.3(b)). Even after 50 iterations (Fig. 5.3(f)), the artifacts still remain. The artifacts were slightly reduced by mixing non-multiplexed and multiplexed data (Fig. 5.3(c)) and were completely eliminated by adding a body support (Fig. 5.3(d)). Without body support the reconstructed image also converges to a uniform phantom, but only after 50 OSEM iterations, which results in a noisy image (Fig. 5.3(g)).

Hoffman phantom

We also simulated a Hoffman brain phantom at two different noise levels. Fig. 5.4 shows the phantom in low noise circumstances, which allows us to assess the presence of artifacts. Both images were post-filtered with a Gaussian filter with a 4 mm FWHM and a kernel size of 25 voxels. The non-multiplexed image (Fig. 5.4(b)) and the time-multiplexed image (Fig. 5.4(c)) are shown at equal noise level (COV=64% before post-smoothing) and we cannot observe any artifacts in Fig. 5.4(c). This confirms that time-multiplexing, in combination with a body support indeed results in

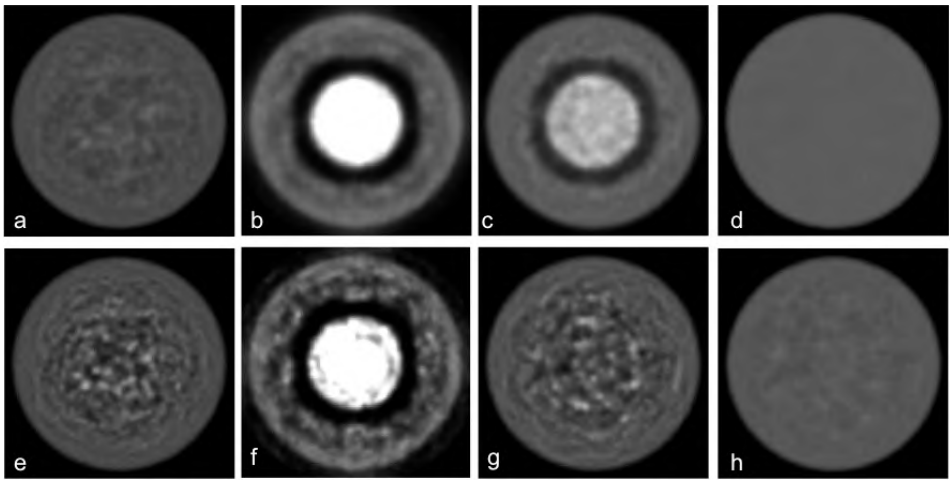

Figure 5.3: The uniform phantom reconstructed using OSEM (a) no multiplexing, 10 iterations, 8 subsets (b) only multiplexing, 10 iterations, 8 subsets (c) time-multiplexing, 10 iterations, 8 subsets (d) time-multiplexing + body support, 10 iterations, 8 subsets (e) no multiplexing, 50 iterations, 8 subsets (f) only multiplexing, 50 iterations, 8 subsets (g) time-multiplexing, 50 iterations, 8 subsets (h) time-multiplexing + body support, 50 iterations, 8 subsets

artifact-free reconstructions.

Fig. 5.5 shows simulated images of the Hoffman phantom at realistic noise level, both for the non-multiplexed (β=1+BS) and time-multiplexed (β=0.2+BS) system, at equal noise (COV = 16.3% after post-smoothing).

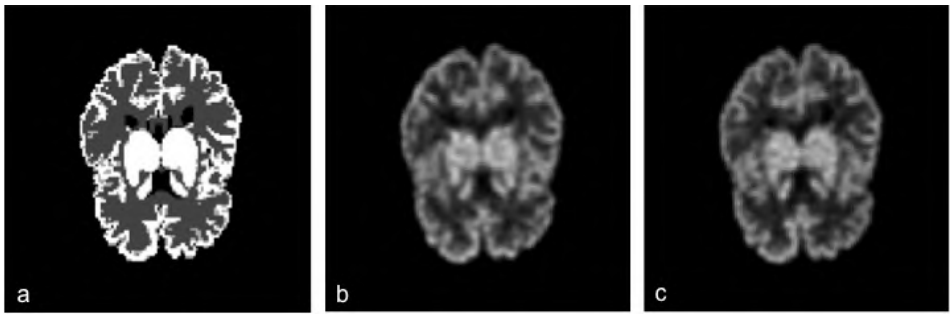

Figure 5.4: (a) The Hoffman phantom, (b) no multiplexing, COV=64% (c) time-multiplexing, COV=64%

All images were post-filtered with a Gaussian filter with a 7.5 mm FWHM and a kernel size of 25 voxels. The images show no artifacts but although the time-multiplexed images seem better than the non-multiplexed images, they still don't clearly visualize the 6mm lesions. For a more quantitative comparison of image quality, we refer to the next section.

Contrast phantom

To evaluate whether this increase in sensitivity also results in increased image quality, we reconstructed a contrast phantom (Fig. 5.6(a)) and measured the CRC and COV for the non-multiplexed (Fig. 5.6(b)) and the time-multiplexed setup (Fig. 5.6(c)). We used a body support for both reconstructions and post-filtered with a Gaussian filter with a 4 mm FWHM and a kernel size of 25 voxels. The contrast-to-noise plots (Fig. 5.7) show improved image quality with time-multiplexing: a 5% improvement in the CRC at 58% noise (COV) compared to no multiplexing.

5.1.7 Discussion

In this section we investigated the potential of time-multiplexing to increase the image quality of our previously developed stationary full-ring multi-lofthole brain SPECT system (chapter 4). We can confirm the results from literature [129][258], which show that multiplexing leads to artifacts and that time-multiplexing can eliminate these artifacts. However, convergence is slow. Adding a body support helps to speed up convergence but even then our simulations show an improvement in CRC of only 5% (for a COV of 58%), despite an increase in sensitivity of 80%. It is important to note that this result is based on a single noise realization and to multiplexing in the transverse direction and it should therefore be seen as an exploratory study. More research is needed to evaluate whether increased sensitivity due to multiplexing results in improved image quality or not. In 5.2.5 we will therefore present a more elaborate study on image quality in multiplexed systems.

5.2 The evaluation of data completeness in multiplexing multi-pinhole SPECT

In the previous section we found that multiplexing artifacts can be removed by combining multiplexed with non-multiplexed data. Other multi-pinhole

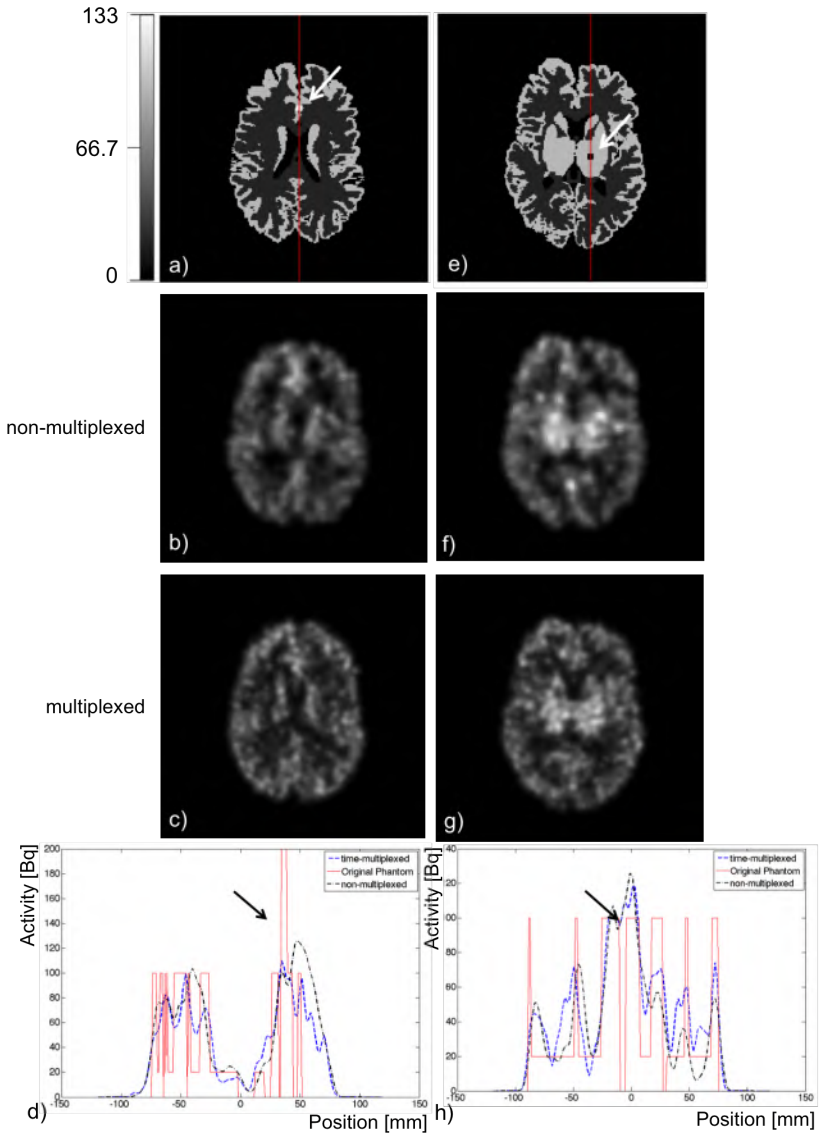

Figure 5.5: Hoffman phantom (a) Transverse slice with a hot lesion of 6 mm (b) non-multiplexed image of slice with hot lesion (33 iterations, 4 subsets) (c) time-multiplexed image of slice with hot lesion (291 iterations, 4 subsets) (d) line profile of hot lesion for non-multiplexed (black dashed line) and time-multiplexed (blue dashed line) (e) Transverse slice with a cold lesion of 6 mm (f) non-multiplexed image of slice with cold lesion (33 iterations, 4 subsets) (g) time-multiplexed image of slice with cold lesion (291 iterations, 4 subsets) (h) line profile of cold lesion for non-multiplexed (black dashed line) and time-multiplexed (blue dashed line)

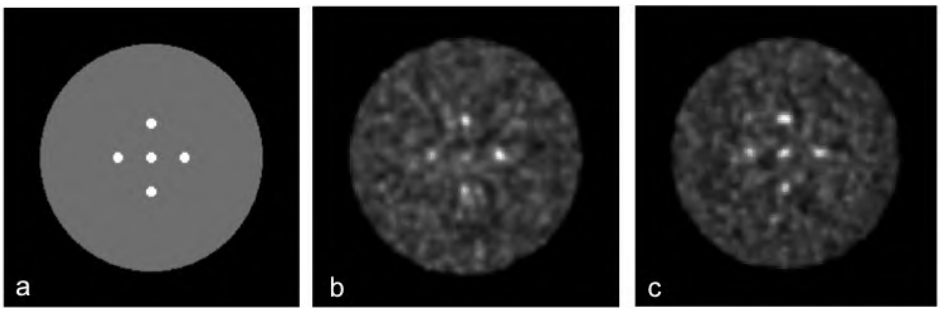

Figure 5.6: (a) The contrast phantom, (b) no multiplexing, COV=58% (c) time-multiplexing, COV=58%

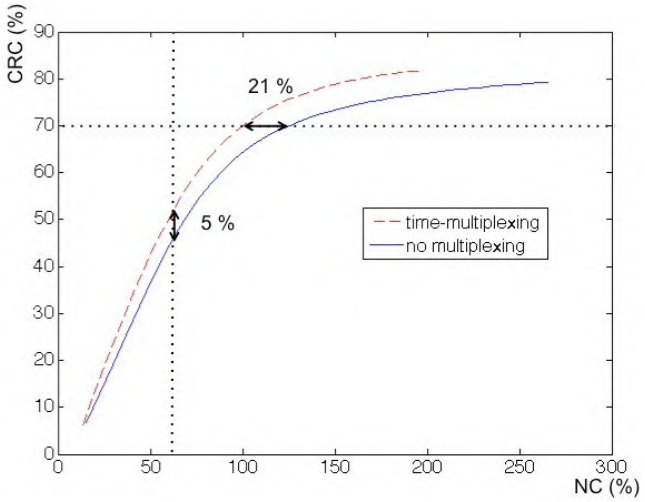

Figure 5.7: (a) Contrast-to-noise plots for the contrast phantom acquired without multiplexing (solid line) and with time-multiplexing (dashed line)

collimators simply try to avoid multiplexing (e.g. [246][260]). They use baffles [260] or extra shielding [246] to remove overlap between the different pinhole projections. Yet, there are examples of multi-pinhole collimators that allow multiplexing and do not show any artifacts (e.g. [208][184]) or only in certain phantoms [46].

In this section we search for a deeper understanding of these observations. We develop a method that predicts wether a certain multiplexing collimator will result in artifacts or not and investigate whether the increased sensitivity from multiplexing results in improved image quality.

In total we performed simulations for 8 different systems, including 100 noise realizations for 5 out of 8 systems. This requires large computational power and to reduce this as much as possible, we decided to perform these simulations for preclinical phantoms and systems. This allowed us to use a smaller detector, resulting in less rays for the pixel-driven forward projector and significantly speed up simulation time.

5.2.1 Introduction

Previous studies investigating multiplexing artifacts already resulted in some general insights. We summarize a few of these insights. Cao [32] optimized the number of pinholes in multi-pinhole SPECT for mouse brain imaging and found that some overlap was beneficial for the overall image quality and that repeating patterns in pinhole arrangement were more likely to produce multiplexing artifacts. Later, Vunckx [258] came to a similar conclusion about the pinhole arrangement in an optimization study for focused field of view mouse imaging. Vunckx also found that once the detector area is entirely used, the contrast-to-noise ratio does not improve with increasing degree of multiplexing [260]. The increase in sensitivity only compensates for the increased ambiguity. Bal [14] studied multiplexing artifacts in a nine-pinhole collimator and found that they were reduced by increasing angular sampling. This is consistent with results from Difilippo [54] who also compared multi-pinhole collimators with regular and irregular pinhole patterns. Mok [155] investigated the effects of object activity distribution in multiplexing pinhole systems and found that more multiplexing can be used when the activity distribution is sparse. Finally, Kench [106] explained multiplexing artifacts based on inconsistent projection data due to truncation.

While previously, the common view was that artifacts are caused by the ambiguity of the overlapping data, there has recently been a shift towards the idea that artifacts are due to the absence of non-multiplexed complete

data. Vunckx [258] was the first to show that adding complete data from a single pinhole collimator, or information from the body contour helps to reduce or eliminate multiplexing artifacts. Later, Mahmood [129] also showed the potential of mixed multiplexed and non-multiplexed projection data and confirmed that the non-multiplexed projection data could be used to resolve multiplexing artifacts. In both studies, the non-multiplexed data were acquired as an extra data set (with an extra detector [260] or at a different time interval [129]) but in many systems non-multiplexed data is already present as only a part of the detector is overlapping. In this section we want to show that when the non-multiplexed data is complete, no artifacts are to be expected.

Recently, an article has been published by Lin [119] in which a method was developed to predict the presence of artifacts in multiplexing systems based on data completeness. This method was developed independently from ours but it shows many similarities. It describes two types of multiplexing systems that are artifact-free. In type I systems, data completeness is achieved from the non-multiplexed data alone. In type II systems, only a part of the FOV is sampled without multiplexing. If this part can be fully reconstructed, then its projection data can be used to resolve other parts of the field of view (FOV). We extend this method with type III multiplexing, based on the concept of de-multiplexing (section 5.2.2).

In the following sections, we will present our method, use computer simulated images to illustrate it and we investigate whether the increased sensitivity, that can be obtained with multiplexing pinholes, results in a better contrast-to-noise ratio and non-prewhitening matched filter signal-to-noise ratio (NPW-SNR).

5.2.1.1 Orlov's conditions

In non-multiplexing pinhole systems, the conditions under which a given three-dimensional object can be reconstructed from a set of projections, were originally described by Tuy and Smith [229][215] and later reformulated by Metzler [147] using Orlov's geometrical language [176] with vantage angles (directions along which voxels are actually measured): "The set of vantage angles on a unit sphere of directions (called the Orlov sphere), from each voxel to each point on the curve of focal points, must have points in common with any arc of a great circle surrounding that voxel". The vantage angle θ is defined as the angle of the projection ray with the horizontal axis in the transverse plane (Fig. 5.9a).

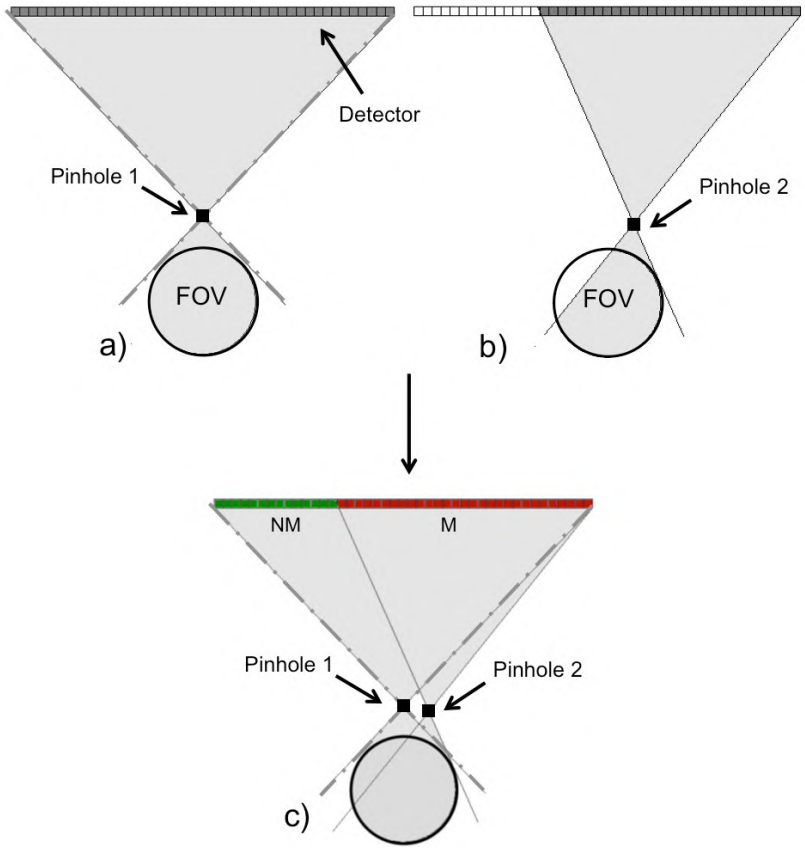

Figure 5.8: The FOV is forward projected through each pinhole separately to determine the multiplexed regions on the detector. (a) Forward projection through pinhole 1. (b) Forward projection through pinhole 2. (c) Pixels that are non-zero in more than one projection set are multiplexed (M) and colored red, the others are non-multiplexed (NM) and colored green.

In a rotating single pinhole system, this condition can only be fulfilled for voxels in the plane determined by the pinhole orbit and only if the set of vantage angles from each voxel spans at least 180°. Geometrically, this means that for a system rotating over 360°, at least half the FOV should be sampled (from the edge to the center).

5.2.1.2 Application of Orlov's conditions in multiplexing systems

We applied Orlov's theory to multiplexing systems by making a distinction between different types of vantage angles: multiplexed (M), non-multiplexed (NM) and de-multiplexed (DM).

Multiplexed and non-multiplexed vantage lines respectively project on an overlapping and non-overlapping detector pixel. To evaluate which pixels are overlapping, we forward project the object through all pinholes separately (Fig. 5.8). In this way we obtain one projection set per pinhole. A pixel is overlapping if it is non-zero in more than one projection set.

The third type of vantage angles (DM) is explained in the next section (5.2.2). In short, some pixels can be resolved as if they were not multiplexed and the vantage angles projecting on these pixels are classified as de-multiplexed.

To evaluate a multiplexing system, we only use the set of vantage angles of type NM and DM. If this set satisfies Orlov's conditions, then data sufficiency is achieved.

5.2.2 De-multiplexing

When a collimator with multiple pinholes (at different positions in the transverse plane) is used, the same set of voxels can sometimes be sampled both with and without multiplexing (through different pinholes and at different rotation angles). For example, a set of voxels j that is projected along L_1 is first sampled without multiplexing (Fig. 5.9a). Then, the gamma camera is rotated and the same set of voxels (along L_1) is projected with the same vantage angle but now through pinhole 2 (Fig. 5.9b). The projection is now multiplexed with the projection along L_2. This can be expressed mathematically as follows:

$$\begin{cases} p_n = \sum_{j \in L_1} H_1(n,j) f(j) & (5.4) \\ p_m = \sum_{j \in L_1} H_2(m,j) f(j) + \sum_{j \in L_2} H_1(m,j) f(j) & (5.5) \end{cases}$$

with p_n the value of the non-multiplexed detector pixel, p_m the value of the multiplexed detector pixel, $f(j)$ the activity concentration in voxel j and H_1 and H_2 the system matrices corresponding to pinholes 1 and 2.

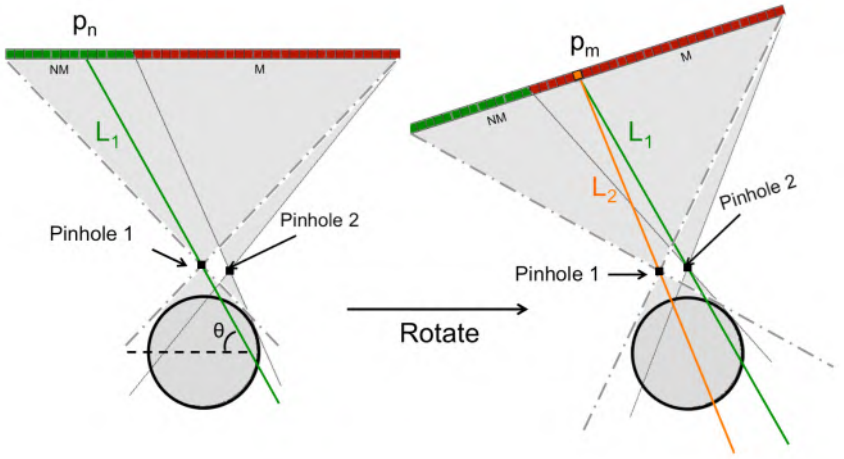

Figure 5.9: Principle of de-multiplexing. (a) A set of voxels along L_1 is projected without multiplexing through pinhole 1. (b) After rotating the camera, the same set of voxels (along L_1) is sampled with multiplexing, but now through pinhole 2. Vantage line L_2 can be de-multiplexed.

If $H_2(m,j) = W.H_1(n,j) \quad \forall j \in L_1$, then we can write a set of equations that is fully equivalent to (5.4,5.5):

$$\begin{cases} p_n = \sum_{j \in L_1} H_1(n,j) f(j) & (5.6) \\ p_m - W.p_n = \sum_{j \in L_2} H_1(m,j) f(j) & (5.7) \end{cases}$$

From (5.7), it follows that L_2 is equivalent to a non-multiplexed vantage line projecting on a pixel with value $p_m - W.p_n$. We would like to emphasize that there is no need to modify the reconstruction algorithm to explicitly de-multiplex detector pixels. We only use the concept to show that some multiplexed vantage lines are equivalent to non-multiplexed ones, which explains why they can be included in the set of vantage lines used to evaluate data completeness.

In many systems condition $H_2(m,j) = W.H_1(n,j) \quad \forall j \in L_1$ is only true by approximation. It assumes perfect pinholes where resolution and penetration effects can be ignored as shown in Appendix A, unless the pinholes are at the same radius of rotation. In this study we use simulations to

investigate whether de-multiplexing is still possible in these non-ideal cases.

De-multiplexing is also applicable in systems with more than two overlapping pinhole projections:

$$p_m = \sum_{n=1}^{N} \sum_{j \in L_n} H_n(m,j) f(j) \tag{5.8}$$

with p_m the value of a multiplexed detector pixel, N the number of overlapping pinhole projections, L_n the vantage line through pinhole n and H_n the system matrix corresponding to pinhole n. Vantage line L_N can be de-multiplexed if there exists a non-multiplexed vantage line L_n for all $n = 1 \ldots N-1$:

$$p_m - \sum_{n=1}^{N-1} W_n p_n = \sum_{j \in L_N} H_N(m,j) f(j) \tag{5.9}$$

In the case of more than two overlapping pinholes, de-multiplexing can also be applied iteratively, i.e. a de-multiplexed vantage angle can, in turn, de-multiplex another vantage angle.

5.2.3 Method to evaluate data completeness

To apply Orlov's conditions to a multiplexing system, we make a distinction between pixels that are multiplexed (M) and non-multiplexed (NM). We back project the NM pixels through their corresponding pinhole (Fig. 5.10a). The back projection of every NM pixel corresponds to one vantage line of type NM. In a system that is circularly rotating over 360°, sufficient data is available from the NM vantage lines only if they sample at least half the FOV (from the edge to the center). Otherwise, data sufficiency can be achieved only if de-multiplexing is possible. A NM vantage line can be used for de-multiplexing by rotating the camera such that the vantage line projects through the other pinhole (Fig. 5.10b). The pixels on which the vantage lines project, can now be classified as de-multiplexed (DM). In the third step, we back project the de-multiplexed pixels to determine the vantage lines of type DM (Fig. 5.10c). In the last step, we evaluate whether the set of vantage lines of type DM and NM sample at least half the FOV. In that case, no artifacts are to be expected. Otherwise, data completeness can only be achieved if more de-multiplexing is possible. A

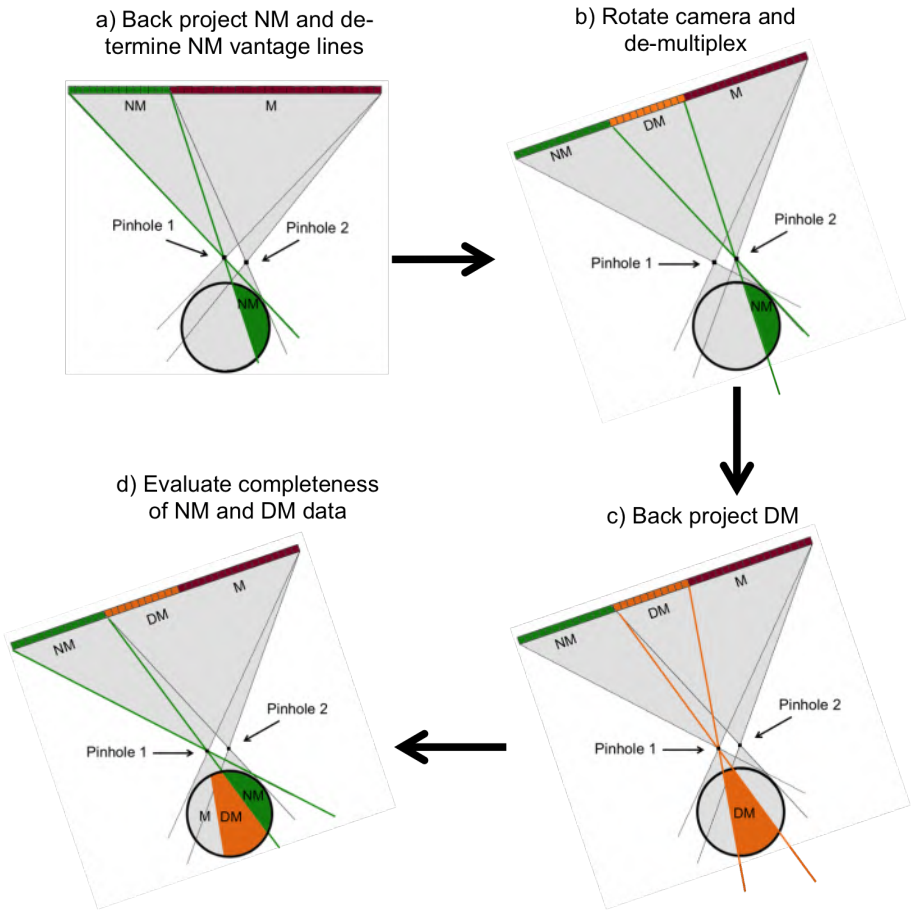

Figure 5.10: Method to evaluate data completeness: (a) The non-multiplexed region (NM) is back projected to determine the NM vantage lines (b) The camera is rotated so that the NM vantage lines project trough pinhole 2. De-multiplexing is now possible. (c) Back project the de-multiplexed region (DM). (d) Evaluate data completeness based on both the de-multiplexed and non-multiplexed vantage lines

second iteration of de-multiplexing can be started. The DM vantage lines can in turn be used to de-multiplex another region.

5.2.4 Validation for pinholes in the same transverse plane

In the previous section we developed a method to evaluate Orlov's conditions in multiplexing systems (Section 5.2.3). Now, we will first validate it for five different rotating (multi-) pinhole systems with all pinholes in the same transverse plane. We evaluate the presence of artifacts in images reconstructed from noiseless projection data.

5.2.4.1 Pinhole arrangements

Five acquisition setups were chosen with the same detector, same FOV (64 mm diameter) and same spatial resolution but with different collimators, resulting in different degrees of multiplexing (Fig. 5.11). All systems are rotating over 360° and have all pinholes in the same transverse plane.

The first setup (SPH) is our reference system. It has a single pinhole that samples the complete FOV and is rotated over 360°. There is sufficient data in the transverse plane and no overlap (Fig. 5.11, SPH). Therefore, we expect no artifacts in the reconstructed images.

Next, in 2MPH A, we added a second pinhole without changing the detector or the first pinhole's position. Consequently, we increase the sensitivity but we also introduce overlap on the detector (50%). The remaining 50% is not overlapping and at one angular position, half the FOV is sampled without multiplexing (Fig. 5.11, 2MPH A). So, after rotating over 360°, all voxels are sampled from vantage angles spanning 180°. Although this system has 50% of overlap, data sufficiency is achieved. Therefore we do not expect any artifacts from this setup.

In the third setup (2MPH B), we investigate the possibility to further increase the amount of overlap (to 67% on the detector) without introducing artifacts. Voxels close to the center are only sampled with multiplexing (Fig. 5.11, 2MPH B). The non-multiplexed data alone is thus insufficient for data completeness. However, some pixels can be de-multiplexed. If we now combine the non-multiplexed vantage angles with the de-multiplexed ones, we see that half the FOV is sampled. So, after rotating over 360°, all voxels are sampled from vantage angles of type DM or NM spanning 180°. Therefore, we do not expect any artifacts.

In the fourth setup (2MPH C), the two pinholes are rearranged but with-

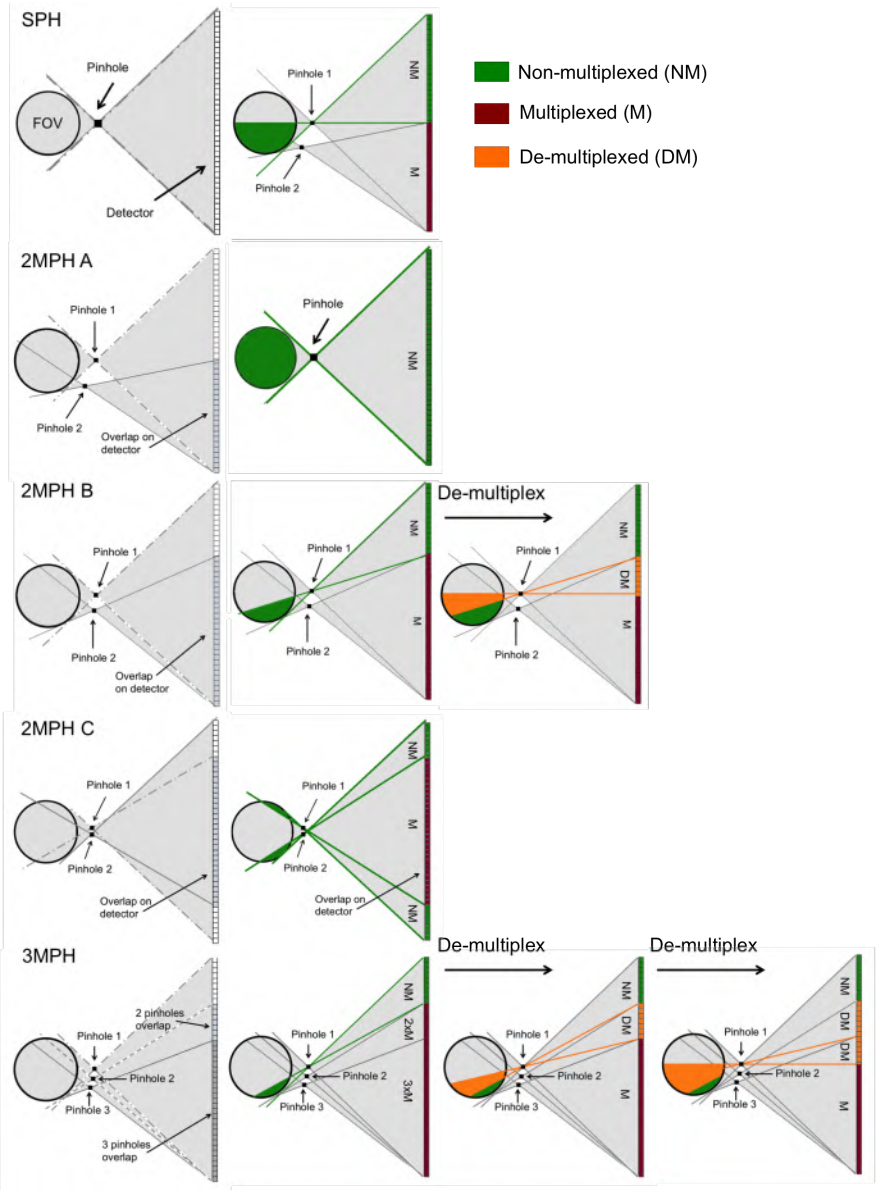

Figure 5.11: Acquisition setups - SPH: Single pinhole - 2MPH A: 2 pinholes with 50% overlap on the detector - 2MPH B: 2 pinholes with 67% overlap on the detector - 2MPH C: 2 pinholes with 67% overlap on the detector - 3MPH: 3 pinholes with 79% overlap on the detector

out changing the amount of overlap (67% on the detector). Only the position of the overlap on the detector is changed. Like in 2MPH B, data completeness is not achieved with NM vantage lines alone. However, NM vantage lines from one pinhole that are forward projected through the other pinhole (step b of the method illustrated in Fig. 5.10), fall outside the detector and therefore, de-multiplexing is not possible. Data completeness can thus not be achieved.

In the last setup (3MPH), we investigate the case where three pinholes (partially) overlap. Only 21% of the detector has no multiplexing. In a first step, only vantage lines that project on pixels with overlap from two pinholes can be de-multiplexed, as NM vantage lines are available from only one pinhole (Fig. 5.11, 3MPH). When three pinholes overlap, two different non-multiplexed vantage lines are needed for de-multiplexing (Section 5.2.2). After this first de-multiplexing step, however, we have vantage lines of the type NM and DM from two different pinholes and as a result, it is now possible to de-multiplex pixels with overlap from three pinholes (Fig. 5.11, 3MPH). If we now combine the vantage angles of type NM and DM, we see that data sufficiency is achieved. Therefore, we do not expect any artifacts.

5.2.4.2 System parameters

We summarized the design parameters in Table 5.2. When two or three values are shown, they correspond to the different pinholes of the setup. d is the physical diameter of the pinhole aperture, h the distance between the pinhole aperture and the detector (Fig. 5.12), o_x the pinhole position's x-coordinate, ϕ the pinhole tilt (pinholes are only tilted in the transverse plane) and α the opening angle of the pinhole. All setups have the same NaI detector with an intrinsic resolution R_i of 2 mm. We used a detector with an area of 215x100 mm^2 (transverse x axial) that rotates with 60 steps over an angular span of 360° with a radius of rotation D of 160 mm. The diameters of the different pinholes are chosen such that all systems have the same spatial resolution of 2.54 mm in the center of the FOV.

Resolution was calculated as follows [12]:

$$R_{CFOV} = \sqrt{\frac{R_i^2}{m^2} + (d_{Reff}(1 + \frac{1}{m}))^2} \tag{5.10}$$

with m the magnification:

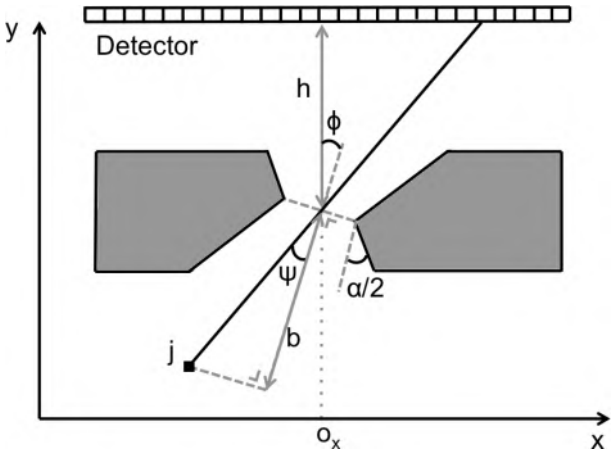

Figure 5.12: Detail of a pinhole with h the distance between the pinhole aperture and the detector, o_x the pinhole position's x-coordinate, ϕ the pinhole tilt, α the opening angle of the pinhole, ψ the angle between the incidence ray and the normal on the pinhole aperture and with b the perpendicular distance between voxel j and the center of the pinhole aperture.

$$m = \frac{h}{D - h} \tag{5.11}$$

and d_{Reff} the resolution effective diameter as described by [7]:

$$d_{Reff} = d + \frac{\ln 2}{\mu_W} tan(\frac{\alpha}{2}) \tag{5.12}$$

μ_W is the attenuation coefficient for tungsten at 140.5 keV (3.3976 mm^{-1}).

In Table 5.1 we also show the volume sensitivity S of the different setups. For the setups that have multiple pinholes, the sensitivity is a sum of the volume sensitivity of all pinholes. The volume sensitivity of one pinhole is defined as follows:

$$S = \frac{1}{J} \sum_{j=1}^{J} g(j) \tag{5.13}$$

with $g(j)$ the point sensitivity at voxel j and J the number of voxels in the FOV (a cylinder with a diameter of 64 mm and an axial length of 64 mm).

	SPH	2MPH A	2MPH B	2MPH C	3MPH
aperture d [mm]	1.50	1.50/1.78	1.50/1.61	1.70/1.70	1.50/1.57/1.66
focal length h [mm]	113	113/121.25	113/115.68	118.92/118.92	113/114.27/116.88
transverse offset o_x [mm]	0.0	0.0/-26.04	0.0/-14.76	5.14/-5.14	0.0/9.04/17.56
pinhole tilt [°]	0.0	0.0/-12.9	0.0/-7.4	-6.9/6.9	0.0/4.4/8.2
opening angle [°]	87	87/42	87/62.6	73/73	87/72.8/58.6
sensitivity S [cps/Bq]	$5.53x10^{-5}$	$8.41x10^{-5}$	$9.95x10^{-5}$	$11.96x10^{-5}$	$13.70x10^{-5}$
overlap d [%]	0	50	67	67	79

Table 5.2: Design parameters of the setups with pinholes in the same transverse plane

The point sensitivity $g(j)$ is described as follows [179]:

$$g(j) = \frac{d_{Seff}^2 \cos^3 \psi}{16 b^2} \tag{5.14}$$

with ψ the angle between the incidence ray and the normal on the pinhole aperture (Fig. 5.12), with b the perpendicular distance between voxel j and the center of the pinhole aperture (Fig. 5.12) and with d_{Seff} the physical diameter d corrected for penetration at the edges of the aperture:

$$d_{Seff} = \sqrt{d(d + \frac{2}{\mu_W} tan\frac{\alpha}{2}) + \frac{2}{\mu_W^2} tan^2\frac{\alpha}{2}} \tag{5.15}$$

5.2.4.3 Phantoms

We simulated projection data for two different phantoms.

Cold rod phantom The cold rod phantom is a cylinder with an outer diameter of 60 mm and cold rods with a diameter of 0.8 mm, 1.1 mm, 1.3 mm, 1.6 mm, 2.1 mm and 2.6 mm. The distance between the centers of two neighboring rods is twice their diameter. We used attenuation values of PMMA for the non-active regions and water for the active regions (with Tc-99m).

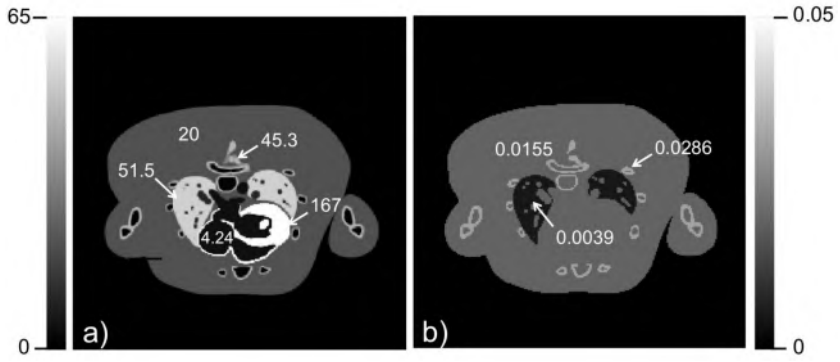

Figure 5.13: Roby phantom (a) activity distribution [MBq] (b) attenuation coefficients [mm^{-1}]

ROBY phantom The ROBY phantom [210] is a digital representation of a rat (Fig. 5.13).We simulated the relative activity distribution of Tc-99m-MIBI in heart, lungs, blood and bone obtained from [24] and [166]. Attenuation coefficients were obtained from the XCOM photon cross section library [91].

Both phantoms were voxelized using a matrix of 480 x 480 x 480 voxels with an isotropic voxel size of 0.133 mm and we limited the axial dimensions of the phantoms to 10 mm. A helical movement could be used to obtain data completeness in an extended axial FOV [149] but this is outside the scope of this work.

5.2.4.4 Data generation

Noiseless projection data were simulated using an existing GPU-implementation [239] based on the ray-driven forward projector [98][279] that was first described in section 2.1.3.1.1. We used pinhole subsampling with 912 rays in an extended circular area around the pinhole aperture such that photons penetrating the pinhole edge with a probability as low as 0.01 are included [73]. Phantom attenuation and sensitivity are modeled analytically using the Beer-Lambert Law (describing the effect of attenuating tissue on the number of measured counts) and equation (5.14) respectively, but without using d_{Seff}, as penetration is already modeled. The detector has a pixel size of 1.6 x 1.6 mm^2 and an intrinsic resolution of 2 mm, which was modeled as a Gaussian blurring operation on the projection data.

5.2.4.5 Image reconstruction

Reconstructions were performed with 1200 iterations of OSEM [88] (which was explained in section 2.1.4.2) using 8 subsets. The forward projector is ray-driven [98][279] (like the simulation code) but it uses only 7 rays for pinhole subsampling [254]. Pinhole penetration is modeled in a more cost-effective (but less accurate) way using d_{Reff} (eq. 5.12) for the pinhole subsampling area and d_{Seff} (eq. 5.15) for the sensitivity model. The reconstructed object is represented using 128 x 128 x 128 voxels with an isotropic voxel size of 0.5 mm and post-processed with a Gaussian filter (FWHM = 1 mm). The back projector is voxel-driven and uses no pinhole subsampling (one ray). Attenuation, sensitivity and resolution were only modeled in the forward projector. Unmatched projector/back projector pairs can be used to speed up the reconstruction process [277].

We evaluated data completeness in 5 different systems with pinholes in the same transverse plane (Fig. 5.14 and Fig. 5.15) and validated our method with reconstructions of noiseless phantom data. Next, we evaluated image quality of the different systems using noisy realizations of a contrast phantom (Fig. 5.16 and Fig. 5.18). Finally, we also evaluated the method for three rotating systems with pinholes in different transverse planes (Fig. 5.20 and Fig. 5.21).

5.2.4.6 Results

The reconstructed images are shown in Fig. 5.14 and Fig. 5.15.

SPH This is our reference setup. We do not expect any artifacts and this is confirmed by the reconstructed data (Fig. 5.14 SPH and Fig. 5.15 SPH).

2MPH A Although this system has 50% of overlap, data sufficiency is achieved and as a result, both the cold rod and the ROBY phantom could be reconstructed without artifacts (Fig. 5.14 2MPH A and Fig. 5.15 2MPH A). We even observe a small improvement in the uniformity of the background. This is due to a better subsampling of the voxels as a result of the second pinhole.

2MPH B This setup has even more overlap (67% on the detector) but de-multiplexing is possible and data sufficiency is achieved. Therefore, we

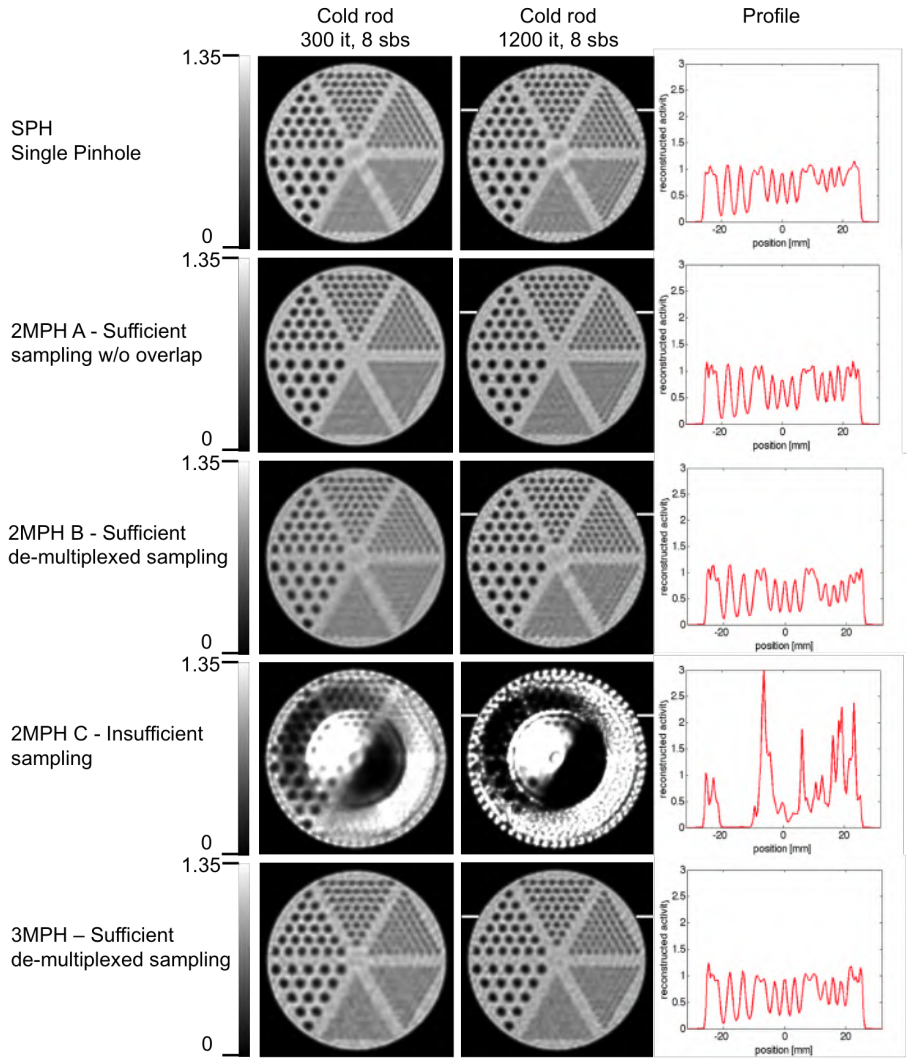

Figure 5.14: Reconstructed cold rod phantom with line profiles

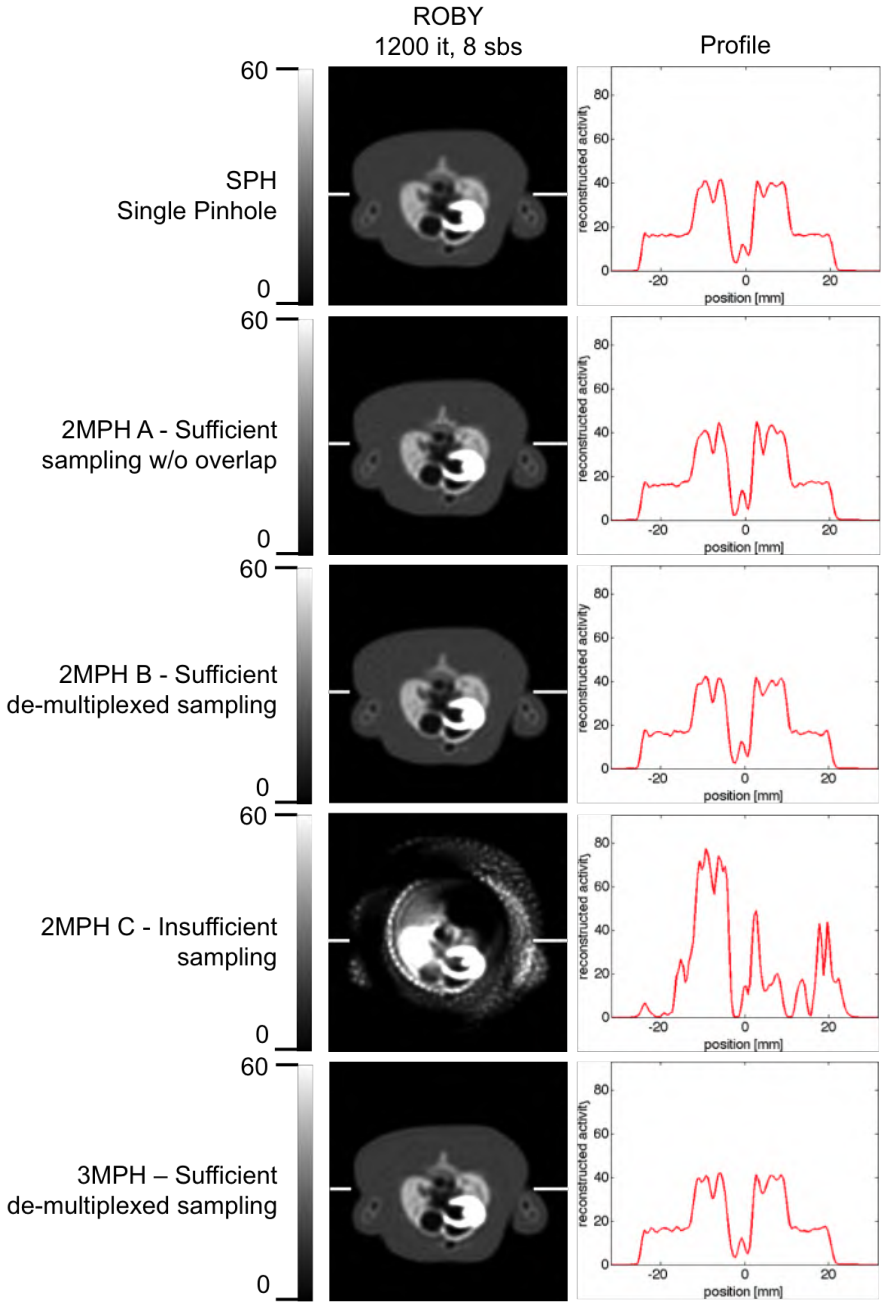

Figure 5.15: Reconstructed ROBY phantom with line profiles

do not expect any artifacts and this is confirmed by the reconstructed data (Fig. 5.14 2MPH B and Fig. 5.15 2MPH B).

2MPH C This setup has the same amount of overlap (67% on the detector) as the previous one. However, the arrangement of the pinholes is less advantageous and data completeness was not achieved. Therefore, it is not surprising that severe artifacts occur in the reconstructed images (Fig. 5.14 2MPH C and Fig. 5.15 2MPH C).

3MPH This setup has three multiplexing pinholes and only 21% of the detector has no multiplexing. However, de-multiplexing is possible and data sufficiency is achieved. Therefore, we do not expect any artifacts and this is confirmed by the reconstructed data (Fig. 5.14 3MPH and Fig. 5.15 3MPH). Again, we observe an improvement in the uniformity of the background. We also found that convergence is slower than with setup SPH. After 300 OSEM iterations (Fig. 5.14 3MPH, it 300), the cold rod phantom is more blurry than with setup SPH (Fig. 5.14 SPH, it 300). But after 1200 OSEM iterations, no obvious visual difference could be found between setup 3MPH and SPH (Fig. 5.14 it 1200, SPH & 3MPH).

5.2.5 The evaluation of image quality in multiplexing multi-pinhole SPECT

In the previous part, we investigated whether artifact-free images can be obtained with multiplexing systems that have complete data. In this part, we study the effect of multiplexing on image quality. We use the same setups as in the previous section except for system 2MPH C which shows too many artifacts. We performed 100 noise realizations of a contrast phantom and calculated the contrast recovery coefficient (CRC) and the non-prewhitening matched filter signal-to-noise ratio (NPW-SNR) to evaluate image quality.

5.2.5.1 Contrast phantom

The phantom is cylindrical (outer diameter of 60 mm). It has hot spheres with a diameter of 4 mm (uptake ratio 7:1) that are arranged on circles with a radius of 7 mm, 18 mm and 27 mm. A total of 6, 15 and 25 spheres were present on the inner, middle and outer ring respectively (Fig. 5.17). The phantom is voxelized to a matrix of 480 x 480 x 480 voxels with an isotropic voxel size of 0.133 mm and we limited the axial dimensions of the phantom

to 10 mm. A helical movement could be used to obtain data completeness in an extended axial FOV [149] but this is outside the scope of this work. We used attenuation values of PMMA for the non-active regions and water for the active regions (with Tc-99m).

5.2.5.2 Data generation

Projection data were simulated as described in section 5.2.4.4. The 100 projection sets were realized by adding Poisson noise to a single noiseless data set. We simulated three different noise levels (corresponding to 3mCi, 10mCi and 30 mCi, scanned for 30 minutes). All images were reconstructed as described in section 5.2.4.5. No post-processing was applied to the images.

5.2.5.3 Image quality metrics

Contrast-to-noise The contrast recovery coefficient of the ith hot sphere of the jth noise realization is defined as follows:

$$CRC_{i,j} = (\frac{\mu_{I,i,j}}{\mu_{b,j}} - 1)/(C-1) \times 100\% \tag{5.16}$$

with C the true sphere-background ratio, $\mu_{I,i,j}$ the mean activity in the ith hot sphere of the jth noise realization and $\mu_{b,j}$ the mean background activity of the jth noise realization. The background activity is averaged over all voxels in the 6 background regions shown in Fig. 5.17. The background regions have a diameter of 4.4 mm and are positioned at a distance of 12 mm from the center.

The CRC is then averaged over all hot spheres in one ring (N_s) and all noise realizations (N_n):

$$CRC = \frac{1}{N_s * N_n} \sum_{j=1}^{N_n} \sum_{i=1}^{N_s} CRC_{i,j} \tag{5.17}$$

The CRC value at each image reconstruction iteration is plotted against the coefficient of variation (COV):

$$COV = \frac{1}{N_n} \sum_{j=1}^{N_n} \frac{\sigma_{b,j}}{\mu_{b,j}} \times 100\% \tag{5.18}$$

with $\sigma_{b,j}$ the pixel-to-pixel percent standard deviation (%SD) in the background region of the jth noise realization.

Lesion detectability The NPW-SNR is a linear observer for lesion detectability tasks (signal-known exactly and background-known exactly, SKE/BKE) that has been shown to agree well with human observer performance [171][172]. The observer response λ_i is defined for the signal present ($i = 1$) and signal absent ($i = 0$) class:

$$\lambda_i = T/N \sum_{j \in ROI} f_i(j) \tag{5.19}$$

with $f_i(j)$ voxel j in the reconstructed image f_i, N the number of voxels in the ROI and T the true difference between the lesion and background activity concentration.

NPW-SNR is then defined as:

$$\text{NPW-SNR} = \frac{\overline{\lambda_1} - \overline{\lambda_0}}{\sqrt{\frac{1}{2}(\sigma_1^2 + \sigma_0^2)}} \tag{5.20}$$

with $\overline{\lambda_i}$ the observer response averaged over all lesions and all noise realizations and with σ_i the standard deviation of the observer response.

5.2.5.4 Results

Contrast-to-noise Fig. 5.16 illustrates the contrast-to-noise curves, where contrast is measured with the contrast recovery coefficient (CRC) as defined in equation (5.16) and noise is measured with the coefficient of variation (COV) as defined in equation (5.18). The reconstructed images (first noise realization) are shown in Fig. 5.17 and table 5.3 summarizes the CRC for a COV of 200%, 120% and 72% for the 3 mCi, 10 mCi and 30 mCi experiments respectively. The CRCs of the inner spheres are higher with the multiplexing setups, while the CRCs of the outer spheres are higher with the SPH setup (Fig. 5.16). However, the difference is small, with a maximum increase of 3.1% (setup 2MPH A, inner ring of spheres, 30 mCi) and a maximum decrease of 2.4% (setup 2MPH D, outer ring of spheres, 10 mCi). The standard deviation on the results of table 5.3 is between 1.7 and 5.5. We also observed that the noise levels at a fixed iteration number are lower in the multiplexing setups: 127.3%, 121.1%, 95.6% and 71.9% for the SPH, 2MPH A, 2MPH B and 3MPH setup respectively (300 OSEM iterations, 10mCi). This is a consequence of the increase in sensitivity. However, we also observe a slower convergence rate in the multiplexing setups (most pronounced in setup 3MPH). When a system is heavily multiplexed,

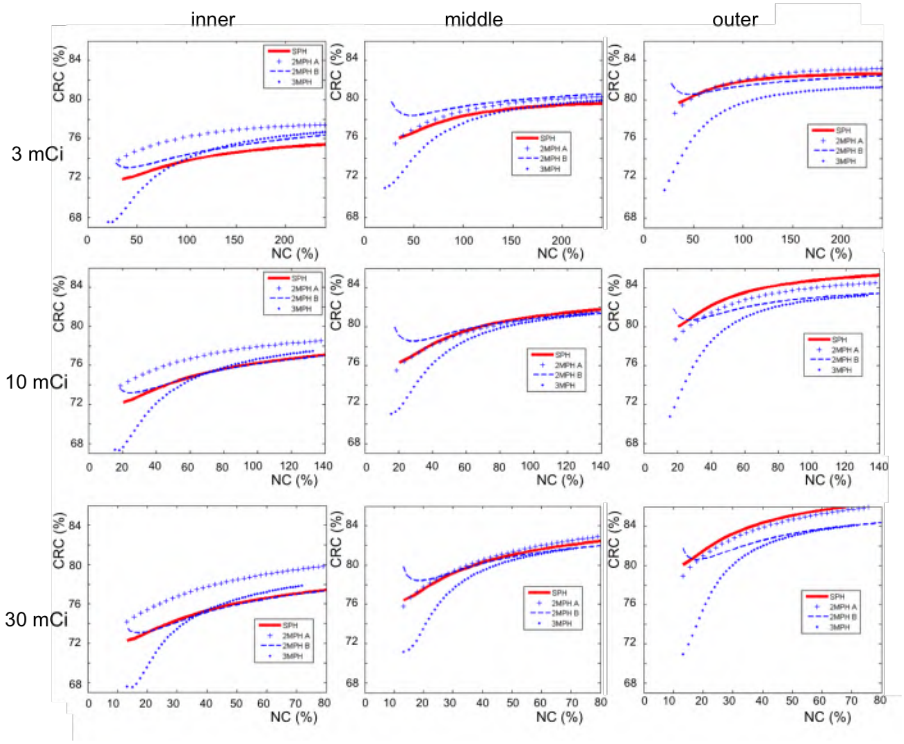

Figure 5.16: Contrast-to-noise for the inner, middle and outer ring of spheres at 3 mCi, 10 mCi and 30 mCi

it takes more iterations to achieve the same resolution. The two effects (higher sensitivity and lower convergence rate) counteract each other and this explains why the difference in contrast-to-noise between multiplexed and non-multiplexed setups is small (in the same order of magnitude as the standard deviation of the CRC).

Lesion detectability Fig. 5.18 shows the NPW-SNR at different reconstruction iterations, with NPW-SNR defined as in equation (5.20). We found that the multiplexed systems show better detectability than the SPH system. This is also confirmed by table 5.4, which summarizes the NPW-SNR after 600 OSEM iterations for the inner, middle and outer ring of spheres at 3 mCi, 10 mCi and 30 mCi. The improvement is highest with

Table 5.3: Contrast recovery coefficient at fixed COV

noise level	3 mCi	10 mCi	30 mCi
COV	200%	120%	72%
SPH			
inner	75.1 ± 5.2	76.7 ± 3.1	77.1 ± 1.9
middle	79.4 ± 5.4	81.5 ± 3.5	82.1 ± 2.3
outer	82.6 ± 5.5	85.1 ± 3.4	86.1 ± 2.3
2MPH A			
inner	77.3 ± 4.7	78.3 ± 2.9	79.5 ± 1.7
middle	80.1 ± 4.8	81.2 ± 3.1	82.6 ± 2.0
outer	83.1 ± 4.8	84.3 ± 3.2	85.8 ± 2.1
2MPH B			
inner	76.0 ± 5.1	76.6 ± 3.1	77.0 ± 1.8
middle	80.3 ± 5.3	81.1 ± 3.6	81.7 ± 2.3
outer	82.2 ± 5.3	83.2 ± 3.5	84.1 ± 2.3
3MPH			
inner	76.3 ± 4.8	77.2 ± 3.0	77.9 ± 1.8
middle	79.6 ± 4.9	81.1 ± 3.4	81.7 ± 2.2
outer	81.2 ± 4.8	83.1 ± 3.3	84.1 ± 2.2

the 3MPH system with an improvement of 38.9% in the inner ring of the 3 mCi experiment. The mean improvement over all multiplexing systems is 12.1%.

5.2.6 Validation for pinholes in different transverse planes

5.2.6.1 Simulations

In the previous sections, we investigated rotating multiplexing systems that have pinholes in the same transverse plane. This is not a necessary condition, certainly not for systems like 2MPH A (which corresponds to multiplexing Type I in [119]). Most systems discussed in literature are of Type I. To illustrate that the pinholes do not necessarily have to be in the same transverse plane, we simulated a system similar to 2MPH A (called 2MPH A off) but with the second pinhole at an axial offset of 7.5 mm. The first pinhole remains in the same position.

However, for systems like 2MPH B, where the data completeness relies

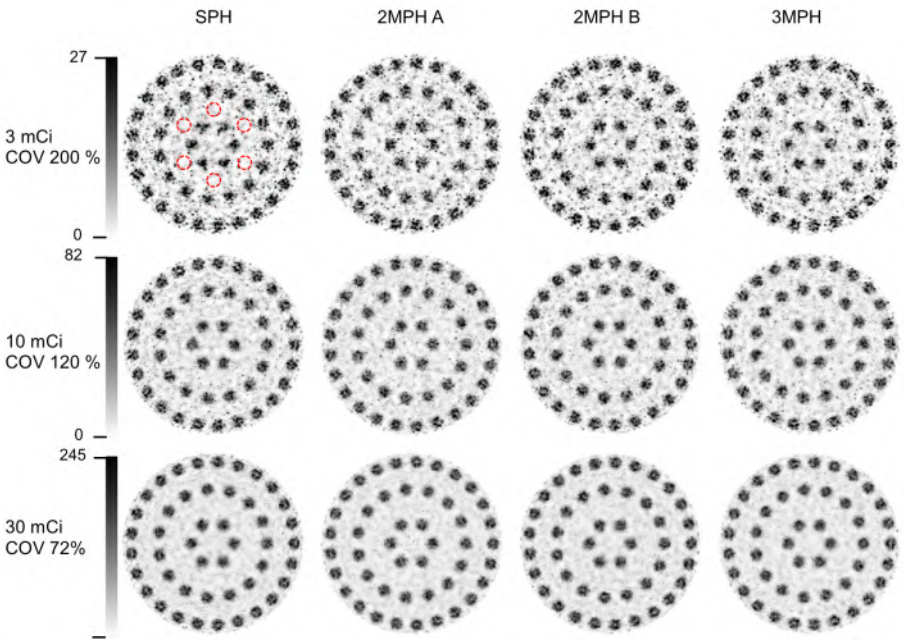

Figure 5.17: Reconstructed contrast phantoms with red marks in the 3 mCi SPH image showing where the background regions were chosen.

Table 5.4: NPW-SNR after 600 OSEM iterations

	3 mCi	10 mCi	30 mCi
SPH			
inner	23.5	36.7	62.6
middle	25.5	37.3	56.2
outer	29.3	41.5	57.9
2MPH A			
inner	27.2	41.5	68.2
middle	27.4	41.2	62.2
outer	31.6	45.1	64.0
2MPH B			
inner	25.8	43.0	73.7
middle	26.5	38.8	59.4
outer	29.2	43.1	62.7
3MPH			
inner	27.8	47.8	86.9
middle	28.5	44.0	65.6
outer	30.4	45.8	66.6

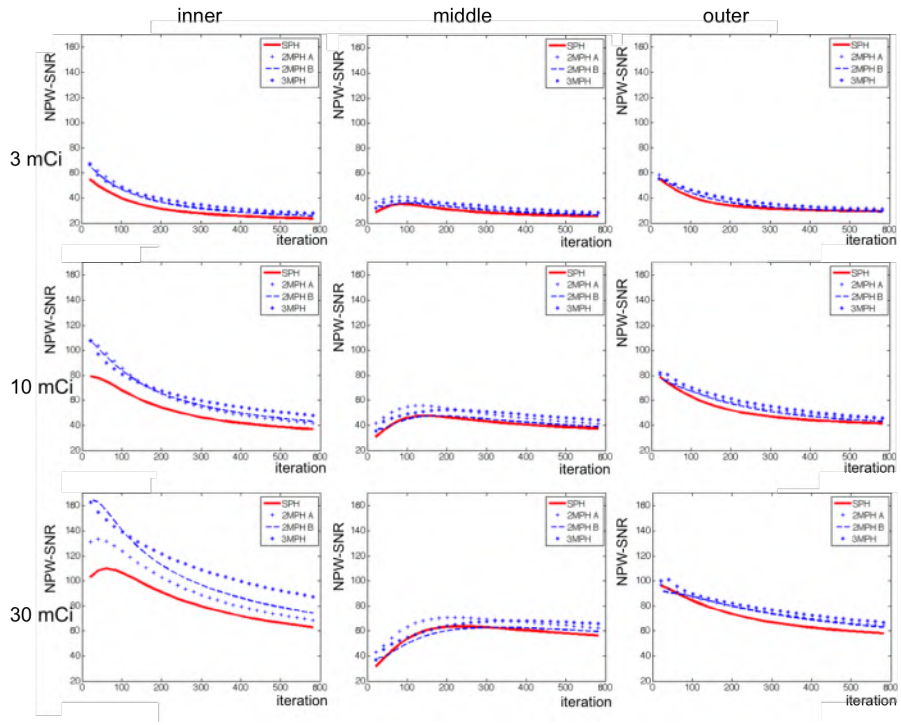

Figure 5.18: NPW-SNR for the inner, middle and outer ring of spheres at 3 mCi, 10 mCi and 30 mCi

on the concept of de-multiplexing, multiple bed positions are needed if the pinholes are not at the same axial position. The axial distance between the pinholes should be a multiple of the distance between the bed positions. To illustrate this, we simulated a system similar to 2MPH B (called 2MPH B off) but with the second pinhole at an axial offset of 7.5 mm. The first pinhole remains in the same position. We used 3 bed positions (-7.5, 0, +7.5 mm).

Finally, we simulated a system with 5 pinholes that are partially overlapping (Fig. 5.19a and Fig. 5.19b). The central pinhole has a diameter of 1.05 mm and an opening angle of 55.2° and the other four pinholes have a diameter of 1.06 mm and an opening angle of 52.4°. All pinholes are focussed on the center of the FOV and their focal length is 91.0 mm. We also investigated data completeness and found that in the central slice the complete FOV was sampled without multiplexing (Fig. 5.19c).

All three setups use a detector with an area of 215x215 mm^2 that rotates

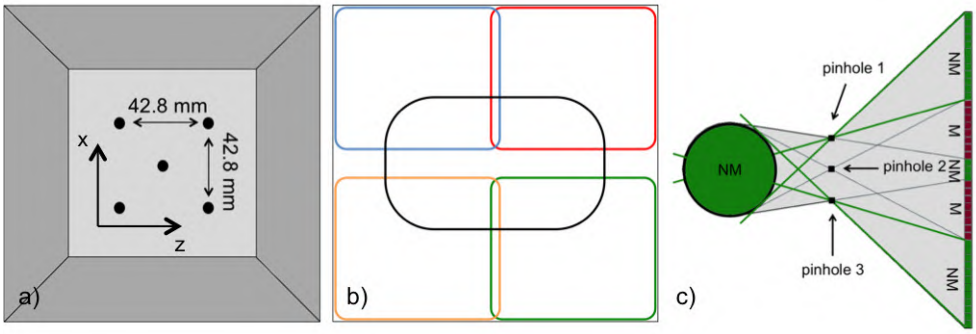

Figure 5.19: Acquisition setup 5MPH: 5 pinholes with 22% overlap on the detector (a) top view of the collimator in front of the detector (b) projections from the different pinholes partially overlapping on the detector (c) central slice: FOV is completely sampled without multiplexing.

with 60 steps over an angular span of 360° with a radius of rotation D of 160 mm. We used the cold rod and ROBY phantoms as described in section 5.2.4.3, except that this time we did not limit the axial length of the phantoms. Their full length is 64 mm. Noiseless projection data were simulated as described in section 5.2.4.4 and all images were reconstructed as described in section 5.2.4.5.

5.2.6.2 Results

2MPH A off In this setup, half the FOV is sampled without multiplexing. So, after rotating over 360°, all voxels are sampled from vantage angles spanning 180° and data completeness is achieved. Therefore, we do not expect any artifacts and this is confirmed by the reconstructed data (Fig. 5.20 2MPH A off and Fig. 5.21 2MPH A off).

2MPH B off In this setup, data completeness relies on the concept of de-multiplexing. As the two pinholes are in different transverse planes (7.5 mm offset), de-multiplexing is only possible because we moved the bed with +/- 7.5 mm. Data completeness is eventually achieved and therefore, we do not expect any artifacts. This is confirmed by the reconstructed data (Fig. 5.20 2MPH B off and Fig. 5.21 2MPH B off).

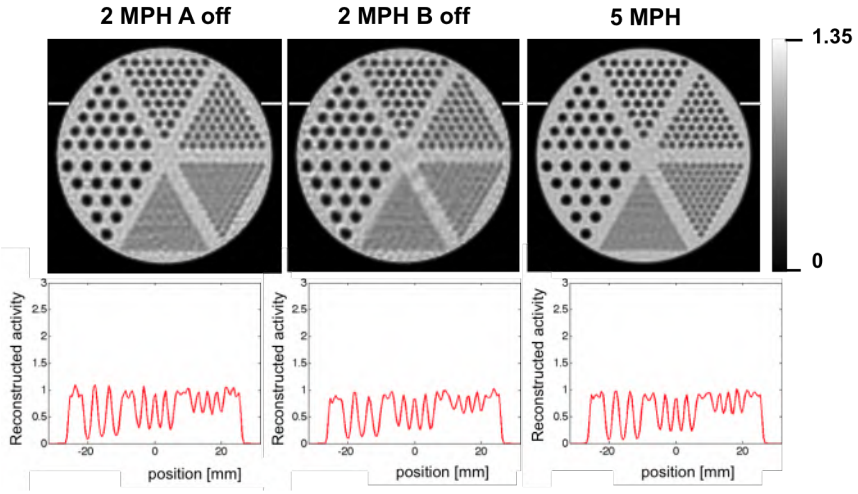

Figure 5.20: Reconstructed cold rod phantom with line profiles

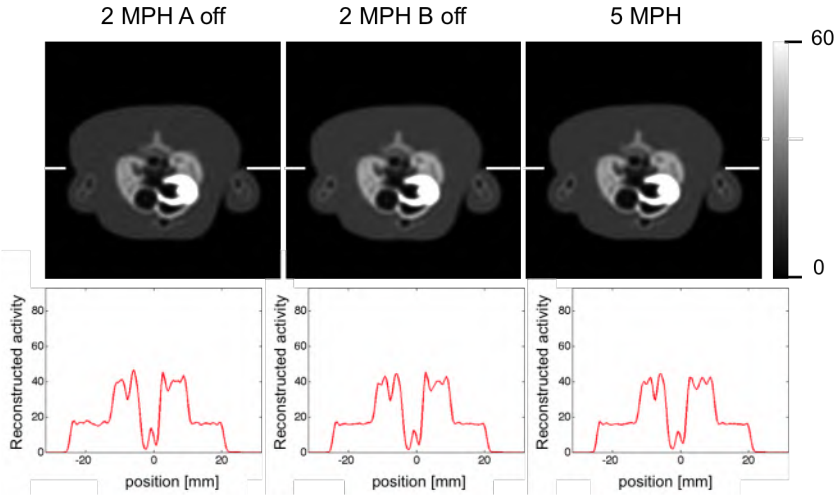

Figure 5.21: Reconstructed ROBY phantom with line profiles

5MPH This setup is comparable to many multiplexing setups described in literature. Data completeness was achieved in the central slices and therefore, we do not expect any artifacts. This is confirmed by the reconstructed data (Fig. 5.20 5MPH and Fig. 5.21 5MPH).

5.2.7 Discussion

We have shown that the amount of multiplexing does not predict whether a system will have artifacts or not. Setup 2MPH C, for example, has less overlap than setup 3MPH but it shows severe artifacts. We developed a method to predict the presence of multiplexing artifacts based on data completeness and showed that a certain activity distribution can be successfully reconstructed when the non-multiplexed data is complete or when the overlap can be sufficiently de-multiplexed. We validated the method using computer simulated phantom data. For example, setups 2MPH A, 2MPH B and 3MPH are multi-pinhole systems and although the degree of multiplexing is quite high (50%, 67% and 79% respectively), data completeness is achieved in all voxels. This indeed results in artifact-free images, both for the cold rod and the ROBY phantom.

Our method was developed independently from the method of Lin on artifact-free projection overlaps [119] but it shows many similarities: both methods are based on data sufficiency. Lin describes two types of overlap that result in artifact-free images. Type I multiplexing requires that data sufficiency is achieved with non-multiplexed data alone (corresponds to our 2MPH A setup). Type II multiplexing requires that data sufficiency is achieved in a part of the FOV so that it can be used to reconstruct another part of the FOV. Our 2MPH B setup could be seen as an extension to their method (Type III). It is based on the concept of de-multiplexing performed at the level of individual vantage angles and does not require data completeness in any part of the FOV.

We showed that, to evaluate data completeness, we need to make a distinction between multiplexed and non-multiplexed vantage angles and that data sufficiency is achieved if the set of non-multiplexed vantage angles satisfies Orlov's conditions. We also showed that some multiplexed vantage lines can actually be de-multiplexed and included in the set of vantage angles as if they were not multiplexed. We provided a proof for this in the ideal case where we can assume perfect pinholes without any penetration effects or for the case where all pinholes are at the same radius of rotation. In many systems, including all multiplexing systems simulated in this study, this condition is only true by approximation. Nevertheless, the simulations show

that de-multiplexing is also applicable in cases where the system slightly deviates from this condition.

We want to emphasize that the reconstruction algorithm used in this study was OSEM, without modifications. The concept of de-multiplexing is only used to evaluate data completeness, not to reconstruct the data. Other methods to reconstruct multiplexed projection data might give different results. For example, Min et al. [152] presented a reconstruction method based on an unmatched projector/backprojector pair which assigns different weighting factors to different pixels during the backprojection step, to assess the reliability of the information obtained at each pixel, depending on the pixel's degree of multiplexing. This method might be particularly interesting when relatively few pixels are multiplexed. Another reconstruction method has recently been presented by Moore et al. [159], where the algorithm estimates not only the voxel values of the reconstructed image but also the de-multiplexed (separated) projection data from each of the pinholes. This method is also applicable to systems with higher degrees of multiplexing and it successfully eliminated multiplexing artifacts with only modes noise amplification.

We also showed that although multiplexing allows us to increase sensitivity dramatically, the improvement in contrast-to-noise ratio is not that obvious. The multiplexing setups converge slower. This counteracts the increased sensitivity and as a result, we found only small differences in contrast-to-noise ratio, in the same order of magnitude as the standard deviation of the CRC (Fig. 5.16 and Fig. 5.17). The same conclusion was drawn by Mok et al. [155] in a study about the effects of object activity distribution on multiplexing multi-pinhole SPECT and by Vunckx et al. [260] who stated that increased sensitivity from multiplexing only compensates for increased ambiguity.

This is different from results obtained by Mahmood et al. [127] and Lin [119], who found a significant increase in contrast-to-noise ratio when combining multiplexed and non-multiplexed data. One difference is that in [119] and [127] the detector area was not equally covered in the multiplexed and non-multiplexed setups. In [119] there is a different coverage at the first and last bed positions and in [127] the detector is not fully covered in the non-multiplexed setup, although an approximate correction factor is used to compensate for this difference. There is insufficient proof to conclude that the higher detector coverage is the cause of the better contrast-to-noise ratio and more research is needed.

In addition, we also evaluated the NPW-SNR (Table 5.4) and found a

small improvement in the multiplexing setups, with a mean improvement of 12%. NPW-SNR is a linear observer that predicts lesion detectability and is often used in time-of-flight Position Emission Tomography (TOF PET) but has not previously been used in multiplexing SPECT articles. Therefore, we could not compare these results with any results from literature.

We thus found different results for the two different image quality metrics used. Further investigation is needed to make a more general conclusion about multiplexing and image quality. Further investigations are also needed to evaluate the effect of more advanced reconstruction techniques on the reconstructed image quality, e.g., noise regularization [76].

Although the improvement in image quality depends on the metric used and is not generally proven, we believe in the advantages of multiplexing. Multi-pinhole systems are often more advantageous than single pinhole systems, for reasons of sensitivity and angular subsampling. For an optimal usage of the detector, overlap is often unavoidable, unless loftholes [50] or internal shielding is used. We advise to use multiplexing in designs where the removal of overlap is difficult because of practical reasons, like weight, or manufacturing cost. As long as sampling completeness is fulfilled, no artifacts are to be expected.

Finally, there are certain limitations to this study. The simulations are based on ray-driven forward projections with added Poisson noise. We did not simulate scatter, depth-of-interaction, sensitivity of the detector and object dependency. Sparse objects for instance might benefit more from multiplexing, as indicated by [155]. Also, we only investigated de-multiplexing in the transverse plane. De-multiplexing vantage lines in the axial plane would require multiple bed positions at distances equal to the inter-pinhole distance, while type II multiplexing [119] is already achieved when bed positions at distances equal to 2 times the inter-pinhole distance are used.

5.3 Conclusion

In the first part of this chapter (section 5.1), we investigated the potential of time-multiplexing to increase the image quality of our previously developed stationary full-ring multi-lofthole brain SPECT system (chapter 4). We found that multiplexing can cause distortions in the reconstructed images but that these can be resolved by combining multiplexed with non-multiplexed projection data. We also found that a body support helps to speed up convergence. Unfortunately, the increased sensitivity in the time-multiplexed setup did not appear to be sufficient to make the 6 mm cold

and hot lesions visible in the hoffman phantom.

In the second part of this chapter (section 5.2), we showed that incomplete sampling is the cause of artifacts in overlapping systems and developed a method to evaluate the sampling of a system, to predict whether the system will show artifacts or not. We used computer simulated phantom data to show that more multiplexing does not necessarily result in more artifacts and that systems with a high amount of multiplexing can still result in artifact-free images if data completeness is achieved, i.e. when the set of non-multiplexed and de-multiplexed vantage angles fulfills Orlov's conditions.

We also simulated images for different overlapping systems and compared them with a non-overlapping system. The results showed that although multiplexing allows us to increase sensitivity dramatically, the improvement in contrast-to-noise ratio is not that obvious. The multiplexing setups converge slower. This counteracts the increased sensitivity and as a result, we found only small differences in contrast-to-noise ratio, in the same order of magnitude as the standard deviation of the results. We also investigated NPW-SNR, and for this task we did find an improvement: on average, the multiplexing setups showed an improvement of 12% in NPW-SNR compared to the single-pinhole setup. We also found that multiplexing can improve angular sampling and concluded that multiplexing can be a good choice for practical reasons (when shielding is difficult) and that no artifacts are to be expected as long as sampling sufficiency is obtained.

Finally, we think that more research is needed make a more general conclusion about the impact of multiplexing on image quality. It would be interesting to incorporate the activity distribution in our method in order to understand the object dependence that is reported in literature. For now, we recommend the use of multiplexing mostly for sparse activity distributions and as a way to optimize detector usage. Multiplexing can provide an alternative to other techniques, such as the use of internal shielding or loftholes [50] which have the disadvantage of extra weight and higher manufacturing complexity, respectively. As long as sampling completeness is fulfilled, no artifacts are to be expected.

5.4 Original contributions

The work presented in this chapter resulted in 2 international conference proceedings [242, 237] and a peer-reviewed publication in the peer-reviewed A1 journal *IEEE Transactions on Medical Imaging* [243].

Chapter 6

Collimator design for a multi-pinhole brain SPECT insert for MRI using high-resolution detector technologies

In chapter 4 we designed an innovative stationary multi-pinhole collimator equipped with a shutter mechanism and optimized it for a very large detector ring based on current low resolution detector technology (intrinsic resolution of 4 mm). However, despite the large detector ring and the multi-lofthole design, we achieved a sensitivity of $1.55\text{x}10^{-4}$ cps/Bq for a spatial resolution of 6 mm in the center of the FOV, which is 2.5x lower than the sensitivity of a dual-head parallel-hole system with a spatial resolution of 9.8 mm. Simulations showed an improvement in contrast-to-noise ratio and lesion detectability for hot lesions, but not for cold lesions.

Therefore, in chapter 5, we investigated the potential of using multiplexing to increase sensitivity. However, although we determined how to obtain artifact-free images with a multiplexing system and were able to increase sensitivity, the improvement in contrast-to-noise ratio was not that obvious. The multiplexing setups appeared to converge slower. This counteracts the increased sensitivity and as a result, we found only small differences (in the same range as the standard deviation) in contrast-to-noise ratio.

In this chapter, we therefore decided to follow an other approach, based

on high-resolution detector technologies which, in the meantime, became commercially available (see also section 2.1.2.1) and to focus on MR-compatibility. In our research group, we developed a high-resolution (0.5 mm) detector based on a 2 mm thick LYSO crystal with digital (and MR-compatible) readout using dSiPMs (digital silicon photomultipliers) [69][23]. dSiPMs have the advantage of being very compact and being MR-compatible. In this chapter we exhibit the good intrinsic detector resolution for optimizing and simulating a compact brain SPECT system that can be used as an insert for MRI.

6.1 Introduction

Combining SPECT with MRI has many advantages. Firstly, MRI provides superior soft-tissue contrast to CT, which is important in brain imaging as the brain consists mainly of cerebro-spinal fluid and white and gray matter. Secondly, MRI does not involve any radiation dose like CT. Moreover, if both modalities could be fully integrated, it would increase patient throughput and reduce total patient examination time.

However, as we explained in section 2.3.2, integrating SPECT with MRI is also very challenging and until now, research on SPECT/MRI has been mostly focussing on detector compatibility and on preclinical system design (for imaging small animals) (section 2.3.3). In this chapter, we focus on the challenge of (i) finding a suitable collimator material and (ii) making the collimator stationary and compact. Currently, brain SPECT imaging is mostly performed with dual- or triple-head gamma cameras with parallel-hole or fan-beam collimators, which are bulky and would not fit inside the bore of an MRI. They also rely on rotation to acquire images at different projection angles, which would disturb the homogeneous B_0 field of the MR.

We suggest to solve these issues by designing a compact stationary SPECT insert based on high-resolution dSPM detectors and a minifying multi-pinhole collimator manufactured with additive manufacturing.

Firstly (in section 6.2), we show that tungsten collimators produced through additive manufacturing have interesting properties and have the potential of being MR-compatible. Secondly (in section 6.3), we will describe the general design of a collimator and detector ring that would fit in a clinical MRI. In traditional multi-pinhole systems (based on low-resolution detectors), the detector is placed relatively far from the pinholes in order to produce a magnified image of the object on the detector. By using a high-resolution detector, we do not need as much magnification [196] and we

can place the detector close to the pinholes, so that the pinholes generate a minifying projection of the FOV (Fig. 3.3). This allows the system to be compact so that we can fit the complete SPECT system in a clinical MRI. As explained in section 3.1.1.3, a minifying pinhole collimator also allows more projections on the detector, which makes it possible to obtain more angular projections simultaneously [250] so that we can achieve complete transverse sampling with a full-ring multi-pinhole tungsten collimator without rotating the camera. We also extend the optimization method from chapter 4 to jointly optimize the collimator and detector ring in order to maximize the volume sensitivity for a target resolution of 7.2 mm in the center of the brain. Although 7.2 mm is larger than the 6 mm target resolution used in chapter 4, it is still smaller than the resolution of most clinical systems (8-10 mm). 7.2 mm is the resolution that can be obtained with a triple-head SPECT camera equipped with ultra-high-resolution fan-beam collimators (UHR FAN) and choosing the same target resolution allows us to easily compare both systems. Finally (in section 6.4), we will simulate and reconstruct both noiseless and noisy phantom data to assess reconstructed spatial resolution and angular sampling and we will compare image quality with the UHR fan-beam system.

6.2 MR-compatibility of the collimator

One of the problems in SPECT/MRI is distortion of the static magnetic field or the gradient fields due to the presence of the SPECT collimator, which is typically made of lead or tungsten. Pure lead has a low susceptibility and conductivity and has shown to be MR-compatible [223] but the density of lead is only 11.34 g/cm^3. This is sufficient for parallel-hole or fan-beam collimators, but in pinholes, this results in high edge penetration and poor resolution. Therefore, pinhole collimators are usually made of tungsten, which has a much higher density (19.25 g/cm^3) but is also very brittle and difficult to machine. Tungsten alloys solve the issue of brittleness but they often contain ferromagnetic components and are therefore not MR-compatible.

In this section, we start with a characterization of the material properties (density and electrical resistivity) of printed tungsten, followed by an investigation of eddy currents in a prototype collimator with simulations and measurements. Printed tungsten is obtained through additive manufacturing, which is a novel production technique based on melting pure tungsten powder as explained in section 3.2. Pure tungsten is paramagnetic and has

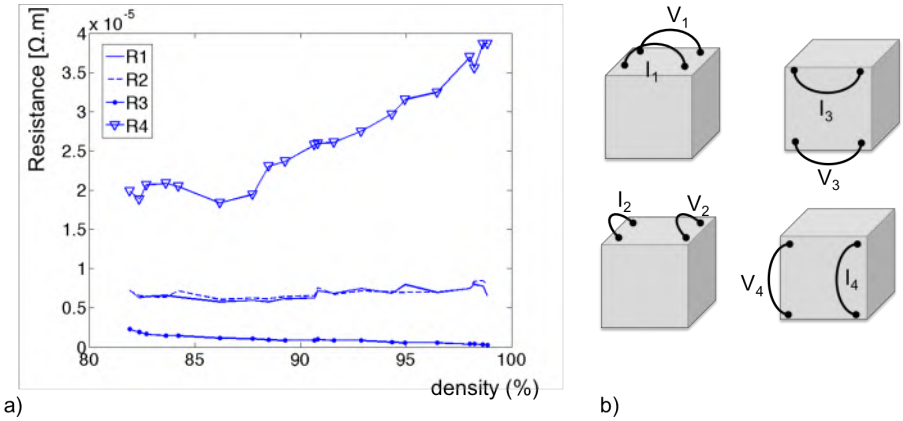

Figure 6.1: (a) Resistance in function of density in four directions as depicted on the right (b) Resistance measurement setup

an electrical resistivity of 52.8 nΩm, which is rather high (e.g. copper has an electrical resistivity of 17.1 nΩm) and as we explained in section 2.3.2.2, a high electrical resistivity is important in order to keep eddy currents as low as possible. The electrical resistivity of printed tungsten is expected to be even higher (as small air gaps often remain between the melted powder particles).

The work in this section was performed in the context of the SIMRET project, which aims at building a preclinical SPECT/MRI insert. Therefore, the measurements were performed on a preclinical 7T MRI and the simulations were performed for a preclinical SPECT collimator ring.

6.2.1 Electrical resistivity of printed tungsten

6.2.1.1 Materials and methods

In section 3.2 we explained that additive manufacturing is based on the process of melting tungsten powder layer by layer using a laser beam. By adapting the strength of this laser beam, the laser spot size and/or changing the duration of the melting process at each position, it is possible to produce collimators with a lower/higher density.

In this section, we determine the density and resistivity of 20 cubic samples, produced with different settings. As the material is built up layer by

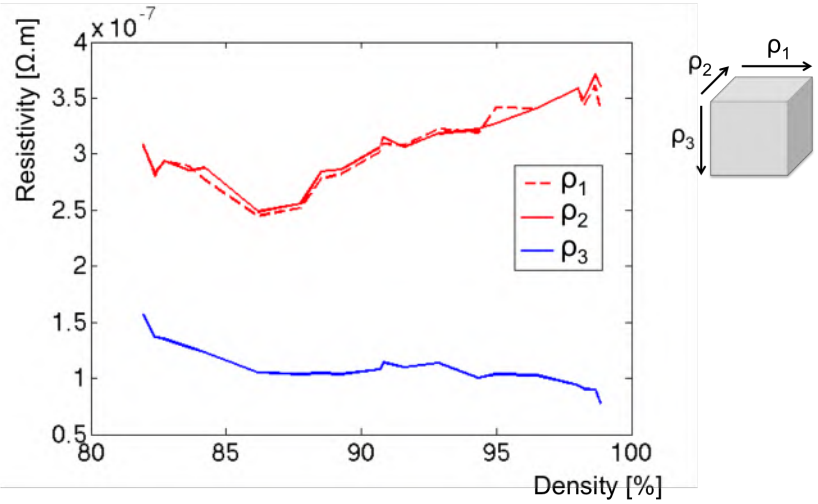

Figure 6.2: Resistivity as a function of density for three directions: ρ_1 is the direction perpendicular to the layers and ρ_2 and ρ_3 are the directions parallel to the layers

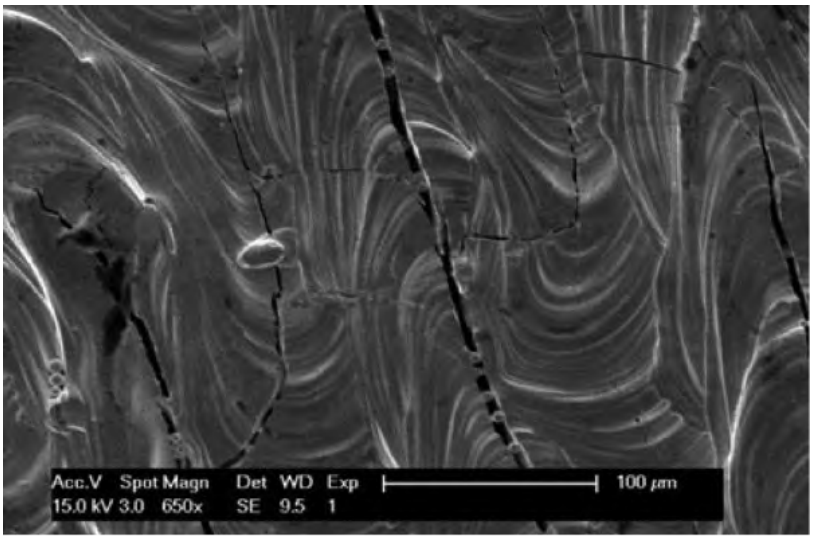

Figure 6.3: Micro-cracks (LayerWise)

layer, we expect the resistivity to be different for directions parallel and perpendicular to the layers. Therefore, we determined resistivity in three directions. For this, we performed resistance measurements along different axes (Fig. 6.1b) with a four-point probe low resistance meter Keithley 6220/2182, which has a precision of 10 nΩ. The resistivity was then computed using the Montgomery [157] method, which is particularly suited for small anisotropic samples. In order to determine resistivity in all directions, Montgomery requires only 3 resistance measurements, but we performed 4 (Fig. 6.1b) in order to have two sets of 3 resistance values and we averaged the two results.

The Montgomery method is based on (i) Wasscher's transformation method [265] to map an anisotropic solid rectangular prism with dimensions l'_1, l'_2 and l'_3 to an equivalent isotropic solid with dimensions l_1, l_2 and l_3, based on resistance ratios R_1, R_2 and R_3 and (ii) relating the resistivity of this isotropic sample with the measured resistance measurements based on the formulae $\rho_1 = H_1 E R_1$, $\rho_2 = H_2 E R_2$ and $\rho_3 = H_3 E R_3$, where E is an effective thickness and H is associated with the isotropic axes length ratios, which can be computed using the series given in [124].

6.2.1.2 Results

The measured resistance values are shown in Figure 6.1a and then converted to resistivity values. Figure 6.2 shows that the resistivity was highest in the direction parallel to the layers (310 to 360 nΩ.m) and lowest in the direction perpendicular to the layers (158 to 78 nΩ.m). The higher resistivity in the parallel layers can be explained by the long micro-cracks in these layers (Fig. 6.3), which are a result of the high temperature that is needed to melt the tungsten powder and the fast cooling down afterwards. The micro-cracks also explain why it is challenging to achieve a density of 100%: the stronger the laser, the higher the density should theoretically be, but the higher the risk for micro-cracks. These micro-cracks are usually not desired as they decrease the strength of the material, but in the context of MR-compatibility and decreasing eddy currents they appear to be advantageous and help to increase resistivity.

In conclusion, all resistivity values are higher than the resistivity of solid tungsten (56 nΩ.m), which is in line with what we expected.

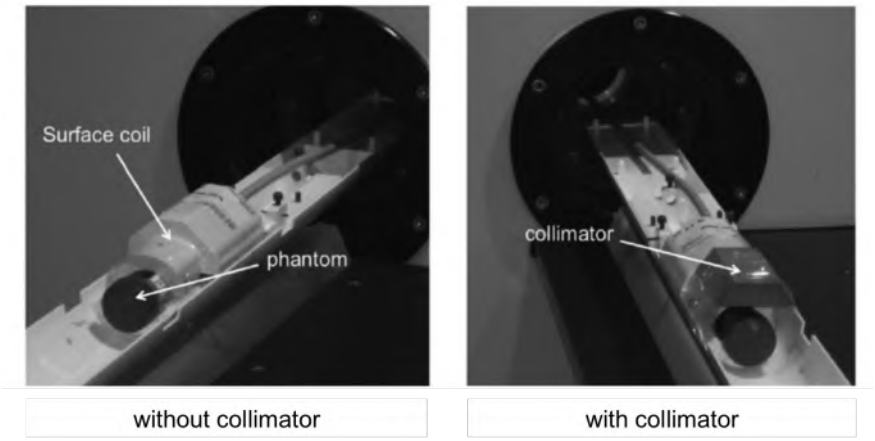

Figure 6.4: Measuring a uniform phantom in a 7T MRI with and without collimator.

6.2.2 MR-compatibility measurements single collimator

6.2.2.1 Materials and methods

In the previous section we showed that the tungsten material has a high resistivity value, which should result in small eddy currents, as explained in section 2.3.2.2 and therefore, we expect the material to be MR-compatible. In this section, we verify this by evaluating distortions in a uniform water phantom when a prototype preclinical collimator [22] is placed inside the MR bore of a 7T Bruker Pharmascan 70/16. The collimator was produced using additive manufacturing and had a density of 17.31$\pm$ 0.10 g/cm^3 (89.92 $\pm$ 0.05 % of pure tungsten). We recorded T1, T2 and T2* images using a RARE , FLASH -T2 and FLASH -T2* sequence, respectively, and using a volume transmit coil (Part No. T1123V3) and a rat brain surface receive coil (Part No. T11425V3). We acquired images with and without the collimator on top of the receiver coil (Fig. 6.4) and compared them based on their line profile.

We also investigated the effect of shimming, which is the adjustment of the magnetic field in case of inhomogeneities (e.g. due to the presence of a ferro-magnetic material), as explained in section 2.3.2.1. We measured the effect of shimming on a uniform phantom scanned with an EPI sequence with and without collimator inside a volume transmit/receive coil (Part No. T1123V3). We used EPI because the sequence is T2* based and typically

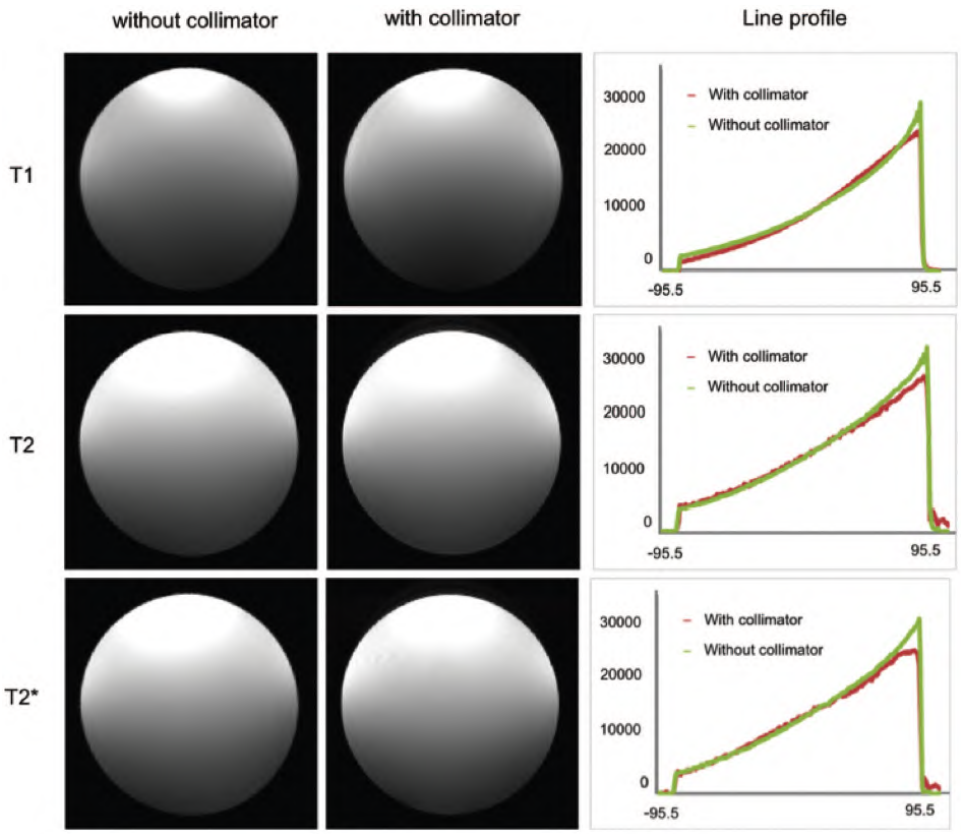

Figure 6.5: Images and line profiles of a uniform phantom with and without collimator.

very sensitive to changes in the magnetic field. Firstly, we measured without the collimator. Secondly, we measured with the collimator and lastly, we performed shimming before measuring again with the collimator using the Bruker second order local MAPSHIM, which is based on the minimization of the B_0 field map variation.

6.2.2.2 Results

The resulting T1, T2 and T2* images of the uniform phantom are shown in Fig. 6.5. The decrease in sensitivity (in the vertical direction) is due to the properties of the receiver coil (which is a surface coil) and is normal. The deviation due to the presence of the collimator is best observed in the

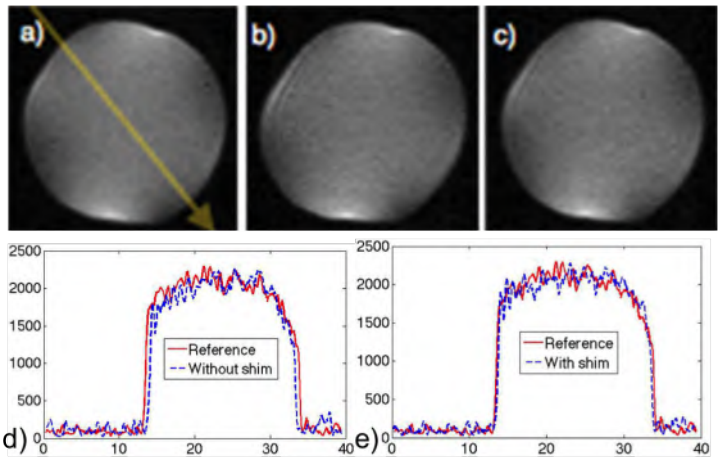

Figure 6.6: EPI image of a uniform phantom a) reference image b) with collimator, no shimming c) with collimator, auto-shim (d,e) line profiles

line profiles. The differences are very limited except for the T2* sequence, which is typically more sensitive to disturbances. In the next section we will show how we can improve this with shimming.

The effect of shimming is shown in Fig. 6.6. A small image deformation (squeezing) can be noticed when the collimator is inserted in the bore (Fig 6.6d). This deformation can be almost completely removed by shimming after inserting the collimator in the bore (Fig 6.6e).

6.2.3 MR-compatibility simulations full-ring collimator

The results from the measurements were promising, but these measurements are for a single collimator element, while the final system consists of five collimator elements, forming a full ring, similar to our collimator ring described in section 6.3.4. As the production of such a full ring is expensive, we investigated the full-ring design based on simulations. In the next sections, we will first describe the numerical model used for the simulations and its validation and then use it to predict the magnetic field caused by eddy currents in the full collimator ring. Finally, we investigate whether we can further reduce eddy currents by leaving small air gaps between neighboring collimators in the collimator ring.

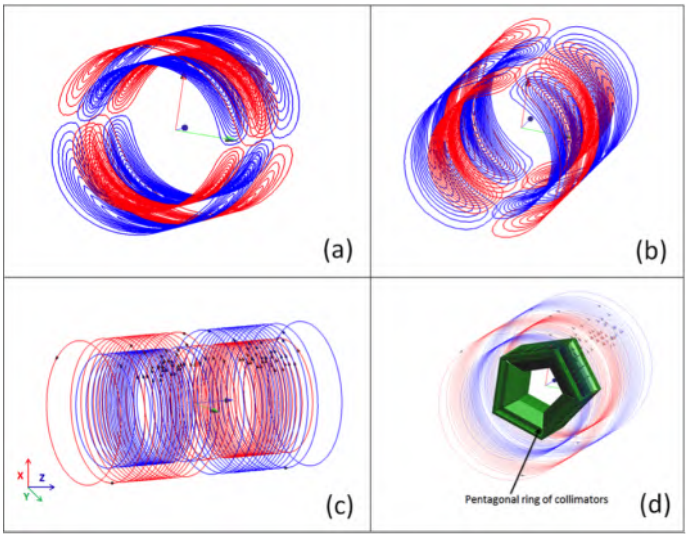

Figure 6.7: Wire patterns for (a) X-gradient coil. (b) Y-gradient coil and(c) Z-gradient coil. (d) Pentagonal ring of collimators centered inside the z-gradient coil. Red and blue colors are used to indicate wires in which there is a different sense of current flow [205].

6.2.3.1 Materials and methods

We performed simulations of the induced magnetic field for a ring of tungsten collimators (produced through additive manufacturing) using FEKO [1], a 3D full-wave electromagnetic simulation platform. FEKO uses the Method of Moments (MoM) that provides full wave solutions of Maxwell's integral equations in the frequency domain. We activated the low-frequency stabilization and we used the Volume Equivalence Principle (VEP) for mesh-

	X coil	Y coil	Z coil
Inner diameter (mm)	100	100	100
Outer diameter (mm)	126	126	126
Length	293	293	232
Gradient strength (mT/m)	500	500	500
Gradient efficiency (mT/m/A)	2.99	2.99	3.08
Applied current (A)	167.24	167.24	162.33

Table 6.1: Parameters of the transverse and the longitudinal gradient coils.

Figure 6.8: A Z-shaped gap, used to electrically isolate two collimator pieces from each other without allowing gamma rays to penetrate the collimator.

ing the collimator.

Table 6.1 lists the properties of the x-, y-, and a z-gradient coils that were used and Fig. 6.7 shows their configuration. We simulated a gradient with a sinusoidal ramp from 500 mT/m to 0 mT/m within 0.25 ms. In FEKO, this was implemented by performing a broadband simulation from 0 to 10 kHz with a step size of 400 Hz covering the full frequency range of the gradient, which was obtained using a fast Fourier transform of the sinusoidal ramp. The output of the simulation was then postprocessed with FEKO's time analysis tool to extract the time response of the system. The collimator was modeled based on the CAD file that was used to produce it and using ρ =108 nΩ.m as material conductivity value. In section 6.2.1 we showed that the material has a different resistivity along the transverse (ρ_t=292 nΩ.m) and the longitudinal (ρ_l=108 nΩ.m) direction. As FEKO does not support anisotropic resistivity distribution and as eddy currents increase with the material conductivity, we cover the strongest eddy currents (worst-case scenario) by taking the lowest of the two values.

Additionally, we also investigated the effect of having small air gaps between the individual collimators in the pentagonal ring such that they were electrically isolated from each other. This prevents eddy currents from flowing through the ring. We chose to make the gaps z-shaped (Fig. 6.8) in order to prevent gamma rays from penetrating the gaps, which would disturb the collimator's functioning.

The magnetic field due to eddy currents was calculated by subtracting the magnetic induction of the gradient coils without collimator (B) from the magnetic induction of the gradient coils with the collimator (B^{col}). We then calculated the maximum value within the FOV (a sphere with a diameter of 3 cm).

This study was performed in collaboration with WiCa (University Ghent), where Samoudi A. M. is doing a PhD on induced eddy currents. Samoudi A. M. performed the simulations and we validated the numerical model and performed all measurements.

6.2.3.1.1 Validation of the numerical model To validate the simulations, we performed measurements on a 7T preclinical MRI from Bruker with a volume coil (Part No. T1123V3) and a rat brain surface receiver coil (Part No. T11425V3). For the validation, we used a 25x10x40 mm^3 block of lead, because pure lead has an isotropic resistivity value (186.43 nΩ.m), which can be perfectly modeled in FEKO. The block was inserted in the MR bore (at position x=20.5, y=0, and z=2 mm, on top of the receiver coil) together with a spherical phantom with an inner diameter of 12.24 mm, filled with $CuSO_4$ (1g/L) in H_2O (CAS nr: 7758-99-8) with an electrical conductivity of 0.057 S/m. Measurements were performed with the phantom positioned at different locations along the z-axis (x=0.35 and y=0.23 mm). We applied a z-gradient with a peak value of 119.35 mT/m (applied for 500 ms) and a sinusoidal ramp up and down (both with duration of 248 μs). Immediately after the ramp-down, we acquired the free induction decay (FID) signal, whose phase relates to the magnetization as follows:

$$\phi(t) = \gamma \int_0^t B_e(t')dt' + \phi_0, \tag{6.1}$$

with ϕ(t) the phase of the FID, γ the gyromagnetic ratio (267.513 rad/s/T for protons), B_e the magnetic field induced by the eddy currents in the lead block and ϕ_0 a constant phase offset due to main field inhomogeneities. To cancel out the constant offset, we acquire the FID after both a positive and a negative gradient:

$$\phi_T(t) = \frac{\phi_+(t) - \phi_-(t)}{2} = \gamma \int_0^t B_e(t')dt' \tag{6.2}$$

The magnetic field due to eddy currents was then retrieved by differentiating the phase:

$$B_e(t) = \frac{1}{\gamma}\frac{d\phi_T(t)}{dt} \tag{6.3}$$

We performed these measurements both with and without the lead block inside the MRI and for different locations of the phantom. We did not modify the pre-emphasis settings of the MRI system.

For the simulations, the phantom was modeled as a sphere of diameter 12.24 mm with electrical conductivity of the $CuSO_4$-$5H_2O$, σ= 0.057 S/m and the lead block was modeled as a cuboid with electrical resistivity ρ = 186.43 nΩ.m. The RF coil was modeled as a half cylinder (central axis =

z-axis, diameter = 37.5 mm, height = 80 mm, thickness = 5 mm) with a perfect electric conductor (PEC) medium (a zero-resistance conductor). The simulated gradient ramp has a sinusoidal shape with a ramp-down time of 248 μs and a gradient strength G = 119.35 mT/m to match the gradient applied in measurements. To determine the magnetic field due to eddy currents from the simulations, we first extracted the z-component of the magnetic induction B from both simulations (with and without the Pb block) and secondly we compared the two components to quantify the added magnetic field due to the lead insertion.

Figure 6.9(a) shows the average value (over a sphere of radius 1 mm, centered at (0.345, 0.23, 2.8) mm) of the magnetic field due to eddy currents for both simulations and measurements. Figure 6.9(b) shows the difference between measurements and simulations compared to the applied gradient field. The maximum variation between measurement and simulation was less than 1% of the applied gradient field. Results show that the model used in simulations is coherent with measurements of the lead block.

6.2.3.2 Results

Figure 6.10 shows the magnetic induction due to eddy currents (B_e) as a percentage of the applied gradient field for longitudinal and transverse gradient coils. The maximum value of the induced magnetic field is 4.66 % and 0.87 % of the applied gradient field (gradient strength = 500 mT/m) for the longitudinal and transverse gradient coils, respectively. The applied gradient field is determined at the point in space where the eddy current is being calculated. We observe that the transverse coils induce less eddy currents than the longitudinal coils. This is due to the wire distribution of the two types of coils and the collimators' position inside the coils.

Finally, having small gaps between the individual collimators in the pentagonal ring resulted in an important decrease in eddy currents, i.e. the maximum value of the induced magnetic field reduced from 4.66 % to 1.13 % of the applied gradient field for the longitudinal gradient coils and from 0.87 % to 0.43 % of the applied gradient field for the transverse gradient coils.

6.2.4 Discussion

We performed measurements and simulations to investigate the compatibility of a full-ring preclinical SPECT collimator with a 7T preclinical MRI.

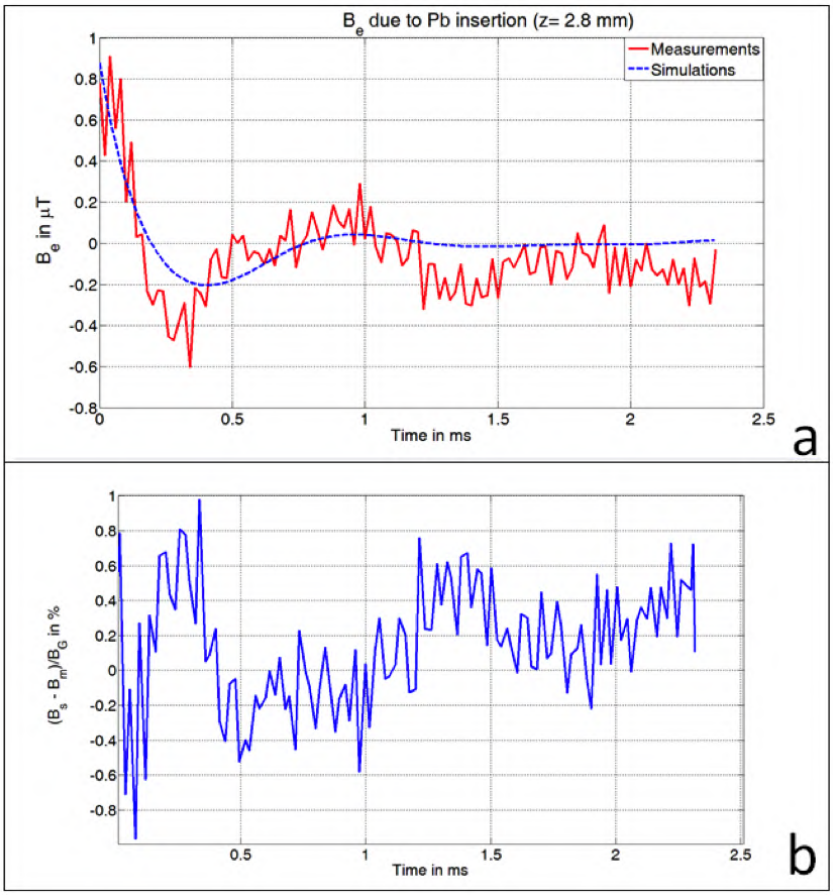

Figure 6.9: Validation of the simulation using the Pb block (a) Measured and simulated magnetic induction due to eddy currents B_e. The phantom is positioned at (0.345, 0.23, 2.8) mm (b) Difference between measured and simulated induced field due to Pb insertion, compared to the applied gradient field. B_s,B_m, and B_G stand for simulated, measured and applied magnetic induction, respectively [205].

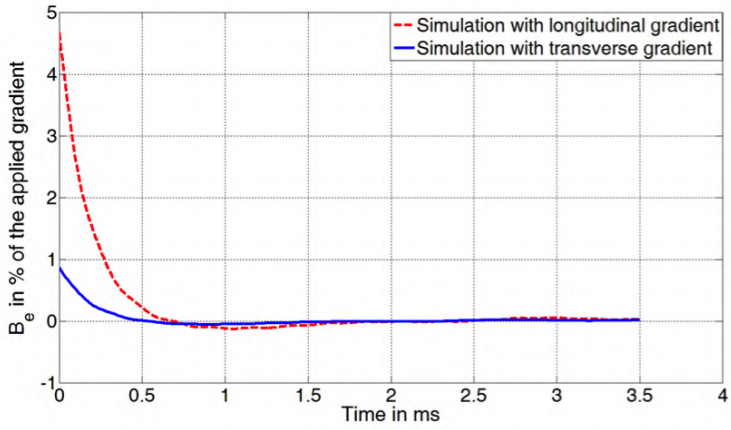

Figure 6.10: B_e in % of the applied gradient field of 500 mT/m for both the longitudinal and the transverse gradient coils in a FOV of 3 cm, after switching off the gradient field [205].

We found that the printed tungsten material (obtained through additive manufacturing) has a higher resistivity than pure tungsten and that it is anisotropic. As a result of this high resistivity, the eddy currents are expected to be limited, which is confirmed by measurements with a prototype collimator piece. Finally, we also performed simulations to investigate the influence of a full-ring collimator (composed of five pieces) and we found a deviation of 4.66% and 0.87 % on the MR gradient fields in longitudinal and transverse directions, respectively. This was later reduced to 1.13% and 0.43 %, respectively, by adding gaps between the collimator pieces, which prevents eddy currents from flowing in the ring.

These deviations (1.13% and 0.43 %) are lower than in a single collimator element, for which we verified that image distortions were sufficiently limited in section 6.2.2. Therefore, we conclude that no eddy-current related interferences should be expected.

6.3 Multi-pinhole system design and optimization

In the previous section, we showed that printed tungsten is a promising material for building an MR-compatible collimator ring, so that in this section we can focus on designing the actual system. Fig. 6.11 illustrates the general design of the SPECT insert that we propose. It is inspired by existing

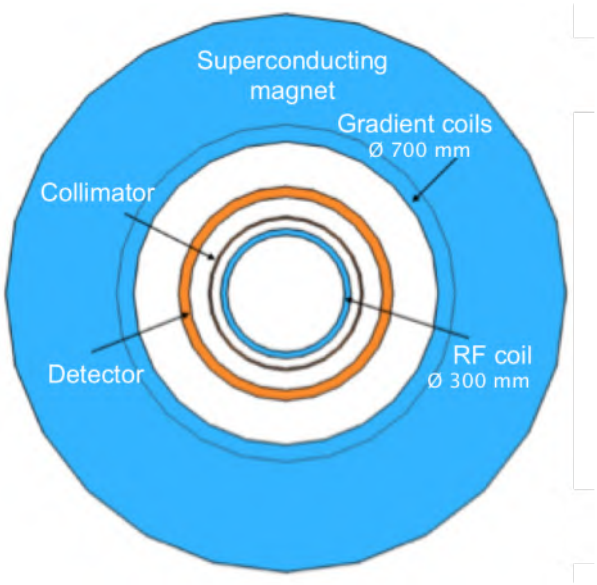

Figure 6.11: Configuration of the SPECT system (collimator and detector) inside the MRI, between the RF coil and the gradient coils. The RF coil is both a transmitter and receiver (Tx/Rx) and its dimensions are based on an 8 channel Rx/Tx head coil (Fig. 2.12(b)).

small-animal SPECT/MRI inserts [29, 27] and consists of a detector ring and a cylindrical multi-pinhole collimator. The insert fits within the MR bore and is positioned between the gradient coils and the Tx/Rx coil, which should be close to the patient's head for optimal performance.

6.3.1 Detector design

The detector geometry is cylindrical, based on dSiPM detector modules of 32x32 mm^2 (Fig. 6.12(c)). The detector modules have shown to be MR-compatible [267] and have an excellent intrinsic resolution (0.5 mm) and an energy resolution of 20% (at 140 keV) when combined with a monolithic 2 mm thick LYSO crystal [23]. Excellent spatial resolution makes it possible to design a multi-pinhole system with minification, which is needed to acquire sufficient angular sampling without rotating the system. An additional advantage of dSiPM detectors is their compactness. They don't require bulky circuit boards for readout, in contrast to analog SiPMs or semiconductor detectors (like CZT). In addition, LYSO has a high stopping power, which

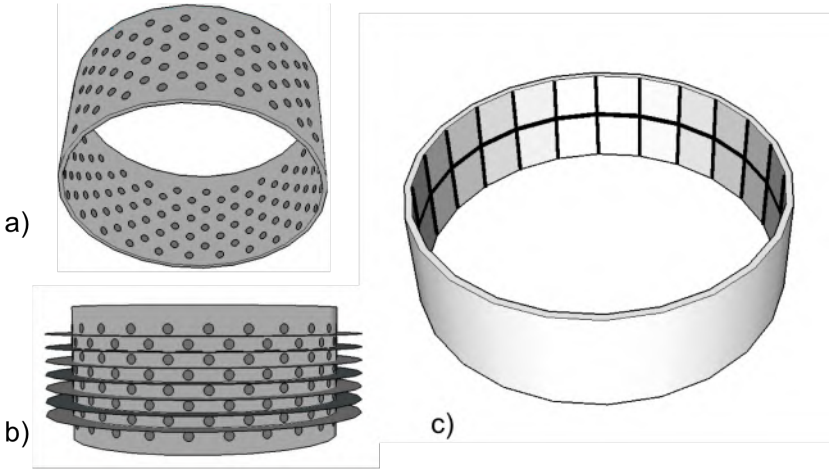

Figure 6.12: (a) Detail of the collimator (b) Collimator with tungsten slats to separate projections in axial direction (c) Detector ring composed of 32x32 mm^2 detector components with a small gap between them.

results in a higher detection efficiency compared to a CZT or CdTe detector with a similar spatial resolution. For example, the CdTe detector used in the MRC-SPECT system [29] achieves a sub-0.5 mm spatial resolution using 350 μm x 350 μm x 2 mm pixels, which results in a detector efficiency of maximally 47% [224], while the detection efficiency of an LYSO-based detector can be 73.5%. Therefore, and based on the promising results in [23], we decided to continue with the dSiPM detector modules.

Measurements showed that, while the modules have a size of 32x32 mm^2, only 30x30 mm^2 can be used for correctly positioning the detected events. This causes gaps in the detector ring (Fig. 6.12(c)), which could introduce artifacts. To investigate this, we also modeled the gaps in the simulation study. The radius of the detector ring is optimized in paragraph 6.3.3.

6.3.2 Collimator design

Fig. 6.13, Fig. 6.12(a) and Fig. 6.12(b) show the collimator in more detail.

All pinholes view the complete transverse FOV without allowing overlap of the pinhole projections.

We don't need to use truncating pinholes like in chapter 4 because the collimator is further away from the edge of the FOV (due to the MRI coil around the patient's head), which results in a decreased pinhole opening

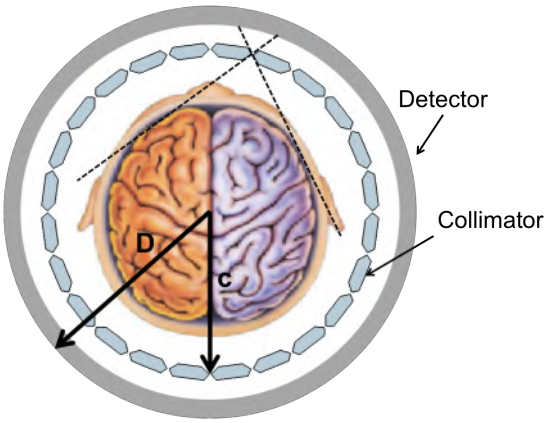

Figure 6.13: A transverse slice of the SPECT system with collimator radius c and detector radius D.

angle and a pinhole penetration ratio comparable to what is common in preclinical multi-pinhole systems. We also don't need to use loftholes for better detector coverage like in chapter 4 because the projections don't require cut-off in the transverse direction (as the edge of the projection corresponds to the edge of the phantom) and because of the tungsten slats cutting off the pinhole projections in the axial direction. Although loftholes would result in slightly decreased penetration, we decided to simplify the design and use pinholes in this feasibility study as they are easier to simulate. The pinholes are positioned on rings that are separated by tungsten slats (5 mm thick) to avoid overlap of pinhole projections in the axial direction. We chose to use 8 rings as a compromise between axial sampling and loss of sensitivity due to the axial slats and the rings are rotated relative to one another to improve angular sampling. Simulations will show that 8 rings are sufficient for this design.

6.3.3 System optimization

It is our goal to optimize the SPECT insert to achieve the highest possible sensitivity while the total detector surface area is fixed and the system spatial resolution matches the current state-of-the-art. We chose a detector surface area of 1393 cm^2 (136 dSiPMs), which corresponds to the area that is maximally irradiated when a human brain is scanned on the clinical triple-head PRISM XP 3000 with a fan-beam collimator, and a spatial resolution

of 7.2 mm in the center of the FOV, which is comparable to the resolution of the UHR fan-beam system. We assume the FOV to be cylindrical with a diameter of 220 mm and an axial length of 124 mm which is representative for an adult human brain [75]. We included 6 design parameters in the optimization study: the detector radius D, the collimator radius c, the pinhole diameter d, the pinhole opening angle α, the number of pinholes per ring N_p and the detector length L_D. Other parameters are collimator material thickness t, pinhole position, pinhole tilt and detector length. To simplify the collimator design, all the pinholes have the same aperture diameter, opening angle and tilt. These pinholes all view the complete transverse FOV without allowing overlap of the pinhole projections, are not tilted in the axial direction and all focus on the center in the transverse direction. The collimator thickness is 5 mm. The axial length of the detector depends on D and the fixed detector surface area.

We used the same analytical optimization process that was previously described in chapter 4, except that we now also optimized the detector radius D:

- Loop over all values of D (between 150-350 mm, respectively the outer radius of an 8 channel Tx/Rx head coil and the gradient inner diameter of a clinical MRI)
- Loop over all values of c (between 150 mm and D)
- For each combination of c and D:
  - Determine the number of pinholes per ring (N_p) and their opening angle (α) using the geometrical relationship that follows from the fact that all pinholes view the complete transverse FOV without allowing overlap of the pinhole projections.
  - Derive the pinhole diameter d needed to achieve the target resolution in the center of the FOV, using the formulae presented by [12] and [7]
  - Determine the axial length of the detector ring by dividing the fixed detector surface area (1393 cm^2) by the circumference of the detector ring ($2\pi D$).
  - Calculate volume sensitivity
- Determine the volume sensitivity for each combination of c and D and find the maximum.

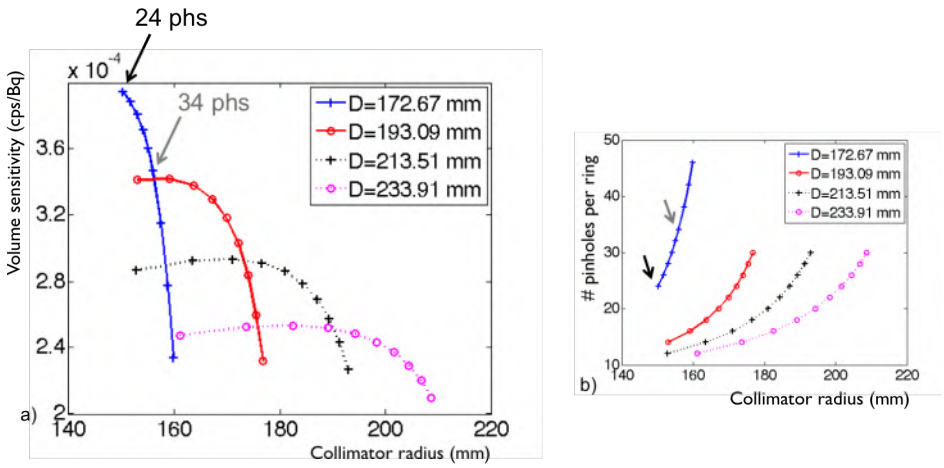

Figure 6.14: (a) Volume sensitivity as a function of the collimator and detector radius (b) Number of pinholes that can be placed in one ring on the collimator, given a certain collimator and detector radius. The arrows indicate which points of the curve correspond to the 24-pinhole and 34-pinhole setup used during the simulations.

To simplify the optimization, we approximated the detector to a perfect ring (instead of a polygon composed of flat detectors).

6.3.4 Optimization results

Fig. 6.14(a) shows the result of the optimization process: the volume sensitivity is plotted as a function of the collimator radius and for different detector radii. The volume sensitivity is maximized for a collimator radius of 150.2 mm and a detector radius of 172.67 mm, which corresponds to 4 rings of 34 dSiPMs. For these parameters, 24 pinholes (phs) with an opening angle of 95 ° can be placed in one ring without having any overlap between the pinhole projections (Fig. 6.14(b)). The pinhole diameter needed to achieve the target resolution of 7.5 mm is 0.62 mm. We used 8 rings of 24 pinholes (phs) for sufficient axial sampling. The rings are rotated relative to one another to improve angular sampling. The first ring has pinholes at 0 °, 15 °, 30 °, 45 °, 60 °, ... The second ring has pinholes at 7.5 °, 22.5 °, 37.5 °, 52.5 °, ... The third ring has again pinholes at 0 °, 15 °, 30 °, 45 °, 60 °, ...

Although the 24-pinhole setup has the highest sensitivity, we wanted to

compare the system with another setup having more pinholes and thus better angular sampling. Therefore, we selected a second setup with more pinholes per ring at the cost of a slightly decreased sensitivity. The second setup has the same detector radius of 172.67 mm but a collimator radius of 156.63 mm so that 34 pinholes with an opening angle of 92.6 ° can be placed in one ring without having any overlap between the pinhole projections (Fig. 6.14(b)). The pinhole diameter needed to achieve the target resolution of 7.5 mm is 0.34 mm. Again, we use 8 rings of pinholes for sufficient axial sampling. The first ring has pinholes at 0 °, 10.59 °, 21.18 °, 31.76 °, 42.35 °, ... The second ring has pinholes at 5.29 °, 15.88 °, 26.47 °, 37.06 °, ... The third ring has again pinholes at 0 °, 10.59 °, 21.18 °, 31.76 °, 42.35 °, ...

The volume sensitivity of the 24- and 34-pinhole systems are 3.95x10^{-4} and 3.45x10^{-4} cps/Bq, respectively.

6.3.5 Discussion

Fig. 6.14(a) depicts the result of the optimization study, which shows that the sensitivity is generally higher for a detector with a smaller radius (and thus longer axial length) compared to a detector with a larger radius (and thus a shorter axial length). For a fixed collimator radius, a smaller detector radius corresponds to more minification and consequently more pinhole projections can be used to fill the detector area, resulting in increased sensitivity. However, when there is too much minification, the sensitivity drops fast (as we can see in the last points of the curve corresponding to D=172.67). The reason for this drop is that at high minification, the pinhole apertures need to be extremely small in order to achieve the target resolution, which results in reduced sensitivity. We found that volume sensitivity is maximized for a detector radius of 172.67 mm, which corresponds to 4 rings of 34 detectors. Further decreasing the detector radius would result in such a high degree of minification that the target resolution of 7.2 mm can no longer be achieved.

Fig. 6.14(a) also shows that the highest volume sensitivity is obtained with a collimator radius of 150.2 mm. Further reducing the collimator radius is not possible as the Tx/Rx MR coil still needs to fit within it.

6.4 Phantom simulations

After optimizing the design, we simulated and reconstructed phantom data to evaluate system performance. Firstly, we evaluated spatial resolution and sampling sufficiency in two different multi-pinhole designs (one with

more pinholes than the other). Therefore, we simulated and reconstructed noiseless projection data of three phantoms, namely a cold-rod phantom (Fig. 6.15(a)), a Defrise phantom (Fig. 6.16(a)) and a contrast phantom (Fig. 6.15(d)). Secondly, we compared the multi-pinhole SPECT insert with a clinical triple-head fan-beam system. Therefore, we simulated noisy data of the contrast phantom and evaluated the contrast-to-noise ratio (CNR) in both systems. Finally, we also simulated and reconstructed noisy projection data of a Hoffman phantom (Fig. 6.19(a)) to represent a more clinically relevant situation and compared the images visually.

6.4.1 Noiseless simulations

All noiseless projection data were simulated using the GPU-based pixel-driven forward projector [98] that was previously described in section 2.1.3.1.1. We used 456 rays to model the finite dimension of the pinhole opening and used an effective pinhole diameter [7] to model pinhole penetration. The phantoms were modeled using a grid with 240x240x240 voxels of 1x1x1 mm^3 and each detector was modeled using 300x300 pixels of 0.1x0.1 mm^2. This results in an active detector area of 30x30 mm^2 and 2 mm gaps between the detectors. After the simulation, we applied a Gaussian blur of 0.5 mm full-width at half-maximum (FWHM) to the projection data to model the intrinsic resolution of the detector and then rebinned the projection data to a Pixel size of 0.5x0.5 mm^2 . Attenuation was modeled analytically based on the assumption that the phantoms are made of Polymethyl methacrylate (PMMA) and filled with water. No scatter was modeled.

6.4.2 Noisy simulations

Noisy simulations were performed using the Monte Carlo simulator GATE version 6.1 (GATE: Geant4 Application for Tomographic Emission) [92]. Monte Carlo simulations were first described in section 2.1.3.2 and we chose GATE because it is specifically designed for nuclear medicine applications, well validated and because a lot of experience with GATE exists in our group [19, 220, 71]. We simulated phantoms filled with 111MBq of Tc-99m and an acquisition time of 30 minutes. The simulation incorporated the full-ring multi-pinhole collimator, the scintillator material (for modeling the stopping power), the detector's intrinsic spatial resolution, the detector's energy resolution and the gaps. Again, the pixel size was rebinned to 0.5x0.5 mm^2 pixels after applying a Gaussian blur to model the intrinsic resolution of the

detector. Scatter and attenuation were modeled based on the assumption that the phantoms are made of PMMA and filled with water. We performed the noisy simulations both for the multi-pinhole SPECT insert and for a clinical fan-beam system.

6.4.3 Phantoms

All phantoms had a cylindrical shape with a diameter of 220 mm and a length of 124 mm.

6.4.3.1 Cold-rod phantom

The cold-rod phantom was used to evaluate the reconstructed spatial resolution of the SPECT insert. The phantom contains 6 segments with rods with diameters of 10, 8, 6.5, 5, 4 and 2 mm. The distance between the cold rods is twice their diameter (Fig. 6.15(a)).

6.4.3.2 Defrise phantom

A Defrise phantom was used to evaluate the axial sampling. It consists of 8 mm-thick disks with a pitch of 8 mm (Fig. 6.16(a)).

6.4.3.3 Contrast phantom

The contrast phantom was used to evaluate contrast-to-noise as a measure of image quality. It has 4 hot rods (uptake ratio 7:1 and diameters of 6, 8, 10 and 12 mm) and 2 cold rods (diameters of 14 and 16 mm) positioned on a circumferential ring of radius 54.5 mm (Fig. 6.15(d)).

6.4.3.4 Hoffman phantom

Finally, we performed noisy simulations of a Hoffman phantom modeled as a voxelized phantom with 1x1x1 mm^3 voxels. The phantom has a spherical cold lesion with a diameter of 9 mm with zero activity (Fig. 6.19(a)). The simulated uptake ratio between grey and white matter is 5:1 as in the physical phantom [107].

6.4.3.5 Clinical triple-head UHR fan-beam system

We compared the performance of the multi-pinhole SPECT insert with a PRISM 3000XP (a clinical triple-head SPECT system) equipped with UHR fan-beam collimators. The PRISM has 3 rotating detector heads with 30 mm-thick NaI crystals and axial and transverse dimensions of respectively 242 and 406 mm. The detector heads are positioned at a distance of 135 mm, which is typically the closest one can get, without touching the patient. The detector intrinsic spatial and energy resolution are 3.0 mm and 10%, respectively. The UHR fan-beam collimator has a height of 34.9 mm, a hole size of 1.4 mm and a focal length of 50 cm, resulting in a calculated system spatial resolution of 7.2 mm in the center of the FOV and a volume sensitivity of 4.80x10^{-4} cps/Bq. The septal thickness is 0.15 mm. We simulated an acquisition with 40 rotation steps, which results in 120 projection angles (as there are 3 detector heads).

6.4.4 Image reconstruction

The noisy and noiseless multi-pinhole projection data were reconstructed with the maximum likelihood expectation maximization (MLEM) algorithm. MLEM was first described in section 2.1.4.1 and implemented using a pixel-driven forward projector modeling the finite dimension of the pinhole opening using 7 rays [254] that cover the pinhole area with Gaussian quadrature weights and a voxel-driven back projector with one ray. Attenuation, sensitivity and spatial resolution are only modeled in the forward projector.

The fan-beam projection data were first rebinned to parallel beam data and then reconstructed using MLEM. For every projection angle, the estimated image was rotated using a cubic spline rotator [201] and then forward projected towards each pixel, while the back projector was voxel-driven. Resolution was modeled using a blurring operation in image space with a distance dependent FWHM. Sensitivity was modeled using a distance dependent weighting factor. We used the sensitivity and resolution formulae described by Moyer [167].

All reconstructed images were represented within a 128x128x128 matrix with 1.785x1.785x1.875 mm^3 voxels.

6.4.5 Contrast-to noise

We compared the fan-beam system and the multi-pinhole insert quantitatively, based on contrast-to-noise ratio. Therefore, we used the contrast

phantom as described in paragraph 6.4.3.3 and plotted the contrast recovery coefficient (CRC) at each image reconstruction iteration as a function of the coefficient of variation (COV). The CRC and COV values are evaluated in nine 7.5-mm slices (spaced 11.25 mm apart) of the contrast phantom and averaged.

The contrast recovery coefficient (CRC) is defined as follows:

$$\mathrm{CRC}(\%) = \frac{1}{N_n}\sum_{j=1}^{N_n}\left(\frac{\bar{L}_j - \bar{B}_j}{\bar{B}_j}\right)/(C-1) \times 100 \tag{6.4}$$

where N_n is the number of averages (9 this case), $\bar{L}_j$ is the mean activity concentration in the lesion volume of interest (VOI) in slice j, $\bar{B}_j$ the mean activity concentration in the background VOI in slice j and C the true lesion-background ratio. Lesion VOIs were delineated based on their known location and size. Background VOIs were delineated as shown in Fig. 6.15(d). The coefficient of variation (COV) is defined as follows:

$$\mathrm{COV}(\%) = \frac{1}{N_n}\sum_{j=1}^{N_n}\frac{\sigma_{B_j}}{\bar{B}_j} \times 100 \tag{6.5}$$

where σ_{B_j} is the pixel-to-pixel percent standard deviation (%SD) in the background region of the slice considered.

We also included the error bars (plus and minus the standard deviation over the 9 CRC values).

6.4.6 Simulation results

6.4.6.0.1 Spatial resolution In the cold-rod phantom, the 24-pinhole setup (Fig. 6.15(b)) performs better than the 34-pinhole setup (Fig. 6.15(c)). With the 24 pinholes, we can distinguish the 5 mm cold rods. The 34-pinhole setup shows a very good resolution at the edge of the phantom but suffers from a sampling issue in the center.

6.4.6.0.2 Sampling On the other hand, the 34 pinholes clearly perform better in a uniform background region like in the contrast phantom (Fig. 6.15(e,f)).

The individual disks of the Defrise phantom are well resolved for both the 24- and 34-pinhole setup, which shows that axial sampling completeness is achieved in both setups (Fig. 6.16(b,c,e,f)).

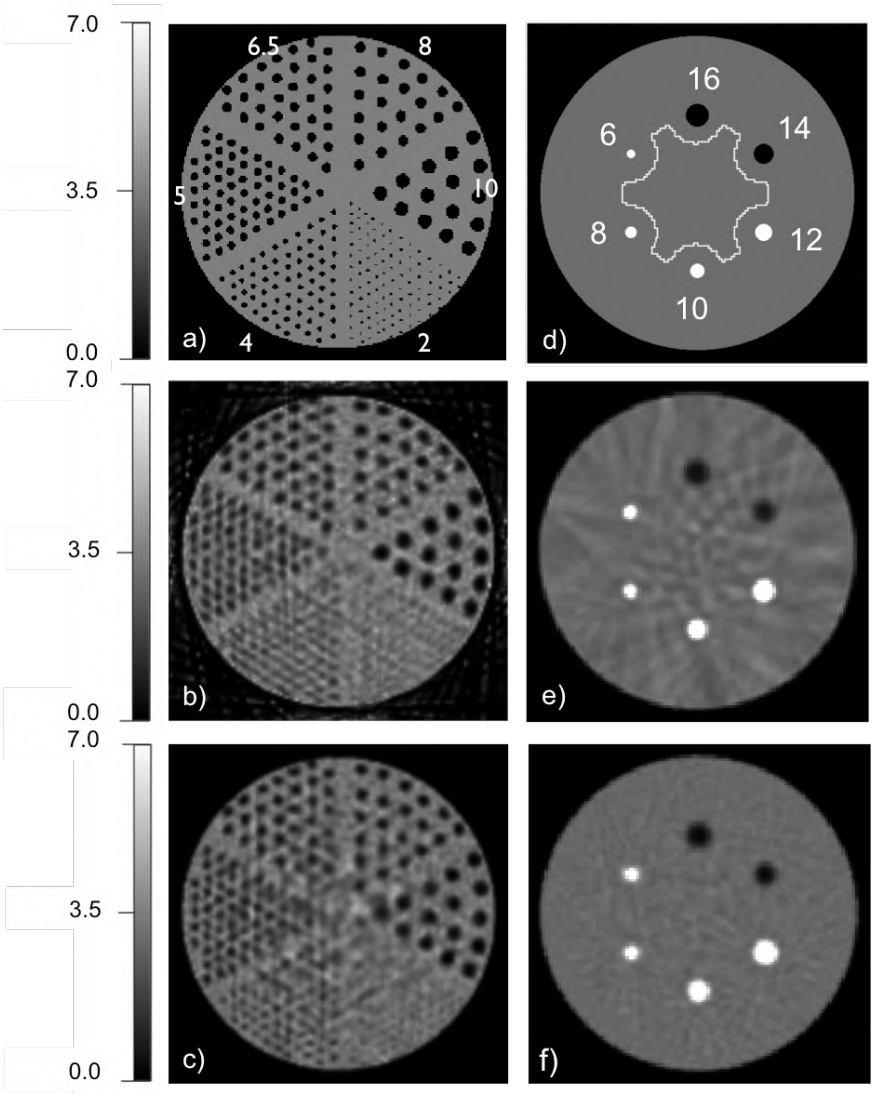

Figure 6.15: Noiseless images of the multi-pinhole systems after 1600 MLEM iterations. (a) Transverse view of the cold-rod phantom (b) Cold-rod phantom with 8x24 pinholes (c) Cold-rod phantom with 8x34 pinholes (d) Transverse view of the contrast phantom with a white line indicating where the background was evaluated for the COV. All hot rods have an uptake ratio of 7:1 (e) Contrast phantom (8x24 phs) (f) Contrast phantom (8x34 phs)

6.4.6.0.3 CNR Fig. 6.17 shows the Monte Carlo simulated contrast phantoms for both the 24-pinhole multi-pinhole system and the UHR fan-beam system. The images are shown at equal noise level (COV=30%) after a Gaussian filter was applied with a FWHM of 6 mm and a kernel size of 25 voxels. We observe that the noise is less correlated with the UHR FAN system than with the multi-pinhole system, but we don't observe any visual differences in contrast. For more quantitative results, we also evaluated the contrast-to-noise ratio (Fig. 6.18). We see that at 30% COV the CRC is 16.2% and 24.7% lower with the 24 pinholes in the 8 mm and 10 mm hot lesions, respectively, but in the 6 mm hot and 16 mm cold lesions the CRC is 12.6% and 10.7% higher, respectively, with the 24-pinhole setup. In the other lesions the difference is smaller than the standard deviation of the CRC.

6.4.6.0.4 Hoffman phantom Fig. 6.19 shows the reconstructed images of the Hoffman phantom after post-smoothing with a Gaussian filter (FWHM of 7.5 mm and kernel size of 25 voxels). The images are shown at equal noise level (COV=30%), with COV calculated in uniform parts of the phantom (the thalamus and the cerebellum). The cold spot is slightly more visible in the multi-pinhole image than in the fan-beam image and on the line-profile we observe a higher peak-to-valley ratio in the multi-pinhole image.

6.4.7 Discussion

We performed noiseless simulations with two different setups. The first setup with 8x24 pinholes and 4 rings of 34 detectors is the one with the highest sensitivity. The second setup with 8x34 pinholes and 4 rings of 34 detectors has more angular projections but it experiences some sampling issues due to the gaps between the detectors (Fig. 6.15(c)). In the 24-pinhole setup, the gaps between the 34 detectors are back projected irregularly, i.e. to different areas in image space. In the 34-pinhole setup, however, in 4 out of the 8 pinhole rings, the gaps between the 34 detectors are always back projected to the center. This is not so much of a problem in the contrast phantom, which has a large uniform background and where we observe better uniformity with the 34-pinhole setup but in the cold rod phantom (which is a more complex phantom) we observe some sampling issues in the center of the FOV. Therefore, we decided to continue with the 24-pinhole setup.

When we compare the 24 pinholes and UHR FAN system in terms of

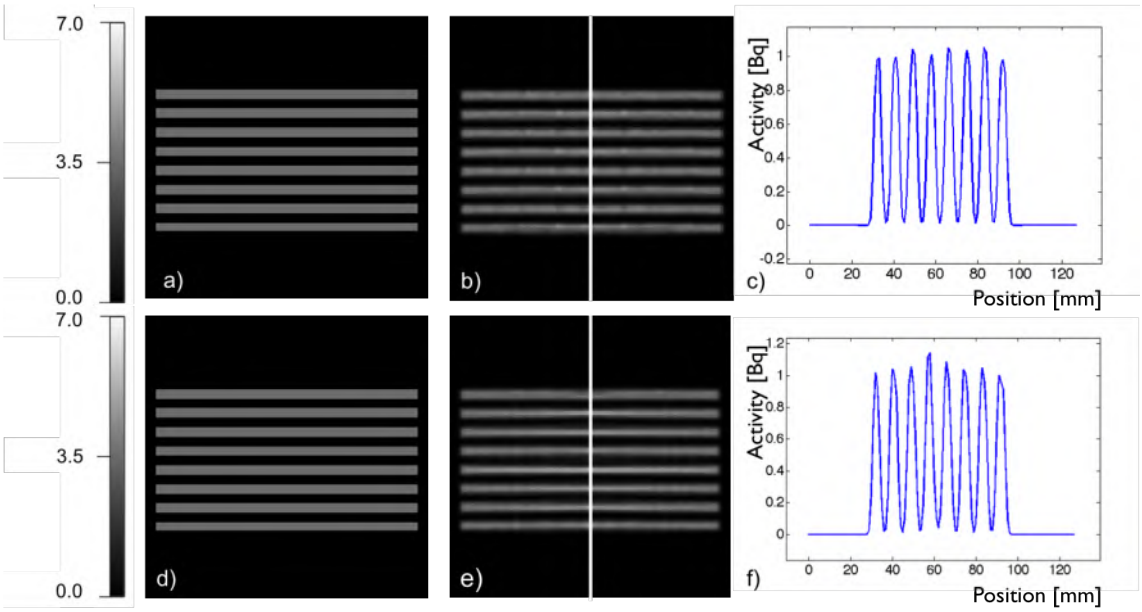

Figure 6.16: (a) Coronal view of the Defrise phantom (b) noiseless simulation of the Defrise phantom (8x24 phs) (c) Axial line profile of the noiseless simulation (8x24 phs) (d) Coronal view of the Defrise phantom (e) noiseless simulation of the Defrise phantom (8x34 phs) (f) Axial line profile of the noiseless simulation (8x34 phs)

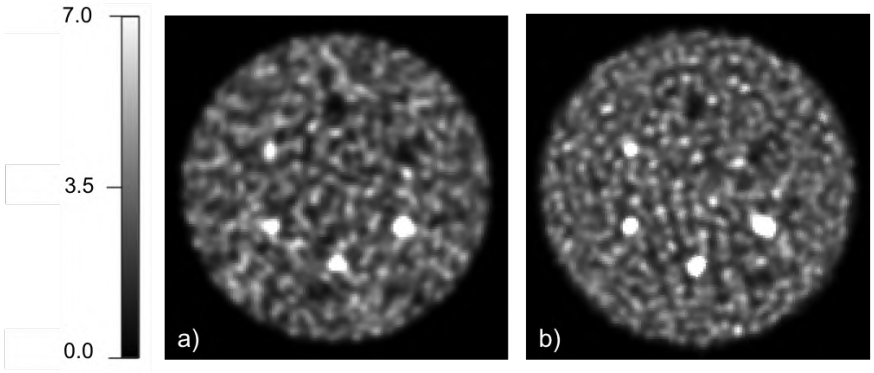

Figure 6.17: Monte Carlo simulations of a contrast phantom at equal noise (COV 30%) with (a) 8x24 pinholes (b) UHR Fan-beam

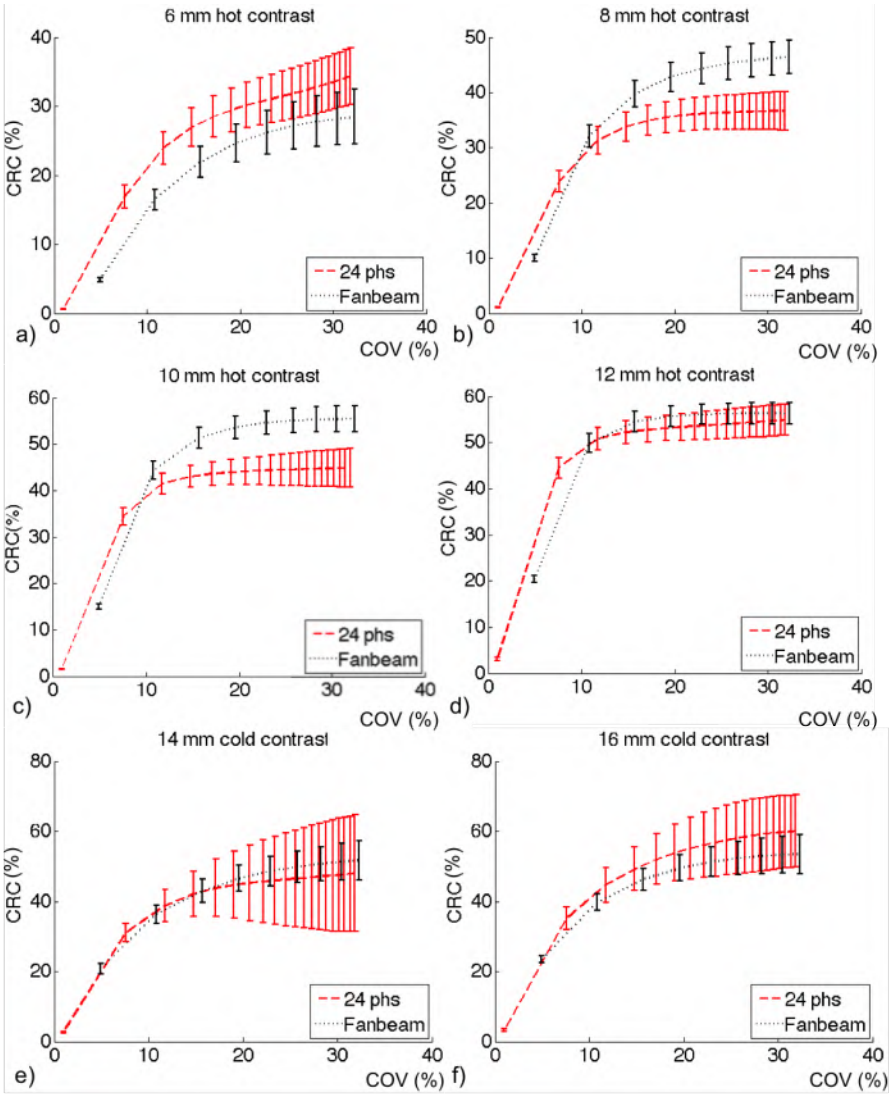

Figure 6.18: Contrast-to-noise plots with error bars (plus and minus the standard deviation) for both the multi-pinhole systems (grey) and the UHR fan-beam collimator (black): (a) 6 mm hot lesion (b) 8 mm hot lesion (c) 10 mm hot lesion (d) 12 mm hot lesion (e) 14 mm cold lesion (f) 16 mm cold lesion

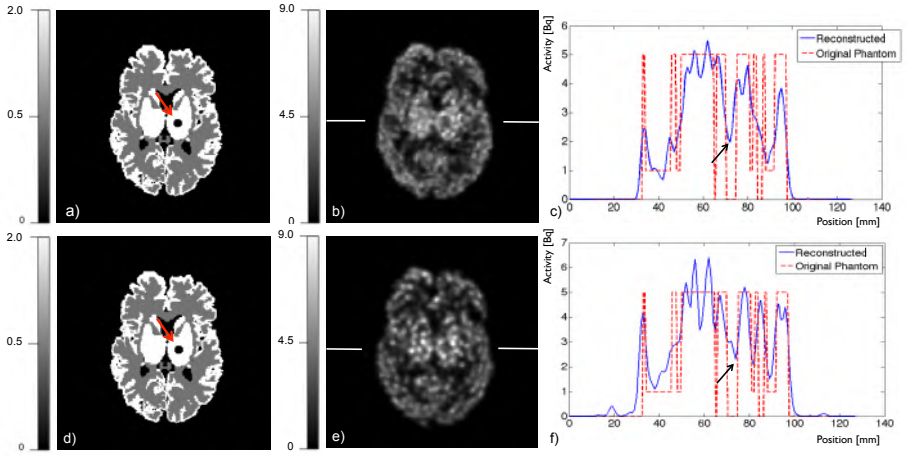

Figure 6.19: Monte Carlo simulations of a Hoffman phantom with the multi-pinhole setup (8x24 pinholes) and the UHR fan-beam setup, compared at equal noise level (COV 30%) (a) Transverse view of the phantom with a 9 mm cold lesion (b) Monte Carlo simulation with the multi-pinhole setup (c) Line profile for the multi-pinhole setup (d) Transverse view of the phantom with a 9 mm cold lesion (e) Monte Carlo simulation with the UHR Fan-beam system (f) Line profile for the UHR Fan-beam system.

contrast-to-noise ratio, we see that the multi-pinhole system performs better in the 6 mm hot and 16 mm cold lesions and worse in the 8 mm hot and 10 mm hot lesions. In the other lesions the difference is smaller than the standard deviation of the measured CRC. We also compared both systems based on a visual evaluation of a Hoffman phantom simulated with a clinically realistic activity and scan time and found that the 9 mm cold lesion was slightly better visible on the multi-pinhole image. Although this visual evaluation of the Hoffman phantom was based on a single noise realization and is not strong enough to be conclusive, it gives us the confidence that brain SPECT/MRI is feasible with a multi-pinhole insert so that in the future we can build the system and continue the comparison based on measured data.

Compared to the design of chapter 4, this system is relatively simple, and building it should be relatively easy. This compact dSiPM-based system is also expected to be less expensive than the multi-lofthole system from chapter 4, which relies on a very large detector ring, made of expensive $LaBr_3$ detectors [150].

6.5 Conclusion

We investigated MR-compatibility of tungsten collimator material produced through additive manufacturing. Measurements and simulations show that eddy currents are limited and can be further reduced by adding gaps between different collimator parts. Therefore, we do not expect any MR-compatibility issues with the collimator and we continued designing a stationary brain SPECT insert for MRI based on high resolution dSiPMs and a full-ring multi-pinhole collimator.

We extended the optimization method that was presented in chapter 4 for jointly optimizing both the collimator and the detector radius. In the method we kept the total detector surface constant, i.e. a larger detector radius results in a shorter detector ring, in order to keep costs under control. We found that the largest detector ring, i.e. exactly fitting the MRI bore, does not maximize sensitivity. This is an interesting result and some researchers have overlooked this in the past, instinctively choosing the detector as large as possible. Analytical calculations predict a system spatial resolution of 7.2 mm in the center of the FOV and volume sensitivity of $3.95\text{x}10^{-4}$ cps/Bq, with the optimized system. This volume sensitivity is lower than a triple head system with fan-beam collimators of the same resolution, but higher than a dual head system.

Finally, we simulated different phantoms to investigate image quality and compared the results with a clinical triple-head fan-beam system. We first performed noiseless simulations of a Defrise and a cold-rod phantom and demonstrated sufficient axial sampling and a reconstructed resolution high enough to resolve rods as small as 5 mm. Moreover, Monte Carlo simulations of a contrast phantom demonstrated a contrast-to-noise ratio comparable to that of a triple-head fan-beam system. Finally, we reconstructed noisy projection data of a Hoffman phantom with a 9 mm cold lesion to illustrate the application of the SPECT/MR insert in a realistic human brain phantom and found that the lesion was slightly better visible on the multi-pinhole image compared to the fan-beam image.

These results show that brain SPECT/MRI is feasible with a multi-pinhole insert and that we can expect image quality to be similar to the best clinical systems available. This gives us the confidence to build the system and continue the comparison based on measured data.

6.6 Original contributions

The work presented in this chapter resulted in a number of international conference contributions [240, 51, 203, 204]. The results were published in the peer-reviewed A1 journal *Medical Physics* [52] (third author) and in the peer-reviewed A1 journal *Magnetic Resonance in Medicine* [205] (second author) and another paper is currently under review at the peer-reviewed A1 journal *Medical Physics* [241] (first author). The MR-compatibility simulations discussed in section 6.2.3.1 were performed by Amine Samoudi. The measurements for the validation of the numerical model, in the same section, were performed by the author of this dissertation.

Chapter 7

General conclusions

In this chapter we summarize the main contributions of the work in this dissertation and draw general conclusions. We also discuss possible future research directions and in the end a final conclusion is made.

7.1 Summary

The purpose of this dissertation was to improve brain SPECT imaging with innovative collimator design and for this, we used two different approaches. In the first approach, we used a very large detector ring based on current low resolution detector technology (intrinsic resolution of 4 mm) in combination with an innovative stationary multi-pinhole collimator equipped with a shutter mechanism. This shutter mechanism did not only ensure sufficient angular sampling without rotating the system, it also allowed us to adaptively change the degree of multiplexing. In the second approach we used new high-resolution detector technology (with an intrinsic resolution of 0.5 mm) in combination with minifying pinholes, which made it possible to design a compact and MR-compatible brain SPECT system.

We will now describe our results and conclusions from these two approaches.

We start with **chapter 2**, where we provided the necessary background about SPECT and MRI. Firstly, we explained the complete chain of a SPECT image acquisition. This includes injecting the tracer (we discussed the different tracers and their applications), acquiring projection data using either a SPECT system or simulations (we discussed the different components of a SPECT system and different types of simulations, like ray-tracing

and Monte-Carlo simulation) and reconstructing the data (we focussed on MLEM and OSEM, the two most commonly used iterative reconstruction algorithms). We discussed applications of SPECT in neurology and made the comparison with PET. Key advantages of SPECT over PET are related to cost and tracer half-life but we also discussed a few clinical examples where SPECT outperforms PET even though clinical PET systems have a higher resolution and sensitivity than SPECT. Secondly, we explained the basic principles of proton nuclear magnetic resonance and of magnetic resonance imaging, which was followed by an explanation of the different components in an MRI system. Finally, we discussed the latest developments in multimodality imaging and the specific challenges in combining SPECT with MRI for brain imaging, which are (i) the need for a stationary and compact system (ii) MR-compatibility of the collimator (iii) MR-compatibility of the detector.

In **chapter 3** we gave an overview of recent advances in collimator technology, both for human and small-animal molecular imaging systems and we provided guidelines for selecting, optimizing and fabricating collimators for different applications. Firstly, we introduced the different types of collimators: parallel-hole, fan-beam, cone-beam, multi-pinhole and other types of collimators. Secondly, we introduced some important concepts like septal penetration, high-energy applications, multiplexing and sampling completeness (e.g. we discussed the necessary sampling conditions needed for reconstructing data from stationary systems). Thirdly, we gave an update of new production techniques that have become available (e.g., direct 3-D printing of metals and 'cold casting' of tungsten-composite materials) and explained their specific advantages and disadvantages. These production techniques have opened up new possibilities for fabrication of complex new collimator designs that would be impossible or extremely expensive to construct by more conventional means. To continue, we provided some general guidelines to select a collimator given a certain target resolution, FOV, intrinsic detector resolution and detector size. Finally, we gave a review of the different collimator optimization techniques that have been published. We discussed techniques based on sensitivity maximization, task-dependent optimization and adaptive SPECT. After this chapter, the reader should be able to understand the challenges of SPECT collimator design and production.

In **chapter 4** we used the guidelines of chapter 3 to design a stationary brain SPECT insert for a large whole-body detector ring (the LaPET [45]) with an intrinsic resolution comparable to clinical SPECT detectors (4 mm).The SPECT insert consists of a full-ring multi-lofthole collimator

equipped with shutters, i.e. small blocks of tungsten connected to actuators that can be used to open/close loftholes. A sequence of shutter movements can then be used to obtain an acquisition that is equivalent to a rotational movement. This idea is novel and is an important outcome of this chapter. It does not only allow to build stationary systems, it also allows us to adapt the degree of multiplexing. Another important outcome of this chapter is the development of an optimization method that maximizes the volume sensitivity of a full-ring multi-pinhole system based on analytical simulations and given a specific target resolution in the center of the FOV and a fixed diameter for the detector ring. However, despite the large detector ring and the multi-lofthole design, we obtained a sensitivity of $1.55\text{x}10^{-4}$ cps/Bq, which is 2.5 times lower than the sensitivity of a dual-head system with low energy high resolution parallel-hole (LEHR PAR) collimators. This is the cost paid for improving the spatial resolution (6 mm with the LaPET insert versus 9.8 mm with the LEHR PAR system). Simulations of a noiseless hot-rod phantom showed that the spatial resolution indeed improved: we successfully reconstructed 4 mm hot rods with the multi-lofthole system. This also resulted in improved CNR, as shown in noisy simulations of a contrast phantom, but only for the hot lesions. The CNR in the cold lesions decreased. Similar results were obtained in the lesion detectability study, where we saw an overall increase in NPW-SNR for the phantom with the hot lesions and an overall decrease for the phantom with the cold lesions. Cold lesions typically suffer more from decreased sensitivity.

In **chapter 5** we therefore investigated the possibility of further increasing sensitivity by opening more loftholes simultaneously, even though this causes the projections to overlap on the detector (also called multiplexing). We found that multiplexing can cause distortions in the reconstructed images but that these can be resolved by combining multiplexed with non-multiplexed projection data, which can be done by opening more or less loftholes with the shutter mechanism. We also found that a body support helps to speed up convergence. This approach finally resulted in a 5% improvement in contrast-to-noise ratio (compared to the non-multiplexed setup in chapter 4). Later in chapter 5, we investigated the necessary conditions for obtaining artifact-free images in more detail. We used computer simulated phantom data to show that more multiplexing does not necessarily result in more artifacts and that systems with a high amount of multiplexing can still result in artifact-free images if data completeness is achieved, i.e. when the set of non-multiplexed and de-multiplexed vantage angles fulfils Orlov's conditions. Both the idea of evaluating a multiplexing system based on vantage lines and the concept of de-multiplexed vantage lines are

novel and they are the most important outcome of this chapter. Finally, we also compared image quality (contrast-to-noise and lesion detectability) between a single pinhole system and different multiplexing multi-pinhole systems using noisy simulations. The results showed that although multiplexing allows us to increase sensitivity dramatically, the improvement in contrast-to-noise ratio is not that obvious. This is because the multiplexing setups converge slower, which counteracts the increased sensitivity. As a result, we found only small differences in contrast-to-noise ratio, in the same order of magnitude as the standard deviation. We also investigated NPW-SNR (non-prewhitening matched filter signal-to-noise ratio), which is a measure for lesion detectability, and for this task we did find an improvement: on average, the multiplexing setups showed an improvement of 12% in NPW-SNR compared to the single-pinhole setup. We also found that multiplexing can improve angular sampling and concluded that multiplexing can be a good choice for practical reasons (when shielding is difficult) and that no artifacts are to be expected as long as sampling sufficiency is obtained.

In the **last chapter**, we changed focus and instead of trying to improve sensitivity and resolution, we investigated the potential of digital silicon photomultiplier (dSiPM) detectors to build a compact, stationary and MR-compatible SPECT insert for brain imaging. The detector modules have shown to be MR-compatible and have an excellent intrinsic resolution when combined with a monolithic 2 mm thick LYSO crystal. Therefore, we don't need magnification to obtain a good system resolution. Instead, we can use minification and build a stationary system with many minifying pinholes, providing sufficient angular sampling without the need for rotation. In this way, we can achieve a sufficiently high resolution, even with a relatively small detector ring such that we can keep the full SPECT system compact enough to fit inside an MRI.

Firstly, we investigated the MR-compatibility of a collimator produced by additive manufacturing with both measurements and simulations and found that a full-ring collimator can be MR-compatible if we include some gaps to prevent eddy currents from flowing in the ring.

Secondly, we extended the optimization method from chapter 4 for jointly optimizing both the collimator and the detector radius. In the method we kept the total detector surface constant, i.e. a larger detector radius results in a shorter detector ring, in order to keep costs under control. We found that the largest detector ring, i.e. exactly fitting the MRI bore, does not maximize sensitivity. This is an interesting result and some researchers have

overlooked this in the past, instinctively choosing the detector as large as possible. Analytical calculations predict a system spatial resolution of 7.2 mm in the center of the FOV and volume sensitivity of $3.95\text{x}10^{-4}$ cps/Bq, with the optimized system. This is lower than a triple head system with fan-beam collimators of the same resolution, but higher than a dual head system.

Finally, we simulated different phantoms to investigate image quality and compared the results with a clinical triple-head fan-beam system. We first performed noiseless simulations of a Defrise and a cold-rod phantom and demonstrated sufficient axial sampling and showed that we were able to resolve the 5 mm rods. Moreover, monte Carlo simulations of a contrast phantom demonstrated a contrast-to-noise ratio comparable to that of a triple-head fan-beam system. Finally, we reconstructed noisy projection data of a Hoffman phantom with a 9 mm cold lesion to illustrate the application of the SPECT/MR insert in a realistic human brain phantom and found that the lesion was slightly better visible on the multi-pinhole image compared to the fan-beam image.

These results showed that brain SPECT/MRI is feasible with a multi-pinhole insert and that we can expect image quality to be similar to the best clinical systems available. This gives us the confidence to build the system and continue the comparison based on measured data.

7.2 Future research possibilities

In the context of the SIMRET project, our research group is currently building a preclinical SPECT insert for a 3T benchtop MR from MR Solutions. A fully integrated preclinical SPECT/MRI will soon be available, which will create new research opportunities in dynamic imaging, for example for the study of drug pharmacokinetics, and for longitudinal studies where the extra radiation of CT would otherwise influence the outcome of the study, for example for the assessment of new therapies in oncology. The remaining challenges are mainly related to practical issues, like cooling the detectors inside an MRI, shielding the detectors and calibrating both the collimators and the detectors (in order to obtain an accurate system matrix).

Once we solved these issues for the SIMRET project (on the scale of a preclinical system), we can start building the clinical brain SPECT insert that was described in chapter 6 and use it to perform clinical brain SPECT/MR studies. This will allow us to compare the diagnostic value of SPECT/CT and SPECT/MR for the applications that we discussed in section 2.3.1:

brain infarction, oncology and epilepsy. More applications might also come up once the system becomes clinically available.

Human brain and preclinical SPECT inserts are thus expected to become available in the near future. Unfortunately, these systems cannot easily be scaled to whole-body SPECT/MRI. Designing a stationary and compact whole-body insert is even more challenging and a multi-pinhole design might not be the best solution due to the size of the FOV and the large distance between the source and the pinholes. Therefore, our research group is currently investigating axially varying tilted parallel-hole collimators as a solution for building compact stationary whole-body systems [44]. These collimators are based on tilted parallel-holes whose viewing direction changes according to their axial position. This allows complete angular sampling using only longitudinal bed movement and results in a very compact design that could potentially fit in an MRI. A fully integrated whole-body SPECT/MRI would allow us to correct for respiratory or cardiac motion and guarantee geometrical coregistration of both images.

Aditionally, it would also be interesting to apply the principles of this dissertation to cardiac imaging. The heart has a size similar to the brain, but on the other hand, it is more central in the body and it is not possible to come as close with the pinholes. A more complex shape of collimator (not simply a ring) might be needed to overcome this issue.

In the meantime, MR systems are also evolving and very high field magnetic resonance imaging (MRI) scanners are becoming available (7T and higher for clinical applications and up to 15.2T for preclinical applications). Integrating a SPECT system in these high fields might be quite challenging and the MR-compatibility of both the detectors and the collimator will have to be reevaluated.

Finally, we discuss two limitations of this dissertation and how they could be overcome in future work.

In the two systems presented in this dissertation (the LaPET insert and the MR insert), we assumed that the pinholes have no axial tilt in order to increase the axial extend of the FOV. However, many preclinical systems use focussed pinholes to increase sensitivity in the center of the FOV. For example for DaTscans (where we are mainly interested in the activity in the basal ganglia, which are quite central), a high sensitivity in the center of the FOV would be an added value and it is worth investigating the effect of tilting the pinholes in axial direction.

Finally, in chapter 5 we developed a method to evaluate sampling conditions in multiplexing systems. In this method we assumed a non-sparse

activity distribution but in future work, it would be interesting to incorporate the activity distribution and explain the object dependence that is reported in literature (e.g. more multiplexing can be used in sparse objects than in uniform phantoms). A full understanding of the object dependence, would open interesting possibilities towards adaptive imaging. We could use the shutter mechanism to change the degree of multiplexing based on a scout scan and the sparsity of the object and thus further increasing image quality.

7.3 Final conclusion

Currently, brain SPECT imaging is mostly performed with clinical dual- or triple-head gamma cameras, which are bulky, non-stationary, non-adaptive, non-MR-compatible and which have a low sensitivity and a bad resolution. We have overcome these limitations using innovative multi-pinhole collimator design and optimization.

For this, we developed an optimization method that maximizes the volume sensitivity of a full-ring multi-pinhole system based on analytical simulations and given a specific target resolution in the center of the FOV. This method can not only be used for optimizing a brain SPECT system, but can be applied for optimizing any ring-shaped collimator for any application.

Secondly, we presented a new alternative for rotation, based on collimating shutters, i.e. small blocks of tungsten connected to actuators that can be used to open/close pinholes, so that we can prevent calibration issues that typically occur when a heavy collimator and/or detector needs to be rotated and so that it can be more easily integrated with an MRI (rotation would perturb the homogeneity of the magnetic field). A sequence of shutter movements is used to obtain an acquisition that is equivalent to a rotational movement. This does not only ensure sufficient angular sampling but also allows one to control the degree of multiplexing.

We also found new insights on multiplexing artifacts, showed that more multiplexing does not necessarily result in more artifacts and that systems with a high amount of multiplexing can still result in artifact-free images if data completeness is achieved, i.e. when the set of non-multiplexed and de-multiplexed vantage angles fulfils Orlov's conditions. Both the idea of evaluating a multiplexing system based on vantage lines and the concept of de-multiplexed vantage lines are novel and can be applied for designing both clinical and preclinical SPECT systems.

Finally, we demonstrated the feasibility of designing a compact multi-

pinhole brain SPECT system that fits inside a clinical MRI, is MR-compatible and that has a similar image quality as current clinical SPECT systems. A simultaneous SPECT/MRI has the potential to fundamentally change brain imaging in the future.

Appendix A

In this appendix, we provide the proof that the condition of $H_2(m,j) = W.H_1(n,j) \quad \forall j \in L_1$, which is needed to derive Equations 5.6 and 5.7 in chapter 5, is true for perfect pinholes (where resolution and penetration effects are neglected). We use the same symbols as in section 5.2.2.

If we assume a perfect pinhole, where resolution and penetration effects are neglected, the value of detector pixel i is:

$$p_i = \sum_{j \in L_1} H_1(i,j) f(j) \tag{7.1}$$

with L_1 the line passing through pixel i and pinhole 1, $f(j)$ the activity distribution in voxel j and $H_1(i,j)$ the probability of detecting photons from voxel j in pixel i. This linear weighting factor is needed due to the geometric efficiency of the collimator, the voxelization of the activity distribution and the pixelization of the detector.

The geometric efficiency g is the probability that a photon is detected through the pinhole, which is position-dependent and described by the following equation [12]:

$$g = \frac{d^2 \cos^3 \psi}{16 b^2} \tag{7.2}$$

with ψ the angle of incidence measured from the plane of the pinhole aperture, b the perpendicular distance from the point in the FOV to the plane defined by the pinhole aperture and d the physical diameter of the pinhole aperture. Note that ψ is a 3D angle (Fig. 5.12).

Next to the geometric efficiency, there is another factor that determines $H_1(i,j)$: as the detector pixels have finite size, all photons from inside a certain sampling volume $G(i,j)$ contribute to the value of detector pixel i. This sampling volume increases with b [257]:

$$G(i,j) = cos\kappa \frac{b^2}{h^2} \Delta u \Delta v \Delta l_j \tag{7.3}$$

with Δu and Δv the pixel dimensions, Δl_j the intersection length at voxel j, κ the inclination angle of the projection ray with respect to the normal of the detector and h the focal length of the pinhole collimator, i.e. the distance between the pinhole and the detector.

We now multiply equations (7.2) and (7.3) to get $H_1(i,j)$:

$$H_1(i,j) = cos^3\psi cos\kappa \frac{d^2}{16h^2}\Delta u \Delta v \Delta l_j \tag{7.4}$$

In this equation, only Δl_j depends on voxel j. The other terms only depend on the pinhole geometry (like d and h) and on the projection line L_1 (like ψ and κ).

If we include eq. (7.4) in eq. (7.1), we can see that W_1 does depend on the projection line L_1 but is independent of j:

$$\begin{aligned} p_i &= \sum_{j \in L_1} cos^3\psi cos\kappa \frac{d^2}{16h^2}\Delta u \Delta v \Delta l_j f(j) \\ &= cos^3\psi cos\kappa \frac{d^2}{16h^2}\Delta u \Delta v \sum_{j \in L_1} \Delta l_j f(j) \\ &= W_1 \sum_{j \in L_1} \Delta l_j f(j) \end{aligned}$$

We can repeat this derivation for the second pinhole and show that: $H_1(n,j) = W_1 \Delta l_j$, $H_2(m,j) = W_2 \Delta l_j$ and thus $H_2(m,j) = W.H_1(n,j) \quad \forall j \in L_1$ with H_1 and H_2 the system matrices corresponding to pinholes 1 and 2, respectively, and with $W = \frac{W_2}{W_1}$

References

[1] FEKO EM Software and Systems S.A. `www.feko.info`. Accessed: 2015-07-29.

[2] Mediso Medical Imaging Systems. `http://www.mediso.com/products.php?fid=2`. Accessed: 2015-07-29.

[3] C. K. Abbey and H. H. Barrett. Linear iterative reconstruction algorithms: study of observer performance. In *Proceedings of the 14th International Conference on Information Processing in Medical Imaging*, pages 65–76, 1995.

[4] C. K. Abbey and H. H. Barrett. Human- and model-observer performance in ramp-spectrum noise: effects of regularization and object variability. *J. Opt. Soc. Am. A*, 18(3):473–488, 2001.

[5] I. R. Abubakirov and A. A. Gusev. Estimation of scattering properties of lithosphere of Kamchatka based on Monte-Carlo simulation of record envelope of a near earthquake. *Phys. Earth Planet. In*, 64(1):52–67, 1990.

[6] R. Accorsi, F. Gasparini, and R. C. Lanza. Optimal coded aperture patterns for improved SNR in nuclear medicine imaging. *Nucl. Instr. Meth. Phys. Res. A*, 474(3):273–284, December 2001.

[7] R. Accorsi and S. D. Metzler. Analytic determination of the resolution-equivalent effective diameter of a pinhole collimator. *IEEE Trans. Med. Imaging*, 23(6):750–63, June 2004.

[8] R. Accorsi, J. R. Novak, A. S. Ayan, and S. D. Metzler. Derivation and validation of a sensitivity formula for slit-slat collimation. *IEEE Trans. Med. Imag.*, 27(5):709–722, May 2008.

[9] D. G. Amen, M. Trujillo, A. Newberg, K. Willeumier, R. Tarzwell, J. C. Wu, and B. Chaitin. Brain SPECT imaging in complex psychiatric cases: an evidence-based, underutilized tool. *Open Neuroimag. J.*, 5:40–48, 2011.

[10] H. O. Anger. Scintillation camera. *Rev. Sci. Instrum.*, 29:27–33, 1958.

[11] H. O. Anger. Scintillation camera with multichannel collimators. *J. Nucl. Med.*, 5:515–531, Jul 1964.

[12] H. O. Anger, M. R. Powell, D. C. van Dyke, L. R. Schaer, R. Fawwaz, and Y. Yano. Recent applications of the scintillation camera. *Strahlentherapie*, 65:70–93, 1967.

[13] S. Azman, J. Gjaerum, D. Meier, L. Muftuler, G. Maehlum, O. Nalcioglu, B. E. Patt, B. Sundal, M. Szawlowski, B. M. W. Tsui, and D. J. Wagenaar. A nuclear radiation detector system with integrated readout for SPECT/MR small animal imaging. *IEEE Nucl. Sci. Symp. Conf. Rec. 2007*, pages 2311–2317, 2007.

[14] G. Bal, P. D. Acton, F. Jansen, and B. H. Hasegawa. Revolving multipinhole SPECT for small animal imaging. In *IEEE Nucl. Sci. Conf. Rec.*, pages 5577–5584, October 2008.

[15] G. Bal, E. V. R. DiBella, G. T. Gullberg, and G. L. Zeng. Cardiac imaging using a four-segment slant-hole collimator. *IEEE Trans. Nucl. Sci.*, 53(5):2619–2627, 2006.

[16] H. H. Barrett, L. R. Furenlid, M. Freed, J. Y. Hesterman, M. A. Kupinski, E. Clarkson, and M. K. Whitaker. Adaptive SPECT. *IEEE Trans. Med. Imag.*, 27(6):775–88, June 2008.

[17] H. H. Barrett and K. J. Myers. *Foundations of image science*. Wiley-VCH, 2003.

[18] H. H. Barrett, J. Yao, J. P. Rolland, and K. J. Myers. Model observers for assessment of image quality. *Proc. Natl. Acad. Sci. USA*, 90(21):9758–9765, November 1993.

[19] J. D. Beenhouwer, S. Staelens, S. Vandenberghe, and I. Lemahieu. Acceleration of GATE SPECT simulations. *Med. Phys.*, 35(4):1476–1485, Apr 2008.

[20] J. A. Bieszk and E. G. Hawman. Evaluation of SPECT angular sampling effects: continuous versus step-and-shoot acquisition. *J. Nucl. Med.*, 28:1308–1314, 1987.

[21] V. Bom, M. C. Goorden, and F. J. Beekman. Comparison of pinhole collimator materials based on sensitivity equivalence. *Phys. Med. Biol.*, 56(11):3199–3214, 2011.

[22] C. Bouckaert, S. Vandenberghe, and R. Van Holen. Design of an MR-compatible SPECT insert for simultaneous SPECT-MR imaging of a mouse. *13th Belgian Day on Biomedical Engineering*, 2014.

[23] C. Bouckaert, S. Vandenberghe, and R. Van Holen. Evaluation of a compact, high-resolution SPECT detector based on digital silicon photomultipliers. *Phys. Med. Biol.*, 59(23):7521–7539, November 2014.

[24] S. Bouquillon, Y. Coulais, M. Dartiguenave, J. A. M. Tafani, and R. Guiraud. Synthesis, characterization and biodistribution of a new Technetium-99m complex with Trimethylsilylmethylisonitrile. Comparison with 99mTc-TBI and 99mTc-MIBI. *Nucl. Med. Biol.*, 22(5):585–588, July 1995.

[25] D. Bovijn. MRI-compatible shutter mechanism. Master's thesis, Howest, University College West Flanders, 2013.

[26] I. Britvitch, I. Johnson, D. Renker, a. Stoykov, and E. Lorenz. Characterisation of Geiger-mode avalanche photodiodes for medical imaging applications. *Nucl. Instr. Meth. Phys. Res. A*, 571:308–311, 2007.

[27] P. Busca, C. Fiorini, A. D. Butt, M. Occhipinti, R. Peloso, R. Quaglia, F. Schembari, P. Trigilio, G. Nemeth, P. Major, K. Erlandsson, and B. F. Hutton. Simulation of the expected performance of INSERT: A new multi-modality SPECT/MRI system for preclinical and clinical imaging. *Nucl. Instr. Meth. Phys. Res. A*, 734(B):141–6, January 2014.

[28] C. L. Byrne. Accelerating the EMML algorithm and releated iterative algorithms by rescaled block-iterative methods. *IEEE Trans. Image Process.*, 7(1):100–109, 1988.

[29] L. Cai, X. Lai, Z. Shen, C.-T. Chen, and L.-J. Meng. MRC-SPECT: A sub-500 μm resolution MR-compatible SPECT system for simulta-

neous dual-modality study of small animals. *Nucl. Instr. Meth. Phys. Res. A*, 734(B):147–51, January 2014.

[30] E. E. Camargo. Brain SPECT in neurology and psychiatry. *J. Nucl. Med.*, 42(4):611–23, April 2001.

[31] E. Candes, J. Romberg, and T. Tao. Stable signal recovery from incomplete and inaccurate measurements. *Comm. Pure Appl. Math.*, 59(8):1–15, 2006.

[32] Z. Cao, G. Bal, R. Accorsi, and P. D. Acton. Optimal number of pinholes in multi-pinhole SPECT for mouse brain imaging - a simulation study. *Phys. Med. Biol.*, 50(19):4609–4624, Oct 2005.

[33] Z. Cao, L. E. Holder, and C. C. Chen. Optimal number of views in 360 degrees SPECT imaging. *J. Nucl. Med.*, 37(10):1740–1744, 1996.

[34] Z. Cao and B. M. W. Tsui. An analytical reconstruction algorithm for multifocal converging-beam SPECT. *Phys. Med. Biol.*, 39:281–291, 1994.

[35] R. M. Capote, N. Matela, R. C. Conceição, and P. Almeida. Optimization of convergent collimators for pixelated SPECT systems. *Med. Phys.*, 40(6):062501 (13pp.), 2013.

[36] A. M. Catafau, F. J. Lomea, J. Pavia, E. Parellada, M. Bernardo, J. Setoain, and E. Tolosa. Regional cerebral blood flow pattern in normal young and aged volunteers: a 99mTc-HMPAO SPET study. *Eur. J. Nucl. Med. Mol.*, 23:1329–1337, 1996.

[37] C. Catana, Y. Wu, M. S. Judenhofer, J. Qi, B. J. Pichler, and S. R. Cherry. Simultaneous acquisition of multislice PET and MR images: initial results with a MR-compatible PET scanner. *J. Nucl. Med.*, 47(12):1968–1976, 2006.

[38] C. Chaix, J. W. Moore, R. Van Holen, H. H. Barrett, and L. R. Furenlid. The AdaptiSPECT imaging aperture. *IEEE Nucl. Sci. Symp. Conf. Rec.*, pages 3564–3567, 2012.

[39] W. Chang, C. E. Ordonez, H. Liang, Y. Li, and J. Liu. C-SPECT a clinical cardiac SPECT/CT platform: Design concepts and performance potential. *IEEE Trans. Nucl. Sci.*, 56(5):2659–2671, October 2009.

[40] S. Cherry. Multimodality imaging: beyond PET/CT and SPECT/CT. *Semin. Nucl. Med.*, 39(5):348–53, September 2009.

[41] S. Cherry, J. Sorenson, and M. Phelps. *Physics in Nuclear Medicine*. Saunders, third edition, 1987.

[42] R. Clack, P. Christian, M. Defrise, and A. E. Welch. Image reconstruction for a novel SPECT system with rotating slant-hole collimators. *IEEE Nucl. Sci. Symp. Conf. Rec. 1994*, 4:1948–1952, 1994.

[43] E. Clarkson, M. A. Kupinski, H. H. Barrett, and L. R. Furenlid. A task-based approach to adaptive and multimodality imaging: computation techniques are proposed for figures-of-merit to establish feasibility and optimize use of multiple imaging systems for disease diagnosis and treatment-monitoring. *Proc. IEEE Inst. Electr. Electron. Eng.*, 96(3):500–511, 2008.

[44] L. da Rocha Vaz Pato, S. Vandenberghe, K. Van Audenhaege, and R. Van Holen. Design and simulation of a stationary SPECT imaging system based on axially varying tilted parallel-hole collimation. In *IEEE Nucl. Sci. Symp. Conf. Rec.* IEEE, 2014.

[45] M. Daube-witherspoon, S. Surti, A. Perkins, C. Kyba, M. Werner, S. Matej, and J. Karp. Imaging Performance of a LaBr3-Based Time-of-Flight PET Scanner. *IEEE Nucl. Sci. Symp. Conf. Rec.*, pages 5463–5467, 2008.

[46] S. Deleye, R. Van Holen, J. Verhaeghe, S. Vandenberghe, S. Stroobants, and S. Staelens. Performance evaluation of small-animal multipinhole μSPECT scanners for mouse imaging. *Eur. J. Nucl. Med. Mol. Imaging*, 40(5):744–758, May 2013.

[47] G. Delso, S. Fürst, B. Jakoby, R. Ladebeck, C. Ganter, S. G. Nekolla, M. Schwaiger, and S. I. Ziegler. Performance measurements of the Siemens mMR integrated whole-body PET/MR scanner. *J. Nucl. Med.*, 52(12):1914–22, December 2011.

[48] G. Delso and S. Ziegler. PET/MRI system design. *Eur. J. Nucl. Med. Mol.*, 36(December 2008):86–92, 2009.

[49] K. Deprez. *Preclinical SPECT imaging based on compact collimators and high resolution scintillation detectors*. PhD thesis, University Ghent, 2014.

[50] K. Deprez, L. Pato, R. Van Holen, and S. Vandenberghe. Characterization of a SPECT pinhole collimator for optimal detector usage (the lofthole). *Phys. Med. Biol.*, 58(4):859–85, jan 2013.

[51] K. Deprez, R. Van Holen, K. Van Audenhaege, and S. Vandenberghe. Additive manufacturing of high density tungsten collimators. In *J. Nucl. Med.*, volume 53 (suppl.1), pages 2394–2394, 2012.

[52] K. Deprez, S. Vandenberghe, K. Van Audenhaege, J. Van Vaerenbergh, and R. Van Holen. Rapid additive manufacturing of MR compatible multi-pinhole collimators with selective laser melting of tungsten powder. *Med. Phys.*, 40(1):012501 (11pp.), January 2013.

[53] J. Dey. Improvement of performance of cardiac SPECT camera using curved detectors with pinholes. *IEEE Trans. Nucl. Sci.*, 59:334–347, 2012.

[54] F. P. Difilippo and S. Patel. Strategies to reduce artifacts and improve accuracy in multiplexed multi-pinhole small animal SPECT. In *IEEE Nucl. Sci. Conf. Rec.*, pages 3151–3154, November 2009.

[55] D. L. Donoho. Compressed sensing. *IEEE Trans. Inf. Theory*, 52(4):1289–1306, 2006.

[56] M. P. Eckstein, C. K. Abbey, F. O. Bochud, J. L. Bartroff, and J. S. Whiting. Effect of image compression in model and human performance. *Proc. SPIE*, 3663:243–252, 1999.

[57] K. Erlandsson, T. Bukki, A. Gola, D. Salvado, A. Butt, G. Nemeth, C. Piemonte, B. F. Hutton, C. Fiorini, et al. Design considerations for INSERT: A new multi-modality SPECT/MRI system for preclinical and clinical imaging. *J. Nucl. Med.*, 55(supplement 1):2139–2139, 2014.

[58] K. Erlandsson, K. Kacperski, D. van Gramberg, and B. F. Hutton. Performance evaluation of D-SPECT: a novel SPECT system for nuclear cardiology. *Phys. Med. Biol.*, 54(9):2635–2649, 2009.

[59] K. Erlandsson, D. Slavado, A. Bousse, and B. F. Hutton. Evaluation of a partial ring design for the INSERT SPECT/MRI system. *Eur. J. Nucl. Med. Mol. Imaging Phys.*, 2(Suppl 1):A47, 2015.

[60] F. P. Esteves, P. Raggi, R. D. Folks, Z. Keidar, J. Wells Askew, S. Rispler, M. K. O'Connor, L. Verdes, and E. V. Garcia. Novel

solid-state-detector dedicated cardiac camera for fast myocardial perfusion imaging: Multicenter comparison with standard dual detector cameras. *J. Nucl. Cardiol.*, 16(6):927–934, 2009.

[61] F. H. Fahey, B. A. Harkness, J. W. Keyes, M. T. Madsen, and V. Zito. Sensitivity, resolution and image quality with a multi-head SPECT camera. *J. Nucl. Med.*, 33(10):1859–1863, 1992.

[62] R. D. Fiete, H. H. Barrett, W. E. Smith, and K. J. Myers. Hotelling trace criterion and its correlation with human-observer performance. *J. Opt. Soc. Am. A*, 4(5):945–953, May 1987.

[63] A. R. Formiconi. Geometrical response of multihole collimators. *Phys. Med. Biol.*, 43(11):3359–3379, November 1998.

[64] W. M. C. Foulkes, L. Mitas, R. J. Needs, and G. Rajagopal. Quantum Monte Carlo simulations of solids. *Rev. Mod. Phys.*, 73(1):33–83, 2001.

[65] M. Freed, M. A. Kupinski, L. R. Furenlid, D. W. Wilson, and H. H. Barrett. A prototype instrument for single pinhole small animal adaptive SPECT imaging. *Med. Phys.*, 35(2008):1912–1925, 2008.

[66] N. Fuin, S. Pedemonte, S. Arridge, S. Ourselin, and B. F. Hutton. Efficient determination of the uncertainty for the optimization of SPECT system design: A subsampled Fisher Information Matrix. *IEEE Trans. Med. Im.*, 33(3):618–635, 2014.

[67] T. Funk, D. Kirch, J. Koss, E. Botvinick, and B. Hasegawa. A novel approach to multipinhole SPECT for myocardial perfusion imaging. *J. Nucl. Med.*, 47(4):595–602, Apr 2006.

[68] F. Garibaldi, R. Accorsi, M. N. Cinti, E. Cisbani, S. Colilli, F. Cusanno, G. De Vincentis, A. Fortuna, R. Fratoni, B. Girolami, F. Ghio, F. Giuliani, M. Gricia, R. Lanza, A. Loizzo, S. Loizzo, M. Lucentini, S. Majewski, F. Santavenere, R. Pani, R. Pellegrini, A. Signore, F. Scopinaro, and P. P. Veneroni. Small animal imaging by single photon emission using pinhole and coded aperture collimation. *IEEE Trans. Nucl. Sci.*, 52(3):573–579, June 2005.

[69] M. Georgiou, G. Borghi, S. V. Spirou, G. Loudos, and D. R. Schaart. First performance tests of a digital photon counter (DPC) array coupled to a CsI(Tl) crystal matrix for potential use in SPECT. *Phys. Med. Biol.*, 59(10):2415–2430, April 2014.

[70] M. S. Gerber and D. W. Miller. Parallel-hole collimator design. *J. Nucl. Med.*, 15:724–725, 1974.

[71] T. Ghekiere, J. De Beenhouwer, and S. Staelens. Using GATE as a forward projector in iterative SPECT reconstruction. *IEEE Nucl. Sci. Symp. Conf. Rec.*, pages 611–615, 2008.

[72] A. Gholamrezanejhad, S. Mirpour, and M. Giuliano. Future of Nuclear Medicine: SPECT Versus PET. *J. Nucl. Med.*, 50(7):16–18, 2009.

[73] M. Gieles, H. W. A. M. de Jong, and F. J. Beekman. Monte Carlo simulations of pinhole imaging accelerated by kernel-based forced detection. *Phys. Med. Biol.*, 47(11):1853–1867, June 2002.

[74] M. C. Goorden and F. J. Beekman. High-resolution tomography of positron emitters with clustered pinhole SPECT. *Phys. Med. Biol.*, 55(5):1265–1277, MAR 7 2010.

[75] M. C. Goorden, M. C. M. Rentmeester, and F. J. Beekman. Theoretical analysis of full-ring multi-pinhole brain SPECT. *Phys. Med. Biol.*, 54(21):6593–6610, OCT 14 2009.

[76] P. J. Green. Bayesian reconstructions from emission tomography data using a modified EM algorithm. *IEEE Trans. Med. Imag.*, 9(1):84–93, September 1990.

[77] J. J. Griesmer, J. Futey, N. Ojha, and M. Morich. Whole-body PET-MR imaging system initial calibration results. *IEEE Nucl. Sci. Symp. Conf. Rec.*, pages 2174–2176, 2010.

[78] G. T. Gullberg and G. L. Zeng. Three-dimensional SPECT reconstruction of combined conebeam and fan-beam data acquired using a three-detector SPECT system. *Proceedings, Fully Three-Dimensional Image Reconstruction in Radiology and Nuclear Medicine*, page 329, 1995.

[79] D. Gunter, K. Matthews, and C. Ordoñez. The optimal design of non-parallel hole collimators. *IEEE Nucl. Sci. Symp. Conf. Rec. (IEEE, Seattle, WA)*, 3:1344–1348, 1999.

[80] D. L. Gunter. *Collimator design for nuclear medicine*, chapter 8, pages 153–168. San Diego, London: Elsevier Academic, 2004.

[81] F. Habte, P. Stenstrom, A. Rillbert, A. Bousselham, C. Bohm, and S. A. Larsson. A cylindrical SPECT camera with de-centralized read-out scheme. *Nucl. Instrum. Meth.*, 471:80–84, 2001.

[82] M. J. Hamamura, S. Ha, W. W. Roeck, L. T. Muftuler, D. J. Wagenaar, D. Meier, B. E. Patt, and O. Nalcioglu. Development of an MR-compatible SPECT system (MRSPECT) for simultaneous data acquisition. *Phys. Med. Biol.*, 55(6):1563–75, March 2010.

[83] J. Hatazawa, E. Shimosegawa, H. Toyoshima, B. Ardekani, A. Suzuki, T. Okudera, and Y. Miura. Cerebral blood volume in acute brain infarction - A combined study with dynamic susceptibility contrast MRI and 99mTc-HMPAO-SPECT. *Stroke*, 30:800–806, 1999.

[84] R. J. Havelin, B. W. Miller, H. H. Barrett, L. R. Furenlid, J. M. Murphy, R. M. Dwyer, and M. J. Foley. Design and performance of a small-animal imaging system using synthetic collimation. *Phys. Med. Biol.*, 58(10):3397–12, May 2013.

[85] P. C. Hawman and E. J. Haines. The Cardiofocal collimator: a variable-focus collimator for cardiac SPECT. *Phys. Med. Biol.*, 39:439–450, 1994.

[86] B. L. Holman, P. A. Carvalho, R. E. Zimmerman, A. P. Smith, S. Genna, K. A. Johnson, and S. S. Tumeh. Brain perfusion SPECT using an annular single crystal camera: initial clinical experience. *J. Nucl. Med.*, 31(9):1456–61, 1990.

[87] M. Horger and R. Bares. The role of single-photon emission computed tomography/computed tomography in benign and malignant bone disease. *Semin. Nucl. Med.*, 36(4):286–294, Oct. 2006.

[88] H. M. Hudson and R. S. Larkin. Accelerated image reconstruction using ordered subsets of projection data. *IEEE Trans. Med. Imaging*, 13(4):601–09, January 1994.

[89] B. F. Hutton. Angular sampling necessary for clinical SPECT. *J. Nucl. Med.*, 37:1915–1916, 1996.

[90] M. Ichise, H. Toyama, L. Fornazzari, J. R. Ballinger, and J. C. Kirsh. Iodine-123-IBZM dopamine D2 receptor and technetium-99m-HMPAO brain perfusion SPECT in the evaluation of patients with and subjects at risk for Huntington's disease. *J. Nucl. Med.*, 34(8):1274–1281, 1993.

[91] ICRU. Report no. 33. Technical report, International Commission on Radiation Units and Measurements, 1980.

[92] S. Jan, G. Santin, D. Strul, S. Staelens, K. Assié, D. Autret, D. Avner, R. Barbier, M. Bardiès, P. Bloomfield, D. Brasse, V. Breton, P. Bruyndonckx, I. Buvat, A. Chatziioannou, Y. Choi, Y. Chung, C. Comtat, D. Donnarieix, L. Ferrer, S. Glick, C. Groiselle, S. Kerhoas-Cavata, A. Kirov, V. Kohli, M. Koole, M. Krieguer, J. van der Laan, F. Lamare, G. Largeron, C. Lartizien, D. Lazaro, M. Maas, L. Maigne, F. Mayet, F. Melot, S. Nehmeh, E. Pennacchio, J. Perez, U. Pietrzyk, F. Rannou, M. Rey, D. Schaart, R. Schmidtstein, L. Simon, T. Song, J. Vieira, D. Visvikis, R. Van de Walle, E. Wieers, and C. Morel. GATE - a simulation toolkit for PET and SPECT. *Phys. Med. Biol.*, 49(19):1–19, 2004.

[93] R. J. Jaszczak, K. L. Greer, J. E. Bowsher, S. D. Metzler, R. Ter-Antonyan, and K. V. Bobkov. Helical-path, half-cone-beam acquisition for SPECT brain imaging. *IEEE Nucl. Sci. Conf. R.*, 3:1837–1841, 2006.

[94] R. J. Jaszczak, J. Li, H. Wang, and R. E. Coleman. Three-dimensional SPECT reconstruction of combined cone beam and parallel beam data. *Phys. Med. Biol.*, 37:535–548, 1992.

[95] R. J. Jaszczak, J. Li, H. Wang, M. R. Zalutsky, and R. E. Coleman. Pinhole collimation for ultra-high-resolution, small-field-of-view SPECT. *Phys. Med. Biol.*, 39:425–437, 1994.

[96] P. Jehenson, M. Westphal, and N. Schuff. Analytical method for the compensation of eddy-current effects induced by pulsed magnetic field gradients in NMR systems. *J. Magn. Reson.*, 90(2):264–278, 1990.

[97] Y. Jin, J. Liu, W. Chang, X. Xu, Y. Liu, and G. Huang. Calibration and correction of a modular cylindrical SPECT system (McSPECT-II). *IEEE Trans. Nucl. Sci.*, 42(6):1777–80, 1995.

[98] P. M. Joseph. An improved algorithm for reprojecting rays through pixel images. *IEEE Trans. Med. Imag.*, 1(3):192–6, January 1982.

[99] M. S. Judenhofer, C. Catana, B. K. Swann, S. B. Siegel, W.-I. Jung, R. E. Nutt, S. R. Cherry, C. D. Claussen, and B. J. Pichler. PET/MR images acquired with a compact MR-compatible PET detector in a 7-T magnet. *Radiology*, 244(3):807–814, 2007.

[100] C. Kamphuis and F. J. Beekman. The use of offset cone-beam collimators in a dual head system for combined emission transmission brain SPECT: a feasibility study. *IEEE Trans. Nucl. Sci.*, 45(3):1250–54, 1998.

[101] C. Kamphuis, F. J. Beekman, and B. F. Hutton. Optimal collimator hole dimensions for half cone-beam brain SPECT. *Proceedings, Fully Three-Dimensional Image Reconstruction in Radiology and Nuclear Medicine*, pages 271–275, 1999.

[102] G. A. Kastis, H. B. Barber, H. H. Barrett, S. J. Balzer, D. Lu, D. G. Marks, G. Stevenson, J. M. Woolfenden, M. Appleby, and J. Tueller. Gamma-ray imaging using a CdZnTe pixel array and a high-resolution , parallel-hole collimator. *IEEE Nucl. Sci. Symp. Conf. Rec.*, 1:553–558, 1999.

[103] R. Kawashima, M. Koyama, H. Ito, S. Yoshioka, K. Sato, S. Ono, R. Goto, T. Sato, and H. Fukuda. Normal cerebral perfusion of 99mTc-ECD brain SPECT–evaluation by an anatomical standardization technique. *Kaku Igaku. Jpn. J. Nucl. Med.*, 33:69–72, 1996.

[104] V. Keereman, Y. Fierens, T. Broux, Y. De Deene, M. Lonneux, and S. Vandenberghe. MRI-based attenuation correction for PET/MRI using ultrashort echo time sequences. *J. Nucl. Med.*, 51(5):812–8, May 2010.

[105] E. L. Keller. Optimum dimensions of parallel-hole, multi-aperture collimators for gamma-ray cameras. *J. Nucl. Med.*, 9(6):233–235, Jun 1968.

[106] P. L. Kench, J. Lin, M. C. Gregoire, and S. R. Meikle. An investigation of inconsistent projections and artefacts in multi-pinhole SPECT with axially aligned pinholes. *Phys. Med. Biol.*, 56(23):7487–7503, December 2011.

[107] H. J. Kim, B. R. Zeeberg, F. H. Fahey, A. N. Bice, E. J. Hoffman, and R. C. Reba. Three-dimensional SPECT simulations of a complex three-dimensional mathematical brain model and measurements of the three-dimensional physical brain phantom. *J. Nucl. Med.*, 32(10):1923–30, October 1991.

[108] W. P. Klein, H. H. Barrett, I. W. Pang, D. D. Patton, M. M. Rogulski, J. D. Sain, and W. E. Smith. FASTSPECT: electrical and mechanical

design of a high-resolution dynamic SPECT imager. *IEEE Nucl. Sci. Conf. R.*, 2:931–33, 1996.

[109] A. Kolb, H. F. Wehrl, M. Hofmann, M. S. Judenhofer, L. Eriksson, R. Ladebeck, M. P. Lichy, L. Byars, C. Michel, H. P. Schlemmer, M. Schmand, C. D. Claussen, V. Sossi, and B. J. Pichler. Technical performance evaluation of a human brain PET/MRI system. *Eur. Radiol.*, 22:1776–1788, 2012.

[110] D. J. Kwekkeboom, H. van Urk, B. K. Pauw, S. W. Lamberts, P. P. Kooij, R. P. Hoogma, and E. P. Krenning. Octreotide scintigraphy for the detection of paragangliomas. *J. Nucl. Med.*, 34(6):873–878, 1993.

[111] M. L-J and N. H. Clinthorne. A modified uniform Cramer-Rao bound for multiple pinhole aperture design. *IEEE Trans. Med. Imag.*, 23(7):896–902, Jul 2004.

[112] C. Lackas, N. U. Schramm, J. W. Hoppin, U. Engeland, A. Wirrwar, and H. Halling. T-SPECT: A novel imaging technique for small animal research. *IEEE Trans. Nucl. Sci.*, 52:181–187, 2005.

[113] Y. H. Lau, B. F. Hutton, and F. J. Beekman. Choice of collimator for cardiac SPET when resolution compensation is included in iterative reconstruction. *Eur. J. Nucl. Med. Mol.*, 28(1):39–47, January 2001.

[114] M.-W. Lee, W.-T. Lin, and Y.-C. Chen. Design optimization of multi-pinhole micro-SPECT configurations by signal detection tasks and system performance evaluations for mouse cardiac imaging. *Phys. Med. Biol.*, 60(2):473–499, January 2015.

[115] J. Li, R. J. Jaszczak, A. Van Mullekom, C. Scarfone, K. L. Greer, and R. E. Coleman. Half-cone beam collimation for triple-camera SPECT systems. *J. Nucl. Med.*, 37(3):498–02, March 1996.

[116] N. Li and L.-J. Meng. Adaptive angular sampling for SPECT imaging. *IEEE Trans. Nucl. Sci.*, 58(5):2205–2218, October 2011.

[117] M. Lijowski, S. Caruthers, G. Hu, H. Zhang, M. J. Scott, T. Williams, T. Erpelding, A. H. Schmieder, G. Kiefer, G. Gulyas, P. S. Athey, P. J. Gaffney, S. A. Wickline, and G. M. Lanza. High sensitivity: high-resolution SPECT-CT/MR molecular imaging of angiogenesis in the Vx2 model. *Invest. Radiol.*, 44(1):15–22, 2009.

[118] S. M. Lim, A. Katsifis, V. L. Villemagne, R. Best, G. Jones, M. Saling, J. Bradshaw, J. Merory, M. Woodward, M. Hopwood, and C. C. Rowe. The 18F-FDG PET cingulate island sign and comparison to 123I-beta-CIT SPECT for diagnosis of dementia with Lewy bodies. *J. Nucl. Med.*, 50(10):1638–1645, 2009.

[119] J. Lin. On artifact-free projection overlaps in multi-pinhole tomographic imaging. *IEEE Trans. Med. Imag.*, 32(12):2215–2229, December 2013.

[120] J. Lin and S. R. Meikle. SPECT using asymmetric pinholes with truncated projections. *Phys. Med. Biol.*, 56(13):4103–4118, July 2011.

[121] K. Lin, I.-T. Hsiao, C. Wietholt, Y. Chung, C. Chen, and T. Yen. Performance evaluation of an animal SPECT using modified NEMA standards. *J. Nucl. Med.*, 49(suppl 1):402P (1pp.), 2008.

[122] C. Liu, J. Xu, and B. M. W. Tsui. Development and evaluation of rotating multi-segment variable-angle slant-hole SPECT. *J. Nucl. Med.*, 48(Supplement 2):161P (1pp.), 2007.

[123] C. Liu, J. Xu, and B. M. W. Tsui. Myocardial perfusion SPECT using a rotating multi-segment slant-hole collimator. *Med. Phys.*, 37(4):1610–1618, 2010.

[124] B. F. Logan, S. O. Rice, and R. F. Wick. Series for computing current flow in a rectangular block. *J. Appl. Phys.*, 42(7):2975–2980, 1971.

[125] J.-F. Lu, H. Zhang, J.-S. Wu, C.-J. Yao, D.-X. Zhuang, T.-M. Qiu, W.-B. Jia, Y. Mao, and L.-F. Zhou. Awake intraoperative functional MRI (ai-fMRI) for mapping the eloquent cortex: Is it possible in awake craniotomy? *NeuroImage Clin.*, 2:132–142, 2013.

[126] M. T. Madsen, W. Chang, and R. D. Hichwa. Spatial resolution and count density requirements in brain SPECT imaging. *Phys. Med. Biol*, 37:1625–1636, 1992.

[127] S. Mahmood, K. Erlandsson, I. Cullum, and B. F. Hutton. Experimental results from a prototype slit-slat collimator with mixed multiplexed and non-multiplexed data. *Phys. Med. Biol.*, 56(14):4311–31, June 2011.

[128] S. T. Mahmood, K. Erlandsson, I. Cullum, and B. F. Hutton. Design of a novel slit-slat collimator system for SPECT imaging of the human brain. *Phys. Med. Biol.*, 54(11):3433–49, June 2009.

[129] S. T. Mahmood, K. Erlandsson, I. Cullum, and B. F. Hutton. The potential for mixed multiplexed and non-multiplexed data to improve the reconstruction quality of a multi-slit-slat collimator SPECT system. *Phys. Med. Biol.*, 55(8):2247–68, April 2010.

[130] O. V. Makarova, G. Yang, P. T. Amstutz, and C. M. Tang. Fabrication of antiscatter grids and collimators for X-ray and gamma-ray imaging by lithography and electroforming. *Microsys. Technol.*, 14:1613–1619, 2008.

[131] G. Mariani, L. Bruselli, and A. Duatti. Is PET always an advantage versus planar and SPECT imaging? *Eur. J. Nucl. Med. Mol.*, 35(8):1560–1565, 2008.

[132] G. Mariani, L. Bruselli, T. Kuwert, E. E. Kim, A. Flotats, O. Israel, M. Dondi, and N. Watanabe. A review on the clinical uses of SPECT/CT. *Eur. J. Nucl. Med. Mol.*, 37:1959–1985, 2010.

[133] G. Mariani and H. W. Strauss. Positron emission and single-photon emission imaging: synergy rather than competition. *Eur. J. Nucl. Med. Mol.*, 38(7):1189–1190, July 2011.

[134] R. L. Mather. Gamma-ray collimator penetration and scattering effects. *J. Appl. Phys.*, 28:1200–1207, 1957.

[135] H. Matsuda, K. Kinuya, S. Higashi, Y. Kawasaki, H. Sumiya, N. Shuke, K. Hisada, J. Yamashita, and N. Yamaguchi. Evaluation of brain perfusion SPECT imaging using 99mTc-ECD. *Kaku Igaku. Jpn. J. Nucl. Med.*, 28(7):701–709, 1991.

[136] S. J. McQuaid, S. Southekal, M. F. Kijewski, and S. C. Moore. Joint optimization of collimator and reconstruction parameters in SPECT imaging for lesion quantification. *Phys. Med. Biol.*, 56(21):6983–7000, October 2011.

[137] D. W. McRobbie, E. A. Moore, M. J. Graves, and M. R. Prince. *MRI from Picture to Proton*. Cambridge university press, 2006.

[138] D. Meier, D. J. Wagenaar, S. Chen, J. Xu, J. Yu, and B. M. W. Tsui. A SPECT camera for combined MRI and SPECT for small animals. *Nucl. Instr. Meth. Phys. Res. A*, 652:731–734, 2011.

[139] D. Meier, D. J. Wagenaar, G. Mæhlum, B. Sundal, B. E. Patt, S. Chen, J. Xu, B. M. W. Tsui, M. Hamamura, S. Ha, W. W.

Roeck, and O. Nalcioglu. Development of pre-clinical SPECT for MRI. *IFMBE Proceedings*, 25(2):798–801, 2009.

[140] S. R. Meikle, P. Kench, M. Kassiou, and R. B. Banati. Small animal SPECT and its place in the matrix of molecular imaging technologies. *Phys. Med. Biol.*, 50:R45–R61, 2005.

[141] S. R. Meikle, P. Kench, A. G. Weisenberger, R. Wojcik, M. F. Smith, S. Majewski, S. Eberl, R. R. Fulton, A. B. Rosenfeld, and M. J. Fulham. A prototype coded aperture detector for small animal SPECT. *IEEE Nucl. Sci. Symp. Conf. Rec.*, 3:1580–1584, 2001.

[142] S. R. Meikle, P. L. Kench, and J. Lin. Design considerations of small-animal SPECT cameras. In H. Zaidi, editor, *Molecular imaging of small animals - Instrumentation and Applications*. Springer, Geneva, Switzerland, 2014.

[143] S. R. Meikle, R. Wojcik, A. G. Weisenberger, M. F. Smith, S. Majewski, P. Kench, S. Eberl, R. R. Fulton, M. Lerch, and A. B. Rosenfeld. CoALA-SPECT: A coded aperture laboratory animal SPECT system for pre clinical imaging. *IEEE Nucl. Sci. Symp. Conf. Rec.*, 2:1061–1065, 2002.

[144] L.-J. Meng, J.-W. Tan, and G. Fu. Design study of an MRI compatible ultra-high resolution SPECT for in vivo mice brain imaging. *IEEE Nucl. Sci. Symp. Conf. Rec. 2007*, pages 2956–60, 2007.

[145] S. D. Metzler, R. Accorsi, A. S. Ayan, and R. J. Jaszczak. Slit-slat and multi-slit-slat collimator design and experimentally acquired phantom images from a rotating prototype. *IEEE Trans. Nucl. Sci.*, 57(1):125–134, 2010.

[146] S. D. Metzler, R. Accorsi, J. R. Novak, A. S. Ayan, and R. J. Jaszczak. On-axis sensitivity and resolution of a slit-slat collimator. *J. Nucl. Med.*, 47(11):1884–1890, 2006.

[147] S. D. Metzler, J. E. Bowsher, and R. J. Jaszczak. Geometrical similarities of the Orlov and Tuy sampling criteria and a numerical algorithm for assessing sampling completeness. *IEEE Nucl. Sci. Conf. Rec.*, 50(5):1241–1245, October 2002.

[148] S. D. Metzler, J. E. Bowsher, M. F. Smith, and R. J. Jaszczak. Analytic determination of pinhole collimator sensitivity with penetration. *IEEE Trans. Med. Imag.*, 20(8):730–41, August 2001.

[149] S. D. Metzler, K. L. Greer, and R. J. Jaszczak. Helical pinhole SPECT for small-animal imaging: A method for addressing sampling completeness. *IEEE Trans. Nucl. Sci.*, 50(5):1575–1583, October 2003.

[150] B. D. Milbrath, J. E. Fast, R. T. Kouzes, B. J. Choate, W. K. Hensley, and J. E. Schweppe. Comparison of LaBr3:Ce and NaI(Tl) scintillators for radio-isotope identification devices. Technical Report AC05-76RL01830, Pacific Northwest National Laboratory, Richland, Washington, April 2006.

[151] B. W. Miller, J. W. Moore, H. H. Barrett, T. Fryé, S. Adler, J. Sery, and L. R. Furenlid. 3D printing in X-ray and Gamma-Ray Imaging: A novel method for fabricating high-density imaging apertures. *Nucl. Instr. Meth. Phys. Res. A*, 659(1):262–268, December 2011.

[152] B. J. Min, Y. Choi, N.-Y. Lee, J. H. Jung, K. J. Hong, J. H. Kang, W. Hu, K. Lee, Y. B. Ahn, and J. Joung. Unmatched projector/backprojector pair for demultiplexing in multipinhole emission computed tomography. *Opt. Eng.*, 49(12):127004, 2010.

[153] B. J. Min, Y. Choi, N.-Y. Lee, K. Lee, Y. B. Ahn, and J. Joung. Design consideration of a multipinhole collimator with septa for ultra high-resolution silicon drift detector modules. *Nucl. Instr. Meth. Phys. Res. A*, 606(3):755–761, July 2009.

[154] L. Moerman, D. De Naeyer, P. Boon, and F. De Vos. P-glycoprotein at the blood-brain barrier: kinetic modeling of 11C-desmethylloperamide in mice using a 18F-FDG μPET scan to determine the input function. *Eur. J. Nucl. Med. Mol. Imaging Res.*, 1(1):1–9, 2011.

[155] G. S. P. Mok, B. M. W. Tsui, and F. J. Beekman. The effects of object activity distribution on multiplexing multi-pinhole SPECT. *Phys. Med. Biol.*, 56(8):2635–2650, April 2011.

[156] G. S. P. Mok, J. Yu, Y. Du, Y. Wang, and B. M. W. Tsui. Evaluation of a multi-pinhole collimator for imaging small animals with different sizes. *Mol. Imaging Biol.*, 14(1):60–69, February 2012.

[157] H. C. Montgomery. Method for measuring electrical resistivity of anisotropic materials. *J. Appl. Phys.*, 42(7):2971–75, 1971.

[158] R. H. Moore, N. M. Alpert, and H. W. Strauss. A variable angle slant-hole collimator. *J. Nucl. Med.*, 24(1):61–65, 1983.

[159] S. C. Moore, M. Cervo, S. D. Metzler, J. M. Udias, and J. L. Herraiz. An iterative method for eliminating artifacts from multiplexed data in pinhole SPECT. *Proceedings, Fully Three-Dimensional Image Reconstruction in Radiology and Nuclear Medicine*, pages 515–517, 2015.

[160] S. C. Moore, M. F. Kijewski, M. Cervo, C. Mauceri, L. Horky, and M.-A. Park. Reconstruction of brain SPECT data from an ultra-short cone-beam collimator paired with a fan-beam collimator. *Proceedings, Fully Three-Dimensional Image Reconstruction in Radiology and Nuclear Medicine, Newport, RI, USA*, 2015. paper 40.

[161] S. C. Moore, M. F. Kijewski, and G. El Fakhri. Collimator optimization for detection and quantitation tasks: application to gallium-67 imaging. *IEEE Trans. Med. Imag.*, 24(10):1347–1356, Oct 2005.

[162] S. C. Moore, K. Kouris, and I. Cullum. Collimator design for single photon emission tomography. *Eur. J. Nucl. Med. Mol.*, 19(2):138–150, 1992.

[163] S. C. Moore, M. MacKnight, M.-A. Park, and R. E. Zimmerman. Reduction of micro-SPECT streak artifacts from imperfect system modeling. *IEEE Nucl. Sci. Symp. Conf. Rec. 2007*, 5:3361–3363, 2007.

[164] M. A. Morich, D. A. Lampman, W. R. Dannels, and F. T. D. Goldie. Exact temporal eddy current compensation in magnetic resonance imaging systems. *IEEE Trans. Med. Imag.*, 7(3):247–254, 1988.

[165] W. W. Moses and K. S. Shah. Potential for RbGd2Br7:Ce, LaBr3:Ce, LaBr3:Ce, and LuI3:Ce in nuclear medical imaging. *Nucl. Instrum. Meth. A.*, 537(1-2):317–20, 2005.

[166] T. Mou, H. Jing, W. Yang, W. Fang, C. Peng, F. Guo, X. Zhang, Y. Pang, and Y. Ma. Preparation and biodistribution of [18F]FP2OP as myocardial perfusion imaging agent for PET. *Bioorg. Med. Chem.*, 18(3):1312–1320, February 2010.

[167] R. A. Moyer. A low-energy multihole converging collimator compared with a pinhole collimator. *J. Nucl. Med.*, 15(2):59–64, 1974.

[168] G. Muehllehner. A diverging collimator for gamma-ray imaging cameras. *J. Nucl. Med.*, 10(4):197–201, 1969.

[169] G. Muehllehner. Effect of resolution improvement on required count density in ECT imaging: a computer simulation. *Phys. Med. Biol.*, 30(2):163–173, February 1985.

[170] G. Muehllehner. Effect of resolution improvement on required count density in ECT imaging: a computer simulation. *Phys. Med. Biol.*, 2:163–73, 1985.

[171] K. J. Myers and H. H. Barrett. Addition of a channel mechanism to the ideal-observer model. *J. Opt. Soc. Am.*, 4(2447):2447–57, 1987.

[172] K. J. Myers, H. H. Barrett, M. C. Borgstrom, D. D. Patton, and G. W. Seeley. Effect of noise correlation on detectability of disk signals in medical imaging. *J. Opt. Soc. Am.*, 2(1752):1752–59, 1985.

[173] P. Nillius and M. Danielsson. Theoretical bounds and system design for multipinhole SPECT. *IEEE Trans. Med. Imag.*, 29(7):1390–400, July 2010.

[174] A. V. Ochoa, L. Ploux, R. Mastrippolito, Y. Charon, P. Lanièce, L. Pinot, and L. Valentin. An original emission tomograph for in vivo brain imaging of small animals. *IEEE Trans. Nucl. Sci.*, 44(4):1533–1537, 1997.

[175] K. Ogawa and M. Muraishi. Feasibility study on an ultra-high-resolution SPECT with CdTe detectors. *IEEE Trans. Nucl. Sci.*, 57(1):17–24, February 2010.

[176] S. S. Orlov. Theory of three-dimensional reconstruction: I. Conditions for a complete set of projections. *Sov. Phys. Crystallogr.*, 20:312–314, 1975.

[177] S. S. Orlov. Theory of three-dimensional reconstruction. II. The recovery operator. *Sov. Phys. - Crystallogr.*, 20:429–433, 1975.

[178] J. G. Ott, F. Becce, P. Monnin, S. Schmidt, F. O. Bochud, and F. R. Verdun. Update on the non-prewhitening model observer in computed tomography for the assessment of the adaptive statistical and model-based iterative reconstruction algorithms. *Phys. Med. Biol.*, 59:4047–4064, 2014.

[179] D. Paix. Pinhole imaging of gamma rays. *Phys. Med. Biol.*, 12:489–00, 1967.

[180] M.-A. Park, M. Kijewski, and S. C. Moore. Effects of hole tapering on cone-beam collimation for brain SPECT imaging. *Nucl. Instrum. Meth. A.*, 569(2):188–92, December 2006.

[181] M.-A. Park, M. F. Kijewski, L. Horky, M. Keijzers, R. Keijzers, L. Kalfin, J. Crough, M. Goswami, and S. C. Moore. Fabrication and calibration of a novel high-sensitivity collimator for brain SPECT imaging. *Annual Meeting of the American Association of Physicists in Medicine (AAPM), Austin, TX*, 41(106), 2014. presentation SU-C-9A-7.

[182] M.-A. Park, S. C. Moore, and M. F. Kijewski. Brain SPECT with short focal-length cone-beam collimation. *Med. Phys.*, 32(7):2236–44, Jul 2005.

[183] M.-A. Park, S. C. Moore, and M. F. Kijewski. System and method for performing Single Photon Emission Computed Tomography (SPECT) with a focal-length cone-beam collimation. *US patent 20080302950 A1*, 12 2008.

[184] K. Parnham, S. Chowdhury, J. Li, D. Wagenaar, and B. Patt. Second-generation, tri-modality pre-clinical imaging system. In *IEEE Nucl. Sci. Conf. Rec.*, volume 3, pages 1802–1805, 2006.

[185] L. Pato, S. Vandenberghe, B. Vandeghinste, and R. Van Holen. Evaluation of Fisher Information Matrix approximation-based methods for fast assessment of image quality in pinhole SPECT. *IEEE Trans. Med. Imag.*, 2015. published online.

[186] A. K. Paul and H. A. Nabi. Gated myocardial perfusion SPECT: basic principles, technical aspects, and clinical applications. *J. Nucl. Med. Technol.*, 32(4):179–187, December 2004.

[187] I. Perali, A. Celani, L. Bombelli, C. Fiorini, F. Camera, E. Clementel, S. Henrotin, G. Janssens, D. Prieels, F. Roellinghoff, J. Smeets, F. Stichelbaut, and F. V. Stappen. Prompt gamma imaging of proton pencil beams at clinical dose rate. *Phys. Med. Biol.*, 59:5849–5871, 2014.

[188] T. E. Peterson and L. R. Furenlid. SPECT detectors: the Anger Camera and beyond. *Phys. Med. Biol.*, 56:R145–R182, 2011.

[189] M. Quadri, G. Cossu, V. Saddi, E. J. Simons, D. Murgia, M. Melis, A. Ticca, B. A. Oostra, and V. Bonifati. Broadening the phenotype of TARDBP mutations: the TARDBP Ala382Thr mutation and Parkinsons disease in Sardinia. *Neurogenetics*, 12(3):203–209, 2011.

[190] J. Radon. Über die bestimmung von funktionen durch ihre integralwerte längs gewisser mannigfaltigkeiten. *Ber. Saechs. Akad. Wiss. Leipzig, Math.-Phys. Kl.*, 69:262–277, 1917.

[191] A. Rahmim and H. Zaidi. PET versus SPECT: strengths, limitations and challenges. *Nucl. Med. Commun.*, 29(3):193–207, March 2008.

[192] A. Rambaut and N. C. Grassly. Seq-Gen: an application for the Monte Carlo simulation of DNA sequence evolution along phylogenetic trees. *Comput. Appl. Biosci.*, 13(3):235–238, 1997.

[193] D. Renker. New trends on photodetectors. *Nucl. Instr. Meth. Phys. Res. A*, 571:1–6, 2007.

[194] M. C. M. Rentmeester, F. van der Have, and F. J. Beekman. Optimizing multi-pinhole SPECT geometries using an analytical model. *Phys. Med. Biol.*, 52(9):2567–2581, May 2007.

[195] C. Robert, G. Montémont, V. Rebuffel, L. Verger, and I. Buvat. Optimization of a parallel hole collimator/CdZnTe gamma-camera architecture for scintimammography. *Med. Phys.*, 38(2011):1806–1819, 2011.

[196] M. M. Rogulski, H. B. Barber, H. H. Barrett, R. L. Shoemaker, and J. M. Woolfenden. Ultra-high-resolution brain SPECT imaging: simulation results. *IEEE Trans. Nucl. Sci.*, 40(4):1123–1129, 1993.

[197] J. P. Rolland and H. H. Barrett. Effect of random background inhomogeneity on observer detection performance. *J. Opt. Soc. Am. A*, 9(5):649–658, 1992.

[198] E. Roncali and S. R. Cherry. Application of silicon photomultipliers to positron emission tomography. *Ann. Biomed. Eng.*, 39(4):1358–1377, 2011.

[199] R. K. Rowe, J. N. Aarsvold, H. H. Barrett, J. C. Chen, W. P. Klein, B. A. Moore, I. W. Pang, D. D. Patton, and T. A. White. A stationary hemispherical SPECT imager for three-dimensional brain imaging. *J. Nucl. Med.*, 34(3):474–80, March 1993.

[200] M. Rozler and W. Chang. Collimator interchange system for adaptive cardiac imaging in C-SPECT. *IEEE Trans. Nucl. Sci.*, 58(5):2226–2233, October 2011.

[201] D. Ruijters, R. ter Haar, B. M., and P. Suetens. Efficient GPU-based texture interpolation using uniform B-splines. *J. Graph. GPU Game Tools*, 13(4):61–69, 2008.

[202] A. Sabbir Ahmed, G. H. Kramer, W. Semmler, and J. Peter. Performance study of a fan beam collimator designed for a multi-modality small animal imaging device. *Nucl. Instr. Meth. Phys. Res. A*, 629(1):368–376, November 2011.

[203] A. Samoudi, K. Van Audenhaege, G. Vermeeren, M. Poole, L. Martens, R. Van Holen, and W. Joseph. Influence of collimator insertion on eddy currents for different resistivities of tungsten. In *Magn. Reson. Med.*, pages 2545–2545, 2014.

[204] A. Samoudi, K. Van Audenhaege, G. Vermeeren, M. Poole, L. Martens, R. Van Holen, and W. Joseph. Temporal analysis of z-gradient coil eddy current in tungsten collimator with different resistivities for SPECT/MRI. In *Eur. J. Nucl. Med. Mol. Imaging Phys.*, volume 1 (suppl.1), page A22, 2014.

[205] A. M. Samoudi, K. Van Audenhaege, G. Vermeeren, M. Poole, E. Tanghe, L. Martens, R. Van Holen, and W. Joseph. Analysis of eddy currents induced by transverse and longitudinal gradient coils in different tungsten collimators geometries for SPECT/MRI integration. *Magn. Reson. Med.*, published online 2014.

[206] D. R. Schaart, H. T. van Dam, S. Seifert, R. Vinke, P. Dendooven, H. Löhner, and F. J. Beekman. A novel, SiPM-array-based, monolithic scintillator detector for PET. *Phys. Med. Biol.*, 54:3501–3512, 2009.

[207] O. Schillaci, L. Filippi, C. Manni, and R. Santoni. Single-photon emission computed tomography/computed tomography in brain tumors. *Semin. Nucl. Med.*, 37(1):34–47, 2007.

[208] N. U. Schramm, G. Ebel, U. Engeland, T. Schurrat, M. Behe, and T. M. Behr. High-resolution SPECT using multipinhole collimation. *IEEE Trans. Nucl. Sci.*, 50:315–320, 2003.

[209] V. Schulz, T. Solf, B. Weissler, P. Gebhardt, P. Fischer, M. Ritzert, V. Mlotok, C. Piemonte, N. Zorzi, M. Melchiorri, S. Vandenberghe,

V. Keereman, T. Schaeffter, and P. K. Marsden. A preclinical PET / MR insert for a human 3T MR scanner. *IEEE Nucl. Sci. Symp. Conf. Rec.*, pages 2577–2579, 2009.

[210] W. P. Segars and B. M. W. Tsui. MCAT to XCAT: The evolution of 4-D computerized phantoms for imaging research. In *IEEE Nucl. Sci. Conf. Rec.*, pages 1954–1968, November 2009.

[211] C. E. Shannon. Communication in the presence of noise. *Proc. IRE*, 37:10–21, 1949.

[212] P. Sharp, D. C. Barber, D. G. Brown, A. E. Burgess, C. E. Metz, K. J. Myers, C. J. Taylor, and R. F. Wagner. Medical imaging - The assessment of image quality. *International commission on radiation units and measurement, Bethesda, MD, ICRU Report*, 54, 1996.

[213] S. Shokouhi, S. D. Metzler, D. W. Wilson, and T. E. Peterson. Multi-pinhole collimator design for small-object imaging with SiliSPECT: a high-resolution SPECT. *Phys. Med. Biol.*, 54(2):207–25, January 2009.

[214] S. Shokouhi, D. W. Wilson, S. D. Metzler, and T. E. Peterson. Evaluation of image reconstruction for mouse brain imaging with synthetic collimation from highly multiplexed SiliSPECT projections. *Phys. Med. Biol.*, 55(17):5151–68, September 2010.

[215] B. D. Smith. Image reconstruction from cone-beam projections: necessary and sufficient conditions and reconstruction methods. *IEEE Trans. Med. Imag.*, MI-4(1):14–25, January 1985.

[216] M. F. Smith and R. J. Jaszczak. An analytic model of pinhole aperture penetration for 3D pinhole SPECT image reconstruction. *Phys. Med. Biol.*, 43(4):761–75, April 1998.

[217] M. F. Smith, R. J. Jaszczak, and H. Wang. Pinhole aperture design for ^{131}I tumor imaging. *IEEE Trans. Nucl. Sci.*, 44(3):1154–1160, June 1997.

[218] M. F. Smith, S. Majewski, and A. G. Weisenberger. Optimizing pinhole and parallel hole collimation for scintimammography with compact pixellated detectors. *IEEE Trans. Nucl. Sci.*, 50(3):321–326, June 2003.

[219] Y. Sonoda, T. Kumabe, T. Takahashi, R. Shirane, and T. Yoshimoto. Clinical usefulness of 11C-MET PET and 201T1 SPECT for differentiation of recurrent glioma from radiation necrosis. *Neurol. Med. Chir.*, 38(6):342–347; discussion 347–348, 1998.

[220] S. Staelens, K. Vunckx, J. De Beenhouwer, F. J. Beekman, Y. Dasseler, J. Nuyts, and I. Lemahieu. GATE simulations for optimization of pinhole imaging. *Nucl. Instr. Meth. Phys. Res. A*, 569(2):359–363, December 2006.

[221] C. D. Stone, M. F. Smith, K. L. Greer, and R. J. Jaszczak. A combined half-cone beam and parallel hole collimation system for SPECT brain imaging. *IEEE Trans. Nucl. Sci.*, 45(3):1219–24, June 1998.

[222] D. Strul, D. Cash, S. F. Keevil, P. Halstead, S. C. R. Williams, and P. K. Marsden. MR-compatible shields for 511 keV gamma photons: a feasibility study. *IEEE Nucl. Sci. Symp. Conf. Rec. 2000*, 3:16/11–16/15, 2001.

[223] D. Strul, D. Cash, S. F. Keevil, P. Halstead, S. C. R. Williams, and P. K. Marsden. Gamma shielding materials for MR-compatible PET. *IEEE Trans. Nucl. Sci.*, 50(1):60–69, February 2003.

[224] T. Takahashi and S. Watanabe. Recent progress in CdTe and CdZnTe detectors. *IEEE Trans. Nucl. Sci.*, 48(4):950–959, 2001.

[225] J.-W. Tan, L. Cai, and L.-J. Meng. A prototype of the MRI-compatible ultra-high resolution SPECT for in vivo mice brain imaging. *IEEE Nucl. Sci. Symp. Conf. Rec. 2009*, 61801:2800–05, October 2009.

[226] R. Ter-Antonyan, R. J. Jaszczak, J. E. Bowsher, K. L. Greer, and S. D. Metzler. Brain SPECT simulation using half-cone-beam collimation and single-revolution helical-path acquisition. *IEEE Trans. Nucl. Sci.*, 54(3):475–79, 2007.

[227] B. M. W. Tsui. Letter. *Phys. Med. Biol.*, 23:1203 (1pp.), 1978.

[228] B. M. W. Tsui, C. E. Metz, F. B. Atkins, S. J. Starr, and R. N. Beck. A comparison of optimum detector spatial resolution in nuclear imaging based on statistical theory and observer performance. *Phys. Med. Biol.*, 23(4):654–676, 1978.

[229] H. K. Tuy. An inversion formula for cone-beam reconstruction. *SIAM J. Appl. Math.*, 43(3):546–552, 1983.

[230] P. E. B. Vaissier, M. C. Goorden, A. Taylor, and F. Beekman. Fast count-regulated OSEM reconstruction with adaptive resolution recovery. *IEEE Trans. Med. Imag.*, 32(12):2250–2261, August 2013.

[231] P. E. B. Vaissier, M. C. Goorden, B. Vastenhouw, F. van der Have, R. M. Ramakers, and F. J. Beekman. Fast spiral SPECT with stationary γ-cameras and focusing pinholes. *J. Nucl. Med.*, 53:1292–1299, June 2012.

[232] V. Valotassiou, G. Wozniak, N. Sifakis, C. Iliadis, and P. Georgoulias. SPECT Imaging and Cerebrovascular Disease. *Vasc. Dis. Prev.*, 4(2):165–170, 2007.

[233] K. Van Audenhaege, D. Bovijn, R. Van Holen, and S. Vandenberghe. An MR-compatible shutter mechanism for stationary multi-pinhole SPECT of large objects. In *PET/MR and SPECT/MR: New Paradigms for Combined Modalities in Molecular Imaging Conference*, pages 65–65, 2012.

[234] K. Van Audenhaege, K. Deprez, S. Vandenberghe, and R. Vanholen. Collimating shutter. *European Patent 11165483.6*, May 10th, 2011.

[235] K. Van Audenhaege, R. Van Holen, K. Deprez, J. Karp, S. Metzler, and S. Vandenberghe. Design of a static full-ring multi-pinhole collimator for brain SPECT. In *IEEE Nucl. Sci. Symp. Conf. Rec. 2011*, pages 4393–4397, November 2011.

[236] K. Van Audenhaege, R. Van Holen, and S. Vandenberghe. Analysis of the trade-off between sensitivity and resolution of a pinhole collimator for SPECT. In *J. Nucl. Med.*, volume 53 (suppl.1), pages 2410–2410, 2012.

[237] K. Van Audenhaege, B. Vandeghinste, S. Vandenberghe, and R. Van Holen. Time-multiplexing using a static full-ring multi-pinhole collimator for brain SPECT. In *IEEE Nucl. Sci. Symp. Conf. Rec. 2012*, pages 3097–3100, November 2012.

[238] K. Van Audenhaege and S. Vandenberghe. Optimization of collimator combinations for brain SPECT. In *11e UGent-FirW Doctoraatssymposium*, pages 66–66, 2010.

[239] K. Van Audenhaege, S. Vandenberghe, K. Deprez, B. Vandeghinste, and R. Van Holen. Design and simulation of a full-ring multilofthole collimator for brain SPECT. *Phys. Med. Biol.*, 58(18):6317–36, September 2013.

[240] K. Van Audenhaege, S. Vandenberghe, C. Vanhove, and R. Van Holen. Collimator design for a multi-pinhole brain SPECT insert for MRI. In *IEEE Nucl. Sci. Symp. Conf. Rec. 2014*, November 2014.

[241] K. Van Audenhaege, S. Vandenberghe, C. Vanhove, and R. Van Holen. Collimator design for a multi-pinhole brain SPECT insert for MRI. *Med. Phys.*, 2015. under review.

[242] K. Van Audenhaege, C. Vanhove, S. Vandenberghe, and R. Van Holen. Data completeness in multiplexing multi-pinhole SPECT. In *IEEE Nucl. Sci. Conf. Rec.*, pages 1–8, November 2013.

[243] K. Van Audenhaege, C. Vanhove, S. Vandenberghe, and R. Van Holen. The evaluation of data completeness and image quality in multiplexing multi-pinhole SPECT. *IEEE Trans. Med. Imag.*, 34(2):474–486, February 2014.

[244] K. Van Audenhaege, C. Vanhove, S. Vandenberghe, and R. Van Holen. Review of SPECT collimator selection, optimization, and fabrication for clinical and preclinical imaging. *Med. Phys.*, 42(8):4796–4813, August 2015.

[245] F. Van Der Have and F. J. Beekman. Penetration, scatter and sensitivity in channel micro-pinholes for SPECT: A Monte Carlo investigation. *IEEE Trans. Nucl. Sci.*, 53(5):2635–2645, October 2006.

[246] F. Van Der Have, B. Vastenhouw, R. M. Ramakers, W. Branderhorst, J. O. Krah, C. Ji, S. G. Staelens, and F. J. Beekman. U-SPECT-II: An ultra-high-resolution device for molecular small-animal imaging. *J. Nucl. Med.*, 50(4):599–605, april 2009.

[247] R. Van Holen. *SPECT imaging with rotating slat collimation*. PhD thesis, University Ghent, 2009.

[248] R. Van Holen, J. W. Moore, E. W. Clarkson, L. R. Furenlid, and H. H. Barrett. Design and validation of an adaptive SPECT system: AdaptiSPECT. *IEEE Nucl. Sci. Symp. Conf. Rec.*, 1:1–6, 2010.

[249] R. Van Holen, S. Staelens, and S. Vandenberghe. SPECT imaging of high energy isotopes and isotopes with high energy contaminants with rotating slat collimators. *Med. Phys.*, 36(2009):4257–4267, 2009.

[250] R. Van Holen, B. Vandeghinste, K. Deprez, and S. Vandenberghe. Design and performance of a compact and stationary microSPECT system. *Med. Phys.*, 40(11):112501 (11pp.), December 2013.

[251] R. Van Holen, S. Vandenberghe, S. Staelens, and I. Lemahieu. Comparing planar image quality of rotating slat and parallel hole collimation: influence of system modeling. *Phys. Med. Biol.*, 53(7):1989–2002, April 2008.

[252] S. Vandenberghe and P. K. Marsden. PET-MRI: a review of challenges and solutions in the development of integrated multimodality imaging. *Phys. Med. Biol.*, 60:R115–R154, 2015.

[253] S. Vandenberghe, R. Van Holen, S. Staelens, and I. Lemahieu. System characteristics of SPECT with a slat collimated strip detector. *Phys. Med. Biol.*, 51(2):391–405, January 2006.

[254] C. Vanhove, A. Andreyev, M. Defrise, J. Nuyts, and A. Bossuyt. Resolution recovery in pinhole SPECT based on multi-ray projections: a phantom study. *Eur. J. Nucl. Med. Mol. Imaging*, 34(2):170–80, February 2007.

[255] C. Vanhove, M. Defrise, T. Lahoutte, and A. Bossuyt. Three-pinhole collimator to improve axial spatial resolution and sensitivity in pinhole SPECT. *Eur. J. Nucl. Med. Mol.*, 35(2):407–15, February 2008.

[256] P. Veit-Haibach, F. P. Kuhn, F. Wiesinger, G. Delso, and G. Von Schulthess. PET-MR imaging using a tri-modality PET/CT-MR system with a dedicated shuttle in clinical routine. *Magn. Res. Mater. Phy.*, 26:25–35, 2013.

[257] K. Vunckx. *High quality image formation of small animals using emission*. PhD thesis, Katholieke Universiteit Leuven, Belgium, 2008.

[258] K. Vunckx, J. Nuyts, B. Vanbilloen, M. De Saint-hubert, D. Vanderghinste, D. Rattat, F. M. Mottaghy, and M. Defrise. Optimized multipinhole design for mouse imaging. *IEEE Trans. Nucl. Sci.*, 56(5):2696–2705, 2009.

[259] K. Vunckx, P. Suetens, and J. Nuyts. Effect of overlapping projections on reconstruction image quality in multipinhole SPECT. *IEEE Trans. Med. Imag.*, 27(7):972–983, July 2008.

[260] K. Vunckx, P. Suetens, and J. Nuyts. Effect of overlapping projections on reconstruction image quality in multipinhole SPECT. *IEEE Trans. Med. Imag.*, 27(7):972–983, July 2008.

[261] R. F. Wagner. Decision theory and the detail signal-to-noise ratio of Otto Schade. *Photogr. Sci. Engr.*, 22:41–46, 1978.

[262] R. F. Wagner and D. G. Brown. Unified SNR analysis of medical imaging systems. *Phys. Med. Biol.*, 30:489–518, 1985.

[263] S. Walrand, M. Hesse, R. Wojcik, R. Lhommel, and F. Jamar. Optimal design of anger camera for bremsstrahlung imaging: Monte Carlo evaluation. *Front. Oncol.*, 4(June):149 (7pp.), 2014.

[264] J. P. Wansapura, S. K. Holland, R. S. Dunn, and W. S. Ball. NMR relaxation times in the human brain at 3.0 tesla. *J. Magn. Reson. Imaging*, 9(4):531–538, 1999.

[265] J. D. Wasscher. On four-point resistivity measurements on anisotropic conductors. *Philips Res. Rep.*, 16:301–306, 1961.

[266] W. Weber, P. Bartenstein, M. W. Gross, and D. Kinzel. Fluorine-18-FDG PET and iodine-123-IMT SPECT in the evaluation of brain tumors. *J. Nucl. Med.*, 38(5):802–808, 1997.

[267] J. Wehner, B. Weissler, P. Dueppenbecker, P. Gebhardt, D. Schug, W. Ruetten, F. Kiessling, and V. Schulz. PET/MRI insert using digital SiPMs: Investigation of MR-compatibility. *Nucl. Instr. Meth. Phys. Res. A*, 734:116–121, January 2014.

[268] A. L. Weinmann, C. B. Hruska, and M. K. O'Connor. Design of optimal collimation for dedicated molecular breast imaging systems. *Med. Phys.*, 36(2009):845–856, 2009.

[269] B. Weissler, P. Gebhardt, P. Diippenbecker, A. Salomon, D. Schug, C. Lerche, D. Wirtz, W. Renz, K. Schumacher, B. Zwaans, P. Marsden, F. Kiessling, and V. Schulz. Design concept of world's first preclinical PET / MR insert with fully digital silicon photomultiplier technology. *IEEE Nucl. Sci. Symp. Conf. Rec.*, pages 2113–2116, 2012.

[270] H. Wieczorek and A. Goedicke. Analytical model for SPECT detector concepts. *IEEE Trans. Nucl. Sci.*, 53(3):1102–1112, June 2006.

[271] D. W. Wilson, H. H. Barrett, and E. W. Clarkson. Reconstruction of two- and three-dimensional images from synthetic-collimator data. *IEEE Trans. Med. Imaging*, 19(5):412–22, May 2000.

[272] H. Zaidi, N. Ojha, M. Morich, J. Griesmer, Z. Hu, P. Maniawski, O. Ratib, D. Izquierdo-Garcia, Z. A. Fayad, and L. Shao. Design and performance evaluation of a whole-body Ingenuity TF PET-MRI system. *Phys. Med. Biol.*, 56(10):3091–106, May 2011.

[273] G. L. Zeng. Helical SPECT using axially truncated data. *IEEE Trans. Nucl. Sci.*, 46(6):2111–2118, 1999.

[274] G. L. Zeng. Revisit of combined parallel-beam/cone-beam or fan-beam/cone-beam imaging. *Med. Phys.*, 40(10):100701 (5pp.), 2013.

[275] G. L. Zeng, D. Gagnon, C. G. Matthews, J. A. Kolthammer, J. D. Radachy, and W. G. Hawkins. Image reconstruction algorithm for a rotating slat collimator. *Med. Phys.*, 29(7):1406–1412, 2002.

[276] G. L. Zeng, J. R. Galt, M. N. Wernick, R. A. Mintzer, and J. N. Aarsvold. *Single-photon emission computed tomography*, chapter 7, pages 127–151. San Diego, London: Elsevier Academic, 2004.

[277] G. L. Zeng and G. T. Gullberg. Unmatched projector/backprojector pairs in an iterative reconstruction algorithm. *IEEE Trans. Med. Imag.*, 19(5):548–555, May 2000.

[278] G. L. Zeng and G. T. Gullberg. A channelized-hotelling-trace collimator design method based on reconstruction rather than projections. *IEEE Trans. Nucl. Sci.*, 49(5):2155–2158, Oct 2002.

[279] G. L. Zeng, G. T. Gullberg, B. M. W. Tsui, and J. A. Terry. Three-dimensional iterative reconstruction algorithms with attenuation and geometric point response correction. *IEEE Trans. Nucl. Sci.*, 38(2):693–702, 1991.

[280] L. Zhou and G. Gindi. Collimator optimization in SPECT based on a joint detection and localization task. *Phys. Med. Biol.*, 54(14):4423–37, July 2009.

[281] L. Zhou, S. Kulkarni, B. Liu, and G. Gindi. Strategies to jointly optimize SPECT collimator and reconstruction parameters for a detection task. *IEEE I. S. Biomed. Imaging (Boston, MA)*, pages 394–397, 2009.

[282] L. Zhou, K. Vunckx, and J. Nuyts. Parallel hole and rotating slat collimators: comparative study using digital contrast phantoms. *IEEE Trans. Nucl. Sci.*, 60(5):3282–3289, October 2013.

[283] F. Zito, A. Savi, and F. Fazio. CERASPECT: a brain-dedicated SPECT system. Performance evaluation and comparison with the rotating gamma camera. *Phys. Med. Biol.*, 38:1433–1442, 1993.